UNIVERSITY OF SOUTHAMPTON

FACULTY OF ENGINEERING, SCIENCE AND MATHEMATICS
Optoelectronics Research Centre

Laser-Assisted Surface and Domain Microstructuring of Lithium Niobate

Jeffrey Gordon Scott

Thesis for the degree of Doctor of Philosophy

June 2005

UNIVERSITY OF SOUTHAMPTON

ABSTRACT

FACULTY OF ENGINEERING, SCIENCE AND MATHEMATICS
OPTOELECTRONICS RESEARCH CENTRE

Doctor of Philosophy

Laser-Assisted Surface and Domain Microstructuring of Lithium Niobate

By Jeffrey Gordon Scott

This thesis presents the results of investigations into the nano-structuring of lithium niobate using the combined or sequential action of laser light and a chemical etch (a mixture of hydrofluoric and nitric acids). Novel methods to characterise ferroelectric domains using Raman spectroscopy and surface second harmonic generation are also described.

The light induced frustration of etching (LIFE) technique, which is the simultaneous exposure of iron-doped lithium niobate to visible laser light at 532 nm and chemical etchant, was studied in detail. The presence of light was found to modify the normal etching process, resulting in either total or partial frustration of etching on the $-z$ face; formation of complex self-organised structures in the partially frustrated areas was observed. Experiments show that the iron dopant concentration, irradiance and duration of etching are the key parameters which define the structures that are formed. The structures were visualised by scanning electron microscopy and the resulting images were analysed with a Fourier transform method. The LIFE structures were also studied using a modified atomic force microscope, capable of detecting surface charges, which revealed that the structures were of the opposite charge to the surrounding area.

Surface structuring was also achieved on undoped lithium niobate, by exposure to ultraviolet wavelengths from a pulsed laser system followed by etching. Both $+z$ and $-z$ lithium niobate faces were studied, with significantly different results from each. The $+z$ face is usually resistant to etching by acids, but following ablation by UV light, etching revealed the existence of trenches which ran along directions parallel to the crystallographic y axes. The trenches had widths of 150 - 300 nm and depths of $\sim$1.8 μm. UV exposure of the $-z$ face was found to induce frustration of etching, forming many small (sub-micron) individual features. Large-scale (mm sized) patterning of these features was achieved using exposure through both phase and amplitude masks.

The use of Raman spectroscopy as a diagnostic technique for recently poled lithium niobate was investigated. The position of several Raman peaks were observed to be shifted following electric-field domain inversion; some these peaks returned to their original positions with a characteristic time constant that is related to the recovery of the internal field of lithium niobate. Surface second harmonic generation was also shown to be able to distinguish between opposite z faces of virgin and poled lithium niobate.

Contents

List of Figures

Declaration of Authorship

I, Jeffrey Gordon Scott, declare that the thesis entitled *Laser-Assisted Surface and Domain Microstructuring of Lithium Niobate* and the work presented in it are my own. I confirm that:

- this work was done wholly or mainly while in candidature for a research degree at this University;
- where any part of this degree has previously been submitted for a degree or any other qualification at this University or any other institution this has been clearly stated;
- where I have consulted the published work of others, this is always clearly attributed;
- where I have quoted from the work of others, the source is always given. With the exception of such quotations, this thesis is entirely my own work;
- I have acknowledged all main sources of help;
- where the thesis is based on work done by myself or myself jointly with others, I have made clear exactly what was done by others and what I have contributed myself;
- parts of this work have been published, as listed in Appendix C.

Signed: .....

Date: .....

Acknowledgements

I would like to start by thanking Rob Eason for his guidance, enthusiasm and support during my time at the ORC and for the many meetings discussing the meaning of LIFE! Thank you also to the group's Postdocs, Sakellaris Mailis and Collin Sones, for their help and the expertise they shared with me. Special thanks go to Rob and Sak for their great company on the fantastic visits to Crete and Munich. I would also like to acknowledge the EPSRC for the funding I have received during the course of my PhD.

I would like to thank the other group members I have had the pleasure of working with, particularly Alex Boyland who livened up the long hours spent using the SEM and Chris Valdivia for the enjoyable trips to Bristol and RAL.

I am also grateful to the other people and groups I have had the opportunity to collaborate with, including Tleyane Sono, originally from the School of Chemistry but now a new recruit to the ORC and Ian Clark at RAL. I am indebted to Nils Benter for looking after me during my visit to Bonn and making me feel welcome despite my total lack of German. Thanks also go to him, his supervisor Karsten Buse and Elisabeth Soergel for the use of their charge-mode AFM.

Thank you to my office-mates, initially of Office 2071 and then later Portacabin A after we were evicted out to the car park, for always being ready for a chat and a cup of tea! Thanks also to my friends within the ORC, for numerous illuminating lunchtime conversations and after work trips to the 'Staffie', which helped keep me sane. And thanks to all my other great friends, despite their jokes about physicists and eternal students!

Last, but definitely not least, thank you to Sarah Denny for always being there and to my parents for all their love and support. I could not have got here without you.

"I'm living in the weirdest dream
Where nothing is the way it seems
Where no one's who they need to be
Where nothing seems that real to me
What can we build our lives upon
No wall of stone, no solid ground
The world is spinning endlessly
We're clinging to our own beliefs"

Tim Booth, from the song *Born of Frustration.*

CHAPTER

ONE

Introduction

The relatively new field of Photonics, the science and technology of generating and controlling light, emerged following the invention of the laser in 1960. This was a key discovery that allowed previously unimaginable control over properties such as the wavelength, power, and pulse length of light. Since then, photonics and the laser have revolutionised many areas of science and technology, and developments continue to the present day. In many ways photonics can be seen as a rival technology to electronics. For instance, fibre-optic systems have a massively higher capacity for transmission of phone calls, television channels and data than possible using an electronic signal over a copper wire.

While electronic devices tend to be based on silicon, a widely used material in photonics is lithium niobate. Due to this material's unusually wide variety of properties it is used in many areas of technological and scientific interest. For instance, it is used in high speed optical modulators for telecommunications devices, optical frequency conversion, waveguides and high speed filters in electronic devices (such as televisions and mobile phones). It is also being investigated for use in holographic data storage which has the potential to store massive amounts of information. Lithium niobate's piezoelectric electric properties also make it suitable for use in the production of Micro-Electro-Mechanical Systems (MEMS). Further discussion of lithium niobate's properties can be found in Section 2.3 and more details of its applications are given in Section 2.5.

Many current and potential future applications of lithium niobate are dependent on the ability to structure the crystal, in one of two ways. The first is the production of surface topographical features, often by etching away material from the crystal face. The second technique involves the modification of the internal ferroelectric structure of the crystal, by a process called domain inversion, or poling. Both frequently require the masking an area or production of a pattern using photolithography with essentially the same process as used for silicon. However, lithium niobate's wide range of properties allow a variety of other novel structuring methods to be developed and used. It is, for instance, strongly affected by exposure to light, with effects varying from changes in the refractive index to ablation of the crystal surface, depending on the exposure conditions.

Domain structuring of lithium niobate is of particular technological significance, primarily for the production of periodically poled lithium niobate (PPLN), which is used in quasi-phase-matching for frequency conversion applications (see Section 2.5.3.2 for more details).

Examples of applications using surface structures include surface relief gratings, which have the advantage over photorefractive gratings that they are less likely to suffer from deterioration over time. There are a number of ways of producing surface relief gratings on $LiNbO_3$, Mailis et al. (2000) used a combination of UV laser exposure and wet etching, while Capmany et al. (2003) have reported producing surface relief diffraction gratings by selective etching of periodically poled lithium niobate, hence using one type of structuring (domain) to produce the other (surface). More complicated surface structures can also be used to produce photonic band gap materials. Surface structures can also be used as rib waveguides and surface trenches like those produced in Chapter 4, could be used as part of a 'lab on a chip', where fluids could be be quickly and simply analysed by lasers, all on a small single crystal wafer.

Surface and domain structuring can also be combined with other technologies to produce useful devices. For instance Das et al. (2003) have demonstrated a distributed feedback (DFB) laser in a lithium niobate waveguide, which produces a stable, narrow-bandwidth output. Surface structuring could also be of use in surface acoustic wave (SAW) devices, by using surface structures as interdigital electrodes. See Section 2.5.4 for further details on SAW devices. Potential uses for surface structuring, and the associated requirements are summarised in Table 1.1.

The three techniques of structuring mentioned earlier, poling, light and etching, may be be combined to give a broader range of control and possibilities for

Table 1.1: Uses of surface structures and the typical dimensions and periods required.

Use	Feature Size	Period	Etch Depth
Rib Waveguides	~2 μm*	N/A	~2 μm*
Surface Relief Gratings	~350 nm	~350 nm	~1 μm
Photonic Band Gap Materials	~350 nm	~350 nm	~1 μm
Surface Acoustic Wave Devices	~0.5 μm	~1 μm*	~2 μm

* Depending on application

surface structuring or domain engineering. This is illustrated in Figure 1.1, where each technique is represented by a circle and the three areas of overlap represent combinations of the techniques.

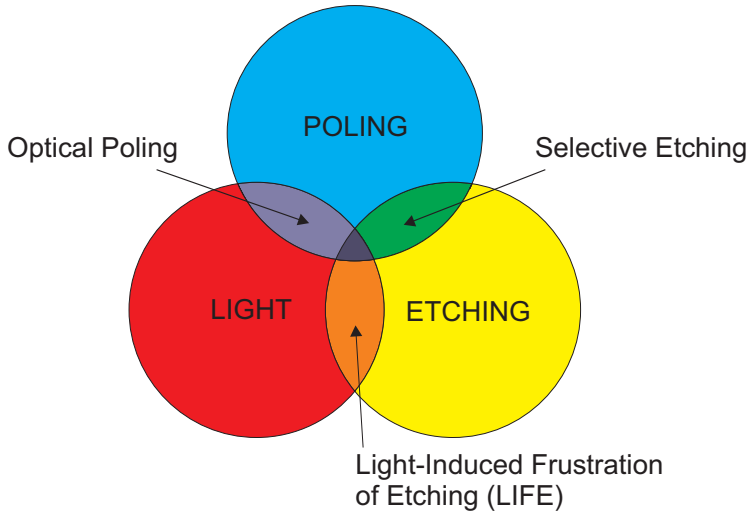

Figure 1.1: The three main techniques for structuring lithium niobate and their possible combinations.

The combination of poling and etching is a commonly used technique for lithium niobate, where one face of a ferroelectric domain experiences a much greater etch rate than that of the opposite face, resulting in selective etching. This results in a very useful technique to visualise domain structures. The dual influence of light and etching results in 'Light-Induced Frustration of Etching' (LIFE), which allows the usual etching properties of lithium niobate to be changed, giving the ability to produce optically-defined surface structures. Additionally, self-organised structures can be produced under the correct conditions and this technique is described in Chapter 3. The combined influence of light and poling is known as 'Optical Poling' and the first observation of this in lithium niobate, to the best of our knowledge, is discussed in Chapter 4. This technique could potentially replace

electric-field poling in the future, allowing the creation of smaller domains and offering simpler fabrication routes.

This thesis describes the results of three years of research into surface and domain structuring of lithium niobate, using the three techniques of etching, poling and light. A variety of related topics are also discussed, including the time-dynamics of domains following poling, observed by Raman spectroscopy and the use of second harmonic generation from the crystal surface for observing the presence of inverted domains.

The thesis starts with a review of lithium niobate in Chapter 2, which discusses its history, crystal structure and growth before moving on to the various properties which make lithium niobate so unique. Techniques for structuring lithium niobate which are relevant to this work are then considered, followed by a summary of the uses and applications of the material.

The technique of Light Induced Frustration of Etching (LIFE) using green visible light is described in detail in Chapter 3 and the influence of factors such as the laser beam parameters and crystal dopant are examined. The chapter contains images of the structures produced in the experiments that were obtained by scanning electron microscopy. Other analysis that has been undertaken is also described. The chapter concludes with a discussion on the possible mechanisms responsible for the results that were obtained.

Chapter 4 contains the results of experiments on the exposure of lithium niobate to light of ultraviolet wavelengths, and shows the differences that occur depending on whether the $+z$ or $-z$ face is exposed. SEM images are again used to illustrate these differences and the structures that are formed. Possible mechanisms are again discussed.

Chapter 5 presents the results of an Raman spectroscopic study of lithium niobate which had been recently domain inverted by electric field poling. The general theory of Raman scattering is applied to the specific case of lithium niobate and then compared with experimental results. The results show the change in position of Raman peaks following poling and the subsequent recovery of some of these peaks with a characteristic time scale.

The use of surface second harmonic generation (SHG) as a diagnostic tool for identifying ferroelectric domains in lithium niobate is described in Chapter 6. The theory of SHG is explained and applied to the case of surface SHG from lithium niobate. Surface SHG is found to be dependent on the angle of polarisation of the

light relative to the crystal, as expected from theory, and also on the orientation of the ferroelectric domain in lithium niobate.

Appendix A gives additional details on some of the instruments used to obtain results shown in this thesis. Appendix B contains the Matlab source code for the programs that were written during the course of this research. Finally, a list of publications arising from this work are presented in Appendix C.

1.1 References

Capmany, J., C. R. Fernandez-Pousa, E. Dieguez and V. Bermudez. "Surface-relief diffraction gratings based on selective etching of periodically poled lithium niobate." *Applied Physics Letters*, **83**(25), 5145 (2003).

Das, B. K., R. Ricken and W. Sohler. "Integrated optical distributed feedback laser with Ti:Fe:Er:$LiNbO_3$ waveguide." *Applied Physics Letters*, **82**(10), 1515 (2003).

Mailis, S., G. W. Ross, L. Reekie, J. A. Abernethy and R. W. Eason. "Fabrication of surface relief gratings on litium niobate by combined UV laser and wet etching." *Electronics Letters*, **36**(21), 1801 (2000).

CHAPTER

TWO

Lithium Niobate

Lithium niobate[1], $LiNbO_3$, is an artificially synthesised crystal, which was found to be ferroelectric by Matthias and Remeika (1949). This was an exciting result, as at the time only a limited number of ferroelectric materials were known. An earlier paper by Zachariasen (1928) described lithium niobate as having a centrosymmetric ilmenite structure; so at the time it was thought that lithium niobate was the first of a new group of ferroelectric crystals, based on the ilmenite structure (which also included lithium tantalate, $LiTaO_3$). The known other groups were based on potassium dihydrogen phosphate, barium titanate and Rochelle salt, the first ferroelectric to be discovered.

However a problem existed. The characteristic feature of ferroelectric crystals is their spontaneous polarisation. But a crystal can only have a spontaneous polarisation if it does not possess a centre of symmetry, i.e. if it lacks inversion symmetry. This makes the notion of a centrosymmetric ilmenite ferroelectric contradictory. This problem persisted until Bailey (1952) carried out X-ray diffraction experiments and determined that while the actual structure was related to ilmenite, there were also significant differences. However, the data could not unambiguously determine the structure; it was shown instead shown that two possible structures, both with the space group R3c, could fit the results. Megaw

[1]This is the modern accepted name, although some early papers refer to it as lithium columbate. Niobium and columbium were both used as the name of the element with atomic number 41 until niobium was officially adopted by the International Union of Pure and Applied Chemistry (IUPAC) in 1950.

(1954) used symmetry arguments to show that one of the possible structures, a distorted perovskite, was very much more likely than the other.

Some questions about the nature of lithium niobate's ferroelectricity remained unanswered; in particular how it would be possible for the direction of polarisation to be reversed. This is crucial, as the reversibility of the spontaneous polarisation is the defining characteristic of a ferroelectric compared to a pyroelectric material (ferroelectrics are a subset of pyroelectrics). Experiments up to this time had not been able to locate the Curie point nor observe polarisation reversal using hysteresis loop techniques. Megaw consequently suggested that lithium niobate was a 'frozen ferroelectric', meaning that while it was theoretically possible to invert the direction of polarisation, the available field strengths were not great enough to overcome the strength of structural forces at room temperature. This idea of a frozen ferroelectric was eventually shown to be mistaken by Camlibel (1969), who used a pulsed-field method to determine the spontaneous polarisation, during which the domain direction was reversed. However, very high fields were required (~300 kV/cm) to achieve this. The technique of controlled electric field domain inversion was not fully developed for many years after this paper was published, due to technological problems associated with the lack of control and dielectric breakdown. For further details see Section 2.4.1

Detailed research into lithium niobate continued during the 1960s, spurred on by the growth of better quality crystals. Ballman (1965) first reported growth of lithium niobate using the Czochralski technique (see Section 2.2 for details), to produce large crystals of higher quality than had been previously obtained using a flux method. This allowed a series of key papers to be published, (Nassau et al., 1965, 1966a,b; Abrahams et al., 1966a,b,c) detailing the growth and structural properties of lithium niobate, based on comprehensive x-ray diffraction experiments. The first observation of differential etch rates between $+z$ and $-z$ faces was also reported. Further details on differential etching are included in Section 2.4.2.

Lithium niobate continues to be the subject of intense scientific research as well as being used for a variety of technological applications. This popularity is due to the unusually wide range of useful properties the material exhibits. It has large pyroelectric, piezoelectric, electro-optic and nonlinear coefficients, it is birefringent (which lead to an early interest in lithium niobate for use in phase matching experiments (Boyd et al., 1964)) and has good acoustic and acousto-optic wave properties. It also has a strong bulk photovoltaic effect, which resulted in lithium niobate being the first material found to show photorefractivity. Applications of these properties are discussed in more detail in Section 2.5.

2.1 Crystal Structure and Symmetry

Lithium niobate experiences a phase change from the ferroelectric state to the paraelectric state when the temperature is increased beyond the Curie temperature, $T_c \approx 1210\,°C$, which is rather close to the melting point at 1260 °C. In the ferroelectric state it exhibits a spontaneous polarisation, P_s, caused by the separation of the centres of charge from their equilibrium positions by elastic forces. There is no spontaneous polarisation in the paraelectric state.

The crystal structure can be described as layers of oxygen atoms in a distorted hexagonal close-packed configuration, with the octahedral interstices alternately filled by lithium atoms, niobium atoms and then vacancies, as illustrated in Figure 2.1.

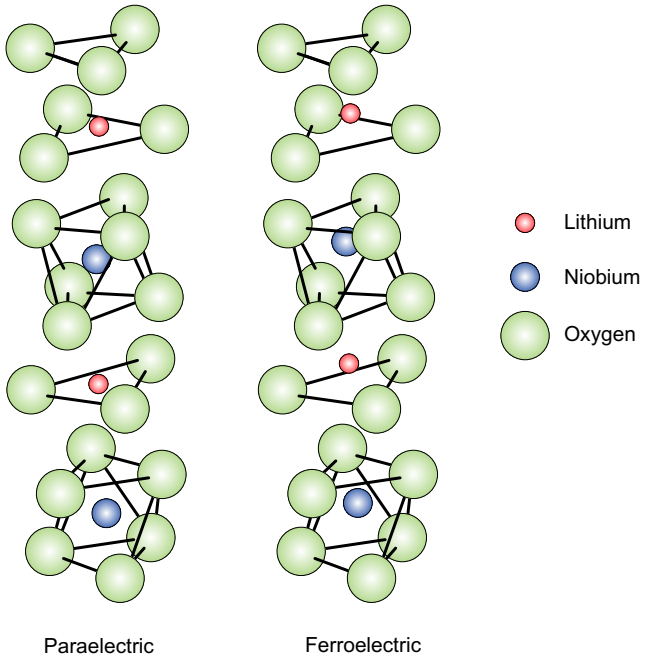

Figure 2.1: The structure of lithium niobate in the paraelectric and ferroelectric phases, after Weis and Gaylord (1985).

In the paraelectric phase, the lithium atoms lie in an oxygen plane, and the niobium atoms are centred between the oxygen layers. However, in the ferroelectric phase the lithium and niobium atoms are displaced, thus defining the direction of the polarisation. This is illustrated more simply in Figure 2.2, where the oxygen layers are represented by lines. Each oxygen layers is 2.310 Å from each other, and the distance to the nearest oxygen plane is 0.897 Å for niobium and 0.714 Å for lithium (Prokhorov and Kuuzminov, 1990). The paraelectric phase has space group $R\bar{3}c$,

which possesses inversion symmetry; this is removed in the ferroelectric phase which has group R3c (Wong, 2002).

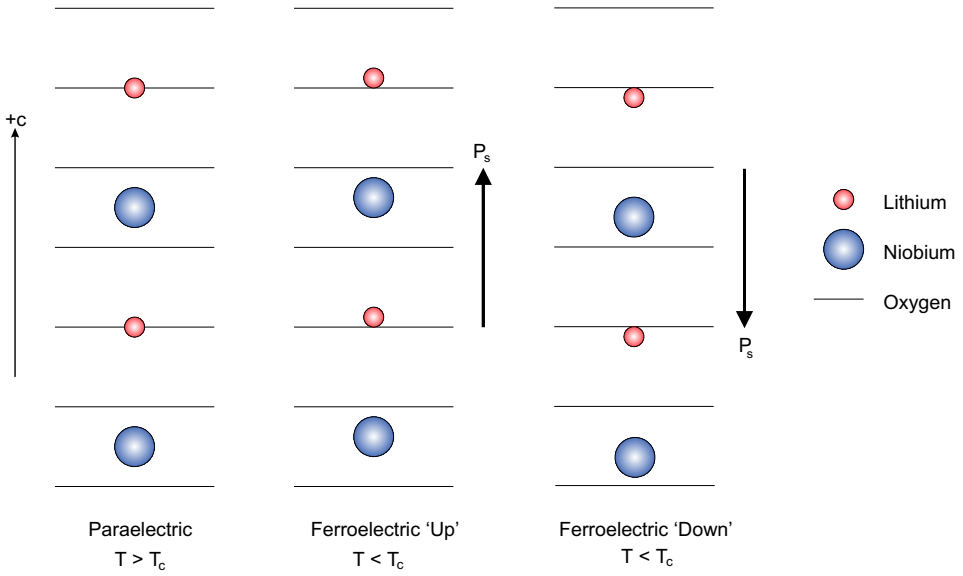

Figure 2.2: The paraelectric and ferroelectric phases of lithium niobate, with the corresponding relative atomic positions. In the ferroelectric phase, the lithium and niobium atoms are displaced either above or below their central paraelectric positions, resulting in two possible domain orientations, with a spontaneous polarisation P_s.

As discussed in the previous section, X-ray diffraction experiments showed that lithium niobate has a distorted perovskite structure. The mineral Perovskite, $CaTiO_3$, shares its basic structure with a number of ferroelectric crystals, all with the general formula ABO_3, such as barium titanate ($BaTiO_3$), lead zirconate ($PbZrO_3$) and lithium tantalate ($LiTaO_3$).

Ferroelectric lithium niobate has a three-fold rotational axis of symmetry about the c axis, and so is classified as part of the trigonal group of crystals. It also has three vertical planes of symmetry at 60° to each other. Together these properties result in $LiNbO_3$ being part of the $3m$ point group (C_{3v} in Schönflies notation).

In common with all trigonal crystals, lithium niobate may be described by either a rhombohedral or hexagonal lattice. The rhombohedral cell is the smaller of the two, containing only 2 formula weights, while the hexagonal cell contains 6 formula weights. The hexagonal cell is the most commonly used, due to the simplicity of the Cartesian coordinates when using this system. The c axis of the cell is parallel to the polar z axis of the crystal, while the x axis is chosen to be parallel to one of the three equivalent a axes, which are 120° apart, and are perpendicular to both the c axis and the planes of symmetry. Consequently the y axis is defined as being

perpendicular to both the x and z axes, and so lies along a plane of symmetry (Weis and Gaylord, 1985). These relationships are illustrated in Figure 2.3, which also shows the hexagonal unit cell.

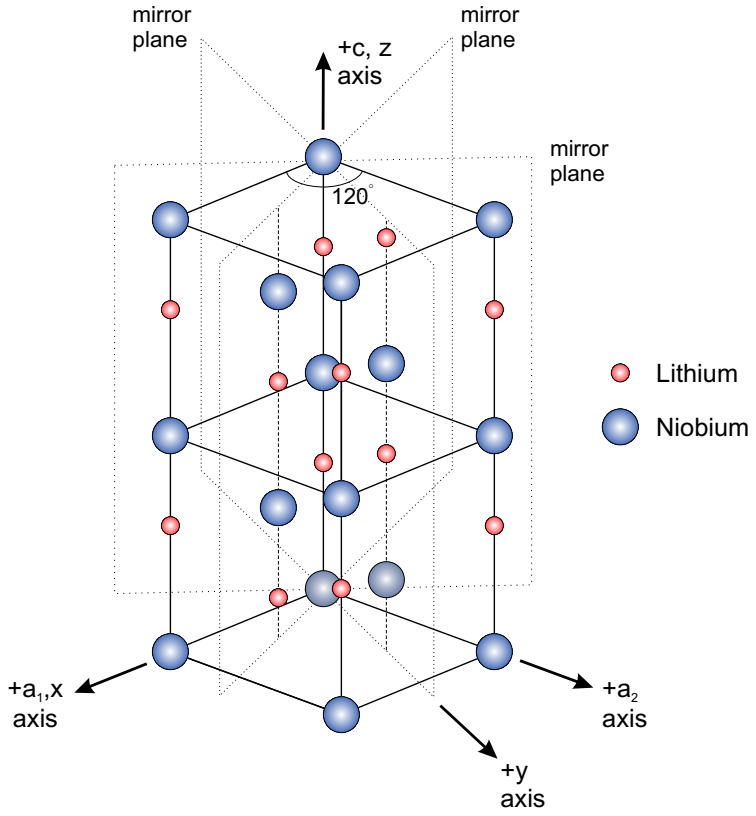

Figure 2.3: The hexagonal unit cell of lithium niobate, with hexagonal and Cartesian axes indicated. The oxygen atoms have been omitted for clarity.

The direction of the c axis can be determined by compressing the crystal; the $+c$ axis is directed out of the c face that becomes negatively charged on compression. This is caused by movement of the Li and Nb ions towards their central positions when the crystal is compressed. Consequently the polarisation is reduced and an excess of compensating negative charge is left on the $+c$ face.

2.2 Crystal Growth and Composition

The annual production of lithium niobate is over 60 tons, most of which is grown using the Czochralski method. To make $LiNbO_3$, pure Li_2O and Nb_2O_5 powders are melted in a platinum crucible. A rotating seed crystal is then dipped into the melt, which is held slightly over the melting point, and gradually withdrawn. Material will attach to the seed crystal, and as it cools single crystal lithium niobate will

form. A uniform direction of polarisation in the crystal is created by the application of a small electric field (0.2 - 5 V/cm) during cooling of the crystal boule after it has been grown. The electric field required is much smaller than would be necessary at room temperature, as the crystal is closer to the Curie temperature. Precise details of the conditions used can be found in Nassau et al. (1966a) or Bordui et al. (1991).

Lithium niobate crystals are generally not stoichiometric, the actual composition deviates away from the ideal Li:Nb:O ratio of 1:1:3 for $LiNbO_3$, with most crystals being lithium deficient. The composition, x_c, is defined by

$$x_c = \frac{[\mathrm{Li}]}{([\mathrm{Li}] + [\mathrm{Nb}])} \tag{2.1}$$

The most common composition is congruently melting, where the composition of the melt is the same as the composition of the crystal grown from that melt, with x_c = 48.5 %. This composition is chosen as it produces the most homogeneous crystals with the highest quality and good repeatability between batches.

Non-congruent crystals have compositions that are different from the composition of the melt from which they are grown, so even if a stoichiometric melt is used, this will not necessarily result in a stoichiometric crystal. An added problem using non-congruent melts is that as the crystal is grown, the composition of the melt will change, resulting in a crystal with a varying composition along its length. If non-congruent crystals are required, then the melt needs to be replenished to maintain its composition using a double crucible Czochralski method. Kitamura et al. (1992) used this technique to produce near-stoichiometric lithium niobate. Another method for making near-stoichiometric crystals has been reported by Malovichko et al. (1992), where potassium is added to the melt. Usually dopants added to the melt are taken up into the crystal, but this does not occur for potassium, instead it appears to 'catalyse' the growth of stoichiometric lithium niobate. This method has the advantage of producing crystals with lower intrinsic defect concentrations than those made using a double Czochralski method (Malovichko et al., 1993).

The composition of a lithium niobate crystal can be determined by measuring the Curie temperature, the refractive index, the birefringence and UV absorption edge (Wohlecke et al., 1996). The composition can have a major effect on crystal properties, such as the coercive field required for domain inversion and the related internal field; both of these fields are considerably reduced in a stoichiometric material (Gopalan et al., 1998).

Lithium niobate crystals with compositions other than stoichiometric, inevitably contain intrinsic defects in their lattices, due to the lithium deficiency. It was reported by Abrahams and Marsh (1986) that, based on x-ray diffraction measurements, 6 % of lithium is missing from each lithium site and every Li^+ ion that is missing is replaced by an antisite Nb^{5+} ion, occupying a Li^+ site (Nb_{Li}). This creates an excess of charge, and so Abrahams proposes that to maintain charge neutrality, niobium ions vacancies (V_{Nb}) are created. However there is also experimental evidence supporting a Li-vacancies (V_{Li}) model for charge compensation (Watanabe et al., 1995).

Extrinsic defects, caused by the presence of chemical impurities, are also common in lithium niobate crystals. Congruent lithium niobate is especially tolerant to impurities due to the large number of intrinsic defects which can compensate for any differences in charge (Malovichko et al., 1999). Common impurity ions include H^+, Mg^{2+}, Zn^{2+}, Cu^{2+}, Fe^{2+}, Fe^{3+}, Ni^+, Ni^{2+}, Ti^{3+}, Ti^{4+} (Wong, 2002). In high enough concentrations these impurities can modify the properties of the lithium niobate crystal, which can be useful. For instance, Mg^{2+} is used to suppress the photorefractive effect, and so allow the use of lithium niobate in high-power laser applications (Zhong et al., 1980). Conversely, Fe ions serve to enhance the photorefractive effect, which can be useful in holographic data storage (Nee et al., 2000) In this way it is possible to purposely dope lithium niobate to tune its properties for use in specific applications.

2.3 Properties of Lithium Niobate

The key physical properties of lithium niobate are summarised in this section.

2.3.1 Ferroelectric effect

Ferroelectric materials have two or more directions of spontaneous electric polarisation, which are reversible by the application of an electric field. Lithium niobate has a polarisation, $\mathbf{P}_s \approx 71\ \mu C/cm^2$, which is orientated in one of two possible directions along the z axis. By definition, all ferroelectrics must also be pyroelectric.

2.3.2 Pyroelectric effect

The pyroelectric effect is a change in spontaneous polarisation with temperature.

$$\Delta \mathbf{P}_s = \boldsymbol{\xi} \Delta T \tag{2.2}$$

In lithium niobate, this is caused by the movement of lithium and niobium ions relative to the oxygen layers, along the z axis, hence the the pyroelectric tensor, $\boldsymbol{\xi}$, is represented by:

$$\boldsymbol{\xi} = \begin{bmatrix} 0 \\ 0 \\ \xi_3 \end{bmatrix} \tag{2.3}$$

with $\xi_3 = -4 \times 10^{-5}$ C/(K m^2).

2.3.3 Piezoelectric effect

A piezoelectric material generates an electric charge when it is mechanically deformed. The converse effect can be used to change the shape of a solid on the application of an electric field. The relationship between the polarisation, the piezoelectric tensor, $\boldsymbol{d}$ and the stress tensor, $\boldsymbol{\sigma}$, is given by

$$\mathbf{P} = \boldsymbol{d\sigma} \tag{2.4}$$

or in tensor component form:

$$P_i = \sum_{j,k} d_{ijk} \sigma_{jk} \tag{2.5}$$

The piezoelectric tensor, $\boldsymbol{d}$, in lithium niobate can be contracted using Neumann's principle, to

$$d_{ijk} = \begin{pmatrix} 0 & 0 & 0 & 0 & d_{15} & -2d_{22} \\ -d_{22} & d_{22} & 0 & d_{15} & 0 & 0 \\ d_{31} & d_{31} & d_{33} & 0 & 0 & 0 \end{pmatrix} \tag{2.6}$$

where

$$d_{15} = 6.9 \times 10^{-11} \text{ C N}^{-1} \qquad d_{22} = 2.1 \times 10^{-11} \text{ C N}^{-1}$$
$$d_{31} = -0.1 \times 10^{-11} \text{ C N}^{-1} \qquad d_{33} = 0.60 \times 10^{-11} \text{ C N}^{-1}$$

from Weis and Gaylord (1985).

2.3.4 Birefringence

Birefringence is the name given to splitting of a single light beam into two components, called the ordinary and extraordinary rays, with perpendicular polarisations. This occurs due to the presence of two refractive indices in a crystal, and is defined as $(n_e - n_o)$. The ordinary ray is defined as being polarised perpendicular to the optic axis of the crystal (the z axis for lithium niobate) and the extraordinary ray is polarised perpendicular to the ordinary ray.

The refractive index that is experienced by the two rays is illustrated by the index ellipsoid, shown in Figure 2.4. The ordinary index is independent of direction of propagation of the beam, unlike the extraordinary ray which does depend on the direction.

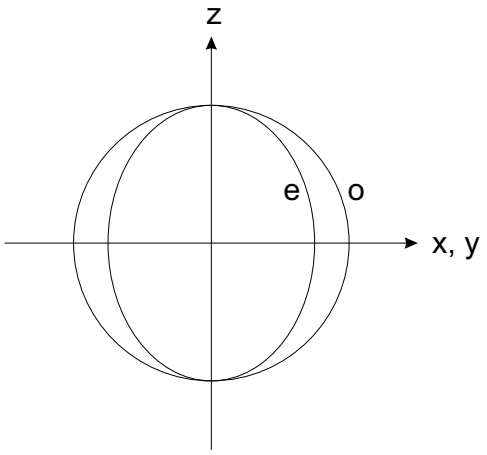

Figure 2.4: Refractive index ellipsoid, illustrating the refractive index for ordinary (o) and extraordinary (e) rays in lithium niobate.

At visible wavelengths the extraordinary index, $n_e \approx 2.2$ and the ordinary index, $n_o \approx 2.3$, consequently lithium niobate is a negative birefringent material. The Sellmeier equations, shown below, are used to estimate the refractive index at a particular wavelength, given in μm (Schlarb and Betzler, 1993).

$$n_o^2 = 4.9048 + \frac{0.11775}{\lambda^2 - 0.04570} - 0.027153\lambda^2 \tag{2.7}$$

$$n_e^2 = 4.5820 + \frac{0.09921}{\lambda^2 - 0.04443} - 0.021940\lambda^2 \tag{2.8}$$

2.3.5 Electro-optic effect

The electro-optic effect is a change in the refractive index of a non-centrosymmetric material in response to an electric field. The linear electro-optic effect is also known as the Pockels Effect and the relation between the refractive index and applied electric field is:

$$\Delta\left(\frac{1}{n^2}\right)_{ij} = \sum_k \boldsymbol{r}_{ijk} E_k \tag{2.9}$$

where $\boldsymbol{r}_{ijk}$ is the linear electro-optic coefficient tensor, which can be shown to be

$$\boldsymbol{r}_{ijk} = \begin{pmatrix} 0 & -r_{22} & r_{13} \\ 0 & r_{22} & r_{13} \\ 0 & 0 & r_{33} \\ 0 & r_{42} & 0 \\ r_{42} & 0 & 0 \\ -r_{22} & 0 & 0 \end{pmatrix} \tag{2.10}$$

where

$$r_{42} = 28 \text{ pm V}^{-1} \qquad r_{13} = 7.7 \text{ pm V}^{-1}$$
$$r_{22} = 3.4 \text{ pm V}^{-1} \qquad r_{33} = 29 \text{ pm V}^{-1}$$

from Weis and Gaylord (1985).

There is also a quadratic electro-optic effect (dependent on E^2), which is referred to as the Kerr effect.

2.3.6 Nonlinear optical properties

The nonlinear optical response of a material can be used to produce a variety of useful effects such as second harmonic generation and frequency mixing, see Section 2.5.3 for further details. The efficiency of such processes are dependent on the material's nonlinear optical coefficients. For lithium niobate, these are:

$$d_{33} = 33 \text{ pm V}^{-1}$$
$$d_{31} = 5.8 \text{ pm V}^{-1}$$
$$d_{22} = 2.8 \text{ pm V}^{-1}$$

according to Prokhorov and Kuuzminov (1990).

2.3.7 Photorefractive effect

The photorefractive effect is a change in the refractive index of a material caused by optically generated charge carriers, such as from the photovoltaic effect. It is actually a combination of charge migration (see Section 2.3.9) followed by an electro-optic effect. The effect can be a limitation to the use of lithium niobate in high power laser applications, but can also be useful, for holographic data storage (Section 2.5.5) for instance.

2.3.8 Internal field and defects

Figure 2.5 shows a typical polarisation hysteresis curve for a 0.5 mm thick virgin lithium niobate single crystal, taken from a paper by Gopalan and Gupta (1997) (the units of spontaneous polarisation have been corrected). It illustrates the two spontaneous polarisation states in which lithium niobate can exist and the coercive field required to switch between these states.

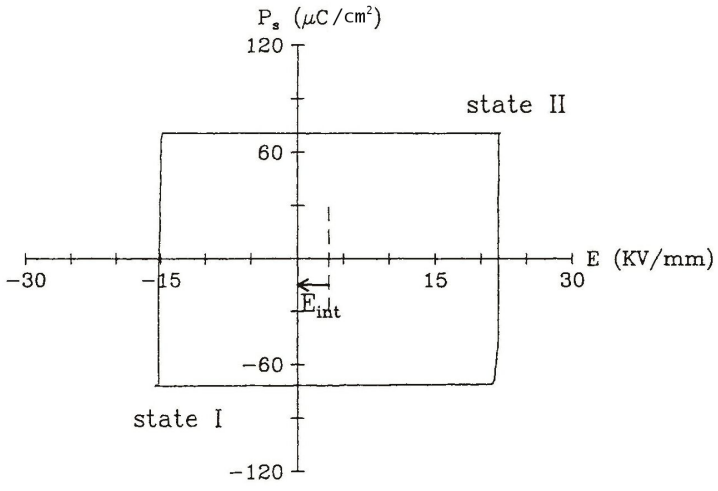

Figure 2.5: The hysteresis loop of a *z*-cut $LiNbO_3$ single crystal from Gopalan and Gupta (1997) with corrected units of P_s.

Gopalan and Gupta noticed a large asymmetry in the hysteresis loop, indicating the presence of an internal field (E_{int} in the diagram). In a later study Gopalan et al. (1999) found that the exact value of the internal field varied from sample to sample, within a range of 2.7 – 3.5 kV/mm.

The internal field is measured by the difference in coercive field required to pole lithium niobate in the 'forward' direction compared to the 'reverse' direction. Forward poling is defined as starting with a virgin crystal (state I) and then domain inverting a region. Reverse poling is the process of poling this area (state II) back to its original domain orientation (state I). The forward and reverse coercive fields are then defined as:

- Forward poling: $E_f = E_c + E_{int}$
- Reverse poling: $E_r = E_c - E_{int}$

Consequently a larger field is required for forward poling than for reverse poling. This is because in a virgin crystal (state I) the internal field is parallel to the polarisation direction. After poling the internal field initially maintains the same direction, so reverse poling needs a smaller field. However, the internal field gradually realigns itself along the new polarisation direction. Gopalan found that this process takes many days at room temperature, but is 80 % complete within two minutes when the sample is heated to over 200 °C. Subsequent work by Ro and Cha (2000) suggests that there are two distinct relaxations, one with a subsecond time scale and another which occurs over several days at room temperature.

The origin of the internal field in lithium niobate was quite a source of controversy. Some early results suggested that hydroxyl ions (OH^-) present in lithium niobate were responsible, on the basis of infrared absorption measurements (Gopalan and Gupta, 1996). The shape of the three peak OH^- band showed changes after forward poling of a crystal which were reversed when the crystal was repoled back to the original state. However in 1998 it was proven that the internal field is actually a result of non-stoichiometric point defects in the congruent material. Stoichiometric lithium niobate showed the same OH^- infrared bands as the congruent material, but experiments showed that no internal fields were present (Gopalan et al., 1998). Consequently the coercive field required for poling of a stoichiometric crystal is much less (by about four times) than is required for congruent lithium niobate. However the crystal composition was found to have very little effect on the spontaneous polarisation.

Lithium niobate may contain several types of lattice imperfections (Malovichko et al., 1999):

- Lithium vacancies $(v_{Li})^-$

- Oxygen vacancies $(v_O)^{2+}$
- Niobium vacancies $(v_{Nb})^{5-}$
- Niobium antisites $(Nb_{Li})^{4+}$
- Niobium on structural vacancy $(Nb_v)^{5+}$
- Lithium on structural vacancy $(Li_v)^{+}$
- Interstitial oxygen (O_i)

The relative concentrations of these defects are unknown, however there are several charge-balanced models of which types of defect are most common:

1. Lithium vacancies and oxygen vacancies (Prokhorov and Kuuzminov, 1990)
2. Niobium antisites and niobium vacancies, $5(Nb_{Li})^{4+} + 4(v_{Nb})^{-}$ (Schirmer et al., 1991)
3. Niobium antisites and lithium vacancies, $(Nb_{Li})^{4+} + 4(v_{Li})^{-}$
4. Ilmenite ordering, Li Nb v Nb Li Li Nb v, etc

The relative merits of each model has been discussed by Kim et al. (2001). The first model, featuring lithium and oxygen vacancies is thought to be unlikely due to an incompatibility with density measurements, while Donnerberg et al. (1991) showed that the formation of niobium vacancies, as suggested by the second model, is energetically unfavourable. However the combination of the niobium and lithium vacancies models essentially results in areas of ilmenite ordering. Yatsenko et al. (1997) used NMR spectra and simulations of ^{7}Li and ^{93}Nb nuclei to study the different models, and reported that the most probable defects are a complex of $(Nb_{Li} + 3v_{Li})$ and a single isolated v_{Li}.

Kim et al. (2001) describe how the niobium antisites and lithium vacancies model $((Nb_{Li})^{4+} + 4(v_{Li})^{-})$ affects the internal field and the poling process in lithium niobate (and lithium tantalate if the niobium is exchanged for tantalum). A Nb_{Li} antisite combined with four v_{Li} vacancies will posses an electric dipole moment with two components, one related to the antisite defect, and the other due to the lithium vacancies. For poling to occur, the niobium and lithium ions have to move from their original positions; the niobium simply moves along the z axis, to an opposite position across the centre of the oxygen octahedron. The lithium ion has to pass

through an opening in the close packed oxygen layer, of similar size to the ion itself. When the lithium is replaced by niobium in a Nb_{Li} antisite defect, the niobium will also have to pass through the oxygen layer. The niobium ionic radius is actually slightly smaller than that for lithium, ~ 64 pm compared to ~ 76 pm (Shannon, 1976), so steric considerations should not be an issue. However, once the antisite niobium has moved, the lithium vacancies around the defect will also need to rearrange to reach a stable state. But as these are thought to only move at temperatures above 150 °C (Battle et al., 2000), a high temperature anneal is required to restore the defect complex to a low energy state. The dipole moment associated with the niobium antisite will be reversed after domain reversal, but at room temperature the lithium vacancy component is not immediately reversed.

Kim et al. (2002) suggest that the dipolar defects give rise to equivalent defect fields, E_{defect}, which tend to increase the coercive field. They state that the defect field is not a real electric field in lithium niobate, but instead can be considered as "the formal equivalent to the energetic difference between the two domain states $+P_s$ and $-P_s$, one stabilized by the dipolar defects by an amount of energy $-E_{defect}P_s$ and another raised in energy by the same amount."

Recent studies of the internal field by the use of the electro-optic effect (Paturzo et al., 2004) and an interferometric method (de Angelis et al., 2004) have been reported. The electro-optic response of a recently poled domain shows a different response to that of a virgin domain, and Paturzo et al. interpret this as the consequence of an elastic dipole component associated with lattice distortions.

In summary, the internal field in lithium niobate can be observed by recording the polarisation hysteresis curve. It is related to the lithium deficiency and resulting crystal defects in congruent lithium niobate, as no internal field has been detected in stoichiometric material. The internal field is also related to the larger coercive field required to induce domain inversion in congruent crystals, however the exact nature of defects responsible are still uncertain. The most likely defect, supported by a variety of experimental evidence, is a charge-balanced complex of a niobium antisite $(Nb_{Li})^{4+}$ with four lithium vacancies $(v_{Li})^{-}$.

2.3.9 Light-induced charge transport.

Light-induced charge transport in lithium niobate is an essential part of the photorefractive effect and is also of particular relevance to work presented in this thesis. Buse has produced a comprehensive two part review on this subject, with

the first concentrating on models and experimental methods (Buse, 1997a) and the second discussing the effect in a range of materials (Buse, 1997b); the main points are discussed below.

The charge transport processes which can take place are dependent on the material, the light intensity, doping and thermal annealing. Consequently, exposure to continuous wave or pulsed light may result in different effects within the crystal. Free charge carriers can move under the influence of three effects;

Drift: Arises from the Coulomb interaction of an electric field (including internal fields) on the charge carriers.

Bulk Photovoltaic Effect: Charges generated in non-centrosymmetric crystals may have to move in a particular direction due to the neighbouring atoms.

Diffusion: Non-uniform illumination generates uneven concentrations of charges, which subsequently result in diffusion currents.

When exposed to continuous wave light, iron or copper doped lithium niobate experiences light induced charge transport that is described well by a one-centre model. This is the simplest model, where electrons are excited from filled traps into the crystal's conduction band and free electrons can move from the conduction band to recombine with empty traps. In lithium niobate, the traps are Fe^{2+} / Fe^{3+} ions; this applies even to undoped material, as lithium niobate inevitably contains some iron impurities. The process is illustrated in Figure 2.6.

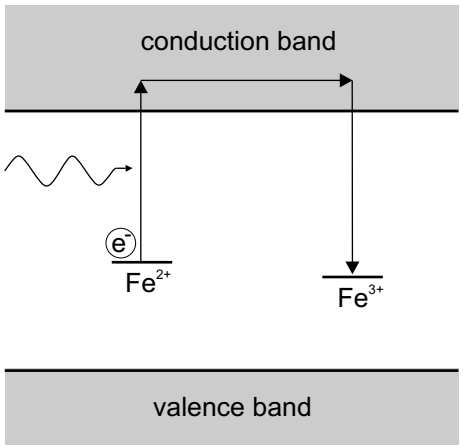

Figure 2.6: Energy level diagram for the one-centre model of charge transport in $LiNbO_3$.

Once the charges are generated, the dominant transport mechanism is the bulk photovoltaic effect (Glass et al., 1974), which causes the free electrons to drift along

the c axis. According to Glass et al. the current density, J, is proportional to the intensity, I:

$$J = k_1 \alpha I \tag{2.11}$$

where α is the absorption coefficient and k_1 is a constant, dependent on the type of absorbing centre and wavelength. However, J is independent of crystal geometry and impurity concentration. No photo-current was detected normal to the polar axis and no light induced absorption changes were observed.

The current density was later found to also depend on the light polarisation (Belinicher et al., 1977), so becomes

$$J = \boldsymbol{\alpha}_{ijk} E_j E_k \tag{2.12}$$

where E_j and E_k are components of the electric field vector of the light, and $\boldsymbol{\alpha}_{ijk}$ is the photovoltaic tensor, which can be written as

$$\boldsymbol{\alpha}_{ijk} = \begin{pmatrix} 0 & 0 & 0 & 0 & \alpha_{15} & -2\alpha_{22} \\ -\alpha_{22} & \alpha_{22} & 0 & \alpha_{15} & 0 & 0 \\ \alpha_{31} & \alpha_{31} & \alpha_{33} & 0 & 0 & 0 \end{pmatrix} \tag{2.13}$$

The photovoltaic current along a particular axis, in crystals of point group 3m, is given by the relevant expression in Table 2.1, taken from Festl et al. (1982). β is the angle formed between the light polarisation plane and the corresponding crystal axis and I is the intensity.

Table 2.1: Components of the photovoltaic current for different current directions and directions of incident light.

current direction	direction of incident light		
	x	y	z
J_x	0	$\alpha_{15} I \sin 2\beta$	$-\alpha_{22} I \sin 2\beta$
J_y	$\alpha_{15} I \sin 2\beta + \alpha_{22} I \cos^2 \beta$	$-\alpha_{22} I \cos^2 \beta$	$\alpha_{22} I \cos 2\beta$
J_z	$\alpha_{31} I + (\alpha_{33} - \alpha_{31}) I \cos^2 \beta$	$\alpha_{31} I + (\alpha_{33} - \alpha_{31}) I \cos^2 \beta$	$\alpha_{31} I$

Fradkin and Magomadov measured the photovoltaic current along all three crystal axes, for various orientations of light polarisation planes and currents were detected for the first time along the x and y axes. The results shown in Figure 2.7 were taken using linearly polarised light of wavelength λ = 500 μm and intensity I = 2.3 $\times 10^{-3}$ W cm^{-2}.

The results fit the theoretical expectations well. The currents along the x and y directions are strongly dependent on the angle to the polarisation plane, β. As the

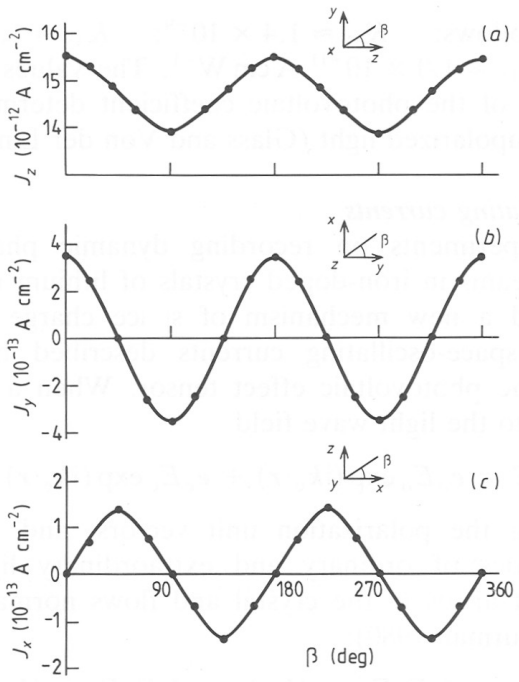

Figure 2.7: Dependence of the photovoltaic current components J_z(a), J_y(b), J_x(c) on the plane of light polarisation in Fe:$LiNbO_3$, taken from Fradkin and Magomadov (1979). The direction of light propagation is shown in the inserts.

polarisation is rotated by 360° the J_x and J_y currents reverse sign twice. Hence when light is polarised perpendicular to a y axis, current still flows, but along the $-y$ direction. The amplitude of these currents is an order of magnitude less than the amplitude of J_z, and never becomes negative (i.e. charge always flows along the $+z$ direction). If the light is propagating along the z axis, then the current $J_z = \alpha_{31} I$ and so is independent of the direction of polarisation. The values of the coefficients are $\alpha_{22} = 1.5 \times 10^{-10}$ A/W, $\alpha_{31} = 6 \times 10^{-9}$ A/W and $\alpha_{33} = 6.8 \times 10^{-9}$ A/W.

Another prediction of the one centre model is a light-induced refractive index change with a saturation value that depends only on the concentration of empty traps. The light intensity only affects the rate of the refractive index change.

The energy band gap of lithium niobate has been reported to be between 3.7 eV to 3.9 eV (Prokhorov and Kuuzminov, 1990), so when lithium niobate is exposed to UV light (e.g. photons with wavelength of 248 nm and energies of 5 eV), direct excitation of the valence band electrons into the conduction band becomes possible, leaving behind holes which can contribute to the conductivity. Electrons can also be excited from the valence band to the Fe^{+3} impurity levels and electrons from Fe^{2+} can recombine with valence band holes (Orlowski and Kratzig, 1978).

At high intensities ($I \geq 10^6$ W/m^2) the one centre model does not sufficiently describe the charge transport which takes place in Fe:$LiNbO_3$. The one centre model predicts a linear photoconductivity increase with light intensity and no light-induced absorption changes. Both of these are true for low light intensities, but are not valid at high intensities. Jermann and Otten (1993) proposed a new model which can quantitatively explain these and other experimental results at both low and high intensities. The model assumes a second centre and allows direct charge transfer between the two centres (Fig. 2.8).

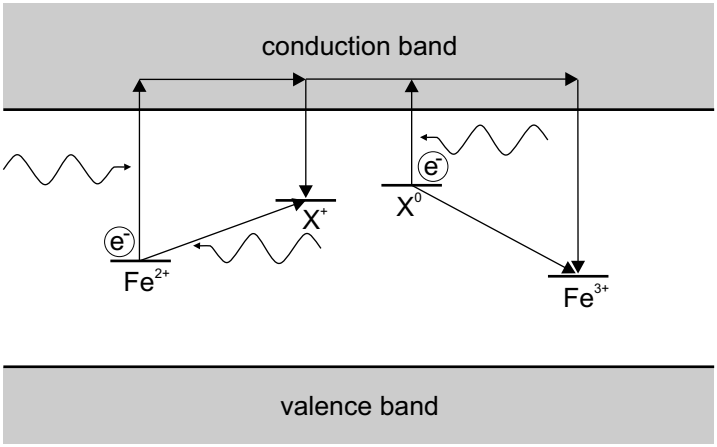

Figure 2.8: Energy level diagram for the two-centre model of charge transport in $LiNbO_3$.

The second centre, which only becomes active at high light intensities, is denoted by 'X', and although has it has not been conclusively proven, there is evidence that these centres are small polarons, $Nb^{3\bullet}_{Li}$ (self-trapped electrons at Nb^{4+} ions on Li^+ sites). Calculations by Jermann and Otten show that the concentrations for X centres are required to be much greater than for the Fe centres, which suggests that the centres consist of intrinsic defects. This is supported by experimental observation that the refractive index changes at high intensities are lower for stoichiometric lithium niobate than for congruent (Malovichko et al., 1992).

2.3.10 Comparison with other ferroelectrics

Table 2.2 compares the key parameters of lithium niobate with other common ferroelectrics, taken from Lines and Glass (2001).

Table 2.2: Comparison of the key properties of some common ferroeletrics.

Name	P_s ($\mu C\ cm^{-2}$)	T_c (°C)	Largest Nonlinear Coeff. (pm V^{-1})
Lithium Niobate	71	1210	$d_{33} = -33$
Lithium Tantalate	50	665	$d_{33} = -21$
Barium Titanate	26	135	$d_{31} = 19$
Potassium Titanyl Phosphate (KTP)	20	936	$d_{33} = 13.7$
Potassium Dihydrogen Phosphate (KDP)	4.8	−150	$d_{36} = 0.43$
Rochelle Salt	0.5	24	-

2.4 Techniques for Structuring Lithium Niobate

2.4.1 Electric field poling

In the ferroelectric phase of lithium niobate, the lithium and niobium ions are displaced from their equilibrium position, leading to charge separation and so creating a spontaneous polarisation within the crystal. The polarisation can be orientated in one of two directions along the z axis. However, the direction of polarisation may be inverted by the application of a sufficiently large electric field of around 22 kV/mm, called the coercive field. Such a large field is required so that the lithium atoms can pass through the oxygen layers.

The technique of domain inversion, or poling, by an electric field was first suggested by Camlibel (1969), although control over the poling was limited. Haycock and Townsend (1986) reported a method of poling $LiNbO_3$ below the Curie temperature, using excitation of the crystal lattice with a beam of electrons while simultaneously applying an electric field. Yamada et al. (1993) and Webjorn et al. (1994) then later suggested using electric field poling alone, to produce periodically poled lithium niobate (PPLN) to allow the generation of blue light through quasi-phase-matching.

The process of domain inversion generates a displacement charge which can be measured as a short-lived current. The total charge required to repole an area of crystal is found by integrating the area under the current peak, when a voltage is applied to a crystal. This allows the charge required for poling to be calculated using:

$$Q = 2aP_s f \tag{2.14}$$

where a is the area to be poled (mm^2), P_s is the spontaneous polarisation (72 $\mu C/cm^2$ for congruent lithium niobate) and f is an empirical factor (typically around 1.3). The factor of 2 is required so that the domain is reversed during the poling process,

without it the charge would only be great enough to cancel out the spontaneous polarisation. An empirical factor is needed to obtain optimal poling results by allowing for the slight differences in structure of lithium niobate supplied from different manufacturers and the influence of defects on the poling.

The process of electric field poling is illustrated in Figure 2.9. By masking parts of the crystal, it is possible to repole only certain areas, leaving masked sections in their original state. The mask can be simply made with insulating tape, or for finer features photolithographically defined patterns in photoresist can be used. A conductive gel is used as a liquid electrode to uniformly apply a large electric field of 22 kV/mm to the unmasked areas.

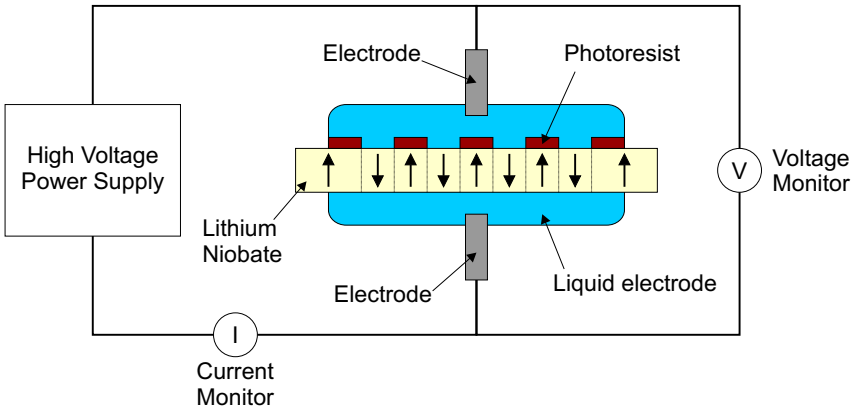

Figure 2.9: A schematic diagram illustrating the electric field poling process.

The poling apparatus is computer controlled, so the power supply is turned off automatically when the correct amount of current needed to completely repole the area of the sample has passed, as calculated using equation (2.14). The current used was 500 μA and a typical charge required was around 40 μC, depending on the size of the area of the sample to be poled.

This technique is used to produce periodically poled lithium niobate (PPLN), where domains are alternately orientated in opposing directions, which is used for quasi-phase matching in optical parametric oscillators for frequency conversion and second harmonic generation; see Section 2.5.3 for further details.

PPLN is produced by masking areas of the crystal which are not required to be poled, using photolithography. A schematic of the process is shown in Figure 2.10.

The first stage in the process is spin coating of the virgin lithium niobate with photoresist at 6000 rpm for 1 minute, resulting in a layer ~ 1 μm thick. The sample is then placed in a mask aligner, where the pattern from a metal mask is transferred

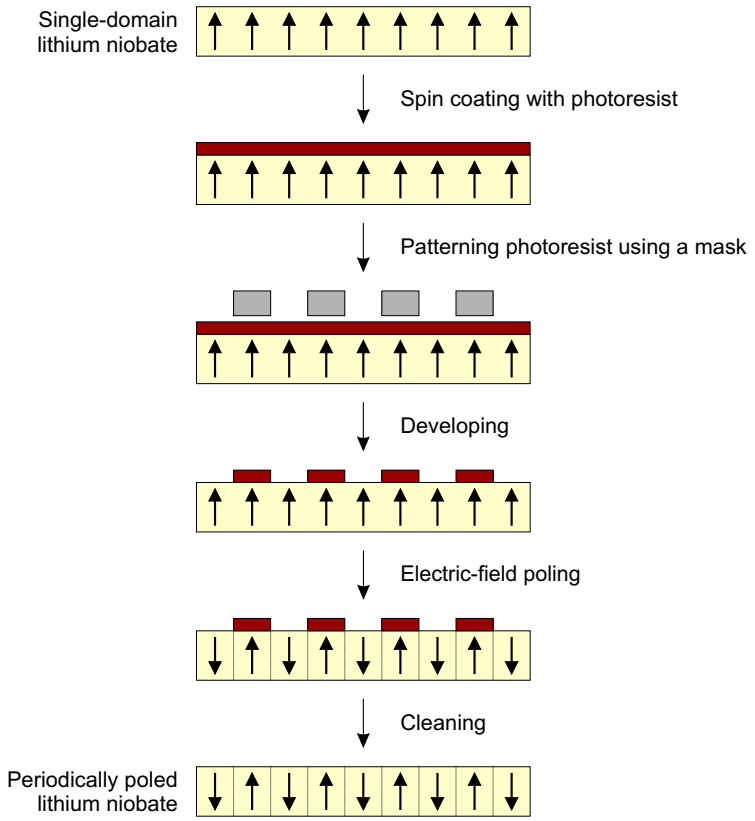

Figure 2.10: Schematic diagram representing the process of producing PPLN.

to the photoresist, by exposing the sample and mask to ultraviolet light. The areas of photoresist which have been exposed to U.V. light are chemically modified, so they become soluble when placed in developer solution, leaving behind the unexposed areas (for the more common positive photoresist; the inverse applies for negative photoresist). The sample is then transferred to the poling rig, where a voltage is applied across the areas of the crystal which are not covered by photoresist, resulting in domain inversion in these areas. The final stage involves thorough cleaning in acetone and isopropyl-alcohol, during which all remaining traces of photoresist are removed.

There are other techniques to produce domain inversion, such as lithium out-diffusion (Yamamoto et al., 1991), Ti-indiffusion (Miyazawa, 1979) and electron-beam radiation (Yamada and Kishima, 1991), but electric-field poling is the most commonly used.

2.4.2 Acid Etching

In one of the first papers on lithium niobate Nassau et al. (1966a) reported that a variety of different substances could be used as etchants, but the best results were obtained using a mixture of one part hydrofluoric acid (HF) to two parts of nitric acid (HNO_3) at 110 °C. They also observed that the rate of etching depended on which face (either the $-z$ or $+z$) of lithium niobate was exposed to the etchant. This property is now commonly used to visualise neighbouring anti-parallel domains that have been formed by electric field poling of lithium niobate.

More recently, Sones et al. (2001) carried out a comprehensive study into the differential etching rates in z-cut lithium niobate. Using the standard mixture of nitric and hydrofluoric acid, they found the etching rate of the $-z$ face at room temperature to be ≈ 0.8 μm/h, rising to ≈ 30 μm/h at 95 °C. However, there was no evidence of etching of the $+z$ face at either of these temperatures. Experiments were also carried out using only HF, which was found to yield better results than the HF/HNO_3 mixture, in terms of faster etch rates (a factor of two higher) and smoothness of the etched surface. No etching was observed using nitric acid alone.

Sones et al. (2001) also proposed reaction pathways for the etching process, when using just HF and a mixture of HF and HNO_3. Protonation of the surface metal hydroxide is the first step in these etching processes which is why the negatively charged $-z$ face (which electrostatically attracts the proton) shows a much greater etching rate than the positively charged $+z$ face (which repels the proton).

The reaction pathway when etching with 48 % HF in water is:

$MOH_s + H^+ \rightleftharpoons M_s^+ + H_2O$	The proton attaches to the surface hydroxide.
$2HF \rightleftharpoons H_2F_2 \rightleftharpoons HF_2^- + H^+$	HF forms a dimer, which then dissociates.
$M_s^+ + HF_2^- \rightarrow MF + HF$	The final step is an electrostatically enhanced attack on the surface metal.

The pathway changes when a mixture of HF and HNO_3 acids are used:

$MOH_s + H^+ \rightleftharpoons M_s^+ + H_2O$	The first step is unchanged.
$M_s^+ + NO_3^- \rightleftharpoons M_sNO_3$	The nitrate covers the surface metal.
$2HF \rightleftharpoons H_2F_2 \rightleftharpoons HF_2^- + H^+$	HF forms a dimer as before.
$M_sNO_3 + H_2F_2 \rightarrow MF + HNO_3$	As the surface is uncharged, the more abundant HF dimer substitutes for the nitrate.

Another result of etching lithium niobate with hydrofluoric acid has been reported by Bermudez et al. (1998) who found that fluorine ions can diffuse into the crystal during etching. In studies with periodically poled lithium niobate (PPLN), secondary ion mass spectrometry (SIMS) revealed concentrations of ^{19}F in the positive domains. When experiments were carried out on the negative face of a monodomain crystal, the only areas with high fluorine concentrations were those which were resistive to etching, due to the presence of defects or microdomains. Thus it appears that the fluorine ions diffuse preferentially into the positive z face of lithium niobate crystals. This would seem to be consistent with the arguments used by Sones et al on the effect of electrostatic attraction, as the negatively charged fluorine ions will be attracted to the areas of positive charge on the crystal surface.

2.4.3 Other Etching Methods

As well as acid etching, Nassau et al. (1966a) also described using melts of potassium hydroxide (KOH), potassium dichromate ($K_2Cr_2O_7$), and potassium permanganate ($KMnO_4$) amongst others to achieve etching. At 400°C KOH was observed to differentiate to some extent between oppositely orientated domains. However, the elevated temperature requirements for KOH make the use of HF simpler.

Other methods of etching which do not require the use of 'wet' liquid chemicals are known collectively as 'dry' etching and some examples are listed below:

- Plasma Etching (PE)
- Ion Beam Etching (IBE)
- Reactive Ion Etching (RIE)
- Reactive Ion Beam Etching (RIBE)

- Laser Ablation

Generally in dry etching a surface is modified either by the impact of ions or through a chemical reaction with reactive species, or a combination of both mechanisms (Madou, 2002). There are two types of plasma-assisted etching, determined by the setup of the equipment; glow discharge and ion beam. In glow discharge systems the plasma is generated in the same chamber as the substrate, while ion beams systems generate the plasma in a separate chamber, from where the ions are directed to the substrate. Kokhanchik et al. (2004) report an etch rate for lithium niobate of about 10 nm/min using microwave plasma etching at the electron cyclotron resonance with a mixture of SF_6 and Ar. They also found that etched $-z$ faces are smoother than etched $+z$ faces.

Ion beam etching uses a beam of ions which are accelerated by a voltage toward the target and etching occurs due to the physical impact with the surface. Control of the beam allows structures to be directly written into the substrate and etching occurs quickly with rates of around 1 μm/min depending on the material being etched. This technique can be enhanced by adding a gas to produce reactive ions that will chemically react with the substrate, so producing volatile reaction products which can be easily removed from the chamber; this is know as reactive ion beam etching. Both ion beam techniques allow the formation of structures with deep trenches and vertical side walls (anisotropic etching) as the process prevents side-etching (Sugawara, 1998). Nutt et al. (1984) used IBE to produce grooves in lithium niobate for fibre alignment, with an etch rate of 40 nm/min from a 1 keV beam of argon ions.

In plasma etching neutral species generated in the plasma diffuse to the substrate, where they react with the surface, again resulting in easily-removed volatile products. In this case the plasma is only required to generate the reactive species, which are often chlorine or fluorine atoms. Reactive ion etching uses a similar process to PE, but the etching is carried out by a combination of chemical and physical effects. RIE is widely used in the manufacture of integrated circuits, due to the good profile control and selectivity that can be achieved.

Winnal and Winderbaum (2000) have applied RIE to lithium niobate, using CF_4:O_2 chemistry and a photolithographically patterned a NiCr layer to define the RIE mask. They reported a maximum etch rate of 3.8 nm/min and the deepest etch they obtained was 1.2 μm. They also found that the etching created a film on the sidewalls, which reduced the smoothness of the features, but this could be minimised by increasing the flow of oxygen, at the expense of etch rate.

Laser ablation can be used for etching and structuring of substrates, and occurs when sufficient energy is absorbed by a volume of material in a short period of time, resulting in rapid heating and vapourisation of the exposed area of the substrate. It is therefore a highly selective technique, with the minimum size of the features determined by the wavelength of light used, due to diffraction effects. Using a pulsed laser system, the ablation etch rate of lithium niobate is ~0.1 μm/pulse from a fluence of 7 J/cm^2 (Greuters and Rivzi, 2002). The etch depth using this technique is essentially unlimited. Additionally, the rate of laser ablation is independent of which crystal face is exposed.

2.5 Uses and Applications

Lithium niobate is used in a wide variety of devices, some of the most common of which are described in this section.

2.5.1 Waveguides

Optical waveguides are devices that confine electromagnetic radiation and so can be used to guide light. There are two main types of waveguide; fibre and planar. Optical fibres are generally used to guide light over long distances and so are widely used in telecommunications, while planar waveguides are ideal for short distances and so are useful for making integrated optical circuits, on a small wafer of a crystal such as lithium niobate. Devices based on planar waveguides include splitters, modulators and interferometers. Planar waveguides may be produced using techniques such as:

- Titanium indiffusion
- Proton exchange
- Ion implantation
- UV direct-write

Titanium indiffused waveguides are produced by depositing a layer of titanium on the lithium niobate substrate, and then heating to ~ 1100 °C. Proton exchange requires a lower temperature, of ~ 200 °C; the substrate is immersed in an acid (often benzoic acid) and the hydrogen ions substitute for the lithium ions in the

crystal. Ion implantation is achieved by using beams of ions, which are directed at the substrate to form the required pattern. The titanium indiffusion and ion implantation techniques have been reviewed by Wong (2002). Finally, UV direct-write is an emerging technique, which although still under development, may prove to be very useful due to the ease of fabrication of waveguides. A computer-controlled stage moves the substrate relative to the focussed beam from a UV laser and the exposed areas of the crystal are subsequently found to guide light.

2.5.2 Electro-optic devices: Modulators and switches

A variety of devices can be produced in lithium niobate which utilise the electro-optic effect, (also known as the Pockels Effect). These devices, called Pockels Cells, work by the application of an electric field across the crystal, so require electrodes to be applied to two opposing faces. Two designs are possible, longitudinal and transverse, which refer to the relative directions of the applied electric field and direction of propagation of the light. In lithium niobate, the transverse design is used, so that light propagates along the z-axis (the optic axis) and electrodes are applied on the crystal faces perpendicular to this, usually the x faces. This design allows access to the r_{22} electro-optic coefficient which has a value of 6.7×10^{-12} m V^{-1} (Wong, 2002).

At zero applied field a light wave travelling along the z axis experiences no natural birefringence, but when an electric field is applied it produces a change in the refractive index of the crystal. The index ellipsoid is modified in shape and orientation, and birefringence is created. In this way the Pockels cell acts as an electrically-controlled phase retarder. If a pair of crossed polarisers is added, as shown in Figure 2.11, then the system can be used as an amplitude modulator, which has applications in the telecommunication industry, for example. Pockels cells are also used as Q-switches to make pulsed lasers.

The change in refractive index, Δn is given by (Pedrotti and Pedrotti, 1996):

$$|\Delta n| = \frac{r_{ij} n_0^3 E}{2} \tag{2.15}$$

and the half-wave voltage is (Koechner, 1976)

$$V_{1/2} = \frac{\lambda d}{2 r_{22} n_0^3 l} \tag{2.16}$$

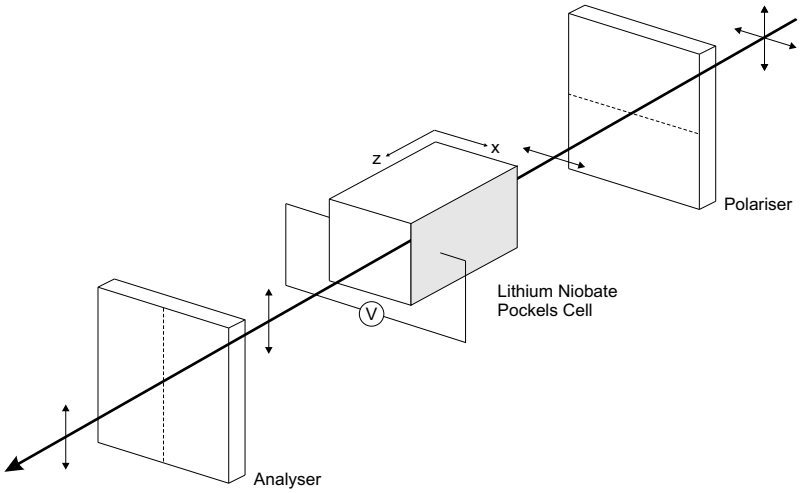

Figure 2.11: Use of a Pockels cell, between crossed polarisers. When a sufficient voltage is applied, the Pockels cell rotates the horizontally polarised incident beam to a vertical polarisation, so allowing the beam to pass through the analyser. This system forms the basis of an electro-optic modulator.

where l is the length of the crystal, and d is the distance between the electrodes.

A recent development in electro-optic devices based on lithium niobate, has been reported by Boyland et al. (2001), who used the effect to produce a beam switch. The switch uses total internal reflection from a boundary between two anti-parallel domains, and operates by the small change in refractive index that is created by the electro-optic effect. As the applied voltage is increased, the angle required for total internal reflection is reduced, so a beam which may pass through the boundary at zero field will be reflected when a field is applied. The authors also reported how the technique can be used to make a beam deflector (Eason et al., 2001), to direct the beam through a continuous range of angles.

2.5.3 Frequency conversion; Optical parametric oscillators

Another use of lithium niobate is in optical parametric oscillators (OPOs). These devices allow frequency mixing, over a wide range of output wavelengths, and so are very useful for producing an easily tunable laser.

Frequency mixing is a nonlinear process, where two incident beams, with frequencies ω_1 and ω_2, in a suitable nonlinear material produce a third, with frequency ω_3. This occurs due to the inability of dipoles in the material to respond to the electric field of light wave in a completely linear way. The deviation from the

linear response is small, but becomes significant when the intensity of light is high. This is discussed further in Chapter 6, on Surface Second Harmonic Generation.

Second harmonic generation is a specific type of frequency mixing, where the two incident beams have the same frequency, and the output wave has twice the frequency (2ω). However, in the general case of frequency mixing, harmonics with frequencies of $2\omega_1$, $2\omega_2$, $\omega_1 + \omega_2$ and $\omega_1 - \omega_2$ may be generated.

Parametric oscillators use difference frequency generation, to convert a single incoming high frequency photon from a pump beam to two lower frequency photons, termed the signal and the idler. The difference with second harmonic generation is illustrated by an energy level diagram, shown in Figure 2.12.

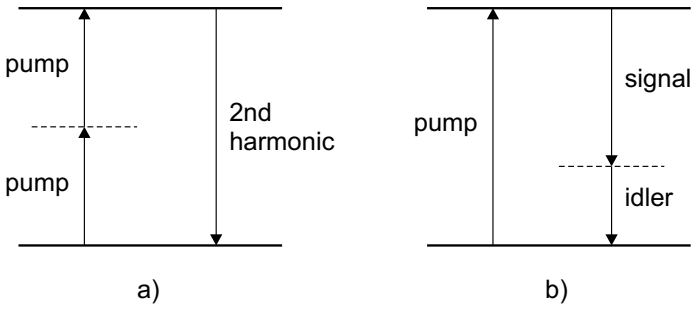

Figure 2.12: Energy level diagrams showing a) Second Harmonic Generation, and b) Difference Frequency Generation.

For successful difference frequency generation (and hence OPO operation), each of the three waves needs to be travelling in the same direction, at the same speed. This is a problem, as each of the frequencies will experience a different refractive index, due to the dispersion (increase of refractive index with frequency) of the material.

The wavevector, $\mathbf{k}$ is defined as

$$\mathbf{k} = \frac{\omega n(\omega)}{c} \tag{2.17}$$

Due to dispersion there will be a wave vector mismatch

$$\Delta\mathbf{k} = \mathbf{k}_3 - \mathbf{k}_2 - \mathbf{k}_1 \neq 0 \tag{2.18}$$

If this is left uncorrected, as the beams propagate through the crystal their phase will become increasingly mis-matched, resulting in less efficient frequency conversion, until eventually the beams will start to destructively interfere. The coherence length is given by

$$l_c = \frac{\pi}{\Delta\mathbf{k}} \tag{2.19}$$

To prevent destructive interference and maximise the conversion efficiency, the beams need to be 'phase-matched', with the ideal phase-matching condition defined as $\Delta\mathbf{k} = 0$.

2.5.3.1 Birefringent phase-matching

Phase-matching is possible using birefringent materials, such as lithium niobate, by making use of the two refractive indices. In this approach, the higher frequency pump wave is polarised along the direction of lowest refractive index, and the other waves are polarised at an angle to the first wave. Because they are travelling at an angle to the two optic axes, they will experience a refractive index that is a combination of the ordinary and extraordinary indices (Boyd, 2003), given by the relation

$$\frac{1}{n^2(\theta)} = \frac{\sin^2\theta}{n_e^2} + \frac{\cos^2\theta}{n_o^2} \tag{2.20}$$

Phase matching can be achieved by varying θ, the angle between the optic axis and the direction of the signal/idler beam, to satisfy the phase matching condition.

Birefringent phase-matching is not an ideal solution, because there are only a limited number of phase-matching angles, and parallel waves of perpendicular polarisations will walk-off from each other. One alternative is to use temperature tuning of the refractive index to achieve phase-matching. However, a more versatile technique is quasi-phase-matching, which has several advantages over birefringence phase-matching.

2.5.3.2 Quasi-phase-matching

Quasi-phase-matching is an alternative to birefringence phase matching, which uses the ferroelectric nature of lithium niobate to prevent a phase-mismatch from occurring during frequency conversion. It uses periodically poled lithium niobate (PPLN), where the direction of the ferroelectric domain is modified to alternate with a regular period, Λ, as shown in Figure 2.13.

Periodic domain inversion results in the sign of the nonlinear coefficient also being inverted with the same period, which compensates for the wavevector mismatch. The period of the alternately inverted domains is chosen to be twice that of the coherence length. Normally, when a generated wave travelling through the crystal goes further than a single coherence length, its amplitude will start to decrease.

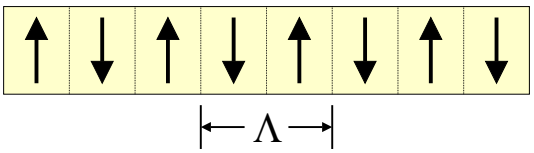

Figure 2.13: Schematic representation of periodically poled lithium niobate (PPLN). The arrows represent the direction of the $+z$ axis, which alternates with period Λ.

However, in PPLN, after a single coherence length the domain is inverted, so the wave experiences a nonlinear coefficient of opposite sign, so instead of decreasing, the amplitude of the wave continues to increase. Figure 2.14 shows the effect on field amplitude through a crystal in the case of ideal phase-matching, quasi-phase matching and no phase-matching.

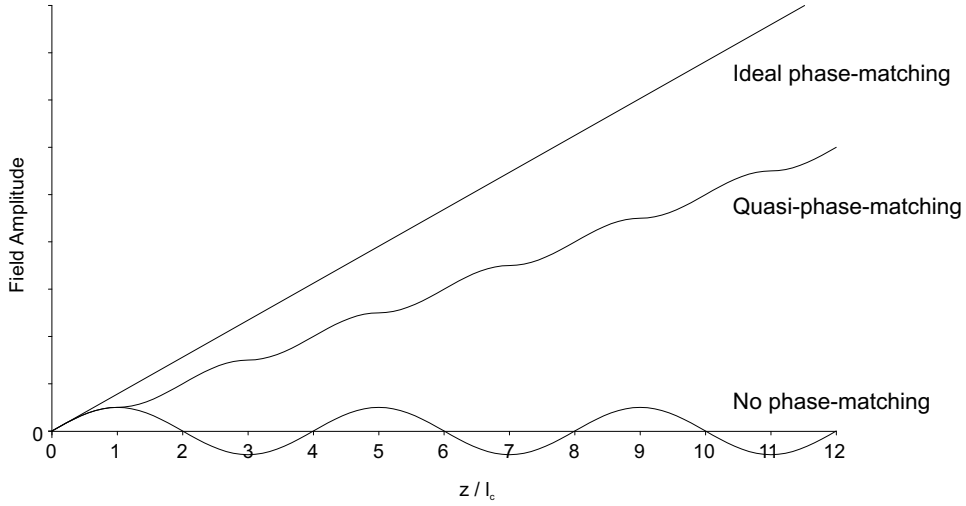

Figure 2.14: The field amplitude of a wave generated in nonlinear frequency conversion through a crystal, under conditions of ideal phase-matching, quasi-phase-matching (QPM) and no phase-matching.

In quasi-phase-matching, the equation for wavevector mismatch has to be modified with an extra term, Δk_g, to take the grating period into consideration, (Myers et al., 1995):

$$\Delta \mathbf{k} = \mathbf{k}_p - \mathbf{k}_s - \mathbf{k}_i - \Delta \mathbf{k}_g \tag{2.21}$$

where

$$\Delta \mathbf{k}_g = \frac{2\pi}{\Lambda} \tag{2.22}$$

hence the optimum period of the PPLN is

$$\Lambda = \frac{2\pi}{(\mathbf{k}_p - \mathbf{k}_s - \mathbf{k}_i)} \tag{2.23}$$

The use of quasi-phase-matching eliminates the dependence on birefringence, so can be used in a material which is not naturally birefringent, and does not require angle tuning which can cause problems with walk-off between the beams. It also allows access to the largest nonlinear coefficients, which may not be possible with birefringent phase-matching, due to the geometry of the crystal and the necessary polarisation of the beams.

For more detailed information on quasi-phase-matching and periodic poling, see, for instance, Houe and Townsend (1995).

2.5.4 Acoustic-wave devices

Surface acoustic waves (SAWs) are high-frequency (ultrasonic) pressure waves that propagate along the surface of a crystal. Lithium niobate is an ideal material for making devices that utilise SAWs, because of its piezoelectric properties. Figure 2.15 shows a schematic of a typical SAW device. A piezoelectric crystal, with thin metal arrays of electrodes defined on the crystal surface using photolithography, acts as a transducer, converting electrical signals to surface acoustic waves (through the piezoelectric effect) and back again. This allows devices to be built, a simple example of which is a RF delay line. These make use of the relatively slow speed of an acoustic wave, compared to that of an electromagnetic wave. A transducer converts a RF electronic signal to an ultrasonic acoustic wave, which propagates along the surface of the crystal, to another transducer, which reforms the electronic signal. Because the acoustic wave is so much slower, a small SAW device can provide the same delay as a much longer piece of electrical cabling. This is used in radar systems to reduce signals scattered from non-moving objects like buildings which would otherwise clutter the displays.

The frequency ν of the surface acoustic wave is given by:

$$\nu = \frac{v}{\lambda} \tag{2.24}$$

where v is the velocity of the SAW and λ is the interdigital electrode period.

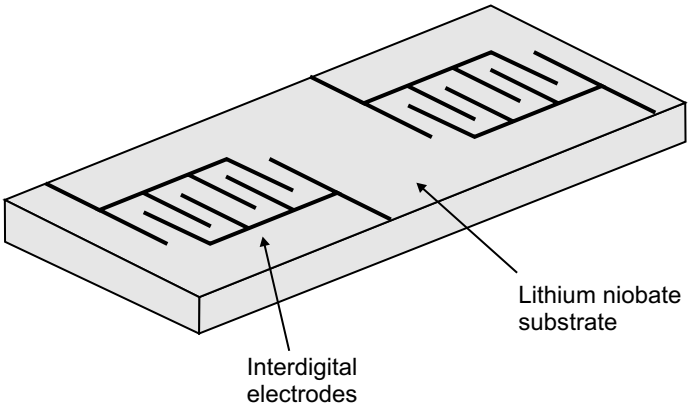

Figure 2.15: Schematic diagram of a typical surface acoustic wave device.

Surface acoustic waves can also be used to make sophisticated filters which are used in wireless telecommunications. Traditional filters (based on coils or capacitors) suffer from cross-talk between closely spaced channels. In cellular telephones systems, for instance, close spacing of channels is necessary to maximise the number of channels available in a particular band. Transversal SAW filters do not suffer from the problem of cross talk, they are also small, cheap to produce (due to mass production), durable and reliable. The frequency selection is achieved through the design of the electrodes, using parameters such as the number, spacing and size of the individual electrode components. A very sharp filter response can be achieved from a small SAW chip, the reason for this can be explained with Fourier analysis. A filter with a rectangular frequency response will, in theory, need to be infinitely long. But by converting an RF voltage to a slower acoustic wave, which has a correspondingly smaller wavelength, many wavelength cycles can take place over a short length of crystal, allowing for a sharp frequency response. SAW filters are also used in televisions, video recorders, satellite receivers and radio transmission.

Lithium niobate can also be used to produce acousto-optic modulators (AOMs), which use acoustic waves to modify the refractive index of the crystal, and so control the frequency, intensity and direction of an incident optical wave. An acoustic wave is a longitudinal series of compressions and rarefactions; as it travels through the crystal, the compressed areas will have a higher refractive index, and the rarefied areas will have a lower refractive index, than the surroundings. As the acoustic wave is periodic, a grating consisting of areas of increased and decreased refractive index will be produced, which can diffract an incident light beam. The operation of an acousto-optic deflector is illustrated in Figure 2.16

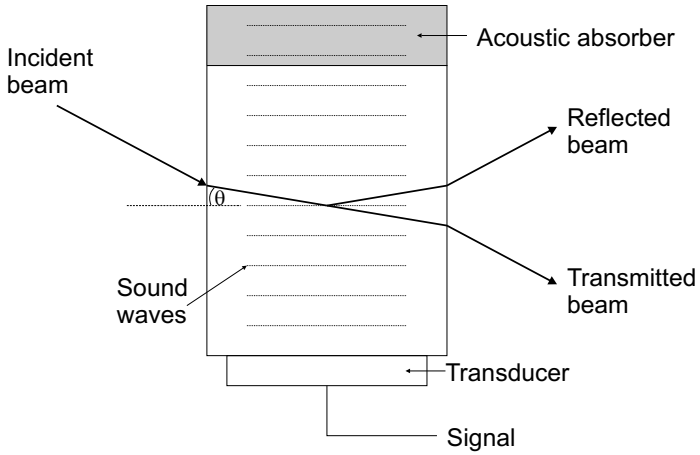

Figure 2.16: Schematic diagram of an acousto-optic deflector.

2.5.5 Holographic data storage

The promise of using holographic techniques for fast, high-capacity data storage has been around for many years, but a commercial device has yet to be made available. However, extensive research into this area is ongoing. One of the most promising routes appears to be the use of photorefractive materials, of which lithium niobate is a popular choice. Holograms store data in a volume of material, not just an area, and many holograms may be recorded in the same volume, by recording at different angles or wavelengths. These properties make the prospect of holographic data storage very attractive, as much larger amounts of data can be stored in a given area than is currently possible. Estimates suggest storage densities of 50 times that of current optical media are possible, with a similar increases in transfer rates.

The storage of holograms in lithium niobate is achieved by illumination of the crystal with a light pattern, which excites electrons from defects, such as impurities. Most lithium niobate crystals contain a small concentration of Fe impurities (Peterson et al., 1971) so electrons are easily excited from Fe^{2+} to the conduction band, from where they migrate by diffusion, drift and the bulk-photovoltaic effect until they are captured by Fe^{3+} ions in dark regions. The trapped charge creates space-charge fields, which affect the refractive index, through the electro-optic effect. Subsequent illumination of the hologram with with a homogeneous laser beam will result in the beam being diffracted by the space-charge fields and so the original optical pattern can be recreated.

To increase the extent of the photorefractive effect, lithium niobate crystals intended for use in holographic storage are purposely Fe-doped. Staebler and Phillips

(1974) produced an early report on the use of iron-doped crystals for storing phase holograms. They found that the once formed the hologram can be erased by exposure to a uniform light beam, which excites the trapped electrons and so allows them to redistribute uniformly. It was reported that only 12 mJ/cm^2 of radiation at 488 nm was required to erase a hologram in reduced lightly-doped lithium niobate (0.05 % Fe), which was nearly three orders of magnitude less than had been previously observed.

Shah et al. (1976) studied eight Fe:$LiNbO_3$ crystals with varying dopant concentrations, half of which had been annealed in oxygen, while the other half were unannealed, for use in holographic storage. The photorefractive sensitivity, defined as:

$$S = (\Delta n/\Delta E)\Gamma \tag{2.25}$$

where Γ represents the ratio of the average beam intensity in the crystal to the incident intensity and Δn is the refractive index change caused by the incident energy density, ΔE, was shown to be mainly sensitive to the concentration of Fe^{2+} ions. The crystal with the best photorefractive sensitivity was found to be unannealed with 0.05 % Fe concentration and with 20 - 25 % of the ions in the Fe^{2+} state.

Shah et al. also used IR spectra to identify hydrogen impurities, which are known to reduce the photorefractive sensitivity, (Smith et al., 1968). Hydrogen diffuses into the crystals during poling or annealing and combines with oxygen to form OH ions, which have a characteristic vibrational band in the near infrared at ~2.86 μm. The motion of protons in lithium niobate crystals has been examined by Engelsberg et al. (1993), who found that there are two temperature dependent regimes of motion. At low temperatures (around room temperature) there appears to be a fast, fluctuating motion of the hydrogen ions between normal and interstitial sites, which suggests the intersitial sites are occupied for a substantial proportion of the time. This could be the reason for reduced photorefractive sensitivity and increased resistance to optical damage.

A problem with holographic data storage which still needs to be addressed is the durability of the data. Retrieval of the holograms can cause the charge fields to be reduced, due to the homogeneous light which is used to read the hologram. The space-charge fields also gradually decay even in the dark, giving a dark storage time, which is a measure of the time until the grating amplitude drops to $1/e$ of its initial value (Nee et al., 2000).

Holograms are often recorded using ultraviolet light, however, this can result in erasure of the holograms during reading. An alternative is to use infrared pulses, but Fe:$LiNbO_3$ suffers from poor sensitivity at these wavelengths. To overcome this, Buse et al. (1995) proposed used a spatially homogenous pulse of green light prior to recording of holograms using infrared illumination, which sensitises the samples for recording and can also erase previous holograms. Reading the hologram with infrared light was found to be non-destructive.

A system using doubly-doped lithium niobate crystals has been recently proposed, by Buse et al. (1998), using iron and and manganese, which improves the stability of stored holograms. The doubly-doped crystal was found to be photochromic, i.e. the absorption of light of a particular wavelength affects the absorption characteristics of light of a second wavelength. In practice, this means that recording is carried out using a combination of red and ultraviolet light. The ultraviolet light, from a mercury lamp, uniformly illuminates the sample and the red light is from a laser source, and contains the data to be recorded in the hologram. For reading the hologram, only the red laser is required. The manganese ions can only be excited by ultraviolet light, because their energy levels are deeper, so the hologram is not degraded by repeated reading, and hence the data can be stored with greater reliability.

During the recording phase, the ultraviolet light excites electrons from deep Mn^{2+} levels, to the conduction band and the iron levels, forming Fe^{2+} ions which can then absorb the modulated red light, which is also present, thus exciting more electrons, which diffuse then recombine with Fe^{3+} and Mn^{3+} ions to create space-charges fields and consequently a hologram is formed. The electrons will be trapped in Fe^{2+} and Mn^{2+} ions, and while ultraviolet light is still present, electrons will be still be able to move between iron and manganese. However, as red light only excites electrons from iron, the build up of charge in manganese levels will begin to mirror the spatial modulation of the red light.

Once the recording phase is complete the ultraviolet illumination is removed. The hologram can then be reconstructed using homogeneous red light. As before, this will quickly 'wash-out' the charge pattern stored in iron traps, but the charge stored in manganese will remain unaffected by the red light, as it is does not have enough energy to excite the electrons from the deeper energy levels. Consequently, the hologram will remain fixed in the crystal, allowing non-destructive read out. The hologram can be simply erased by uniformly illuminating the crystal with ultraviolet light.

2.6 Conclusion

In this chapter the basic structure of lithium niobate has been discussed, in terms of the crystalline structure, symmetry and composition, the latter which is largely determined by the growth conditions. The numerous and varied physical properties of lithium niobate, a consequence of the crystal structure, have been described, and many applications utilising these properties have been illustrated. The techniques of electric field poling, and etching in acid have also been discussed, as these are of relevance to work described in the experimental chapters.

2.7 References

Abrahams, S. C., W. C. Hamilton and J. M. Reddy. "Ferroelectric lithium niobate 4. Single crystal neutron diffraction study at 24°C." *Journal of Physics and Chemistry of Solids*, **27**(6-7), 1013 (1966a).

Abrahams, S. C., H. J. Levinstein and J. M. Reddy. "Ferroelectric lithium niobate 5. Polycrystal x-ray diffraction study between 24°C and 1200°C." *Journal of Physics and Chemistry of Solids*, **27**(6-7), 1019 (1966b).

Abrahams, S. C. and P. Marsh. "Defect structure dependence on composition in lithium niobate." *Acta Crystallographica B*, **42**, 61 (1986).

Abrahams, S. C., J. M. Reddy and J. L. Bernstein. "Ferroelectric lithium niobate 3. Single crystal x-ray diffraction study at 24°C." *Journal of Physics and Chemistry of Solids*, **27**(6-7), 997 (1966c).

de Angelis, M., S. De Nicola, A. Finizio, G. Pierattini, P. Ferraro, S. Grilli and M. Paturzo. "Evaluation of the internal field in lithium niobate ferroelectric domains by an interferometric method." *Applied Physics Letters*, **85**(14), 2785 (2004).

Bailey, P. Ph.D. thesis, Bristol (1952).

Ballman, A. A. *Journal of the American Ceramic Society*, **27**, 1013 (1965).

Battle, C. C., S. Kim, V. Gopalan, K. Barkocy, M. C. Gupta, Q. X. Jia and T. E. Mitchell. "Ferroelectric domain reversal in congruent $LiTaO_3$ crystals at elevated temperatures." *Applied Physics Letters*, **76**(17), 2436 (2000).

Belinicher, V. I., V. K. Malinovskii and B. I. Sturman. "Photogalvanic effect in a crystal with polar axis." *Soviet Physics JETP*, **46**(2), 362 (1977).

Bermudez, V., F. Caccavale, C. Sada, F. Segato and E. Dieguez. "Etching effect on periodic domain structures of lithium niobate crystals." *Journal of Crystal Growth*, **191**(3), 589 (1998).

Bordui, P. F., R. G. Norwood, C. D. Bird and G. D. Calvert. "Compositional uniformity in growth and poling of large-diameter lithium niobate crystals." *Journal of Crystal Growth*, **113**(1-2), 61 (1991).

Boyd, G. D., R. C. Miller, K. Nassau, W. L. Bond and A. Savage. "$LiNbO_3$: An efficient phase matachable nonlinear optical material." *Applied Physics Letters*, **5**(11), 234 (1964).

Boyd, R. W. *Nonlinear Optics* (Academic Press, San Diego, 2003), 2nd edition.

Boyland, A. J., S. Mailis, J. M. Hendricks, P. G. R. Smith and R. W. Eason. "Electro-optically controlled beam switching via total internal reflection at a domain-engineered interface in $LiNbO_3$." *Optics Communications*, **197**, 193 (2001).

Buse, K. "Light-induced charge transport processes in photorefractive crystals I: Models and experimental methods." *Applied Physics B*, **64**, 273 (1997a).

Buse, K. "Light induced charge transport processes in photorefractive crystals II: Materials." *Applied Physics B*, **64**, 391 (1997b).

Buse, K., A. Adibi and D. Psaltis. "Non-volatile holographic storage in doubly doped lithium niobate crystals." *Nature*, **393**, 665 (1998).

Buse, K., F. Jermann and E. Kratzig. "Infrared holographic recording in linbo3:fe and linbo3:cu." *Optical Materials*, **4**(2-3), 237 (1995).

Camlibel, I. "Spontaneous polarization measurements in several ferroelectric oxides using a pulse-field method." *Journal of Applied Physics*, **40**(4), 1690 (1969).

Donnerberg, H. J., S. M. Tomlinson and C. R. A. Catlow. "Defects in $LiNbO_3$ - ii. Computer simulation." *Journal of Physics and Chemistry of Solids*, **52**(1), 201 (1991).

Eason, R. W., A. J. Boyland, S. Mailis and P. G. R. Smith. "Electro-optically controlled beam deflection for grazing incidence geometry on a domain-engineered interface in $LiNbO_3$." *Optics Communications*, **197**, 201 (2001).

Engelsberg, M., G. C. do Nascimento and L. H. Pacobahyba. "H atomic motion in proton-exchanged $LiNbO_3$." *Journal of Applied Physics*, **74**(10), 6427 (1993).

Festl, H. G., P. Hertel, E. Kratzig and R. v. Baltz. "Investigations of the photovoltaic tensor in doped $LiNbO_3$." *Physica Status Solidi B*, **113**, 157 (1982).

Fradkin, V. M. and R. G. Magomadov. "Anomalous photovoltaic effect in $LiNbO_3$:Fe in polarized light." *JETP Letters*, **30**, 686 (1979).

Glass, A. M., D. von der Linde and T. J. Negra. "High voltage bulk photovoltaic effect and the photorefractive process in $LiNbO_3$." *Applied Physics Letters*, **25**(4), 233 (1974).

Gopalan, V. and M. C. Gupta. "Origin of internal field and visualization of 180 degree domains in congruent $LiTaO_3$ crystals." *Journal of Applied Physics*, **80**(11), 6099 (1996).

Gopalan, V. and M. C. Gupta. "Origin and characteristics of internal fields in $LiNbO_3$ crystals." *Ferroelectrics*, **198**, 49 (1997).

Gopalan, V., T. E. Mitchell, Y. Furukawa and K. Kitamura. "The role of nonstoichiomery in 180 degree domain switching of $LiNbO_3$ crystals." *Applied Physics Letters*, **72**(16), 1981 (1998).

Gopalan, V., T. E. Mitchell and K. E. Sickafus. "Switching kinetics of 180 degree domains in congruent $LiNbO_3$ and $LiTaO_3$ crystals." *Solid State Communications*, **109**, 111 (1999).

Greuters, J. and N. H. Rivzi. "Laser micromachining of optical materials with a 157 nm fluorine laser." Technical report, Exitech Ltd, Oxford, UK (2002).

Haycock, P. W. and P. D. Townsend. "A method of poling $LiNbO_3$ and $LiTaO_3$ below T_c." *Applied Physics Letters*, **48**(11), 698 (1986).

Houe, M. and P. Townsend. "An introduction to methods of periodic poling for 2nd harmonic generation." *Journal of Physics D: Applied Physics*, **28**(9), 1747 (1995).

Jermann, F. and J. Otten. "Light-induced charge transportation in $LiNbO_3$:fe at high light intensities." *Journal of the Optical Society of America B*, **10**(11), 2085 (1993).

Kim, S., V. Goaplan and A. Gruverman. "Coercive fields in ferroelectrics: A case study in lithium niobate and lithium tantalate." *Applied Physics Letters*, **80**(15), 2740 (2002).

Kim, S., V. Gopalan, K. Kitamura and Y. Furukawa. "Domain reversal and nostoichiometry in lithium tantalate." *Journal of Applied Physics*, **90**(6), 2949 (2001).

Kitamura, K., J. K. Yamamoto, N. Iyi, S. Kimura and T. Hayashi. "Stoichiometric $LiNbO_3$ single crystal growth by double crucible czochralski method using automatic powder supply system." *Journal of Crystal Growth*, **116**(3-4), 327 (1992).

Koechner, W. *Solid-state laser engineering* (Springer-Verlag, New York, 1976).

Kokhanchik, L., E. Yakimov and S. Shapoval. "Effect of ecr plasma treatment on lithium niobate surface state." *Ferroelectrics*, **300**(1), 147 (2004).

Lines, M. E. and A. M. Glass. *Principles and Applications of Ferroelectrics and Related Materials* (Oxford, 2001).

Madou, M. J. *Fundamentals of Microfabrication* (CRC Press, London, 2002).

Malovichko, G., V. Grachev and O. Schirmer. "Interrelation of intrinsic and extrinsic defects - congruent, stoichiometric, and regularly ordered lithium niobate." *Applied Physics B*, **68**(5), 785 (1999).

Malovichko, G. I., V. G. Grachev, E. P. Kokanyan, O. F. Schirmer, K. Betzler, B. Gather, F. Jermann, S. Klauer, U. Schlarb and M. Wohlecke. "Characterization of stoichiometric lithium niobate grown from melts containing K_2O." *Applied Physics A*, **56**, 103 (1993).

Malovichko, G. I., V. G. Grachev, L. P. Yurchenko, V. Y. Proshko, E. P. Kokanyan and V. T. Gabrielyan. "Improvement of $LiNbO_3$ microstructure by crystal growth with potassium." *Physica Status Solidi A*, **133**, K29 (1992).

Matthias, B. T. and J. P. Remeika. "Ferroelectricity in the ilmenite structure." *Physical Review*, **76**, 1886 (1949).

Megaw, H. "Ferroelectricty and crystal structure II." *Acta Crystallographica*, **7**, 187 (1954).

Miyazawa, S. "Ferroelectric domain inversion in Ti-diffused $LiNbO_3$ optical waveguide." *Journal of Applied Physics*, **50**(7), 4599 (1979).

Myers, L. E., R. C. Eckardt, M. M. Fejer, R. L. Byer, W. R. Bosenberg and J. W. Pierce. "Quasi-phase-matched optical parametric oscillators in bulk periodically poled $LiNbO_3$." *Journal of the Optical Society of America B*, **12**(11), 2102 (1995).

Nassau, K., H. J. Levinstein and G. M. Loiacono. "The domain structure and etching of ferroelectric lithium niobate." *Applied Physics Letters*, **6**(11), 228 (1965).

Nassau, K., H. J. Levinstein and G. M. Loiacono. "Ferroelectric lithium niobate. 1. Growth, domain structure, dislocations and etching." *Journal of Physics and Chemistry of Solids*, **27**(6-7), 983 (1966a).

Nassau, K., H. J. Levinstein and G. M. Loiacono. "Ferroelectric lithium niobate. 2. Preparation of single domain crystals." *Journal of Physics and Chemistry of Solids*, **27**(6-7), 989 (1966b).

Nee, I., M. Muller, K. Buse and E. Kratzig. "Role of iron in lithium-niobate crystals for the dark-storage time of holograms." *Journal of Applied Physics*, **88**(7), 4282 (2000).

Nutt, A. C. G., J. P. G. Bristow, A. McDonach and P. J. R. Laybourn. "Fiber-to-waveguide coupling using ion-milled grooves in lithium niobate at 1.3 μm wavelength." *Optics Letters*, **9**(10), 463 (1984).

Orlowski, R. and E. Kratzig. "Holographic method for the determination of photo-induced electron and hole transport in electro-optic crystals." *Solid State Communications*, **27**(12), 1351 (1978).

Paturzo, M., D. Alfieri, S. Grilli, P. Ferraro, P. De Natale, M. de Angelis, S. De Nicola, A. Finizio and G. Pierattini. "Investigation of electric internal field in congruent $LiNbO_3$ by electro-optic effect." *Applied Physics Letters*, **85**(23), 5652 (2004).

Pedrotti, F. L. and L. S. Pedrotti. *Introduction to Optics* (Prentice-Hall International, London, 1996).

Peterson, G. E., A. M. Glass and T. J. Negra. "Control of the susceptibility of lithium niobate to laser-induced refractive index changes." *Applied Physics Letters*, **19**, 130 (1971).

Prokhorov, A. M. and Y. S. Kuuzminov. *Physics and chemistry of lithium niobate* (Hilger, Bristol, 1990).

Ro, J. H. and M. Cha. "Subsecond relaxation of internal fields after polarization reversal in congruent $LiNbO_3$ and $LiTaO_3$ crystals." *Applied Physics Letters*, **77**(15), 2391 (2000).

Schirmer, O. F., O. Thiemann and M. Wohlecke. "Defects in $LiNbO_3$ – i. Experimental aspects." *Journal of Physics and Chemistry of Solids*, **52**(1), 185 (1991).

Schlarb, U. and K. Betzler. "Refractive indicies of lithium niobate as a function of wavelength and composition." *Journal of Applied Physics*, **73**(7), 3472 (1993).

Shah, R. R., D. M. Kim, T. A. Rabson and F. K. Tittel. "Characterization of iron-doped lithium niobate for holographic data storage applications." *Journal of Applied Physics*, **47**(12), 5421 (1976).

Shannon, R. D. "Revised effective ionic radii and systematic studies of interatomic distances in halides and chalcogenides." *Acta Crystallographica*, **A32**, 751 (1976).

Smith, R. G., D. B. Fraser, R. T. Denton and T. C. Rich. "Correlation of reduction in optically induced refractive-index inhomogeneity with OH content in $LiTaO_3$ and $LiNbO_3$." *Journal of Applied Physics*, **39**(10), 4600 (1968).

Sones, C. L., S. Mailis, W. S. Brocklesby, R. W. Eason and J. R. Owen. "Differential etch rates in z-cut $LiNbO_3$ for variable HF/HNO_3 concentrations." *Journal of Materials Chemistry*, **12**, 295 (2001).

Staebler, D. L. and W. Phillips. "Fe-doped $LiNbO_3$ for read-write applications." *Applied Optics*, **13**(4), 788 (1974).

Sugawara, M. *Plasma Etching* (Oxford University Press, Oxford, 1998).

Watanabe, Y., T. Sota, K. Suzuki, N. Iyi, K. Kitamura and S. Kimura. "Defect structures in $LiNbO_3$." *Journal of Physics: Condensed Matter*, **7**(18), 3627 (1995).

Webjorn, J., V. Pruneri, P. S. J. Russell, J. R. M. Barr and D. C. Hanna. "Quasi-phase-matched blue light generation in bulk lithium niobate, electrically poled via periodic liquid electrodes." *Electronics Letters*, **30**(11), 894 (1994).

Weis, R. S. and T. K. Gaylord. "Lithium niobate: Summary of physical properties and crystal structure." *Applied Physics A*, **32**, 191 (1985).

Winnal, S. and S. Winderbaum. "Lithium niobate reactive ion etching." Technical report, Electronics and Surveillance Research Laboratory, Salisbury, Australia (2000).

Wohlecke, M., G. Corradi and K. Betzler. "Optical methods to characterise the composition and homogeneity of lithium niobate single crystals." *Applied Physics B*, **63**(4), 323 (1996).

Wong, K. K. (ed.). *Properties of lithium niobate*. EMIS datareviews (INSPEC, London, 2002).

Yamada, M. and K. Kishima. "Fabrication of periodically reversed domain structure for shg in $LiNbO_3$ by direct electron beam lithography at room temperature." *Electronics Letters*, **27**(10), 828 (1991).

Yamada, M., N. Nada, M. Saitoh and K. Watanabe. "First-order quasi-phase matched $LiNbO_3$ waveguide periodically poled by applying an external field for efficient blue second-harmonic generation." *Applied Physics Letters*, **62**(5), 435 (1993).

Yamamoto, K., K. Mizuuchi, K. Takeshige, Y. Sasai and T. Taniuchi. "Characteristics of periodically domain-inverted $LiNbO_3$ and $LiTaO_3$ waveguides for second harmonic generation." *Journal of Applied Physics*, **70**(4), 1947 (1991).

Yatsenko, A. V., E. N. Ivanova and N. A. Sergeev. "NMR study of intrinsic defects in congruent $LiNbO_3$. 1. "Unoverlapping" defects." *Physica B: Condensed Matter*, **240**(3), 254 (1997).

Zachariasen, W. H. *Skrifter Norske Videnskans-Akad*, **4** (1928).

Zhong, G. G., J. Jin and Z. K. Wu. In "Proceedings of the 11th International Quantum Electronics Conference," 631 (USA, 1980).

CHAPTER

THREE

Light Induced Frustration of Etching

The production of photonic crystals, MEMS systems, scanning probe tips, ridge waveguides and gratings all require some form of microstructuring of the substrate material and thus the ability to produce structures on crystal surfaces is of great technological importance.

This chapter describes experiments that were carried out using the technique of light induced frustration of etching (LIFE), to produce microstructures on lithium niobate. LIFE describes the simultaneous exposure to light and an acid etchant. The presence of light in localised areas on the crystal surface can prevent etching from taking place and so can be used to carry out spatially selective etching and etch-frustration, leading to the production of three-dimensional structures.

3.1 Introduction

Etching of lithium niobate using hydrofluoric acid (HF) is a routine diagnostic tool for examining ferroelectric domains, as was discussed in Section 2.4.2. It relies on the faster etch rate of a $-z$ face compared to a $+z$ face (which experiences almost no etching). This property gives a useful route to fabricate three-dimensional structures on the crystal surface, such as micro-cantilevers (Sones et al., 2002).

While structuring lithium niobate using selective etching of domains gives good control over the shapes that are produced, the process requires the pattern to be defined using photolithography and the sample to be poled before any etching can take place. Additionally, a metal mask with the required pattern is needed for the photolithography. These disadvantages reduce the flexibility, speed and ease of use of the technique.

An alternative to using domain-selective etching to make structures is to instead illuminate areas of a crystal with laser light, which can also influence the etch rate. Barry et al. (1999) found that the simultaneous exposure of the $-z$ face of an iron-doped lithium niobate crystal to an acid mixture (1:2 HF:HNO_3) and illumination at a wavelength of 488 nm from an argon ion laser reduced the rate of etching on the $-z$ face to near zero. This was an unexpected result as other authors had reported enhanced etch rates in the presence of light, for example during etching of silicon (Lau et al., 1995) and GaN (Youtsey et al., 1998).

An interesting feature of the frustrated etching occurs at the edges of the frustrated region, where the intensity of light is not quite sufficient to totally stop the etching and instead partial frustration is observed. This etching behaviour is characterised by the formation of self-organised, sub-micron scale features. In Barry's experiments, a tightly-focussed laser beam was used, so only small areas experienced partial or near total frustration. Boyland et al. (2000) then showed that it was possible to modify the technique to favour the deliberate creation of such features instead of achieving complete frustration, by reducing the laser intensity to below some threshold level.

The research presented in this chapter investigates the phenomenon of partial frustration in greater depth than in previous work, and reports on the factors that determine the features that are formed. The key results have been published in Applied Surface Science (Scott et al., 2004).

3.2 Experimental Details

The LIFE process uses iron-doped lithium niobate because it experiences greater optical absorption at the visible wavelengths which are used than undoped lithium niobate, which is almost entirely transparent to visible light. The absorption increases as the concentration of iron impurities is increased, as shown by the absorption spectra in Figure 3.1.

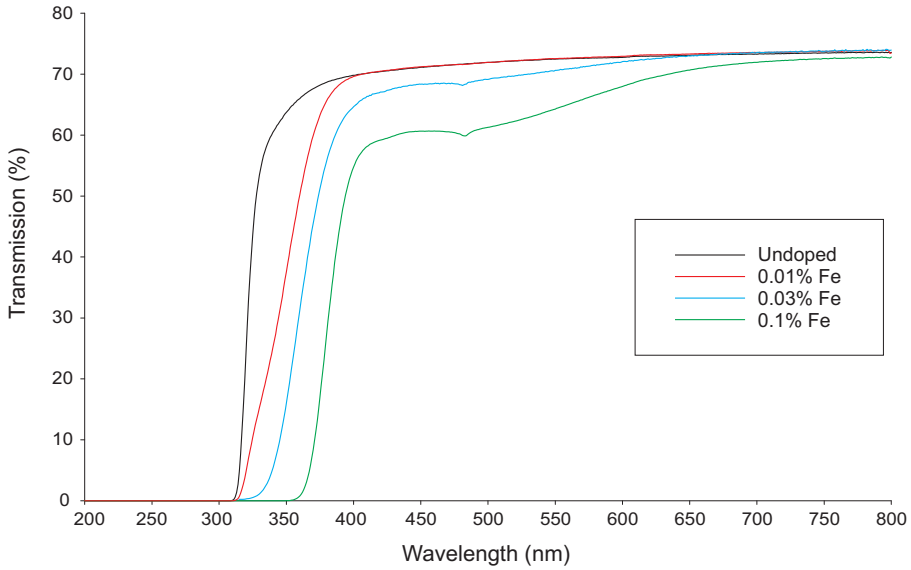

Figure 3.1: Optical transmission spectra of 0.5 mm thick iron-doped lithium niobate crystals.

A 1 cm × 1 cm × 0.5 mm ($x \times y \times z$) lithium niobate crystal was placed in a custom-made acid resistant cell, made from stainless steel and PTFE. The cell was designed to allow exposure of the $-z$ face of the crystal to an etchant, a 2:1 mixture of nitric (HNO_3)and hydrofluoric (HF) acids. The crystal was simultaneously illuminated by a 300 mW continuous wave laser beam with wavelength of 532 nm from a frequency doubled Nd:YAG laser (Laser Quantum, Ventus 532), focussed on to the $-z$ face. The beam entered from below through a hole milled in the bottom of the cell. A rubber 'O' ring placed over the crystal sealed the cell to prevent acid leakage. A schematic of the apparatus is given in Figure 3.2.

Experiments were carried out to investigate the influence of the following factors on the frustrated etching:

- Intensity of beam.
- Duration of exposure.
- Iron dopant concentration.
- Surface defects.
- Polarisation of light used.

Once the exposures were complete, the samples were examined with a scanning electron microscope (SEM), see Appendix A for details on the operation of this

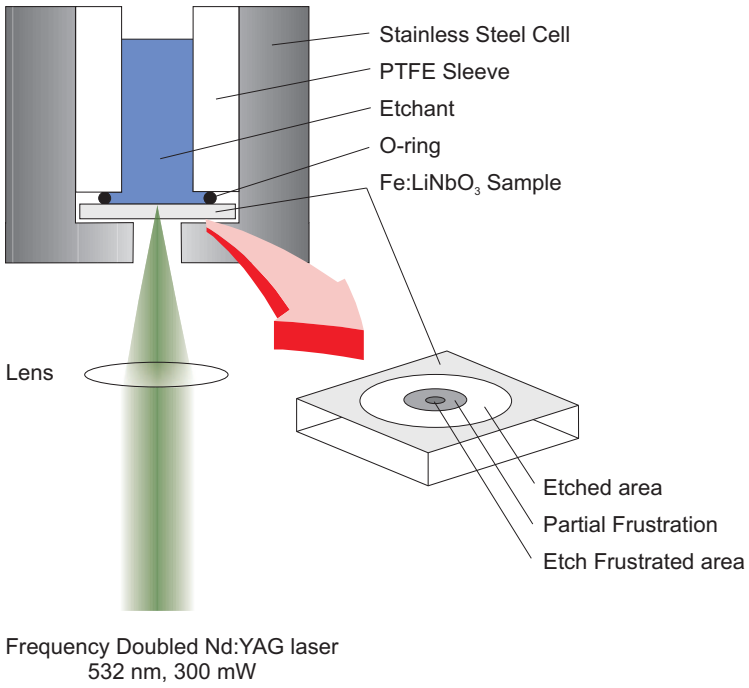

Figure 3.2: Schematic diagram of the cell used to conduct LIFE experiments.

instrument. As lithium niobate is an insulator, a thin gold coating is required to prevent charge build-up on the sample when in the SEM. This can be easily applied using a sputterer.

3.3 Results

Figure 3.3 shows an SEM image of a typical LIFE site, and a magnified view taken at an edge of the site. It was created on a 0.03 % Fe-doped $LiNbO_3$ crystal by 60 minutes of simultaneous exposure to light and acid. The incident laser beam had a Gaussian profile and was tightly focussed to a spot size of $\omega \approx 28$ μm. Three regimes of etching are visible; at the edge of the site (labelled A) etching has taken place as usual, while in the centre (C), etching has been mostly prevented. The effect of total frustration of etching on surface topography can be clearly seen from the surface profiler trace, (Figure 3.4), where the central (unetched) area is approximately 1.2 μm higher than the rest of the crystal face. The sample had been etched for an additional 60 min before the surface profile was measured, hence the etch rate was 0.6 μm h^{-1}. Immediately surrounding the total frustration is an area of partial frustration (region B), consisting of intricate patterns made of lines and

dots. The patterns become denser towards the centre of the site where the laser intensity is at its maximum.

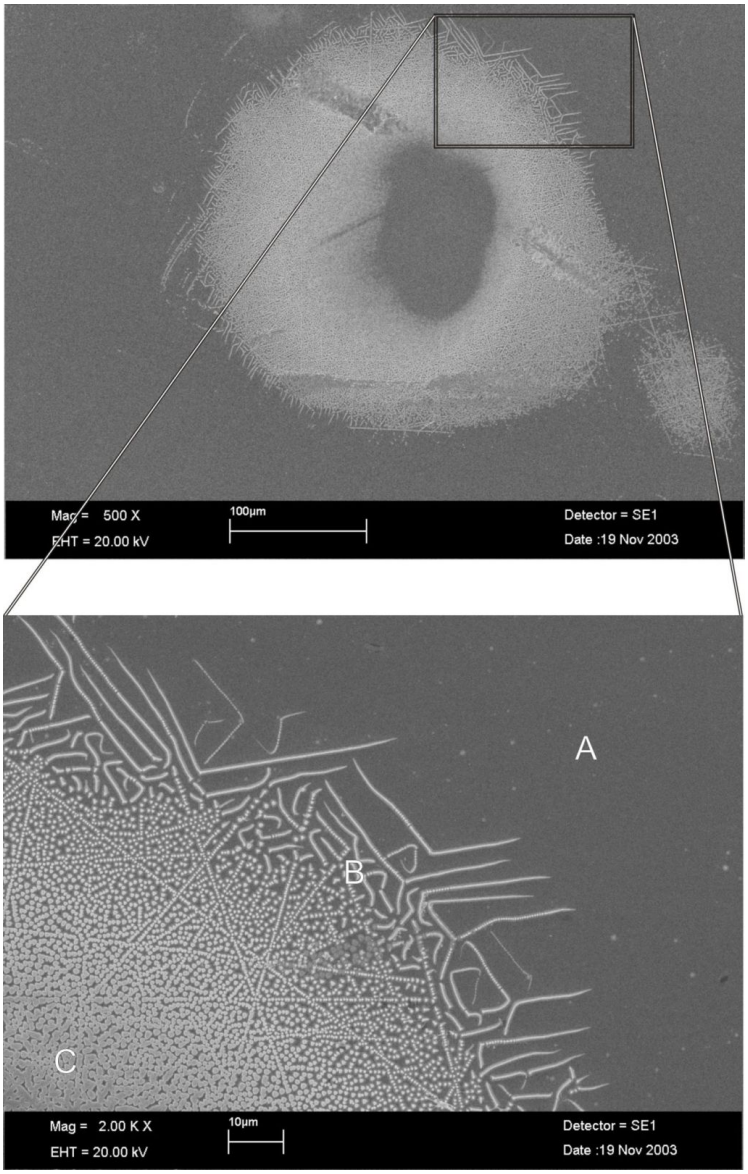

Figure 3.3: A typical site formed by the LIFE process, on 0.03 % Fe-doped $LiNbO_3$, and a magnified view showing the partially frustrated structures that are formed near the edges of the site.

3.3.1 Beam intensity

The intensity of the light used to illuminate the crystal during etching has a major influence on the etching characteristics. This factor was studied by varying the distance of the crystal surface from the focal point of the lens (and hence the spot

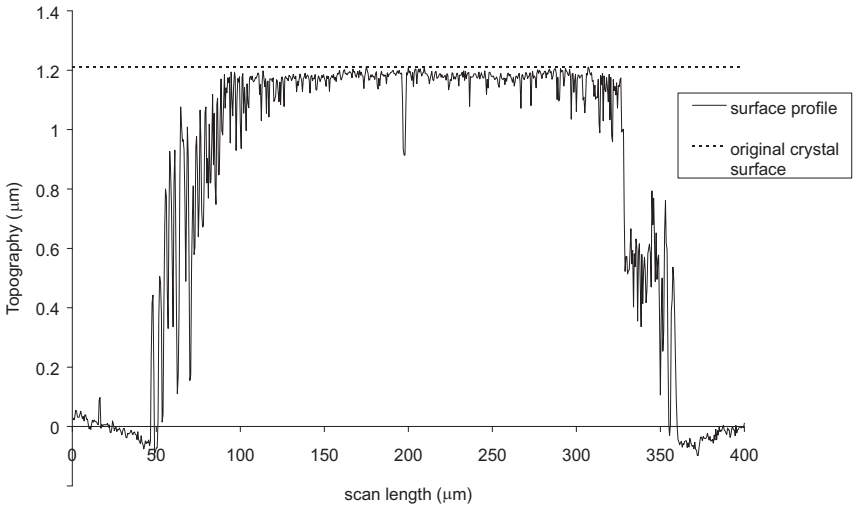

Figure 3.4: Surface profile of the LIFE site shown in Figure 3.3, showing the topography after 2 hours of exposure to etchant (the sample was etched for an additional hour after the first hour of exposure to acid and light).

size of the beam) and also by using the natural Gaussian intensity profile of the beam.

Figure 3.5 shows a site that was created with a deliberately defocussed beam, with a larger spot size ($\omega \approx 120$ μm) and a correspondingly lower power density. The iron dopant concentration was 0.1 % in this experiment and the etch duration was 80 min. The SEM image reveals a much larger site than that in Figure 3.3, with a diameter of approximately 2 mm compared to the ~ 350 μm of the previous experiment, both of which are significantly larger than the corresponding beam spot sizes. The site consists mostly of partially etch-frustrated features. The expanded view shows a representative example of the complex and visually intriguing patterns which are formed towards the edge of the site. It is clear from this figure that the pattern formation follows rules of both symmetry and scale.

The Gaussian profile of the beam results in higher light intensities at the centre of the site than at the edges and this causes different structures to be formed at different positions across the site. This is illustrated in Figure 3.6, which shows a selection of SEM images taken across the site. Fig. 3.6(a) was taken at the extreme edge of the site, while Fig. 3.6(f) shows the central region. The other images were taken at regular intervals between these extremes.

Figure 3.6(a) shows a typical pattern found at the edges, where the laser intensity is very low; the structures are spread out and have narrow line widths. It is also clear that some of the lines are composed of even smaller point-like structures. It

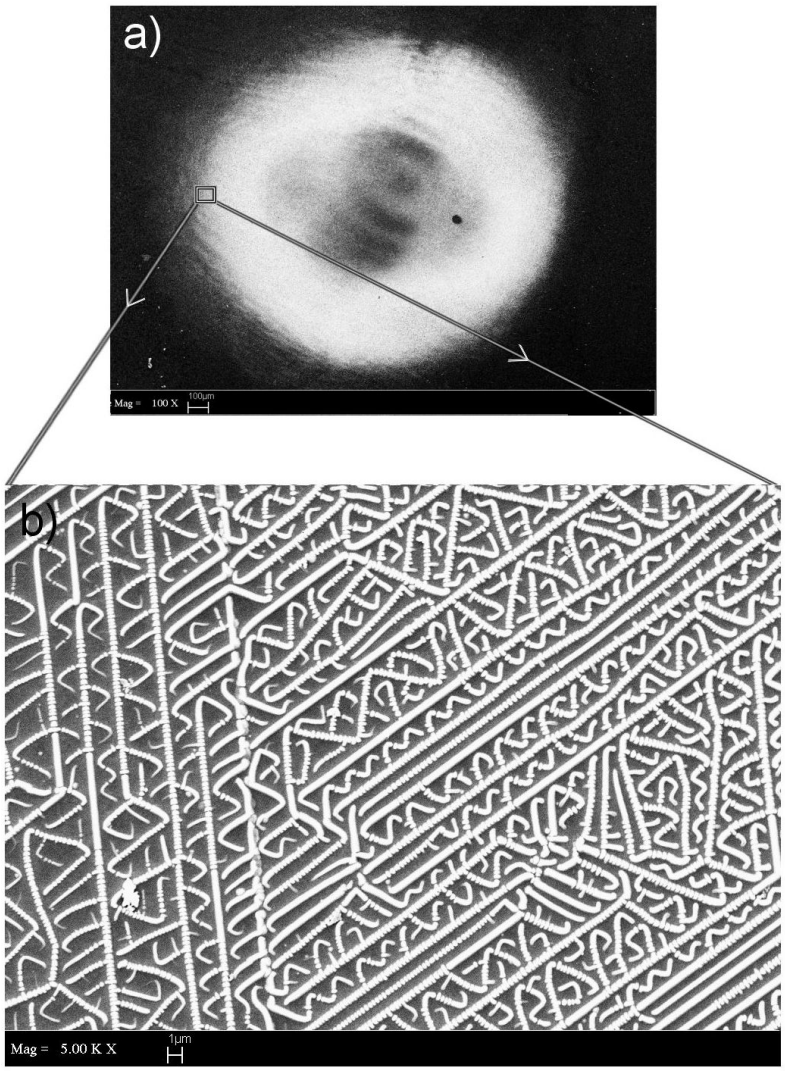

Figure 3.5: A larger LIFE site produced using 0.1 % Fe:$LiNbO_3$ and a defocused beam.

appears that the lines form along one of three directions, 120° apart, suggesting a close affinity for patterning along the three equivalent trigonal *a* axes of the crystal unit cell. Moving closer to the centre, Figures 3.6(b) and 3.6(c) show denser packing of the structures, with the etch-frustrated lines curving around one-another to fill the available space. This trend continues with images shown in Figures 3.6(d) and 3.6(e), until the centre, Fig. 3.6(f), where the intensity is greatest and the packing density is high enough to prevent any observable orientational preference. However topography can still be observed, so etching has not been completely frustrated.

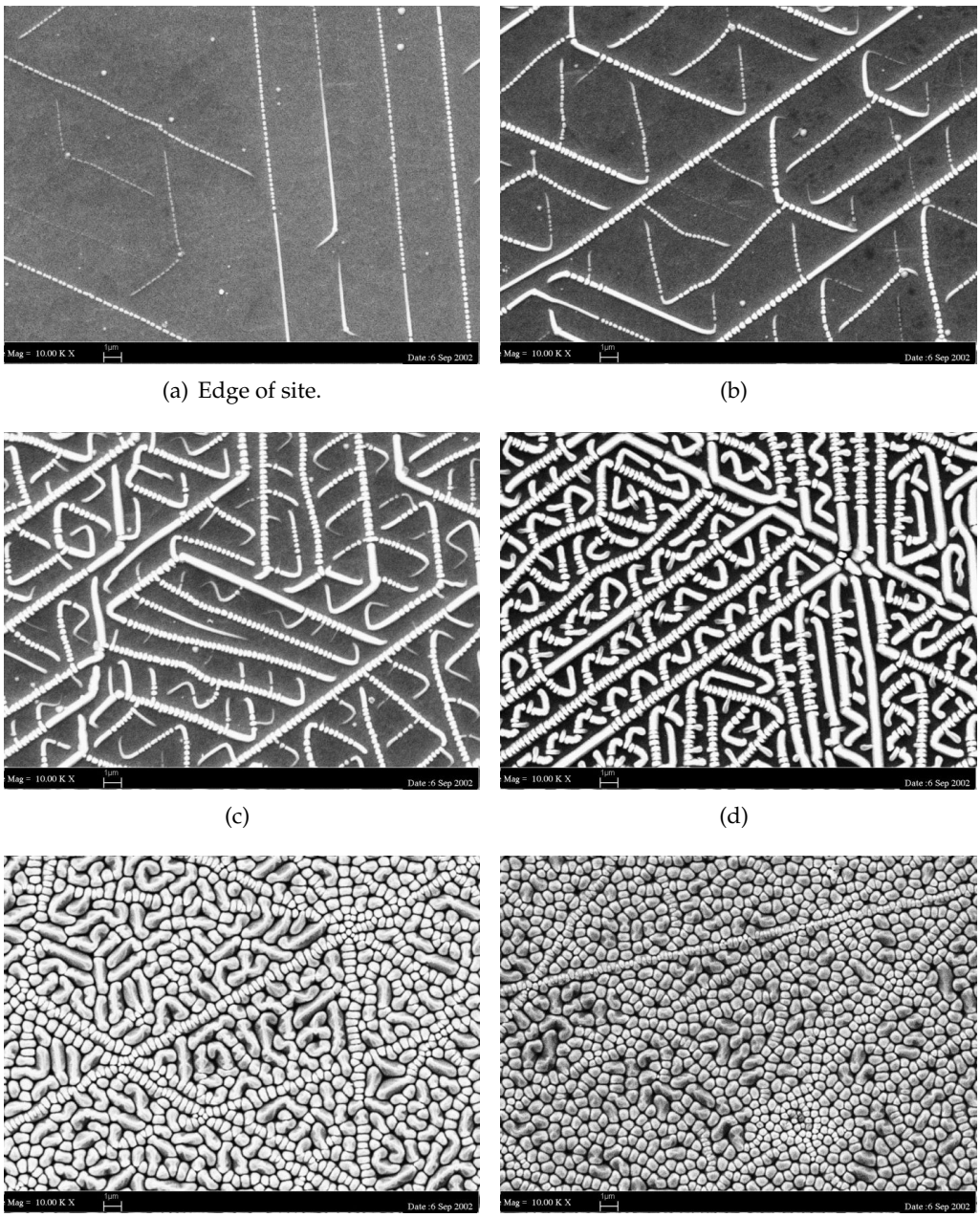

(a) Edge of site. (b)

(c) (d)

(e) (f) Centre of site.

Figure 3.6: Variation of structures formed across a site in a LIFE experiment, using a 0.1 % Fe-doped $LiNbO_3$ crystal.

The gradual change in density and pattern of structures formed can be observed in the SEM image in Figure 3.7, where the edge of the site is on the left hand side of the image.

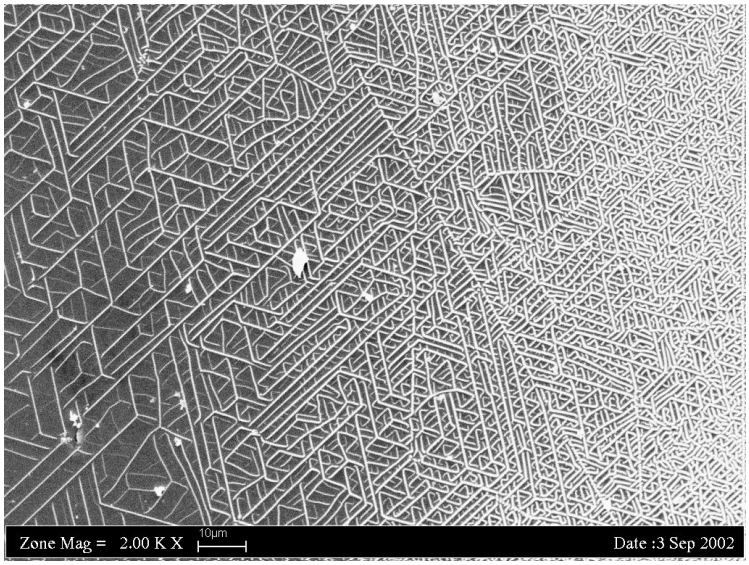

Figure 3.7: SEM image illustrating the increase in density of the LIFE features towards the centre of the site.

Examining the higher magnification SEM image in Figure 3.8, it is clear that lines which form during a LIFE experiment may be either solid or broken. The components of the broken lines appear to have a fairly regular periodicity of less than half a micrometre.

The irradiance of the laser beam on the crystal surface at a certain distance from the centre of the spot may be calculated using Gaussian beam optics. The spot size of a laser beam is defined as the radius at which the beam intensity has decreased to $1/e^2$ of its peak value. When the beam is at focus, the spot size (ω_1) is given by

$$\omega_1 = \frac{\lambda f}{\pi \omega_0} \tag{3.1}$$

where λ is the wavelength of the laser and ω_0 is the spot size of the beam emitted from the laser. At a distance z from the focus, the actual spot size (ω_2) becomes larger, according to:

$$\omega_2 = \omega_1 \left[1 + \left(\frac{\lambda z}{\pi \omega_1^2} \right)^2 \right]^{\frac{1}{2}} \tag{3.2}$$

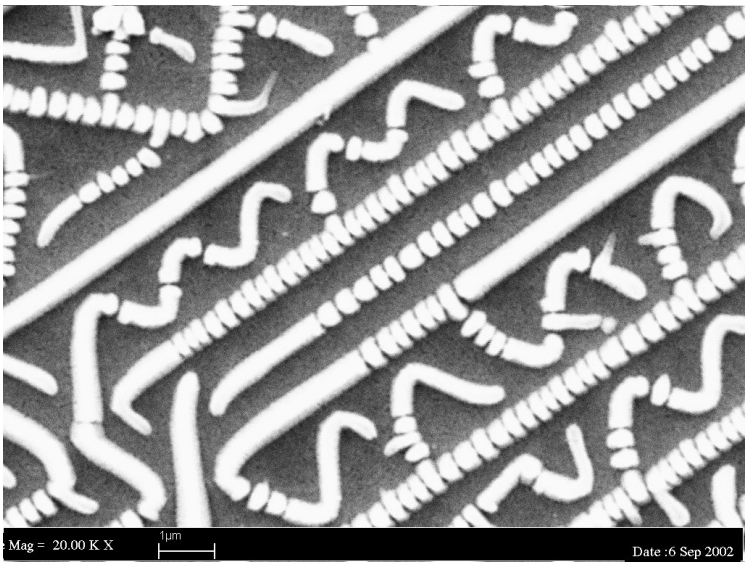

Figure 3.8: Solid and broken lines that may form during a LIFE experiment.

The irradiance distribution, $I(r)$, across the spot can then be calculated using

$$I(r) = I_0 \exp\left(\frac{-2r^2}{\omega_2^2}\right) = \frac{2P}{\pi\omega_2^2} \exp\left(\frac{-2r^2}{\omega_2^2}\right) \tag{3.3}$$

where P is the power of the beam and r is the distance from the centre of the spot. In the rest of the text, ω represents the actual spot size used.

Figures 3.9 and 3.10 show the calculated values of irradiance superimposed on SEM images of two samples, one created using a focussed beam and the other with a defocussed beam (N.B. the site in Fig. 3.10 is much larger than the one in Fig. 3.9).

The two samples also had differing iron dopant concentrations, but the irradiance is the dominant factor. As would be expected, the irradiance is much higher at the centre of the spot in Figure 3.9, where the beam is at focus. However, both sites are much larger than their corresponding beam spot sizes, with the irradiance effectively zero at the edges. This suggests that the sites grow outwards from the central areas of higher irradiance.

3.3.2 Duration of exposure

Using a focussed beam from a laser ($\omega \approx 25$ μm), LIFE features have been observed to form after only two seconds of exposure to light and etchant. Figure 3.12 shows SEM images of eight sites formed by exposure to a laser beam for varying periods

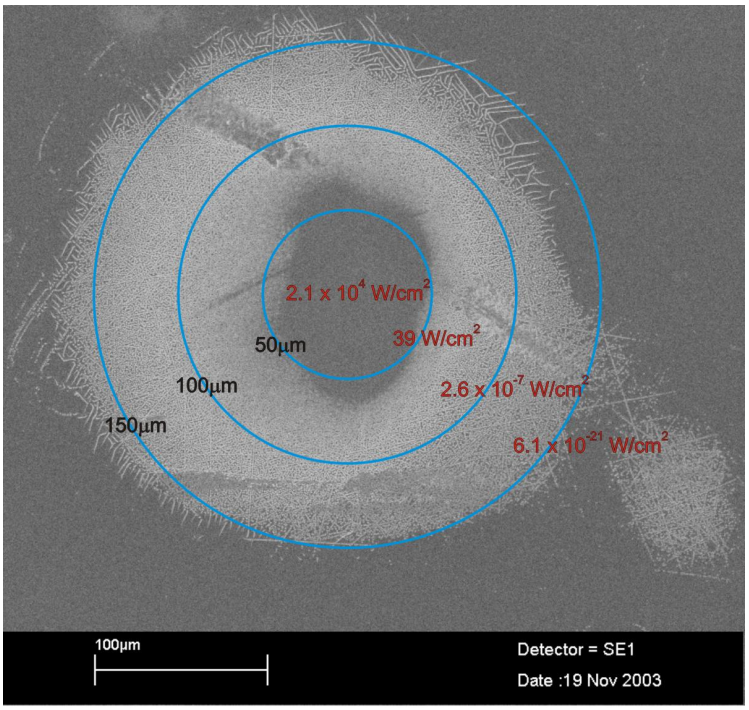

Figure 3.9: Irradiance across a LIFE site produced using 0.03 % Fe:$LiNbO_3$ and a focussed beam ($\omega \approx 28$ µm).

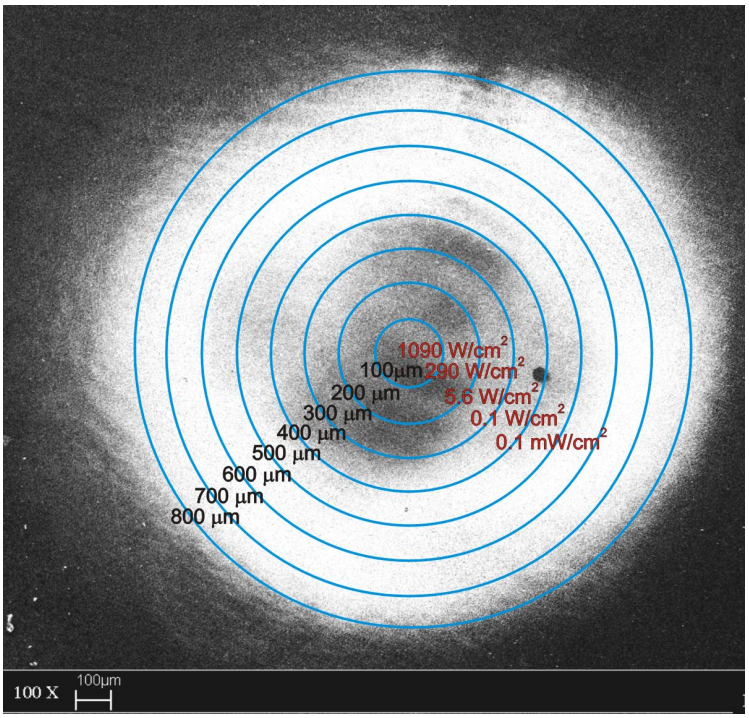

Figure 3.10: Irradiance across a LIFE site produced using 0.1 % Fe:$LiNbO_3$ and a defocused beam ($\omega \approx 120$ µm).

of time (between 5 s and 16 min) while in the presence of acid. Each site was formed on the same crystal, one after another, and the total etching time for each was forty minutes.

For illumination times of less than two minutes, LIFE sites are clearly visible, consisting mainly of 'dots' and randomly orientated 'lines of dots'. After two minutes distinctive lines begin to form, and by eight minutes a typical but small (diameter $\sim$ 250 μm) LIFE site has formed, with a densely packed centre and lines extending outwards. The 120° symmetry is especially apparent in this case, as the lines spreading out from the centre tend to be parallel to each other within the same 120° segment (Fig. 3.11). This effect is probably a result of the small radius of the site. At the edge the lines have self-organised to favour a quasi-periodic spacing.

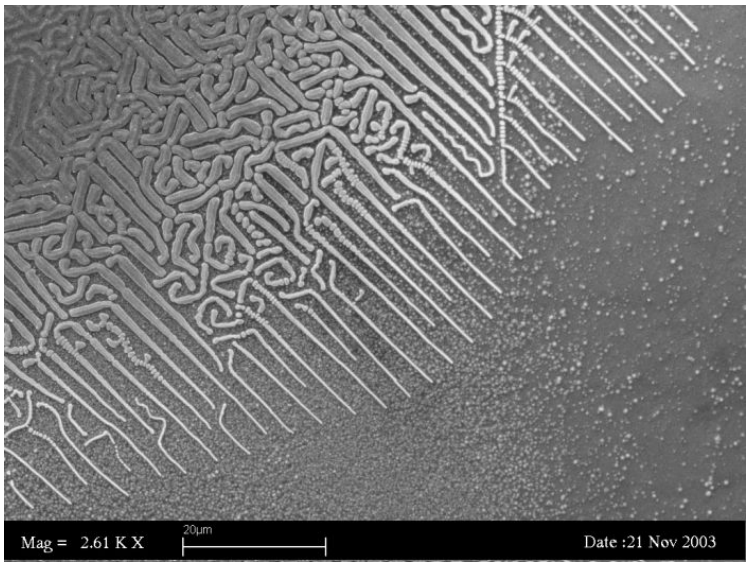

Figure 3.11: A site exposed to light for 8 min; lines at the edge are generally parallel and are directed away from the centre.

When using a defocussed beam ($\omega \approx 120$ μm) sites can still form quickly. A series of experiments was conducted, exposing different crystals to light and acid for 5, 10, 20, 40 and 80 minutes. The sites formed are much larger, due to the larger beam spot size and consequently the whole area cannot be shown in a single SEM image while preserving detail; instead a survey of images was taken at regular intervals across the radius of each site. Too many images were collected to present them all here, however, key images have been selected to illustrate particular points.

Figure 3.13 shows two areas of a LIFE site after five minutes of etching. At the centre of the site dense arrangements of dots are produced, while at the edges the features are less dense, and some short (length $<$ 5 μm) lines have begun to form, starting

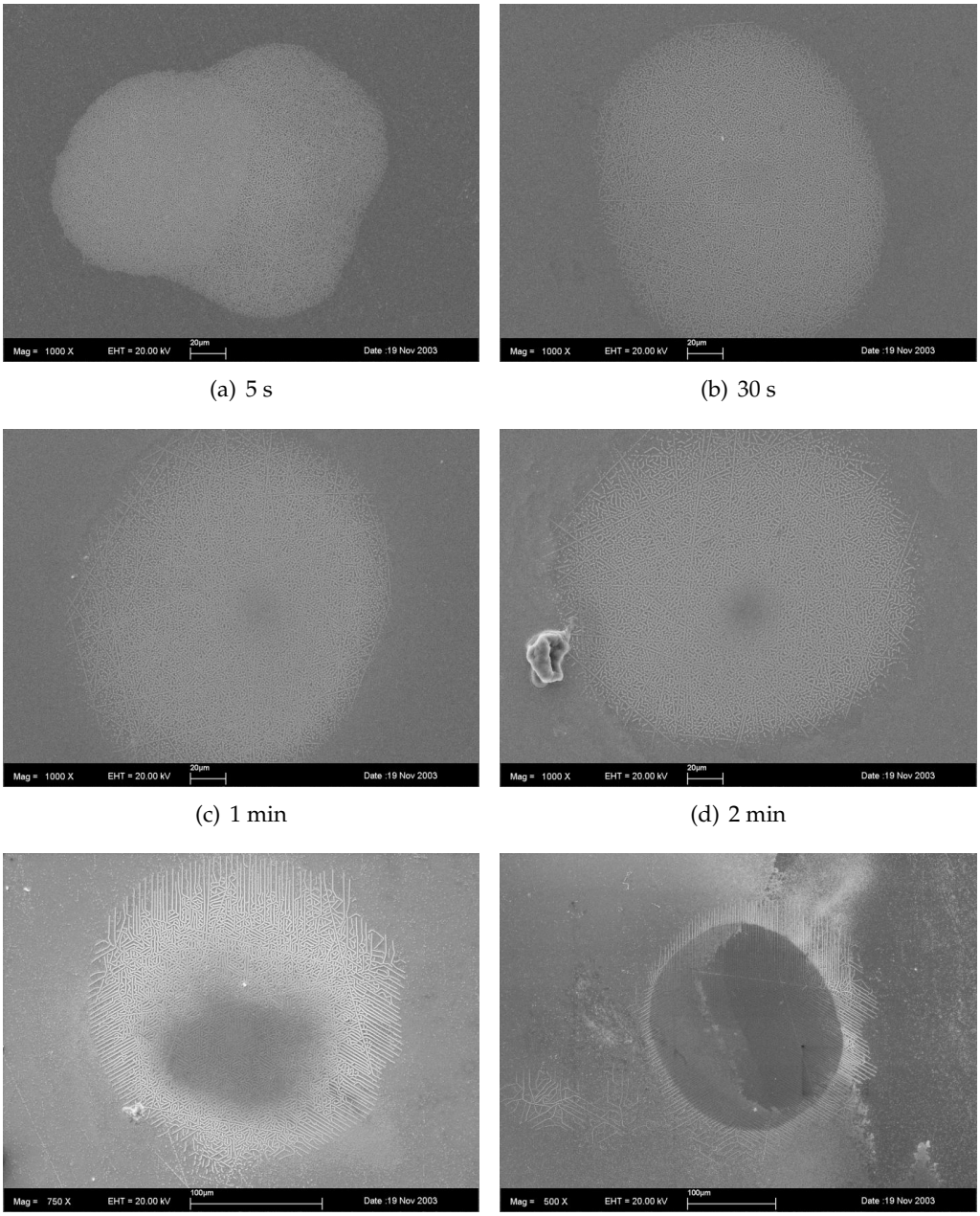

(a) 5 s (b) 30 s

(c) 1 min (d) 2 min

(e) 8 min (f) 16 min

Figure 3.12: Sites formed in a LIFE experiment after varying exposure times, using a 0.03 % Fe-doped $LiNbO_3$ crystal and a focussed beam.

from a dot. These appear to have the same symmetry as previously observed. The lines of dots in Figure 3.13 which do not follow the 120° symmetry are believed to be related to scratches resulting from the polishing process.

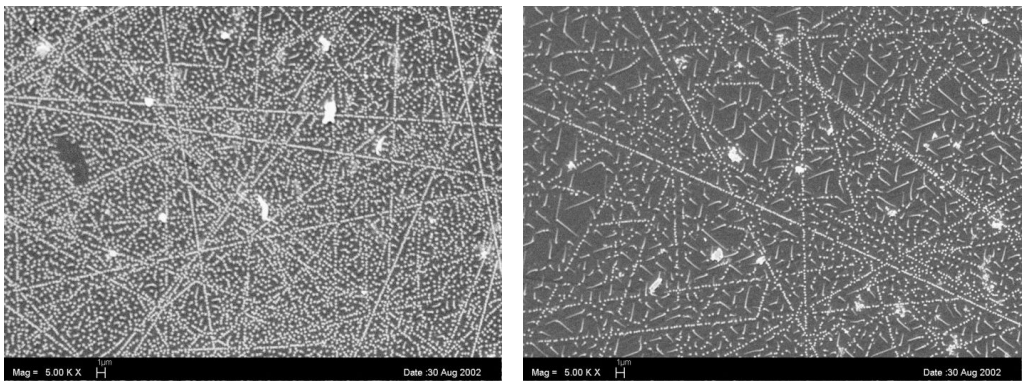

(a) Centre of site. (b) Edge of site.

Figure 3.13: A LIFE site formed after 5 minutes exposure to light and etchant.

Figure 3.14 shows areas of a crystal that was etched and illuminated for 20 min. The density of spots in the centre is higher than for the 5 minute sample and longer lines are observed at the edge of the site.

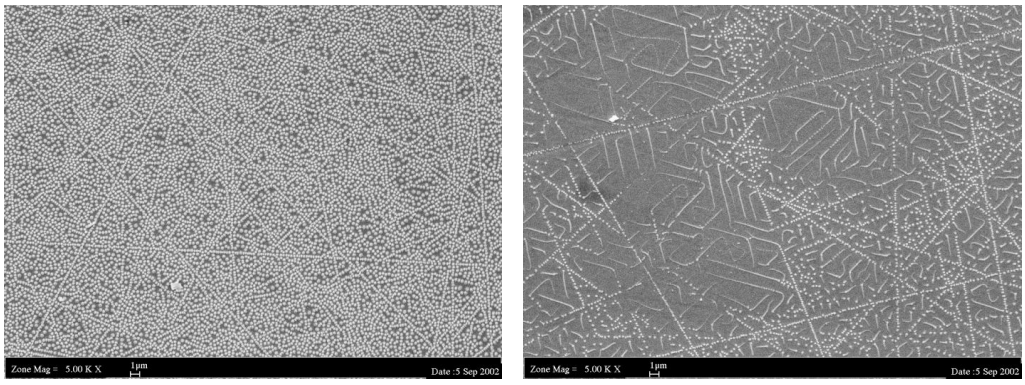

(a) Centre of site. (b) Edge of site.

Figure 3.14: A LIFE site after 20 minutes exposure to light and etchant.

After 40 minutes, the LIFE site appears very different, particularly at the edges. (Figure 3.15). Here lines extend all the way across the image, and the 120° symmetry is immediately apparent. Figure 3.15(c) shows an SEM image taken at lower magnification, which illustrates the increase in density of the lines towards the centre of the site (from left to right in the image). A higher magnification view, Figure 3.15(d), shows the denser packing of lines. Here lines can be seen to extend across the field of view, as before, but short lines have also formed between the

longer lines. The shorter ones are more likely to change direction to make maximum use of the available space, and so have small curved sections while the rest of the line maintains trigonal symmetry.

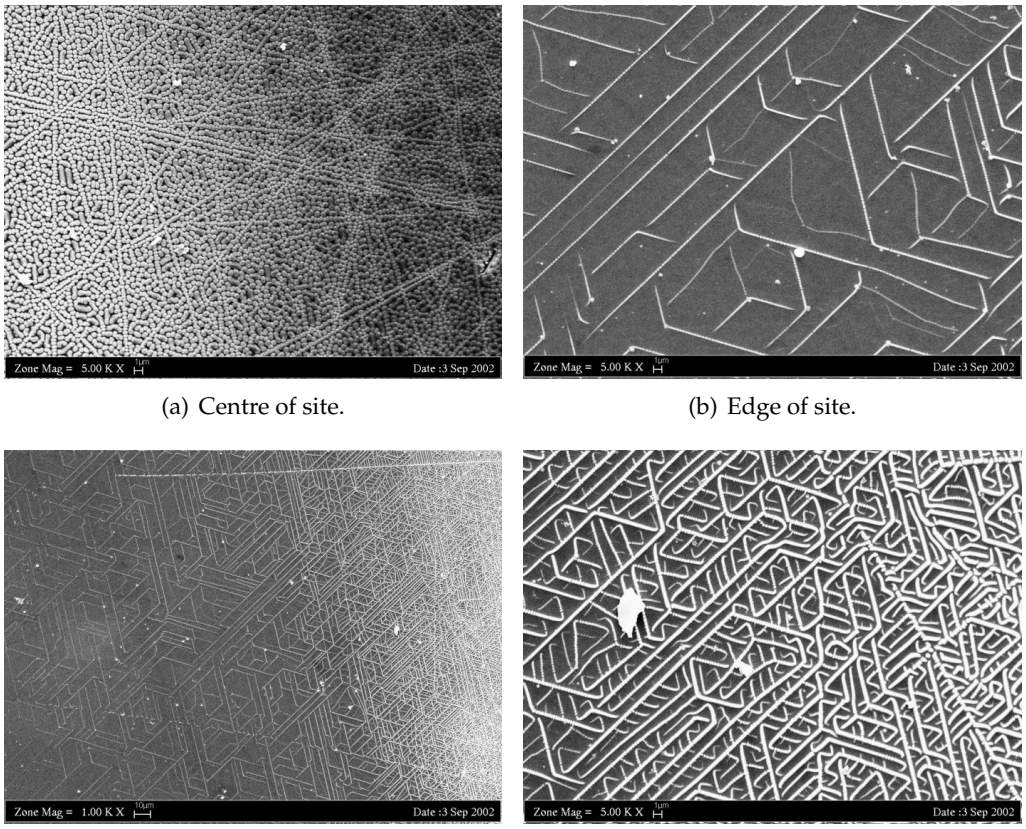

(a) Centre of site. (b) Edge of site.

(c) Lower magnification view. (d) Higher magnification view.

Figure 3.15: A LIFE site after 40 minutes exposure to light and etchant.

The duration of exposure also influences the dimensions on the LIFE site. As previously mentioned, the sites grow outwards from their centre, so after only a few minutes the site is small, ≈ 0.4 mm, but this increases to over 2 mm after etching for 40 min and using a defocussed beam. Figure 3.16 shows the plot of site diameter versus duration of etching, measured from the SEM image of each site. The graph suggests that for a particular beam spot size, a maximum site size will be reached given sufficient exposure to light and acid.

The size of the features formed is dependent on the distance from the centre of the site. Figure 3.17 shows a graph of the widths of the lines formed on 0.1 % Fe-doped samples, after three different etching times (20, 40 and 80 min) against the distance from the centre of the site. At the centre no lines are formed, only the densely packed

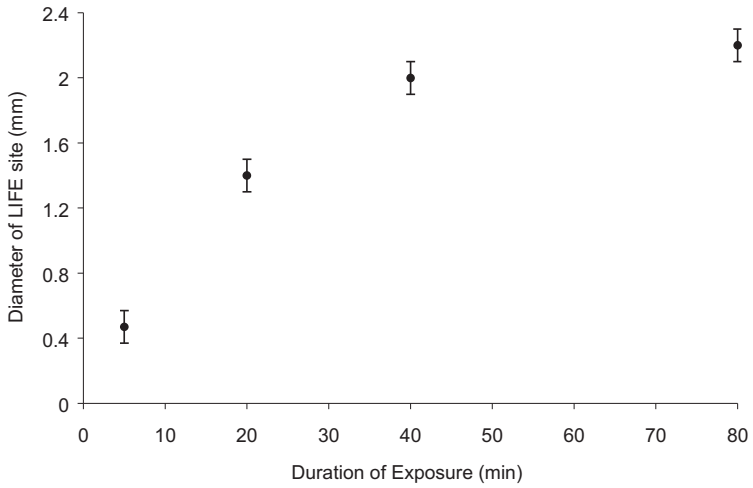

Figure 3.16: A graph showing the variation of diameter of LIFE sites with duration of experiment, using a defocussed beam ($\omega \approx 120$ μm).

'dots'. Away from the centre broad lines are observed, which become progressively narrower as the distance from the centre increases.

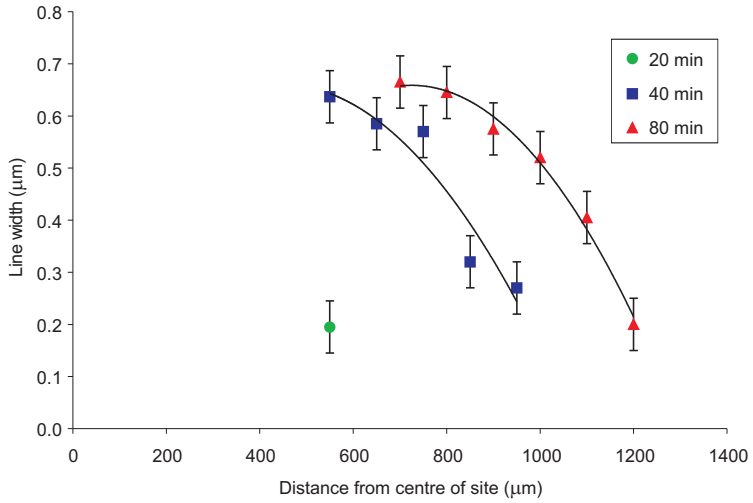

Figure 3.17: A graph showing the variation of the widths of lines formed in a LIFE site with distance from the centre of the site, for three etching times.

Although increased etching times produced larger sites, the relationship between line width and distance from the centre remains approximately constant. A polynomial best-fit curve to the data for the 40 and 80 min samples indicates the apparent maximum width of the lines. There was only one area on the 20 min sample with lines of measurable widths, so only a single data point could be obtained.

The results discussed thus far were obtained using the *simultaneous* exposure of the sample to acid and laser light. However, we also observed that if a sample was

left in acid, with the illuminating laser beam turned off, the structures remained. Additionally, the height of the structures (compared to the surrounding area) continued to increase, indicating that once formed the features can continue to grow without the presence of light. However, when a crystal is illuminated then subsequently etched (i.e. not at the same time), no etch resistance is observed.

The etch-resistant nature of the features therefore seems to require initial exposure to light to start, but once formed the structures remain etch-resistant. Figure 3.18 shows SEM images of a sample that was initially etched, in the presence of light, for 1 hour, after which it was etched for an additional 48 hours, without light. Fig. 3.18(a) gives an overview of part of the site, and Fig. 3.18(b) is a magnified view. Fig. 3.18(c) is a tilted view, which gives a better impression of the height of the features. The height is larger than most LIFE sites, due to the long etching time of this sample.

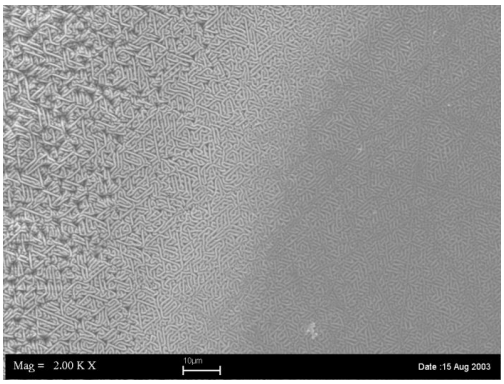

(a) Overview of site.

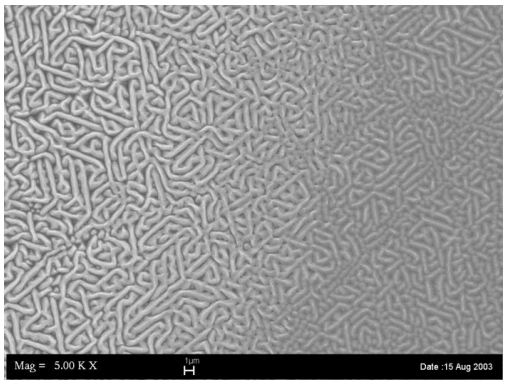

(b) Edge of site.

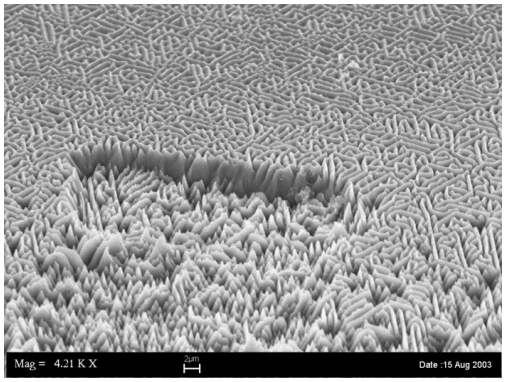

(c) High magnification tilted view.

Figure 3.18: A LIFE site after 48 hours additional etching.

3.3.3 Iron dopant concentration

The concentration of the iron dopant also influences the shape and extent of the patterns that are formed. Dopant concentrations between 0.03 to 0.2 % give nearly identical results to the SEM images shown already, however, a Fe concentration of 0.01 % produces a very different looking site as illustrated by Figure 3.19. This image represents the entire site after 60 mins of etching; when compared to similar pictures taken on other samples it is clear that the structures are much wider (approximately 2.5 μm) than those obtained using higher dopant concentrations (approximately 0.5 μm wide). There is also far less variation in both line density and width over the whole of the site and the lines are less constrained to travelling along directions at 120° to each other.

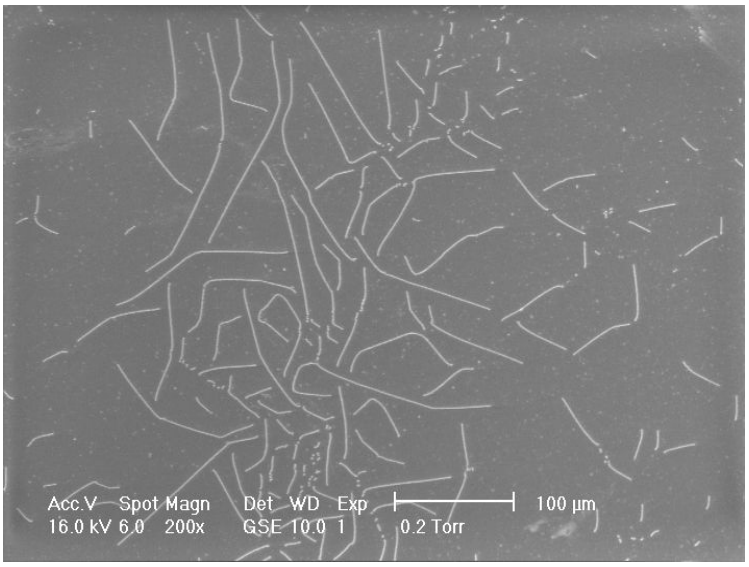

Figure 3.19: LIFE site on a 0.01% Fe-doped $LiNbO_3$ crystal; the results are significantly different to those observed with a higher dopant concentration.

3.3.4 Ion milled sample

Some of the previously shown SEM pictures have a few lines that run at unusual angles that are not at 120° to each other, as most of the other lines are. The likely cause of this was thought to be surface or subsurface damage that occurs as a result of the polishing process. Surface damage can include fractures, scratches, microcracks and residual stress. Subsurface damage consists of three layers: the polished layer at the surface, followed by a defect layer below and then a deformed layer (Shen et al., 2005).

The extent of subsurface damage has been observed to be approximately 3 to 4 times the surface microroughness (as determined by peak-to-valley measurements) for a variety of materials, and for lithium niobate can extend for up to 15 μm into the crystal (Randi et al., 2005).

Surface and subsurface damage therefore may affect the production of LIFE structures. To investigate this possibility, a 0.1 % Fe:$LiNbO_3$ crystal was ion-beam milled to remove the top few tens of microns of the surface and then a LIFE experiment was carried out on the sample. Figure 3.20 shows a selection of SEM images taken of this sample after etching. Figure 3.20(a) shows the centre of the site, which unusually still has large areas of ordered lines, instead of the densely-packed dots which are commonly observed at the centre. Figures 3.20(c)and 3.20(d) show an area with a surprising number of parallel lines along a single direction (with the spaces between filled in by short curving lines).

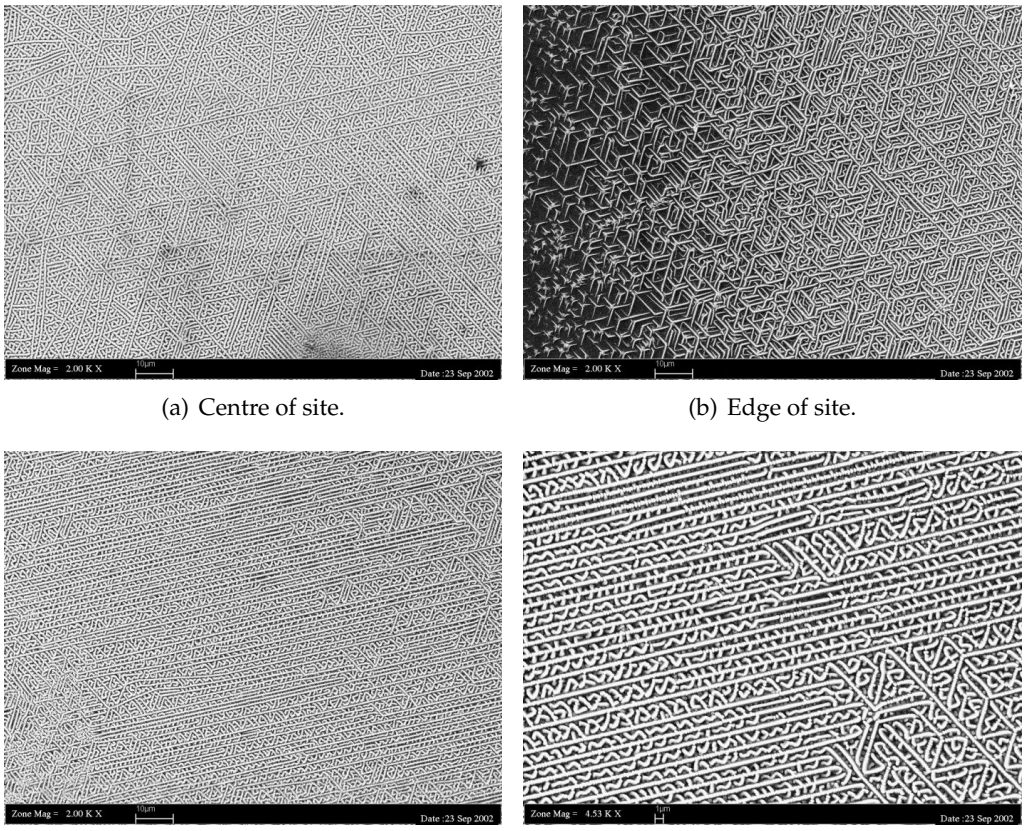

(a) Centre of site. (b) Edge of site.

(c) Large area of parallel lines. (d) Higher magnification view.

Figure 3.20: SEM images of an ion milled sample.

Even after ion beam milling the lithium niobate surface, characteristic LIFE structures are still formed, so proving they are not purely a result of surface or

subsurface defects. However the SEM images show no evidence of the broken lines which form at unusual angles on the untreated samples, indicating that these are a result of polishing damage. These unusual lines are typically observed on samples that have had a short etch time, but are not present on samples that have had a longer etch time. This suggests that the etching process, given enough time, removes the damaged surface and subsurface layers.

3.3.5 Polarisation of incident light

Experiments described thus far were carried out using linearly-polarised light emitted by the laser. To check that the polarisation of light was not a factor in determining the structures produced, a LIFE experiment was carried out using circularly polarised light (from a quarter wave plate). No differences between this sample and one made using linearly polarised light were observed.

3.3.6 Phase mask

We wished to investigate whether using a structured laser beam would have any effect on the etching process. Normally a uniform Gaussian beam was used, resulting in a circular LIFE site, with self-organised lines tending to form along directions at 120° to each other, with approximately equal probability along each of the three directions, except at the very edge of certain sites. If a structured beam was used instead, it was thought that the frustration of etching may take place in a different way, such as creating non-circular sites and potentially favouring line formation along a single direction. This would be very desirable, as it could increase the level of control over the process and so allow for the production of user-defined patterns.

A phase mask is a surface relief grating, usually etched in fused silica, which acts as a diffraction grating. A single beam incident on the grating is diffracted into several diverging orders, which produce an interference pattern with a period one half the period of the phase mask. By placing a phase mask in the path of the laser beam it is hence possible to structure the illumination incident on the crystal surface.

The angles of diffraction from a phase mask are given by:

$$\sin \theta_m = \frac{m\lambda}{\Lambda} \tag{3.4}$$

where λ is the wavelength used (532 nm), Λ is the period of the grating and m is the order of the diffracted light. When using a grating of period 4.5 μm, the angle of diffraction of the first order beam is 6.8°. A photo showing the operation of a photo-resist phase mask prepared on a test sample is shown in Figure 3.21.

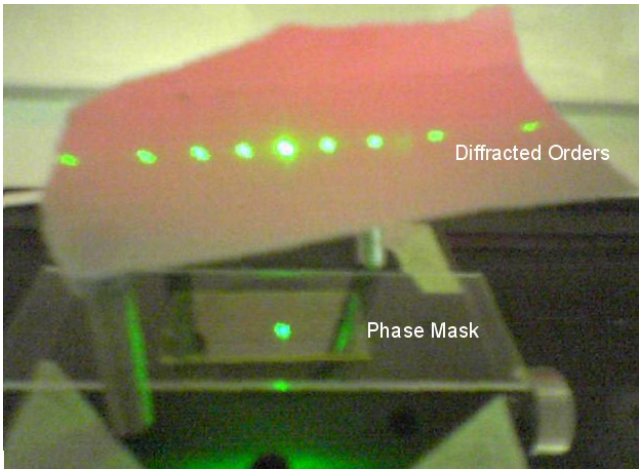

Figure 3.21: Diffraction from a phase mask.

The use of a separate mask in this situation was undesirable, due to the damage to the mask that would occur in the event of an acid spill and a lack of space in the LIFE cell for the lithium niobate crystal and a phase mask. The alternative was to pattern a phase mask directly on the reverse side (+z face) of the lithium niobate crystal that was being etched, using photo-resist. This had the additional benefit of not suffering from any relative movement between the mask and the crystal, which would affect the interference pattern produced on the −z face. The process for this is the same as used for making periodically-poled lithium niobate (PPLN), which was illustrated in Figure 2.10, but missing out the final electric-field poling step. The resulting mask was not as perfect as a silica mask would have been, as the photo-resist was not totally transparent to the green laser light and was relatively thick (~1 μm), which resulted in some amplitude mask character, but it was judged that the benefits of using a photo-resist mask outweighed the disadvantages.

An SEM image of a LIFE site produced using light from a phase mask is shown in Figure 3.22 (0.03 % Fe:$LiNbO_3$ exposed for 60 min). Compared to a normal site it is more rectangular and appears to consist of three overlapping circles. There is no evidence of total frustration of etching; this is due to some of the power of the beam being diverted into other orders, so the intensity on the surface of the crystal is insufficient. Partial frustration appears to have taken place as usual. However, the presence of an interference pattern has not caused any apparent change in the

etching behaviour. This is consistent with previous results, where the sites produced are much larger than the spot size of the beam used to create them, so any small periodic modulation of intensity at the centre of the site created by the phase mask are probably insignificant.

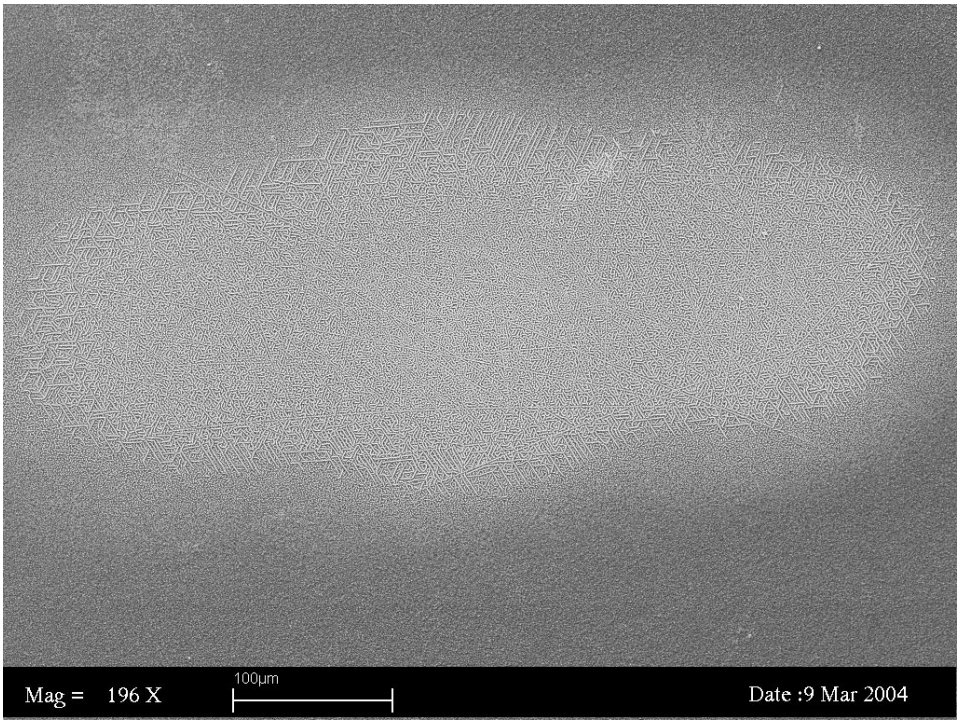

Figure 3.22: LIFE site produced using illumination from a phase mask.

3.4 Analysis of Structures Produced

In this section, further analysis of the results is described. A modified Atomic Force Microscope (AFM, see Appendix A for details) was used to study physical properties of the surface features that were produced and more detailed investigation into the patterns which were formed were conducted by taking the spatial Fourier transforms of SEM images. A computer simulation of the formation of these patterns was also developed.

3.4.1 Electric-field Atomic Force Microscopy

To determine whether the LIFE features were, or remained, charged following exposure to hydrofluoric acid, the samples were examined with an atomic force

microscope (AFM) which had been modified to detect surface charge as well as topography. This technique has been successfully applied to ferroelectrics (Luthi et al., 1993) and lithium niobate in particular; Tsunekawa et al. (1999) have reported the use of electrostatic force microscopy (EFM) to observe microdomains. They found that the $-z$ crystal face has a positive charge and the $+z$ microdomains on it were negatively charged in air. Soergel et al. (1998) have also used EFM to study charge distributions on $Bi_{12}SiO_{20}$ (BSO) crystal surfaces.

The experiments discussed here were carried out using equipment at the University of Bonn, Germany, with the assistance of Prof. Dr. Karsten Buse, Dr. Elisabeth Soergel and Nils Benter. Electrostatic force microscopy measures the force between surface charges and a periodic charge induced on the conductive (Al-coated) AFM tip, by a voltage $V_0 \cos \omega_2 t$. A lock-in amplifier was used to measure the electrostatic force; the phase signal from the lock-in also allowed discrimination between areas of positive and negative charge.

To detect charges the AFM has to be operated in non-contact mode. The amplitude of the voltage used was 10 V, with a frequency of 2 kHz. To reduce the effect of vibrations, the AFM was mounted on a floating table, and was covered with a shield. Nitrogen gas was used to purge the air surrounding the tip and sample, to reduce the water content which was known to affect charge detection.

The best results were obtained when an initial AFM scan was performed in contact mode (non-charge detecting), to remove any surplus surface charges generated by the pyroelectric and photorefractive effects. The pyroelectric effect causes charges to accumulate at the crystal faces, which compensate for the change in spontaneous polarisation that occurs with change in temperature. This results in the $+z$ face to become more positively charged on cooling. After the initial contact mode scan, the measurement was repeated in non-contact mode to detect the static charge distribution.

Two periodically poled lithium niobate samples were used to test the operation of the instrument. The first (Fig. 3.23) had been etched before examination by AFM, so had topographic features, while the second (Fig. 3.24) was unetched so had no topography. In both sets of results charge was detected and in the case of Fig. 3.23 the charge image matched that of the topography. The resolution of the charge image from the unetched PPLN does not appear to be as good as that from the etched sample, but the scan is of a smaller size (20 μm compared to 40 μm), and it does show that charge can be detected independent of topography.

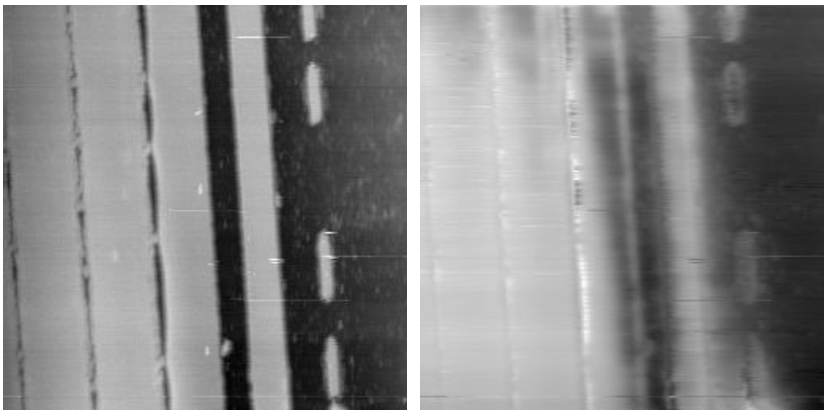

(a) Topography (b) Charge

Figure 3.23: Topographic and charge images of an etched PPLN sample recorded by AFM. Area shown is 40 μm by 40 μm.

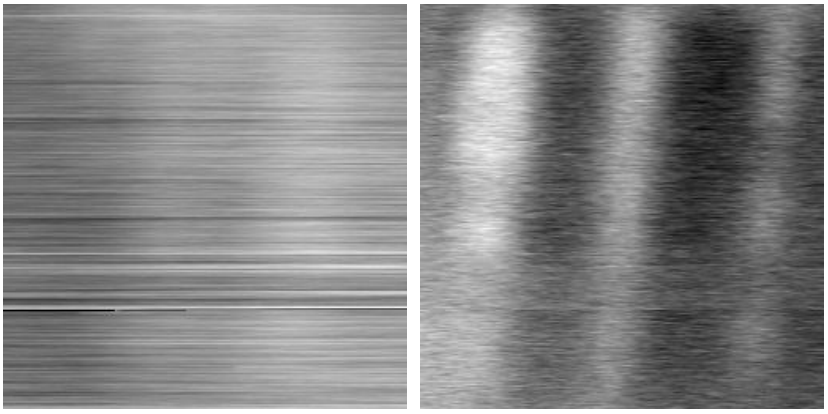

(a) Topography (b) Charge

Figure 3.24: Topographic and charge images of an unetched PPLN sample recorded by AFM. Area shown is 20 μm by 20 μm.

After the operation of the AFM had been confirmed in topographic and charge-detecting modes, a 0.1 % Fe:$LiNbO_3$ LIFE sample was examined. A good quality topography image was obtained, as shown in Figure 3.25. However, a charge image could not be obtained, due to the unusually high number of surface charges which caused the AFM tip to be strongly attracted to the surface. The attraction was such that the AFM could not even operate in non-contact mode, even after several scans in contact-mode which should have removed the surface charges. The excess charge was thought to be a consequence of the relatively high iron-dopant concentration.

A sample with 0.01 % iron dopant concentration gave better results, as shown in Figure 3.26. The topographic image shows a single etch-frustrated feature, which

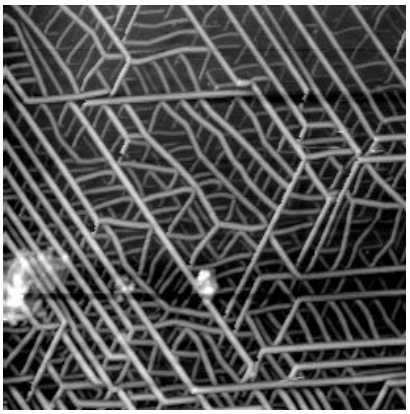

Figure 3.25: AFM topographic image of a 0.1% Fe:$LiNbO_3$ LIFE sample. Area shown is 20 μm by 20 μm.

is higher than the surrounding areas. The stucture is considerably larger than those shown in Fig. 3.25, which is to be expected due to the lower iron dopant concentration (as discussed in Section 3.3.3). The charge image strongly resembles an inverted topography image; the feature is darker than the surrounding areas, which shows it is more postively charged than the surroundings.

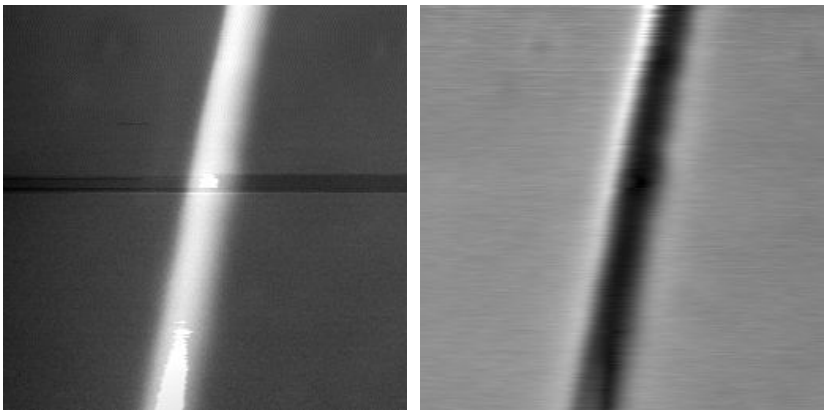

(a) Topography (b) Charge

Figure 3.26: AFM topography and charge images of a feature on a 0.01 % Fe:$LiNbO_3$ LIFE sample. Area shown is 15 μm by 15 μm.

A small area of the crystal around the LIFE site was then repoled to become a $+z$ domain. The area of domain inversion is visible in the polarised optical microscope picture shown in Figure 3.27, and includes the LIFE structures, visible at the top of the image. The crystal surface appears quite rough as it had been etched during the LIFE process.

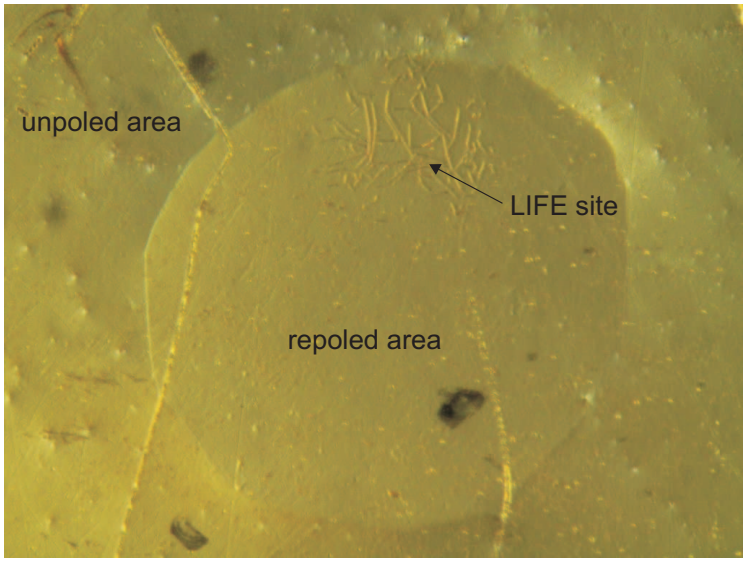

Figure 3.27: Polarised optical microscope image showing the repoled LIFE site and surrounding area.

Following repoling, further AFM scans were taken of the LIFE structures. The results in Figure 3.28 show that while the topography is unchanged, the charge of the feature is almost indistinguishable from the surrounding ($+z$) area.

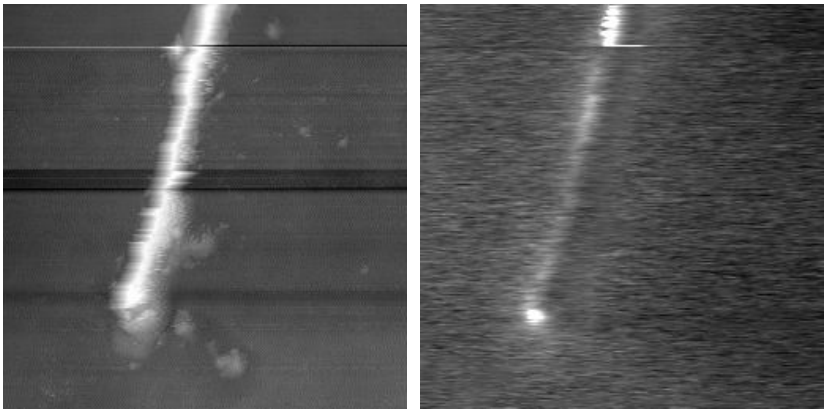

(a) Topography (b) Charge

Figure 3.28: AFM topography and charge image of a *repoled* LIFE site. Area shown is 20 μm by 20 μm.

The charge image also reveals that the surroundings are darker than those in Fig. 3.26, which confirms that domain inversion has taken place and that both the feature and surrounding crystal surface are positively charged.

The results are consistent with the etching behaviour that was observed. As discussed previously, the $-z$ face of lithium niobate is susceptible to etching by HF

acid, while the $+z$ face is known to resist etching. The opposite sign of the charge of the etch frustrated feature compared to the normally etched $-z$ surroundings is hence likely to be the cause of the etch-frustration. Further evidence of this was obtained by poling the entire region, after which the charge of the new $+z$ domain surrounding area changed sign to become the same as that of the etch frustrated feature. The actual polarity of the unmodified $-z$ surface was found to be negative, while the $+z$ surface was positive. This is contrary to the results of Tsunekawa et al. (1999), who reported that $-z$ planes have a positive charge. However, lithium niobate surfaces are known to attract compensating charges (Weis and Gaylord, 1985) due to the dipoles which exist in the bulk material, so it is possible that Tsunekawa et al. were detecting these, while in the present experiments surface charges were removed by the contact-mode scan that was carried out before the non-contact, charge-detecting scan. However, it is the difference in charge between the etch-resistant features and the surrounding $-z$ surface that is of particular importance.

It was not possible to obtain charge images for 0.1% iron dopant concentration samples, however future experiments could be conducted using a different gas surrounding the sample (instead of N_2), which may help to reduce the surface charges. Mirza et al. (1978) studied light emission from the surface of lithium niobate as a crystal was heated and cooled, and found that the luminescence was primarily a surface controlled effect. Indeed, while strong emission was observed in a vacuum, the presence of CO_2 or O_2 almost totally quenched the light. The authors believe that light is seen on heating as the pyroelectric effect creates a large electric field and subsequently electrical breakdown may occur, during which some energy is liberated as luminescence.

3.4.2 Fourier transforms of SEM images

We have used a Fourier transform (FT) technique to analyse the SEM pictures of LIFE sites. This mathematical function separates a waveform into sinusoidal components of different frequency from the original waveform. The result of this is to effectively convert a function from a time domain into a frequency domain. The transform can also convert a spatial domain to spatial-frequency domain. The Fourier transform of a time-varying function $f(t)$ to a frequency-varying function $f(v)$ is:

$$f(v) = F[f(t)] = \int_{-\infty}^{\infty} f(t)e^{-2\pi ivt}dt \tag{3.5}$$

When using a computer to calculate Fourier transforms, the discrete version of the equation (Discrete Fourier Transform, DFT) is required. This is:

$$F[f(t)] = \sum_{k=0}^{N-1} f_k e^{-\frac{2\pi i n k}{N}} \tag{3.6}$$

The actual algorithm used is the 'Fast Fourier Transform' or FFT, which reduces the number of calculations required from $2N^2$ to $2N \log_2 N$, where N is the number of points.

To calculate the Fourier transform of an image, a two-dimensional Fourier transform has to be carried out. This can be done by taking the FT of each column of an image, then taking the FT of the result. The Fourier Transform of an image will hence have the same number of pixels as the original image, and so the number of frequencies present will depend on the original image. The software used for this analysis, Matlab version 6, by The Mathworks Inc, comes with a two-dimensional Fast Fourier Transform function ('fft2') built-in.

An example of the usefulness of Fourier transforms in image analysis is shown in Figure 3.29. A series of square lines is decomposed by the Fourier transform into the spatial frequencies that are required to make up the picture. As the lines correspond to a square wave or grating, only the zero and odd terms of the frequency components are present, as would be expected from Fourier theory.

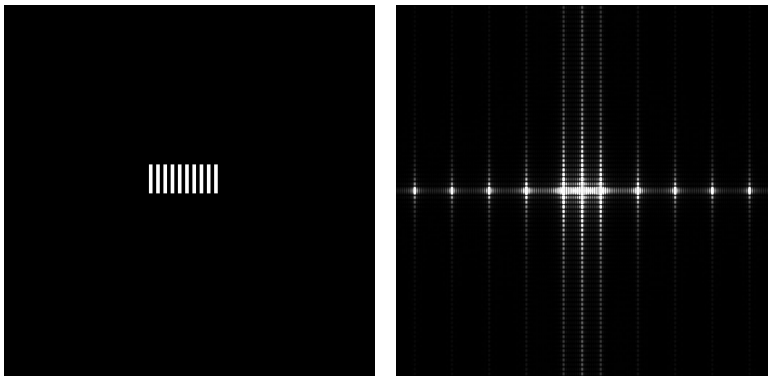

(a) Original image (b) Fourier transform

Figure 3.29: The Fourier transform of a series of lines, with square-wave profile.

To produce useful Fourier transforms of the SEM pictures the following steps need to be taken:

1. The SEM image needs to be cropped to a square, to simplify the resulting Fourier transform (otherwise the axis scales would not be the same, leading to a 'squashed' transform. Also the text (scale, magnification etc) is removed.

2. The scale of the transformed image is calculated from the length and value of the scale bar in the SEM image. The size of the pixel (microns) in the SEM image, Δx , is related to the size of the pixel (inverse microns) in the Fourier transform image, Δu, by the relation (Gonzalez and Wintz, 1987):

$$\Delta u = \frac{1}{N\Delta x} \tag{3.7}$$

   where N is the number of samples along the x axis (ie number of pixels width of the image).

3. The Fourier transform image is produced by taking the absolute values of the resulting transform, and then taking the logarithm of the absolute values. This is a common procedure in Fourier analysis, which although without physical basis, improves the contrast of the FT image which is initially poor due to the large value of the DC-component compared to the harmonics.

4. The axes of the FT image are also rearranged so that the zero-order (DC) term is at the centre of the resulting image.

An example of a typical Fourier transform of a LIFE SEM image is given in Figure 3.30. The star-shaped Fourier transform clearly shows the strong preference of the lines to form along directions at 120° to each other. The length of each lobe of the star pattern shows that there is a range of frequencies present in those particular directions.

Figure 3.31 shows another SEM and Fourier transform image pair. This SEM image was taken closer to the centre of the site, and shows a denser pattern of lines. The widths of the lobes of the star pattern in the Fourier transform are wider than those in Figure 3.30, indicating that while the patterns are still forming along the preferred directions, there is some variation in the exact direction they take. As the density is higher, the lines are trying to fill the available space more efficiently; this requires slight deviations from the preferred direction, and so results in broadening of the Fourier transform lobes.

The Fourier transform of an SEM image taken near the centre of the site on the 40 minute sample (Figure 3.32) shows quite a different pattern however, as the directional dependence has been lost. Due to a greater density of structures, no

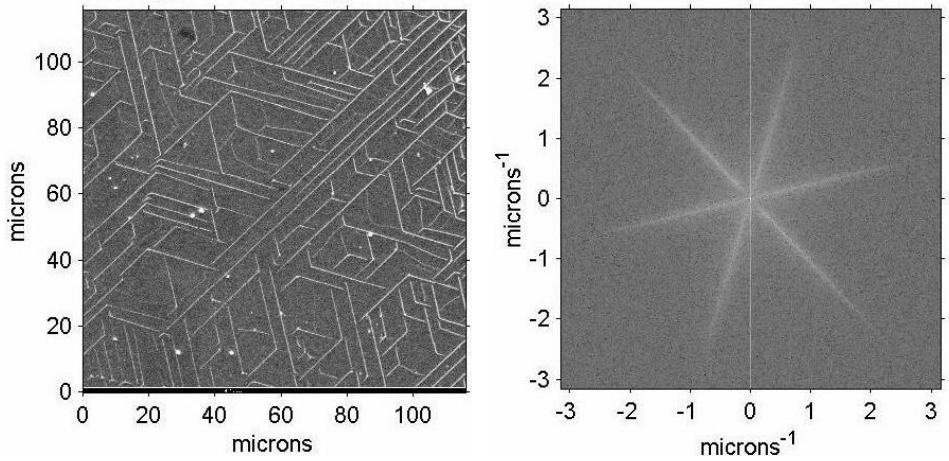

(a) Cropped area of original image (b) Fourier transform

Figure 3.30: Cropped SEM image taken at the edge of the 40 minute sample and the corresponding Fourier transform.

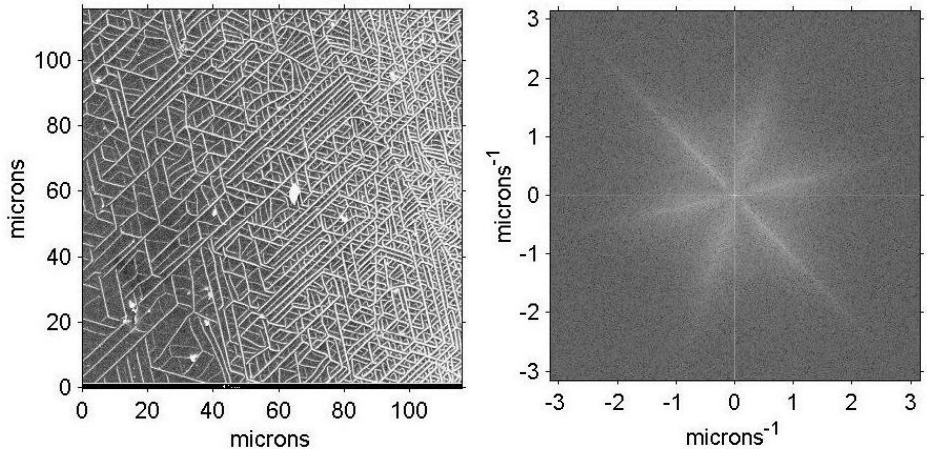

(a) Cropped area of original image (b) Fourier transform

Figure 3.31: Cropped SEM image taken near the edge of the 40 minute sample and the corresponding Fourier transform.

long lines are able to form, and so the Fourier transform only shows a 'halo'. There is still a range of periods that have been formed, but these may be in any direction.

Figure 3.33 shows the SEM image taken at the centre of the site, where almost total etch frustration has occurred. The only structures that are seen are small dots, and long scratch lines. The Fourier transform gives very little information, as there are no periodic structures in the image.

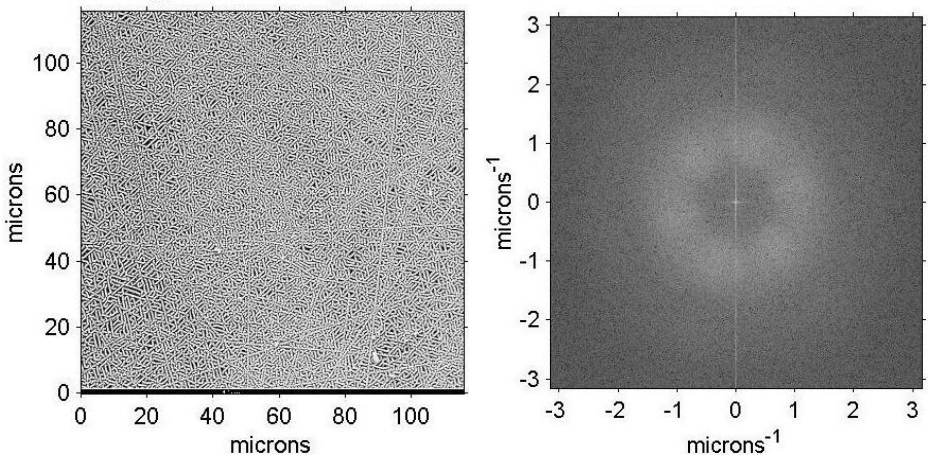

(a) Cropped area of original image (b) Fourier transform

Figure 3.32: Cropped SEM image taken near the centre of the 40 minute sample and the corresponding Fourier transform.

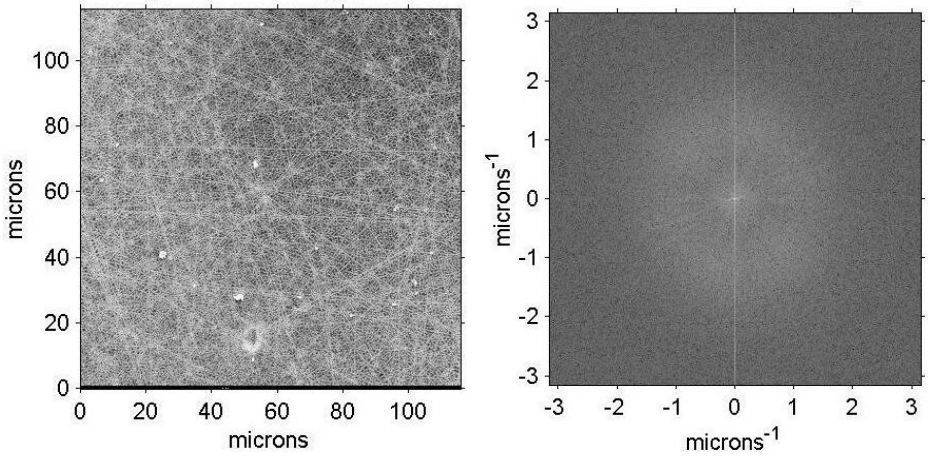

(a) Cropped area of original image (b) Fourier transform

Figure 3.33: Cropped SEM image taken at the centre of the 40 minute sample and corresponding Fourier transform.

In some Fourier transforms of the images, a second series of peaks can be seen at higher spatial frequencies than the first. An example of this is illustrated in Figure 3.34.

The best Fourier transform results were obtained using SEM images of 2000× magnification, as these had features that were clearly visible yet also presented a large enough area to give a representative result. At this magnification, each pixel of the SEM image represents a distance of 0.137 μm, which corresponds to 0.010 μm^{-1} for the Fourier transform image pixels. Thus some of the very high

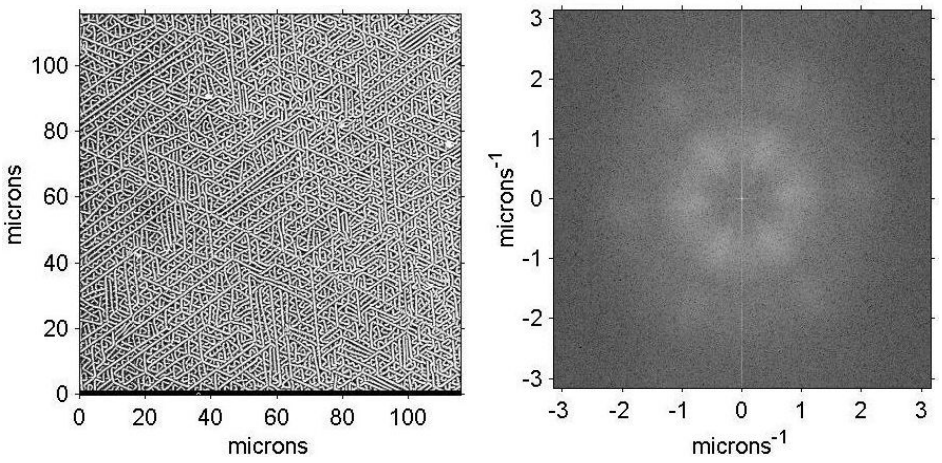

(a) Cropped area of original image (b) Fourier transform

Figure 3.34: Cropped SEM image of the 80 minute sample and corresponding Fourier transform.

frequency components will be a consequence of the pixelised nature of the original image, but other high frequency components will arise due to the width of the individual lines. The very low frequency components are a consequence of the rectangular image as a whole.

Fourier transforms were carried out on each 2000× magnification SEM image from the survey of 20, 40 and 80 minutes LIFE sites and a method was developed to allow automated analysis of these transforms. This was achieved by recording the intensity value of each pixel along a line in the FT image, rotating the line by 1°, and then adding the value of the pixels along the new line to those from the old line. This process was then repeated over 360°, which resulted in a one-dimensional line that represented all of the data from the 2D Fourier transform. Figure 3.35 shows a typical result. A Gaussian curve has been fitted to the broad peak in the data, and the centre of this curve then corresponds to the most common spatial frequency in the SEM picture. While this clearly is not the only frequency that appears in the images, it does give a good indication of the average and so allows for a quick comparison between the transforms of several SEM images.

This process was applied to each Fourier transform of the 2000× magnification SEM images, and so a value for the average period present in each image was obtained. The results are shown in Figure 3.36, where the average period is plotted against distance from the centre of the site.

The best results were obtained for Fourier transforms of the 'halo' type instead of the 'star' type, so the results in Figure 3.36 do not represent the full radius of the site.

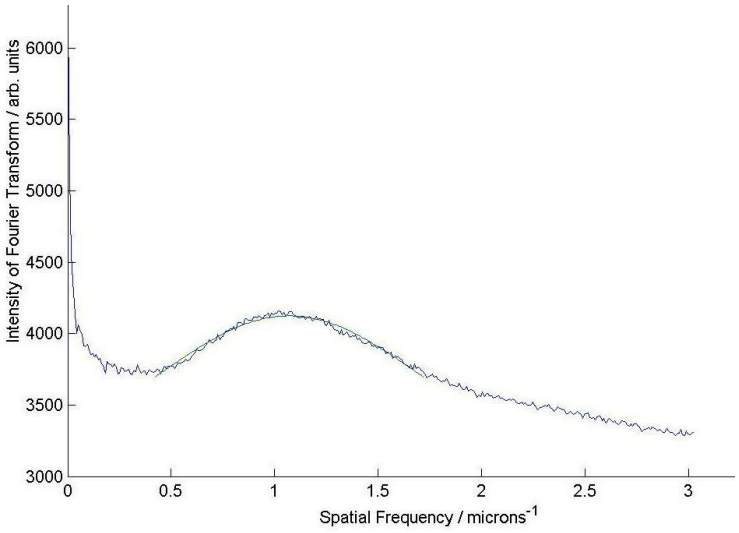

Figure 3.35: 1D Sum of 2D Fourier Transform.

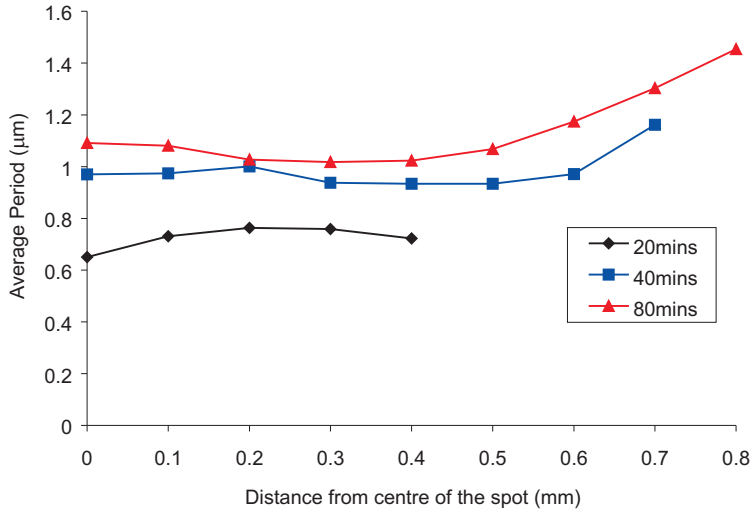

Figure 3.36: The variation of typical spatial period versus distance from the centre of site, for 3 different exposure times.

The results show that the period increases with the length of time the sample has been etched for, but the difference between the 80 and 40 min samples is less than that between the 40 and 20 min samples. Additionally, the periods are generally greater at the edge of the site than at the centre, as would be expected from visual inspection of the SEM images, which show less densely packed structures occur away from the centre of the site.

3.4.3 Computer model of LIFE results

A simple model has been developed to try and replicate the results of the LIFE experiments and the Fourier analysis of the SEM images. It is based around the gradual growth of lines from starting dots, and follows a series of 'rules' that have been derived from examining the SEM images.

1. Lines grow from dots.
2. Lines can propagate along one of three directions at 120° to each other.
3. Lines cannot touch or cross over each other.
4. Lines may change direction to avoid another line.

The execution of the program is summarised in Figure 3.37. If a line is detected as being too close to another line it is given the chance to change direction, as shown in the flow diagram. However, if it tries to change direction more than twice in a single cycle, then that line is stopped. When all the lines are marked as stopped the program is complete. This represents a sufficiently long period of etching time so that the lines are completely formed.

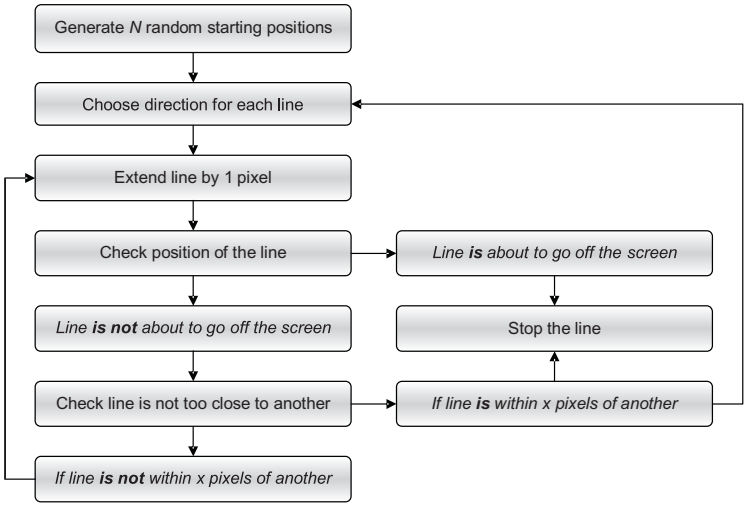

Figure 3.37: Algorithm for LIFE computer model.

The main variable is N, the number of starting dots. The number of dots in a fixed area is equivalent to the density, which in turn is believed to be related to the intensity of light at a particular point on the crystal surface and distance from the

centre of the site. So by changing the value of N, the program can simulate different areas of site; namely the densely packed centre and the edge regions with lower density and longer features, or lines.

The LIFE program also produced a Fourier transform of the simulation results to allow comparison with the experimental results. The results from a series of simulations with varying values of N, the number of starting points, are shown in Figure 3.38. For a simple model, the results compare well with those obtained experimentally, and show all the characteristic features. The Fourier transforms also bear a close resemblance to those of the SEM images. As N is increased the density of the structures becomes higher, and the length of the lines decrease, as there is less space available. For $N = 5000$, there are no large-scale patterns formed and the results appears to be very similar to SEM images taken at the centre of the site.

The Fourier transforms of the images with low N values show the same star-shaped pattern as found experimentally, but with some extra detail. This pattern changes as N is increased; the width of the lobes increases and the length (frequency) of each lobe decreases. At $N = 5000$ the Fourier transform shows only a little direction dependence, again as would be expected from the experimental evidence.

The model initially had a totally random distribution of starting points, but to try and simulate an entire LIFE site this was adapted to feature a Gaussian distribution of starting points. The results of this approach are shown in Figure 3.39.

The success of the model in matching the results obtained by experiment shows that the rules which were defined to create the model must be realistic and somehow arise from the physical properties of the crystal, under exposure to light and etchant. While the assumption that lines will simply stop and change direction once they reach a certain distance from another line is probably an over-simplification it does produce reasonable results. Instead of this 'hard sphere' type repulsion a more accurate model would make the repulsion distance-dependent, and so make the effect more gradual. However the improvement this would make probably does not warrant the extra complication of the model, as the results would only be slightly different. The model does show that the assumption of lines growing from starting dots is reasonable, and that the lines can only grow in one of three directions, although perhaps a little simplistic, again gives good results. Finally, the model also supports the suggestion that more of these growth dots are formed towards the centre of the site where the laser intensity is highest, as the patterns and Fourier transforms from the model are very close to those obtained experimentally.

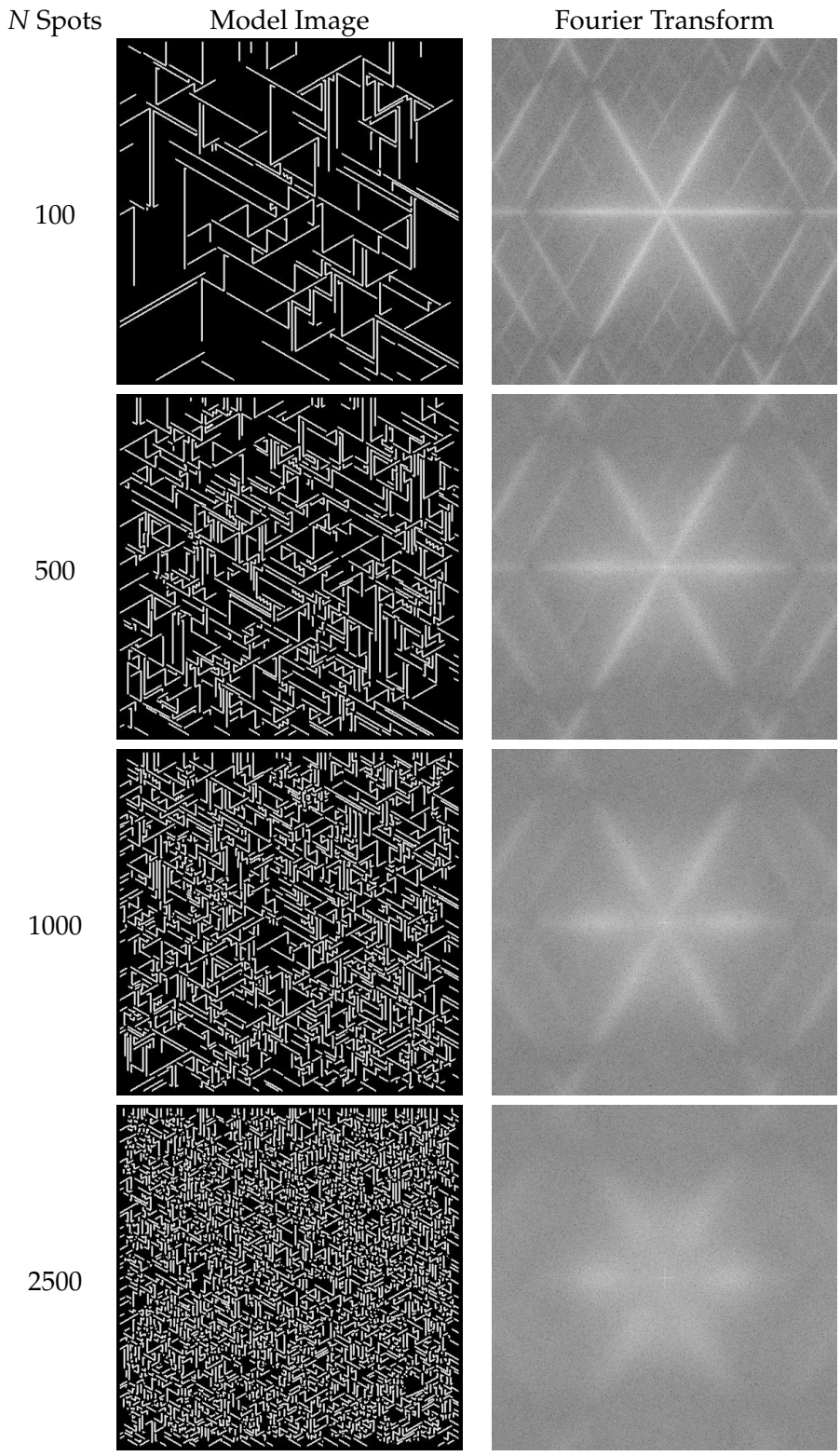

Figure 3.38: Results of the LIFE computer model and corresponding Fourier Transforms

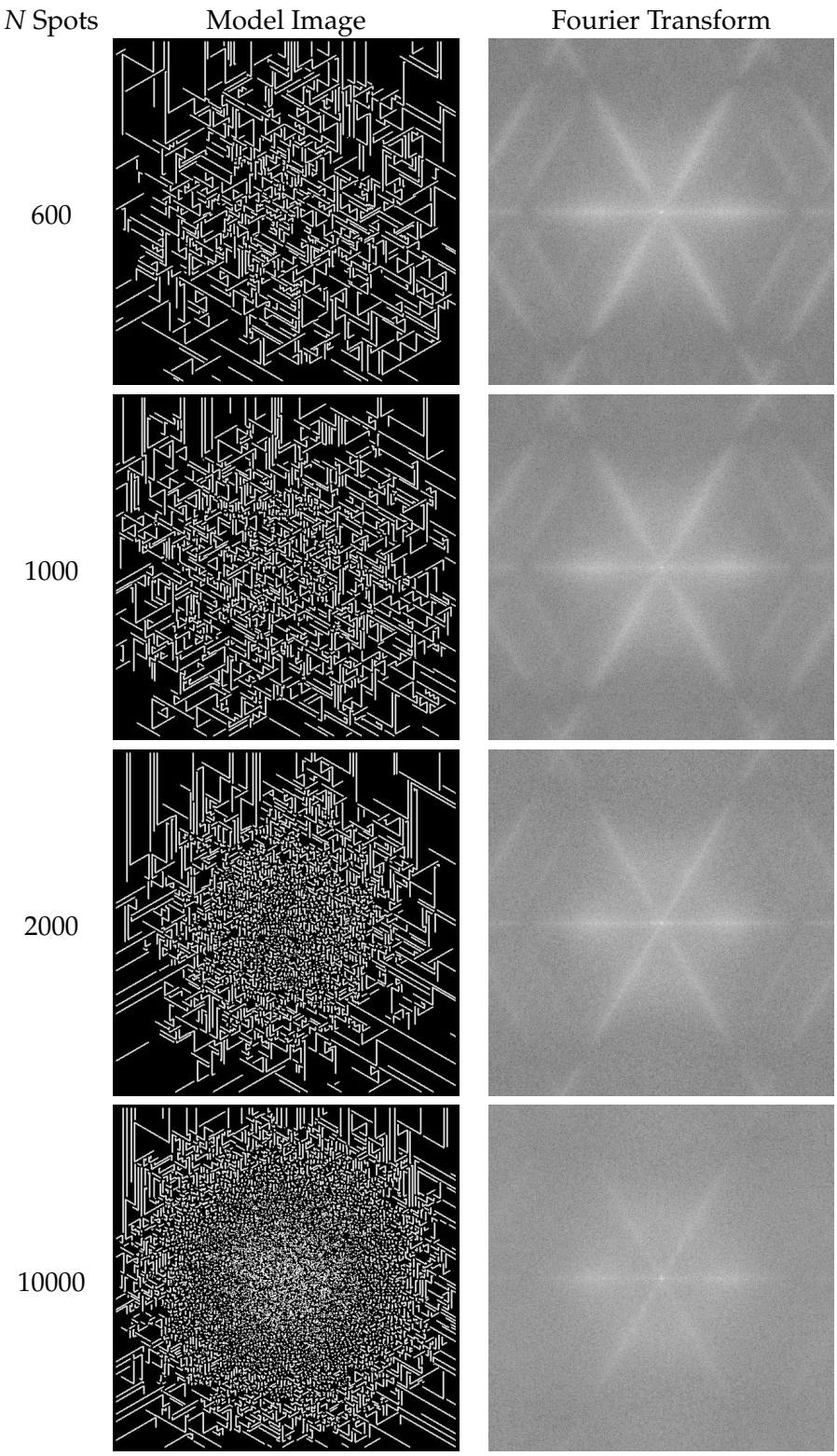

Figure 3.39: Results of the LIFE computer model using a Gaussian distribution of starting points and corresponding Fourier transform images.

Finally, it should be noted that although the model grows the lines by extending the existing lines pixel by pixel, this is not believed to be a literal representation of the processes that are occurring. Instead the lines are thought to grow as the areas around them are removed by the action of the acid while the lines themselves resist etching by acid.

3.5 Discussion

It is thought that the observed patterns are formed initially from localised spots, which are created by the interaction of light with the iron dopant, through the photovoltaic effect. The number of spots that are formed is dependent on the intensity of the light, hence at the centre many spots form and are therefore tightly packed. However, at the edges the laser intensity is lower, due to the Gaussian beam profile, so fewer spots occur. These may then grow as the surrounding areas are etched away, and so form lines. More complicated patterns can then arise to fill the space between the lines. When using a tightly focussed beam, we observe the formation of sites that are smaller in diameter than would be formed using a larger spot size (with the same laser power and the etching time). These smaller sites are more likely to have a central region of total frustration of etching. Larger sites ($>$ 500 μm) generally do not have totally frustrated areas, but instead have very dense packing of partially etch frustrated features.

The existence of etch hillocks formed during chemical etching of the $-z$ face of lithium niobate is well known, and was first reported by Niizeki et al. (1967). These etch resistant centres are revealed during normal etching (i.e. without the presence of light), resulting in etch hillocks on the $-z$ surface and corresponding etch pits on the $+z$ crystal face. The origin of these features is thought to be due to the presence of microdomains, which are very small needle-like domains of opposite polarity to the surrounding bulk area (Ohnishi and Lizuka, 1974). A microdomain on the $-z$ face of the crystal would be a small area of $+z$ character and would therefore resist etching, resulting in a hillock.

Later studies by Holstein (1997) suggest that dislocations can also be responsible for the formation of etch hillocks and pits, with large pits being attributed to microdomains, and smaller pits due to dislocations. The experiments by these authors provide some interesting parallels to our results, but with some significant differences. The presence of microdomains would explain the raised, etch-resistant areas we observe in the LIFE process. This implies that the laser light is creating the

microdomains, and in the case of total frustration, a very large-area microdomain. However, the light needs to be present simultaneously with the acid for frustrated etching to occur; exposure to light, followed by etching does not give rise to any features. Therefore, if indeed domains are formed, then they are unlikely to be permanent. As only one face is exposed in our experiments, it is not known whether corresponding etch pits could be formed, if both sides were etched (although etching of both sides of a LIFE sample after the initial experiment does not produce any topographical features on the $+z$ face). This further suggests that any domain inversion would only be temporary but this may be sufficient to instigate etch frustration. Even a superficial cap of domain inverted material would prevent etching, and so could hence shield material underneath.

Dislocations generally result in small features up to 12 μm, according to Holstein, but it is possible that dislocations could be at least in part responsible for the patterns observed in partially frustrated LIFE experiments. However, as dislocations can be observed by etching alone, while the LIFE features require simultaneous etching and light it would seem likely that dislocations alone cannot be responsible for the structures we observe. The other factor could be that defects prefer to cluster around dislocations (Arsenovici and Townsend, 1972) and so when activated by light could influence the etching to give the patterns that were observed. This possibility could be examined by using EDX (energy dispersive x-ray) mapping.

A possible mechanism for the production of microdomains is that of charge liberation within the crystal following exposure to laser light, caused by the photovoltaic effect. Morozovska et al. (2003) have produced a theory of this. However, the bulk photovoltaic effect itself may be responsible for the observed etch frustration, without the production of microdomains.

Photovoltaic current has been measured by Fradkin and Magomadov (1979) and Festl et al. (1982), when Fe-doped lithium niobate crystals are exposed to visible wavelengths light, as discussed in Section 2.3.9. The current depends on the direction of the incident light and the angle formed between the polarisation vector and the direction of current. For uniform illumination along the z direction, the photovoltaic currents along the major axes are:

$$J_x = \alpha_{22} I \sin 2\beta \tag{3.8}$$

$$J_y = \alpha_{22} I \cos 2\beta \tag{3.9}$$

$$J_z = \alpha_{31} I \tag{3.10}$$

The largest currents were measured along the z direction, which were found to be an order of magnitude greater than those along the x or y directions. Using light with a wavelength of 500 nm and intensity of 2.3 $\times$ 10^{-3} W/cm^2 Fradkin and Magomadov found the peak values of the currents to be J_z = 15.5 $\times$ 10^{-12} A cm^{-2}, while J_y = 3.5 $\times$ 10^{-13} A cm^{-2} and J_x = 1.5 $\times$ 10^{-13} A cm^{-2}.

J_z was found to have no periodic dependence on the angle β when light is incident along the z direction, so J_z is always of positive sign and hence the flow of current is always along the $+z$ direction. The charges generated by excitation of electrons from filled Fe^{2+} traps then propagate along the $+z$ direction, thus $-z$ face becomes more positively charged due to the empty Fe^{3+} traps that remain. This causes the etching process to be frustrated, as the first stage in the etching reaction pathway (surface attack by the acidic proton) is prevented due to electrostatic repulsion from the now positively charged $-z$ crystal face. This is equivalent to the usual etch-resistance of a $+z$ face (see Section 2.4.2).

In the case of partial frustration of etching, the intensity of light incident at that location on the crystal is insufficient to completely prevent etching. However, it is possible that the contribution from currents J_x or J_y, although small, may be responsible for the observed etch-frustrated structures and patterns. The preference for these structures to grow along particular directions then arises from the fact that the crystal is trigonal, and hence has three y axes 120° apart. However, due to the $\cos 2\theta$ dependence of J_y, the current along each y axis may not be equal, depending on the angle β. This is illustrated by the plot of Equation (3.9) in Figure 3.40. Additionally, when the light polarisation vector is aligned along one of the three y axes, current also flows along the *negative* directions of the other two y axes.

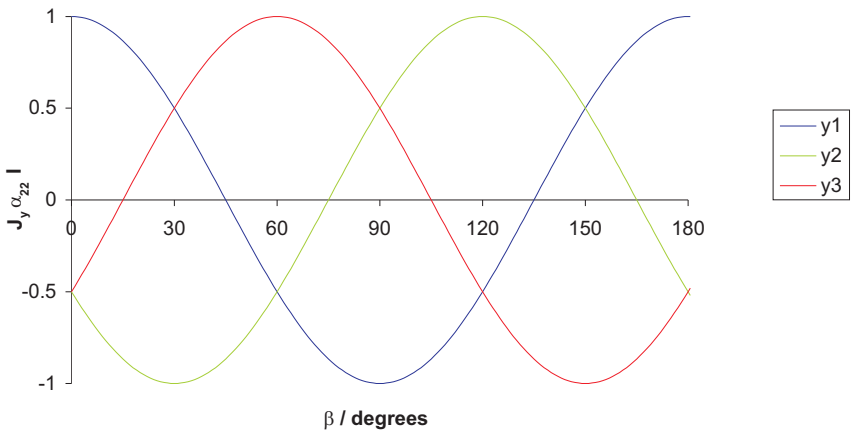

Figure 3.40: The dependence of the photovoltaic current along each of the three y axes in lithium niobate on the angle β between the light polarisation vector and the $y1$ axis.

Figure 3.41(a) shows a representation of the resulting current vectors and the y axes for the case when light is polarised along the $y1$ axis. In Figure 3.41(b) the current vectors have been redrawn to show how this theory can explain the characteristic angles of 60° and 120° that the LIFE structures form. The presence of these angles is illustrated using an annotated SEM image of a LIFE site in Figure 3.42.

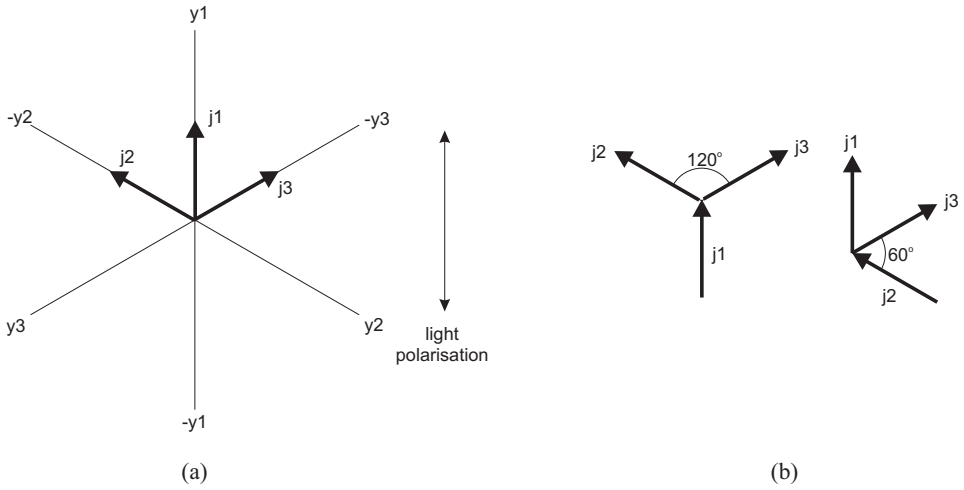

Figure 3.41: The possible directions of current, j, represented by arrows, created by light polarised along the $y1$ axis. (a) shows the current flow relative to the three y axes of lithium niobate and (b) shows the current vectors redrawn to illustrate how structures may form 120° or 60° angles.

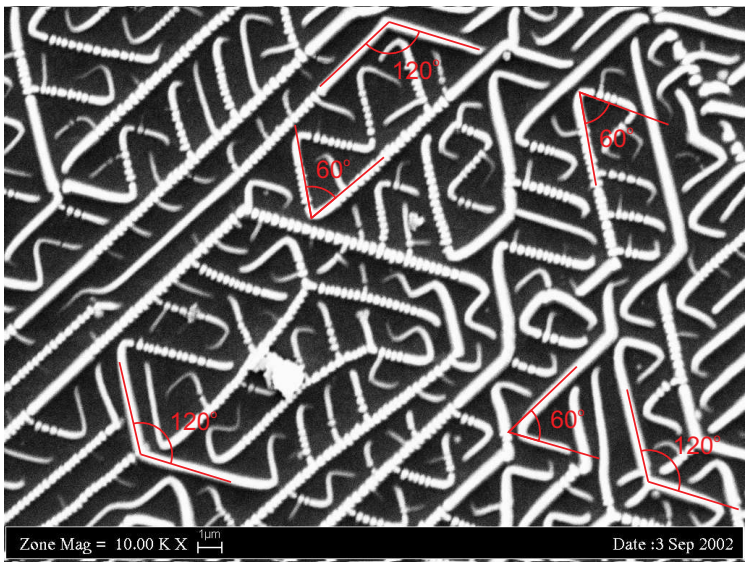

Figure 3.42: A typical SEM image of part of a LIFE site, showing the 60° and 120° angles that are formed between the structures.

The ability of a single line to change direction multiple times is another characteristic feature of the LIFE structures. This normally occurs when one structure is close to

another, so it is likely that during their formation repulsion between the charges occurs, resulting in the change in direction for one of the structures. Further evidence of a charge mediated mechanism can be seen in formation of quasi-periodic structures, which occur under certain circumstances, as shown in Figure 3.43. Optically generated charges at the edge of the LIFE site will arrange themselves into their lowest energy configuration, which may not require any changes in direction, and so form periodic surface patterns, which in this case lead away from the centre of the site.

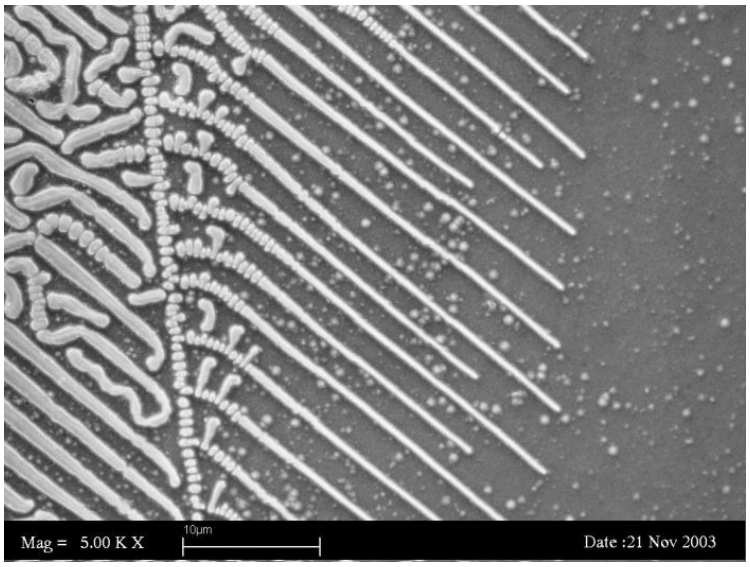

Figure 3.43: SEM image of quasi-periodic structures formed at the edge of a LIFE site on a 0.03 % Fe:$LiNbO_3$ crystal.

However, photovoltaic currents cannot explain all of the results that have been obtained. Figure 3.44 shows an entire LIFE site, where three sets of parallel unetched lines at the edges extend out into the normally etched area. This trigonal symmetry is entirely consistent with the underlying crystal symmetry, but is different to that expected from the basis of photovoltaic currents as shown in Fig. 3.41, which does not allow for current vectors along the $+y1$, $+y2$ and $+y3$ directions at the same time. This deviation could be a consequence of the illumination conditions that are used to make LIFE sites, which are approximately uniform on a small scale but become inhomogeneous when the entire site is being considered. This difference may allow the flow of current away from the centre of the site along all $+y$ directions.

One final possibility to explain the production of the LIFE features involves the scattering of light from the features themselves as they grow, resulting in the trigonal symmetry. This sort of phenomenon has been reported previously by numerous authors, for instance Guosheng et al. (1982) observed the spontaneous

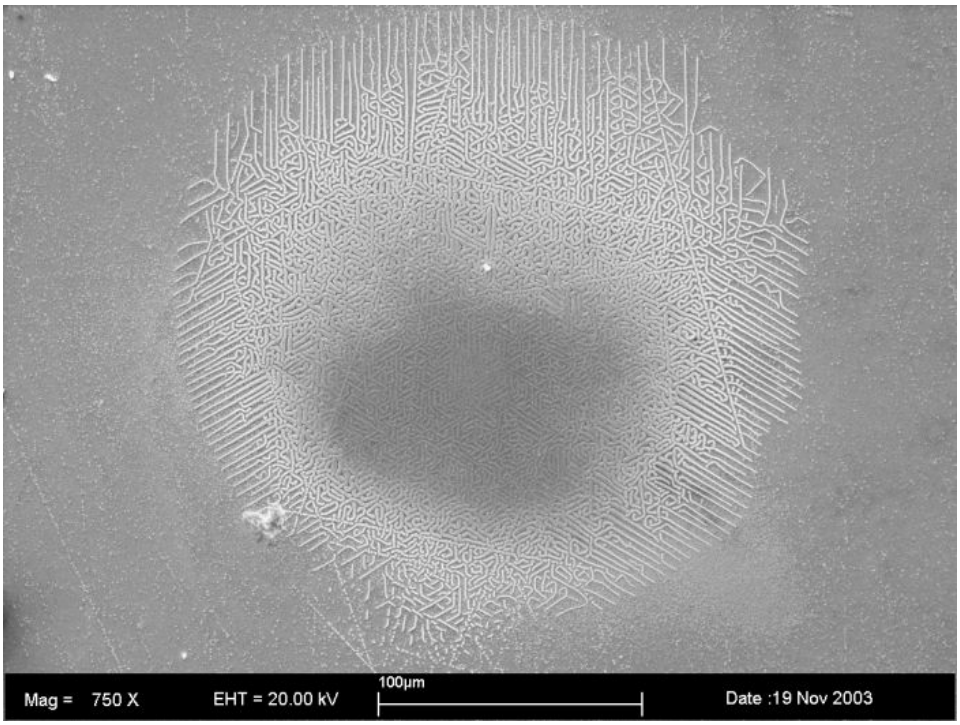

Figure 3.44: An entire LIFE site, showing three sets of parallel lines formed at the edges, at 120° to each other.

growth of periodic surface structures on a variety of materials (including metals, semiconductors and dielectrics) during laser illumination. They found that the period of ripples was dependent on the illuminating wavelength and angle of incidence. However, their experiments were not carried out simultaneously with etching and the ripples produced appear rather different to the structures produced in this work.

3.6 Summary

Surface structures in iron-doped lithium niobate structures were produced using the combined influence of laser light and acid etchant. Total and partial frustration of etching was observed, and in the partially etched areas complicated, self-organised, patterns developed that were related to the underlying crystal symmetry. Scanning electron microscopy (SEM) was used to visualise these structures.

Experiments were conducted to investigate the influence of beam intensity, duration of exposure, dopant concentration and polarisation of light used, on the type and pattern of structures formed. The beam intensity and duration of exposure were

found to be the most important factors, with high intensities resulting in total frustration. However, partial frustration occurred at positions on the sample surface where the irradiance was essentially zero, which suggested that the LIFE sites grow outwards from the centre, given sufficient exposure time. Using a defocussed laser beam with a spot size of 120 μm resulted in sites with diameters between 0.4 mm for 5 min exposure to 2.2 mm for 80 min exposure. But even a short period of exposure can result in a site; small sites were seen to develop after only 5 s.

The LIFE structures were analysed using electric-field atomic force microscopy (E-AFM), which showed they more positively charged than their surroundings. Fourier transform analysis was also carried out on the SEM images, which showed the strong preference for structures to form along directions parallel to the crystalline axes. A simple computer model was developed which replicated the type of patterns found in partially frustrated LIFE experiments, based on empirically derived rules about the growth of the structures.

Finally, although not known for certain at this time, possible mechanisms for the growth of the sites were considered in the Discussion.

3.7 References

Arsenovici, L. C. and P. D. Townsend. "The spatial distribution of defects produced in alkali halides by electron irradiation." *Philosophical Magazine*, **25**(2), 381 (1972).

Barry, I. E., R. W. Eason and G. Cook. "Light-induced frustration of etching in Fe-doped $LiNbO_3$." *Applied Surface Science*, **143**(1-4), 328 (1999).

Boyland, A. J., S. Mailis, I. E. Barry, R. W. Eason and M. Kaczmarek. "Latency effects and periodic structures in light-induced frustrated etching of Fe:doped $LiNbO_3$." *Applied Physics Letters*, **77**(18), 2792 (2000).

Festl, H. G., P. Hertel, E. Kratzig and R. v. Baltz. "Investigations of the photovoltaic tensor in doped $LiNbO_3$." *Physica Status Solidi B*, **113**, 157 (1982).

Fradkin, V. M. and R. G. Magomadov. "Anomalous photovoltaic effect in $LiNbO_3$:Fe in polarized light." *JETP Letters*, **30**, 686 (1979).

Gonzalez, R. C. and P. Wintz. *Digital Image Processing* (Addison-Wesley, 1987), 2nd edition.

Guosheng, Z., P. M. Fauchet and A. E. Siegman. "Growth of spontaneous periodic surface structures on solids during laser illumination." *Physical Review B*, **26**(10), 5366 (1982).

Holstein, W. L. "Etching study of ferroelectric microdomains in $LiNbO_3$ and MgO:$LiNbO_3$." *Journal of Crystal Growth*, **171**, 477 (1997).

Lau, H. W., G. J. Parker, R. Greef and M. Holling. "High aspect ratio submicron silicon pillars fabricated by photoassisted electrochemical etching and oxidation." *Applied Physics Letters*, **67**(13), 1877 (1995).

Luthi, R., H. Haefke, K.-P. Meyer, E. Meyer, L. Howald and H.-J. Guntherodt. "Surface and domain structures of ferroelectric crystals studied with scanning force microscopy." *Journal of Applied Physics*, **74**(12), 7461 (1993).

Mirza, K. A., P. D. Townsend and G. L. Destefanis. "Light emission from the surface of $LiNbO_3$." *Physica Status Solidi A*, **47**, K63 (1978).

Morozovska, A. N., E. A. Eliseev, V. V. Obukhovsky and V. V. Lemeshko. "Photo-microdomains in ferroelectrics: formation and light scattering caused by them." *Semiconductor Physics, Quantum Electronics and Optoelectronics*, **6**(3), 324 (2003).

Niizeki, N., T. Yamada and H. Toyoda. "Growth ridges, etched hillocks and crystal structure of lithium niobate." *Japanese Journal of Applied Physics*, **6**(3), 318 (1967).

Ohnishi, N. and T. Lizuka. "Etching study of microdomains in $LiNbO_3$ single crystals." *Journal of Applied Physics*, **46**(3), 1063 (1974).

Randi, J. A., J. C. Lambropoulos and S. D. Jacobs. "Subsurface damage in some single crystalline optical materials." *Applied Optics*, **44**(12), 2241 (2005).

Scott, J. G., A. J. Boyland, S. Mailis, C. Grivas, O. Wagner, S. Lagoutte and R. W. Eason. "Self-ordered sub-micron structures in Fe-doped $LiNbO_3$ formed by light-induced frustration of etching." *Applied Surface Science*, **230**(1-4), 138 (2004).

Shen, J., S. Liu, K. Yi, H. He, J. Shao and Z. Fan. "Subsurface damage in optical substrates." *Optik*, **116**, 288 (2005).

Soergel, E., W. Krieger and V. I. Vlad. "Charge distribution on photorefractive crystals observed with an atomic force microscope." *Applied Physics A*, **66**, S337 (1998).

Sones, C. L., S. Mailis, V. Apostolopoulos, I. E. Barry, C. Gawith, P. G. R. Smith and R. W. Eason. "Fabrication of piezoelectric micro-cantilevers in domain-engineered

$LiNbO_3$ single crystals." *Journal of Micromechanics and Microengineering*, **12**(1), 53 (2002).

Tsunekawa, S., J. Ichikawa, H. Nagata and T. Fukuda. "Observation of ferroelectric microdomains in $LiNbO_3$ crystals by electrostatic force microscopy." *Applied Surface Science*, **137**, 61 (1999).

Weis, R. S. and T. K. Gaylord. "Lithium niobate: Summary of physical properties and crystal structure." *Applied Physics A*, **32**, 191 (1985).

Youtsey, C., I. Adesida, L. T. Romano and G. Bulman. "Smooth n-type GaN surfaces by photoenhanced wet etching." *Applied Surface Science*, **72**(5), 560 (1998).

CHAPTER

FOUR

Ultraviolet Exposure of Lithium Niobate

Following the experiments on Light Induced Frustration of Etching, described in Chapter 3, where etch-resistant features were formed on the surface of iron-doped lithium niobate by the combined action of etching with simultaneous exposure to visible light (of wavelength 532 nm), we wished to investigate the potential for all-optical poling in undoped lithium niobate. This chapter describes work carried out towards this goal, using pulsed light at ultraviolet wavelengths. Etching was used to reveal the structures that were formed by light, but was not an integral part of the process as it was in the previous chapter.

The experimental work was carried out by myself with other members of the group, with the exception of some $+z$ face exposures with a phase mask and the scanning force microscopy measurements which were conducted by Chris Valdivia and Collin Sones, and collaborators at Pennsylvania State University, USA and the University of Bonn, Germany.

4.1 Introduction

Optical poling has several advantages over the traditional electric field poling technique that was described in Section 2.4.1. The major limitation of electric field poling is that the smallest period of domains that can be produced with acceptable uniformity is approximately 1 μm (Mizuuchi et al., 2004). Some exciting future

applications (such as ultraviolet second harmonic generation) require sub-micron domain periods, so a new method of producing domains is needed. A possible solution to this problem is to use optical poling, which could allow the production of domains of the same size as the wavelength of light used. Optical poling would also be a simpler technique than electric field poling, as it requires only a single-step process, without the need for photolithography. Previous attempts by Houe and Townsend (1995) at optical poling have required elevated temperatures (400°C) and application of a uniform electric field (60 V), however experiments reported here were conducted at room temperature and without application of an external field.

To attempt optical poling, ultraviolet (UV) wavelengths around the optical absorption edge of lithium niobate were used, as the absorption at these wavelengths is much higher than at visible wavelengths. This is illustrated in Figure 4.1 which shows the optical transmission spectrum of lithium niobate around 320 nm, where the edge is situated in undoped material. We used UV light with wavelengths ranging between 248 nm and 329 nm; at 248 nm the light is totally absorbed while at higher wavelengths (above ≈ 310 nm) the transmission begins to increase, so the light will penetrate further into the crystal.

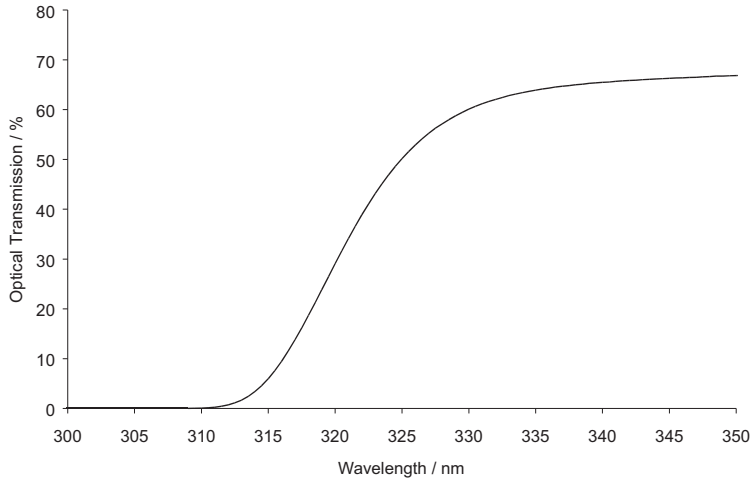

Figure 4.1: Optical Transmission Spectrum of Lithium Niobate around the UV absorption edge.

The absorption can be characterised by the absorption coefficient, α, which is defined as

$$\alpha = \frac{-\ln T}{d} \tag{4.1}$$

from the expression for attenuation

$$T = \frac{I}{I_0} = e^{-\alpha d} \tag{4.2}$$

where T is the fractional transmission (transmitted irradiance I over the incident irradiance I_0) through a material at a depth d. The intensity will have decreased to $1/e$ of the incident intensity (or 36.7 % transmission) at a depth in the material equal to the inverse of the absorption cofficient. This $1/e$ depth for lithium niobate is shown in Figure 4.2. At wavelengths below 310 nm, the graph shows that almost all of the light will be absorbed in the first 50 μm of the crystal. Below 300 nm this depth will be even smaller but cannot be accurately measured as essentially no light is transmitted through the crystal.

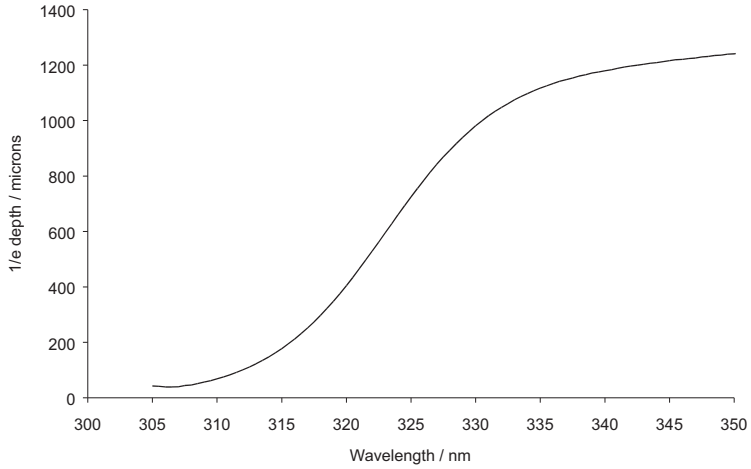

Figure 4.2: Graph of the 1/e absorption depth for wavelengths around the UV absorption edge of lithium niobate.

After exposure to UV light, the lithium niobate samples were etched in HF and examined using a scanning electron microscope (SEM).

4.2 Experimental Details

Two pulsed laser systems were used to obtain the required wavelengths; a KrF excimer laser (Lambda Physik LPX 200) operating at 248 nm (~20 ns pulses) and a tunable dye laser (Sirah Precision Scan). Access to the dye laser system was provided by the Central Laser Facility at the Rutherford Appleton Laboratory. The laser used a mixture of Rhodamine B and 101 dyes which, when frequency-doubled, produced wavelengths between 298 and 329 nm with ~7 ns pulses. The dye laser was pumped by a frequency doubled Q-switched Nd:YAG laser (Continuum Powerlite 8000) operating at 532 nm. The operation of the dye laser is shown schematically in Figure 4.3.

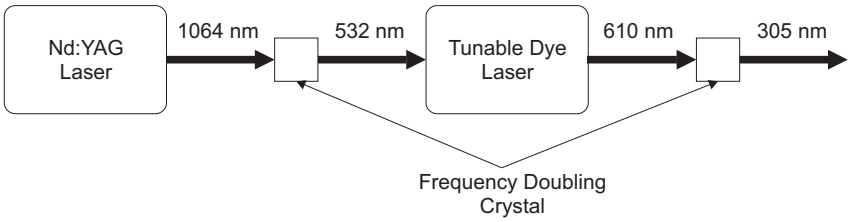

Figure 4.3: Schematic diagram illustrating the operation of the dye laser.

Both lasers suffered from poor spatial homogeneity of the beam (the beam profile of the dye laser is given in Fig. 4.4), however the effect of this was minimised by using an aperture to define a section of the beam which appeared to be most uniform. The beam was then focussed on to either the $+z$ or the $-z$ face of a lithium niobate sample. The sample was mounted on an xyz translation stage to allow for easy positioning, so that multiple exposures could be made on a single crystal and so the sample could be moved towards or away from the lens, and hence vary the power density. The variables that were investigated were:

- Wavelength.
- Energy density (Fluence)
- Number of pulses (Total Exposure).

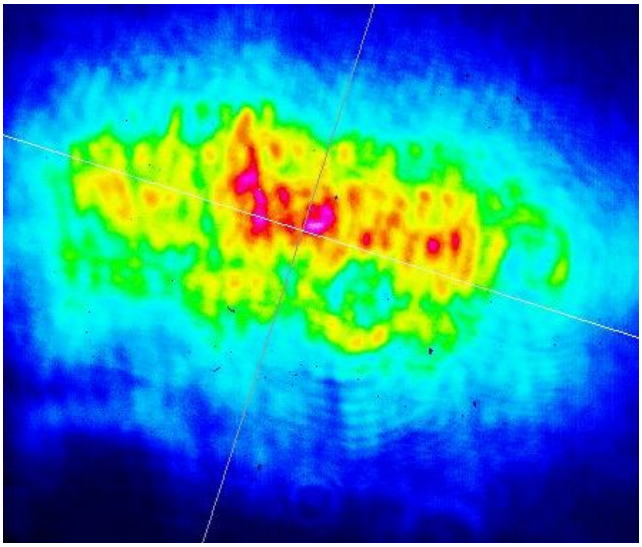

Figure 4.4: Profile of the beam from the RAL dye laser. The beam had dimensions ~5.1 mm by ~2.8 mm.

4.3 Results

Experiments were carried out with a range of fluences, between 0.5 and 10 J cm^{-2}. At energies near the ablation threshold of lithium niobate (~0.5 J cm^{-2}) there was little evidence of surface damage, but as the fluence was increased, the amount of ablation increased. Due to the spatial inhomogeneity of the beam, ablation initially appeared to be uneven, with some parts of the exposed areas experiencing ablation while others remained undamaged. More uniform ablation was achieved by using more than one pulse. Five pulses with fluence of ~10 J cm^{-2} at 298 nm resulted in an ablation pit ~1.5 μm deep. An SEM image of a typical area which has experienced ablation caused by a pulsed laser beam is shown in Figure 4.5. The effects of UV exposure depend strongly on whether the $+z$ or $-z$ face was exposed. The case for $+z$ exposure will be discussed first.

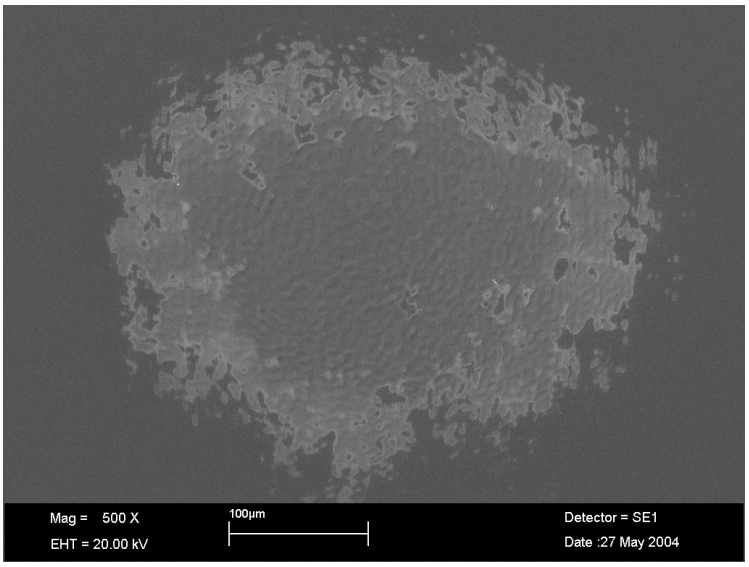

Figure 4.5: Ablated region after 5 pulses (1 mJ / pulse) at wavelength 298 nm.

4.3.1 Exposure of $+z$ face

Interesting features were observed when the $+z$ face of an ablated crystal was etched in 48 % hydrofluoric acid solution for ~30 min. The etchant revealed a series of lines and patterns within the ablated region, as shown in Figure 4.6, which closely resemble the features produced using Light Induced Frustration of Etching (LIFE), described in Chapter 3. However, in this case the lines are actually trenches on the crystal surface, not ridges as in the case of LIFE sites. This difference can be

explained by the fact that in these experiments the $+z$ face is being irradiated, while the $-z$ face was used in LIFE experiments. Under normal conditions, the $+z$ face of lithium niobate is resistant to etching, so any change to normal etch characteristics would inevitably result in a higher etch rate.

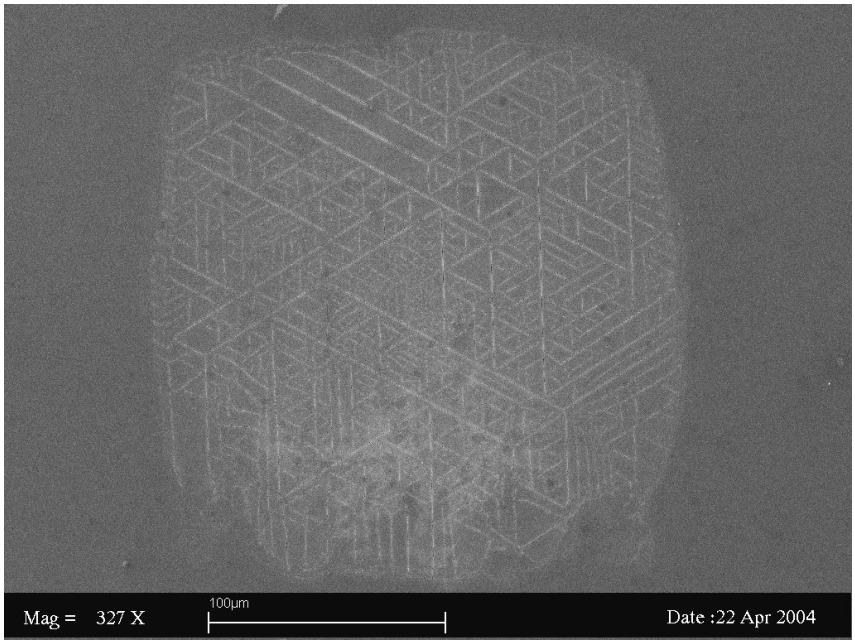

Figure 4.6: Patterns formed in an ablated region of lithium niobate, created by a single pulse of wavelength 298 nm.

The trenches formed along the crystallographic y axes, and like the LIFE structures, change direction to avoid coming in to contact with each other. This is clearly shown in Figure 4.7; some features can also be seen that are not aligned along a direction corresponding to a crystal axis, but these are broken and irregular. The complete trenches appear to change direction when they reach a certain distance from another trench, Figure 4.8 shows that this distance is ~1.8 µm. The change in direction is usually by 60°, so distinctive triangular shapes are created and the available space efficiently filled (Figure 4.9). The trenches are between 150 - 300 nm wide and some were seen to extend right across the ablated areas, which had a typical width of ~300 µm.

To evaluate the depth of these features a sample was etched for an extended period of time (18 hours) to ensure the trenches were fully formed, then a focussed ion beam (FIB) system (courtesy of FEI, Bristol) was used to mill a channel perpendicular to two trenches. The FIB was then used to image the cross-sections of the two trenches, which were now visible due to the channel. This image is reproduced in Figure 4.11, which shows the depths of the trenches were 1.9 and 1.8 µm. As the etch rate of

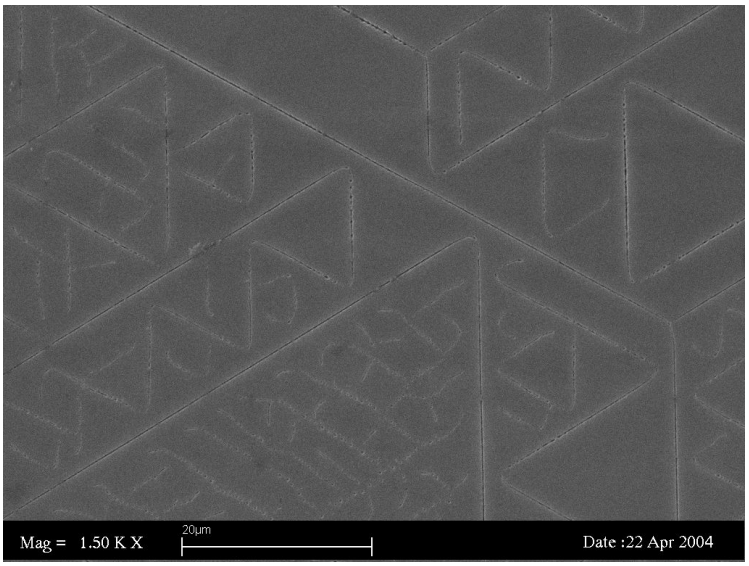

Figure 4.7: Trenches may change direction, often forming characteristic triangular patterns.

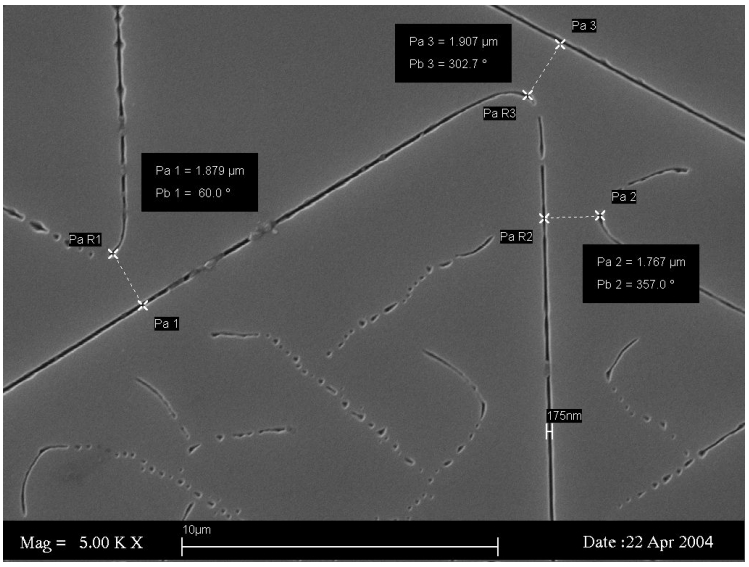

Figure 4.8: Higher magnification view of the area shown in Fig. 4.7, showing the minimum distance between lines of ~1.8 µm.

lithium niobate in HF acid is ~0.8 µm h^{-1} (Sones et al., 2002), we are confident that the trenches would not become any deeper with a longer etch duration, and that ~2 µm is the natural depth of the features that are formed. The extended exposure to HF has however allowed some sideways etching to occur, which is why the channels in the FIB image are wider than normal, at ~0.4 µm wide. This still represents a large aspect ratio of ~5:1.

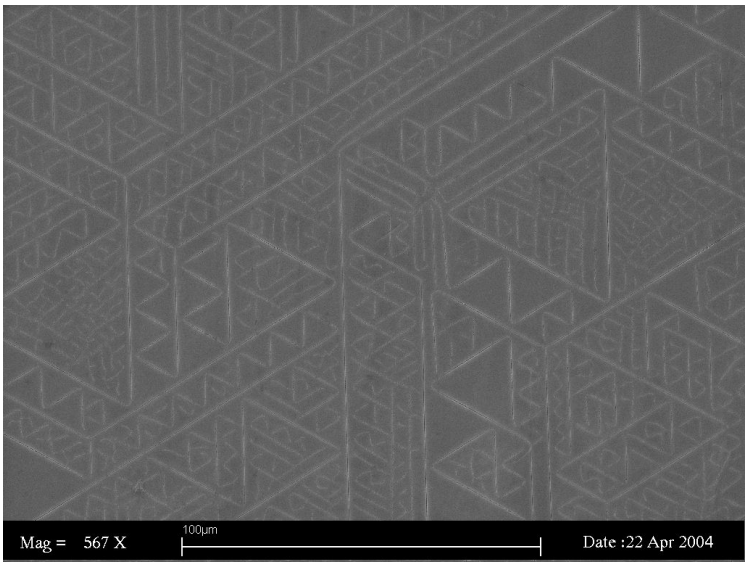

Figure 4.9: Space-filling behaviour of UV-induced trenches.

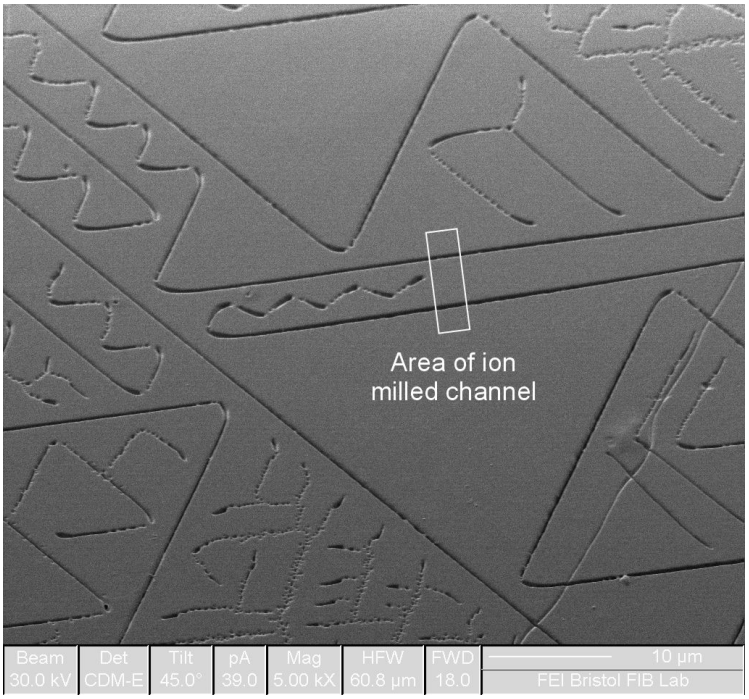

Figure 4.10: Image taken by FIB system, at 45°to the crystal surface, showing features created by 2 UV pulses (~1.5 J cm^{-2}) at 298 nm, with the area to be ion-milled marked.

Wavelengths of 244 nm and between 298 - 329 nm were used to irradiate the samples, but the UV-induced features were only formed by wavelengths below 307 nm. This was due to the apparent requirement that some ablation must have taken place before features were observed, and no ablation was observed when irradiating

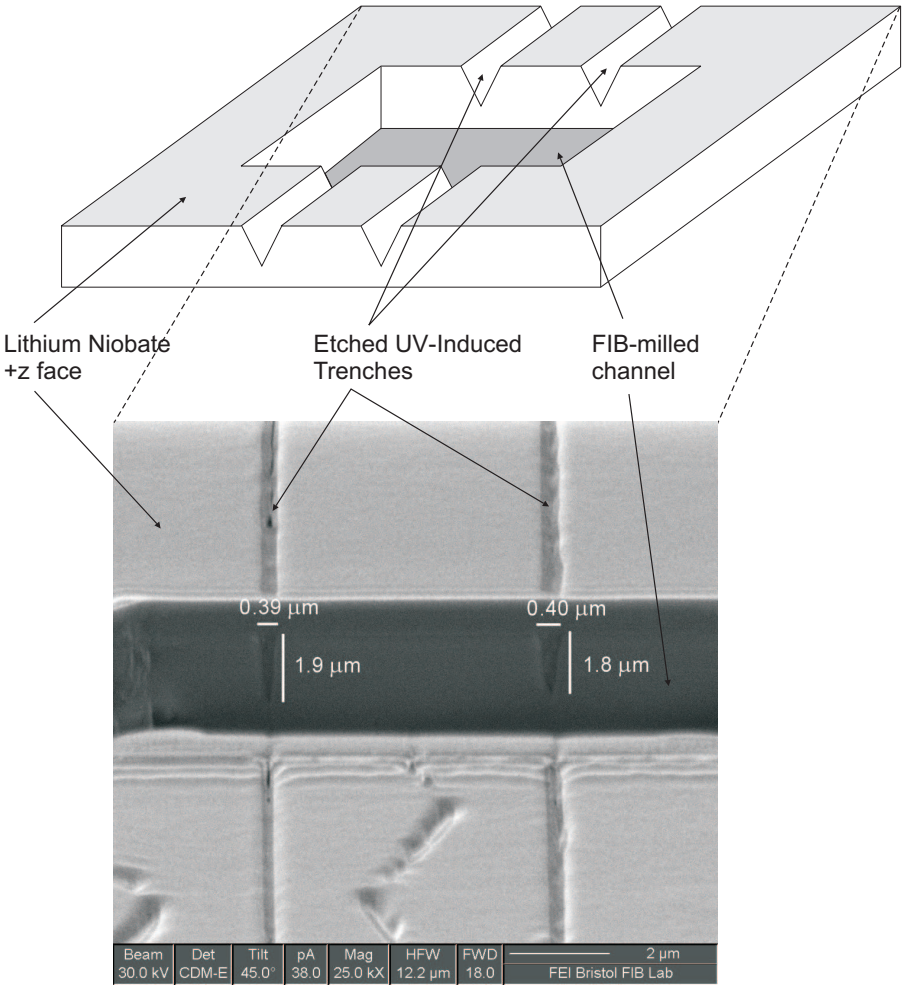

Figure 4.11: Channel formed by Focussed Ion Beam milling, across two UV-induced trenches.

above 307 nm, due to the lower absorption at this wavelength. It may be possible to create features using longer wavelengths that 307 nm, but this would probably require fluences greater than the 10 J cm^{-2} that were available.

The fluence was varied by controlling the energy per pulse (energies up to 6 mJ / pulse were available) and the spot size of the beam (and hence energy density). Figure 4.13 shows a variety of sites that were formed using either two or five pulses, at varying distances (z) from the focal point of the lens. The widths of the sites varied between 100 - 300 µm. The patterns of trenches formed on each site are all unique, but look broadly similar, despite the range of fluences and number of pulses that were used to create the sites. In each case the features extend across the ablated area and form trenches with the same symmetry as the crystal. This is evident from

the Fourier transform shown in Figure 4.12, where the lobes of the transform are extremely narrow, which shows the strong directional preference of the trenches.

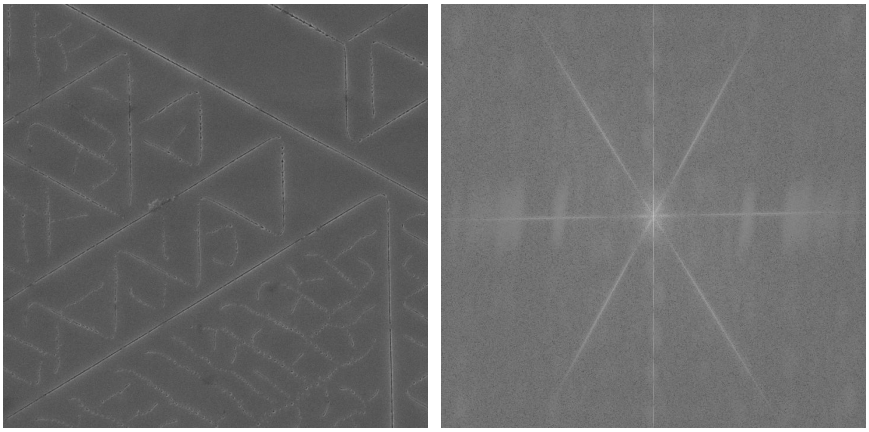

(a) UV-induced trenches (b) Fourier Transform

Figure 4.12: Fourier transform of SEM image of UV-induced trenches.

4.3.2 Exposure of -*z* face

UV exposure experiments conducted on the $-z$ face of a lithium niobate crystal gave ablation when sufficiently high fluences were used, as on the $+z$ face, but no additional features or patterns were revealed when these ablated areas were etched with HF acid.

However, UV exposed areas had previously been observed to be etch resistant by Mailis et al. (2001) using fluences below the ablation threshold. During the limited available time at the Rutherford Appleton labs, experiments were concentrated on the potentially more interesting $+z$ face exposure. However, on return to Southampton further experiments were conducted on the $-z$ face, using the KrF excimer laser operating at 248 nm, mostly by other group members including Sakellaris Mailis, Collin Sones and Chris Valdiva. These are described below.

Total frustration of frustration of etching was observed with laser fluences around 70 mJ cm^{-2}, although the inhomogeneity of the excimer laser beam made determining accurate values difficult. Etch frustration was found to be sensitive to laser intensity, but the number of pulses applied was much less significant. As a typical excimer pulse has an irregular intensity profile, exposure of lithium niobate crystal results in some areas that were etch frustrated while other regions etched normally. To study this effect in more depth, a section of the excimer beam

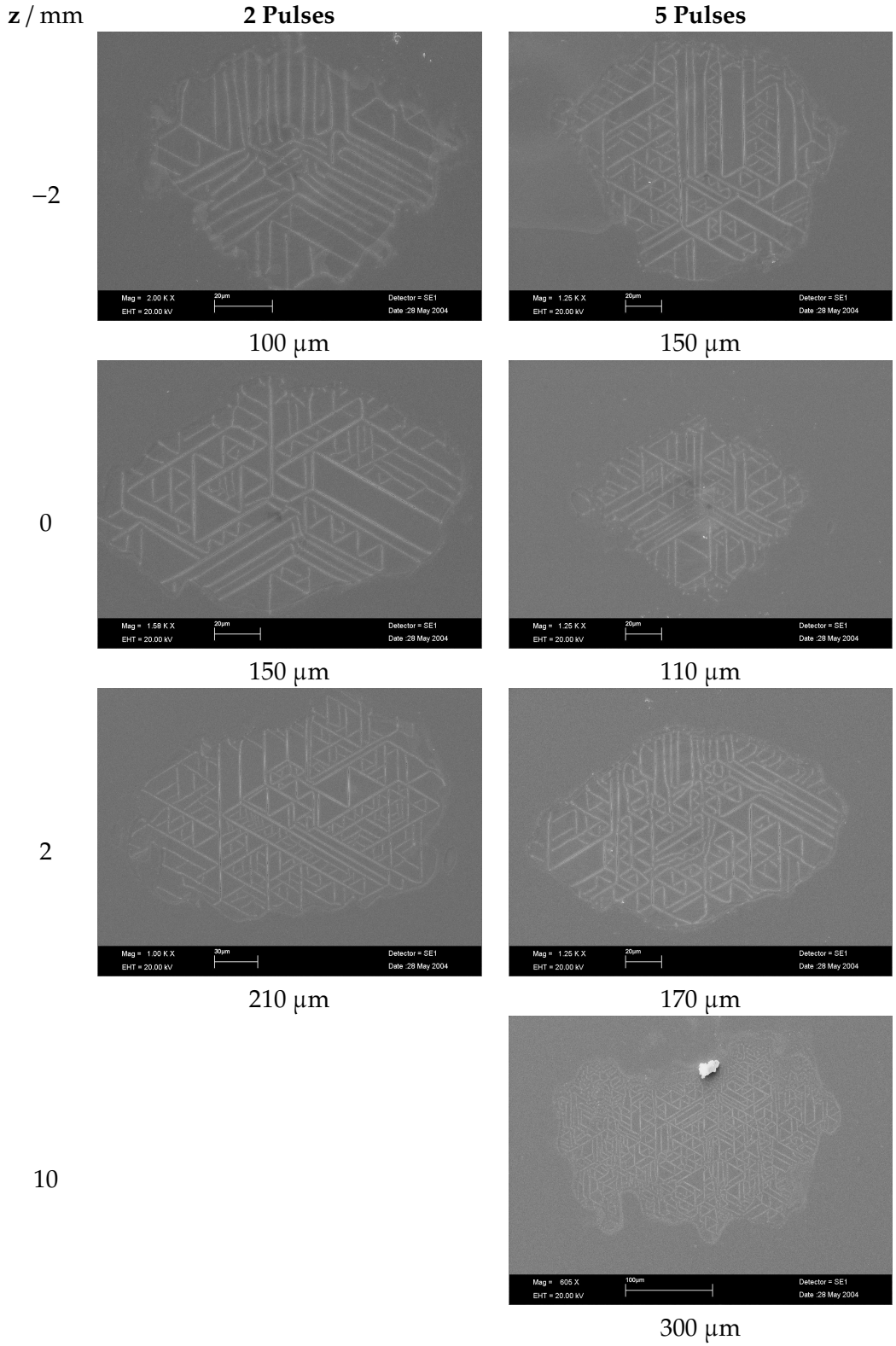

Figure 4.13: UV-induced sites formed at distance z from beam focus on a $+z$ face (1 mJ / pulse, 2 or 5 pulses) and measured site widths.

with a wide range of intensities was selected. The beam profile was recorded on thermal paper, which was then digitised with a scanner, as shown in Figure 4.14. The thermal paper exposure is not necessarily linear, however it gave a qualitative representation of the beam profile. The beam had an energy of 80 mJ / pulse, distributed over an area of 12.2 mm by 8.4 mm.

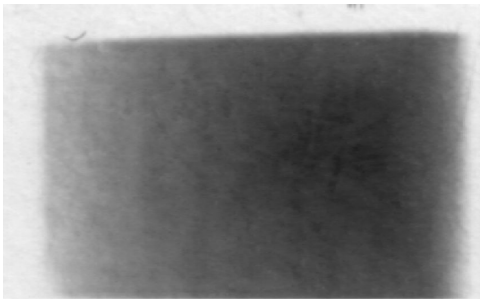

Figure 4.14: Expanded intensity profile of the excimer laser beam, recorded on thermal paper. The beam had dimensions of 12.2 mm by 8.4 mm.

A lithium niobate sample was subsequently exposed using the same portion of the beam that was used to record the profile. The sample was then etched and a surface profiler scan was taken, which revealed two narrow areas that had experienced etch frustration, surrounded by areas where normal etching had occurred.

Figure 4.15 shows the cross section of the beam intensity profile, formed by taking the average of five cross sections of the digitised image, using tools in Matlab software. This gives a qualitative representation of the intensity across the beam profile, and shows the significant variation that is present. Superimposed on this image is the surface profiler trace, calibrated to the same scale. The presence of two areas of etch frustration, shown by the peaks in the trace, is consistent with the intensity profile of the beam, as the cross section curve shows that two areas across the spot will experience similar intensities. This is illustrated by the shaded areas in Fig. 4.15, which relate the areas of etch frustration to the intensity required to form them. This confirms that etch frustration is sensitive to the laser intensity and only occurs for a narrow range of intensities.

The rest of the experiments described here used a more uniform section of beam, and hence more uniform intensities, but some variations were inevitable. To achieve patterning of the etch-resistant features, the beam was structured using either a phase or amplitude mask. The amplitude mask consisted of an 11 μm thick copper grid of hexagonal apertures that was produced for use in Transmission Electron Microscopes (TEMs). The TEM grids were available with hexagonal openings of widths 90 μm, 50 μm and 35 μm, and these sizes determined the size of the

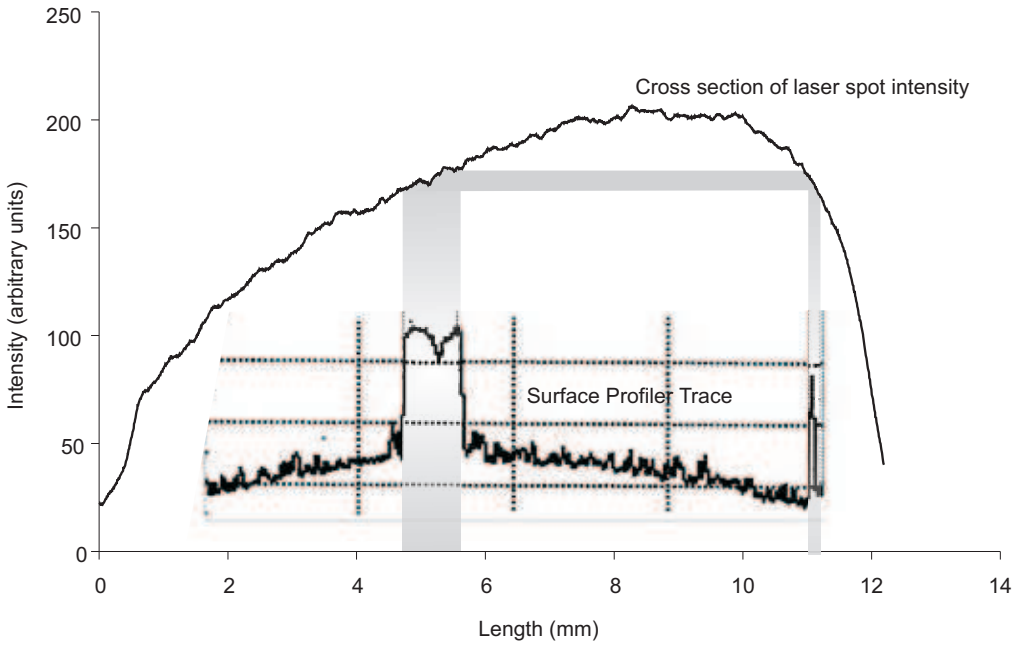

Figure 4.15: Intensity cross section of excimer beam profile (top) and the surface profile trace of the exposed area of the crystal (bottom), calibrated to the same scale. The shaded areas represent areas which are subjected to similar intensity levels, which results in etch frustration.

hexagons that were formed on the crystal surface. The mask was secured over the sample before exposure to UV radiation, then subsequent etching in HF acid revealed the TEM pattern that had been transferred to the lithium niobate surface. An example of this is shown in Figure 4.16. An array of etch-resistant hexagonal shaped features was created, with each individual hexagon consisting of sub-micron features. The repeating structure within the hexagon is thought to be caused by near-field (Fresnel) diffraction effects from the edge of the TEM grid.

The use of an amplitude mask resulted in relatively large overall feature size, although the component features were much smaller, and so had only limited potential for producing structures with over-all sizes of less than 1 μm. To overcome this limit on minimum feature size, a series of experiments was carried out using a phase mask instead of an amplitude mask. The phase mask had a grating period of 720 nm, and so produced a periodic intensity pattern of 360 nm on the crystal surface. The phase mask was spaced away from the surface using pieces of 125 μm diameter optical fibre to ensure a uniform separation.

Results of UV exposure through a phase mask are shown in Figure 4.17. The etch-frustrated areas again consist of small individual etch-resistant features, which appear to be regularly ordered in vertical lines. The features do not cover the entire

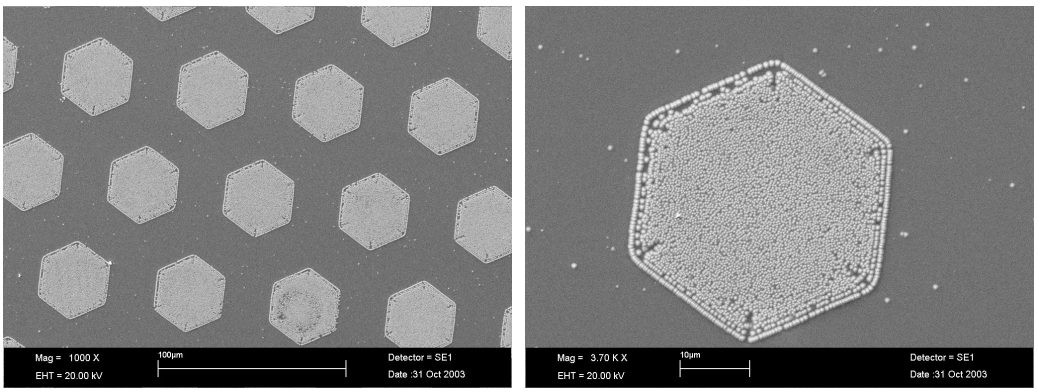

(a) Multiple hexagonal sites (b) Higher magnification image of a single site

Figure 4.16: SEM image of etch resistant features on a $-z$ face of $LiNbO_3$, created by UV exposure through a hexagonal amplitude mask.

exposed area, this is a result of the spatial variation in intensity of the illuminating laser beam.

In Fig. 4.17(a) concentric rings appear around certain points which are likely to originate from diffraction due to dust on the crystal surface. Although the sample was cleaned and etched in a clean room environment, the laser was not situated in a clean room, so a small amount of contamination was inevitable. The period spacing in Fig. 4.17(a) directly corresponds to the period of the phase mask (720 nm), while the image in Fig. 4.17(b) exhibits periods of 720 nm and 360 nm ($\Lambda/2$). It is clear that the size of the individual features is also proportional to their period.

4.4 Discussion

The mechanism behind the formation of the light-induced structures that have been presented in this chapter is still uncertain. There are clear similarities to the results described in Chapter 3 using the LIFE technique, but also significant differences in the methods used. These are summarised in Table 4.1 below. Hence, while the mechanisms behind the two effects may be related, they are not necessarily the same.

The two most likely mechanisms responsible for ultraviolet-induced patterning on lithium niobate surfaces are again either charge-related effects or domain formation, as for the LIFE experiments. To investigate these possibilities, a simple experiment was conducted by uniformly sprinkling standard toner particles (from a laser printer cartridge) on to two recently UV-exposed lithium niobate samples. The excess toner

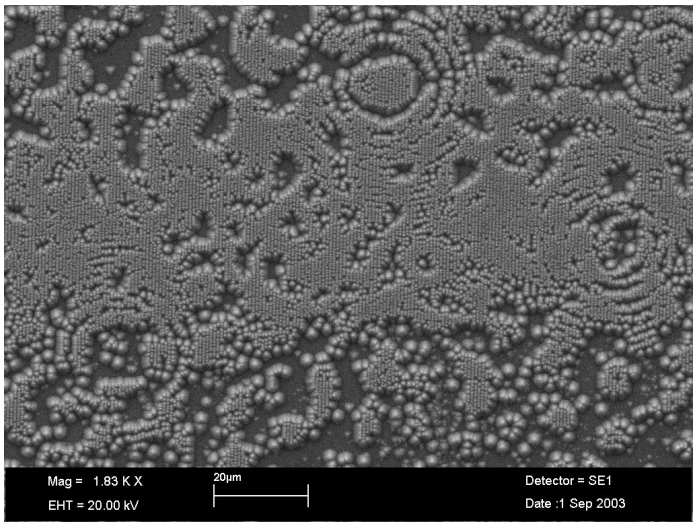

(a) Central area of laser spot; relatively uniform intensity

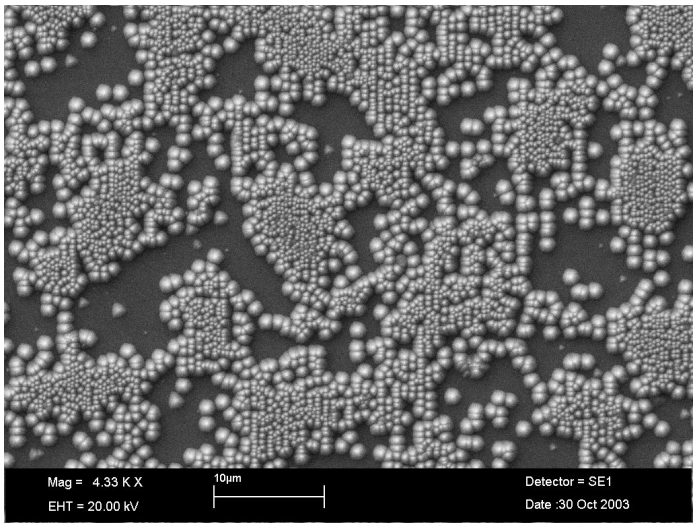

(b) Edge of laser spot; larger variations in intensity

Figure 4.17: Etch-frustration created by UV exposure through a phase mask, showing periodically ordered features.

was then removed from the surface by shaking, leaving some toner remaining, mostly on the exposed areas. The results are shown in Figure 4.18.

One of the samples was exposed on the $-z$ face, while the other was exposed on the $+z$ face. Each sample had three sites, where between 100 to 500 pulses were applied, with a fluence of around 70 mJ / cm^2. The sites are defined by the toner, with more toner being retained on the $-z$ face than the $+z$. Additionally, on the $-z$ face more toner is retained by areas which had been subjected to a greater number of pulses, with the 500 pulse site almost entirely covered by toner particles. However, each

Table 4.1: Comparison of the conditions used for UV exposure with those used in LIFE experiments.

Property	UV	LIFE
Laser mode:	Pulsed	Continuous wave
Wavelength:	UV wavelengths	532 nm green light
Crystal dopant:	None	Iron
Etching procedure:	After exposure	During exposure

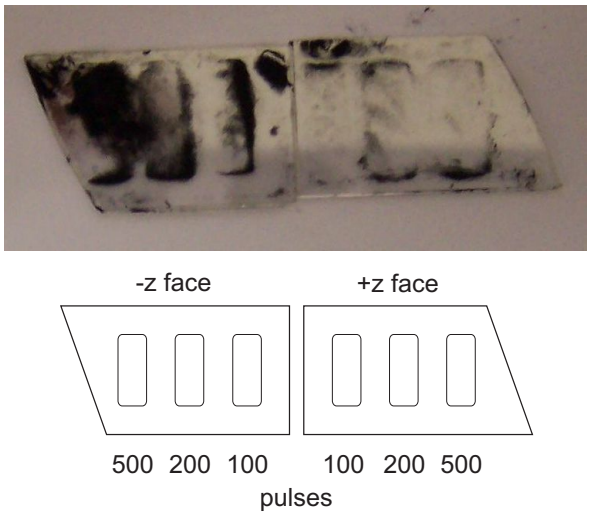

Figure 4.18: UV-exposed lithium niobate samples with exposed areas defined by toner particles. The schematic shows the number of pulses each area had received and which crystal face was exposed.

site on the $+z$ face only retains a small amount of toner, mostly around the edges of the exposed area.

Light induced charged generation and transport was discussed in Section 2.3.9. At UV wavelengths direct excitation of electrons from the valence band to the conduction band is possible, hence the liberated charge generated at the surface (due to the high level of absorption at 244 nm) will influence the adhesion of the negatively charged toner particles. A greater number of pulses results in more adhesion of the toner on the $-z$ face, which is related to the increased charge generation. However, this trend does not continue for the $+z$ face. The reason for this is that after electrons are excited from the valence band to the conduction band by the UV light, they are transported along the $+z$ axis direction by the bulk photovoltaic effect. Thus the $-z$ face becomes depleted of electrons, so allowing adhesion of the negatively charged toner particles. But on the $+z$ face, negative charge builds up, which repels the toner particles. This results in the toner patterns that were observed, with most toner concentrated around the edges of the exposed areas on the z face. These two cases are illustrated schematically in Figure 4.19.

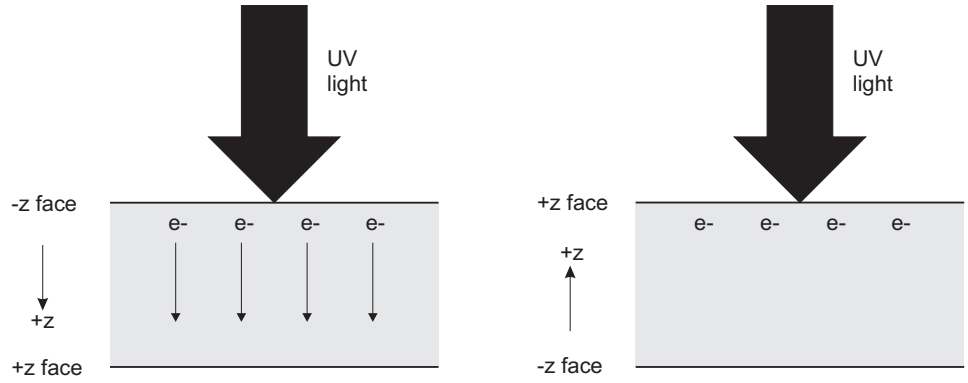

Figure 4.19: Schematic diagram illustrating optical charge generation and transport by the photovoltaic effect for $-z$ and $+z$ face exposure to UV light.

The $+z$ faces of lithium niobate are well known to resist etching by HF acid (see Section 2.4.2), because the positive charge prevents the acidic proton from attacking the crystal surface (Sones et al., 2001), while $-z$ faces etch normally. If light induced charge generation is responsible for the behaviour of toner particles on UV exposed areas, it might also explain the etch-frustration effects on $-z$ faces that have been discussed in this chapter. The positively charged areas, created by UV exposure, on the $-z$ face then resist etching in the same way that $+z$ faces do naturally.

This explanation is similar to that proposed in Chapter 3 for light-induced frustration of etching. However, a crucial difference between the two techniques is that UV exposure affects the etching behaviour of the crystal even days after exposure, while LIFE only occurs when the etchant is applied to the crystal simultaneously with light. This suggests that a different mechanism is responsible for the observed behaviour following UV exposure. This is reasonable as the energy densities from the pulsed UV light are much greater than those required for LIFE, and lithium niobate is almost entirely absorbing at UV wavelengths.

Electron emission has also been observed from lithium niobate faces during heating (caused by pulsed light absorption or a thermal heater), due to the pyroelectric effect. Electrons were emitted from the $+z$ face on heating and from the $-z$ face on cooling, with the maximum current found to be 10^{-7} A cm^{-2}. See Rosenman et al. (2000) for a comprehensive review on this subject.

The other possible mechanism to explain the UV-induced frustration of etching or trench formation is that domain inversion has occurred. For instance, the SEM images in Figure 4.20 taken by Chris Valdivia show typical UV-induced trenches on a $+z$ face of a magnesium-doped lithium niobate crystal. The trenches appear to originate from a hexagonal region; these regions are common in MgO:$LiNbO_3$

and are known to be domains of opposite orientation to the surrounding areas. As the trenches extend from this point it would seem likely that the trenches are also domains of the same orientation as the hexagonal centre point.

If the features are indeed domains, it is likely that thermal effects play a significant part in their formation. The temperature increase from each pulse may be estimated using the following equation:

$$\Delta T = \frac{Q}{mC_p} \tag{4.3}$$

with

$$m = \rho \times \pi r^2 \times d \tag{4.4}$$

where ΔT is the change in temperature, Q is the energy per pulse (~1 mJ), m is the mass, C_p is the specific heat capacity (0.628 J g^{-1} °C^{-1}), ρ is the density (4.644 g cm^{-3}), r is the beam radius (~100 μm) and d is the depth affected (estimated to be 1 μm due to the high absorption of UV light by lithium niobate). Using these figures, the increase in temperature for one pulse is estimated to be 1090 °C. As this is close to the Curie temperature (T_c = 1210 °C), it is possible that the features are thermally-induced domains.

To further investigate the possibility of UV-induced domain formation, scanning force microscopy was used to study other UV-exposed samples.

4.4.1 Scanning force microscopy (SFM)

Scanning force microscopy (SFM) is the general name given to a diagnostic technique based on an atomic force microscope (AFM) but modified to give additional information, in this case on the domain structure of the lithium niobate samples studied. The technique has the advantage of being non-destructive, as it does not require the sample to be acid-etched before examination. There are several techniques with different names, but similar modes of operation, such as 'dynamic contact electrostatic force microscopy' (DC-EFM) developed by a group at the University of Bonn, Germany and 'piezeoelectric force microscopy' (PFM) used at Pennsylvania State University, USA. DC-EFM is a development of the EFM which was used to study samples in Chapter 3. Other groups have reported the use of 'high-voltage atomic force microscopy' (HVAFM) to actually produce sub-micron domain structures in lithium niobate (Rosenman et al., 2003; Terabe et al., 2003).

Scanning force microscopes can be used to visualise ferroelectric domain structures by applying a modulated AC voltage to a silicon tip, which has been made

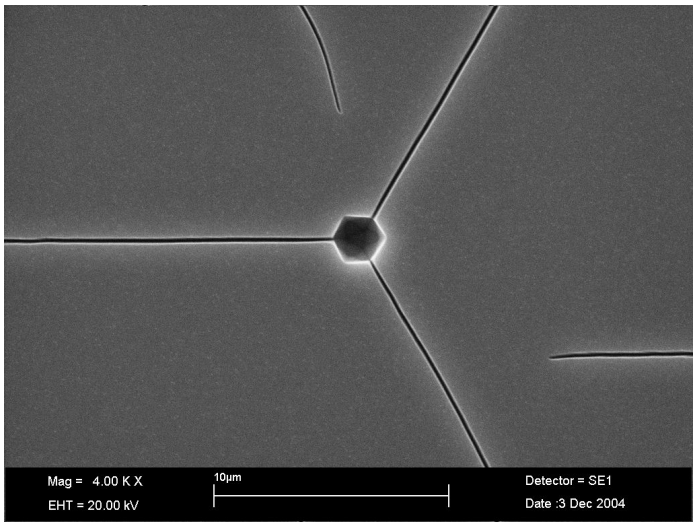

(a) Trenches extend in 3 directions, from a central hexagonal point.

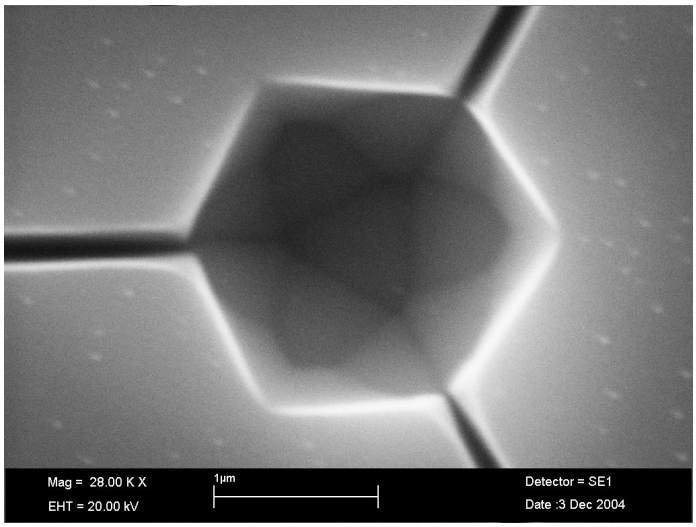

(b) Higher magnification image of hexagonal region; detailed structure is visible.

Figure 4.20: SEM images of UV-induced trenches in MgO-doped $LiNbO_3$.

electrically conductive by applying a thin metal coating. The exact mechanism responsible for domain contrast is still under discussion, but is thought to be related to the piezoelectric effect. In this case, when the tip is brought in to close contact with the lithium niobate surface (at a distance of 0.1 to 1 nm) the applied voltage causes a deflection of the surface, due to the converse piezoelectric effect. The contrast between oppositely orientated domains is obtained due to the alternate signs of electromechanical/piezoelectric response from the 180° orientated domains.

The tip voltage V_{tip} has AC and DC components

$$V_{tip} = V_{dv} + V_{ac}\cos(\omega t + \Phi) \tag{4.5}$$

and when this is applied to a piezoelectric surface, the deflection, d, will be

$$d = d_0 + A\cos(\omega t + \phi) \tag{4.6}$$

where ω is the angular frequency of oscillation, A is the amplitude of the oscillation, Φ is the phase of the tip voltage and ϕ is the phase of the piezoresponse of the surface.

Neighbouring antiparallel domains are expected to have equal amplitude responses determined by the d_{33} piezoelectric coefficient, while the phase of the signal is related to the polarisation direction. The direction of spontaneous polarisation for a $-z$ surface is down into the crystal, and upwards for a $+z$ surface. Consequently the application of a tip with a positive bias to a $-z$ face will cause an expansion of the crystal surface, while a $+z$ face will experience contraction. If the bias voltage is oscillating then a $-z$ surface will oscillate in phase, and a $+z$ will oscillate 180° out of phase with the driving voltage.

Based on these theoretical expectations, the phase response should give more information about the orientation of domains than the amplitude response. However, this assumes that the domains extend all the way through the crystal. This assumption is not necessarily valid for the UV-induced features that are under discussion, for instance the trenches formed on the $+z$ face were found to be ~1.8 μm deep (see Figure 4.11). If a domain does not extend through the entire depth of the crystal, then the signal detected by SFM will have contributions from both the surface and bulk domains. As the electric field decays rapidly away from the SFM tip, the relative importance of the surface and bulk contributions will depend largely on the surface domain depth. Figure 4.21 shows a possible situation where a small surface domain reduces the amplitude of the response from the bulk region but the phase of the combined signal remains unchanged.

The applied voltage used was 10 V (peak to peak) at frequencies between 35 - 38 kHz, and a cantilever with a large stiffness constant (14 - 20 N/m) was used, so that the scanning tip was more sensitive to the piezoelectric response than the electrostatic signal (Hu et al., 2002).

The results of SFM experiments presented here were obtained by Chris Valdivia and Collin Sones with the aid of Prof. V. Gopalan at Pennsylvania State University, USA

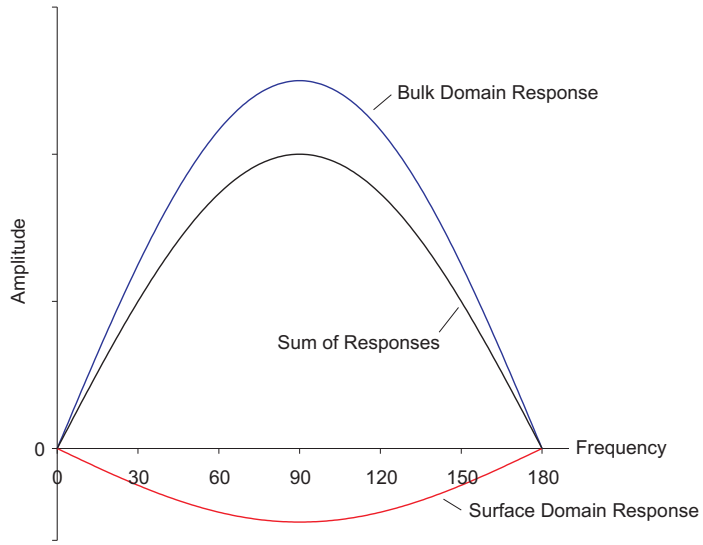

Figure 4.21: Illustration of the possible SFM piezo-response signal from a shallow surface domain combined with a large bulk domain of the opposite polarisation.

and Dr E. Soergel at the University of Bonn, Germany. Figure 4.22 shows a test SFM image of an electric-field surface-poled lithium niobate sample, which had surface domains ~10 μm deep. The oppositely orientated domains are clearly defined in both the piezo amplitude and phase response images. Evidently domains of this depth are sufficiently deep to effect the amplitude as well as the phase.

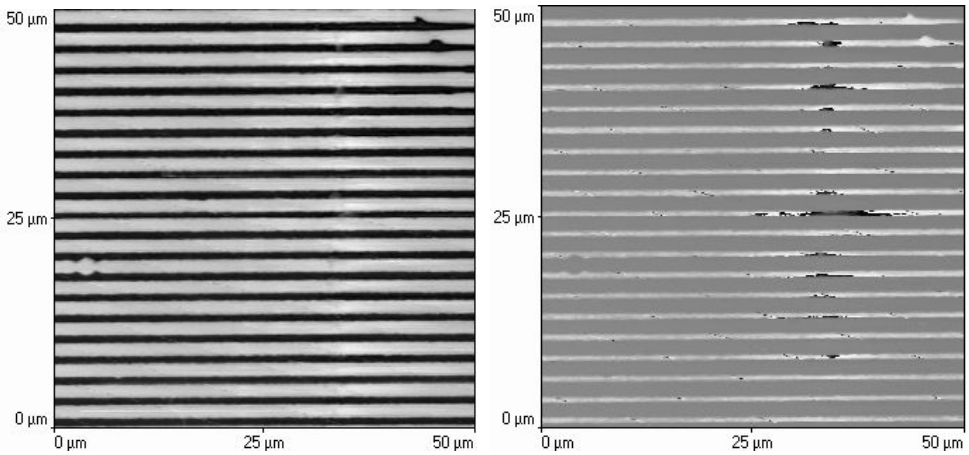

(a) Amplitude response image (b) Phase response image

Figure 4.22: SFM piezo-response of a surface-poled lithium niobate sample.

The SFM amplitude response to a $+z$ face of lithium niobate that had been exposed to 5 pulses of 298 nm wavelength UV light is shown in Figure 4.23. The sample had not been etched before being studied by SFM, so trenches were not visible by

optical or topographic examination, yet the patterns revealed are identical to those obtained by selective etching followed by SEM imaging (as shown in Figure 4.7). The phase-response images do not show any patterns related to the UV-induced features. This may be a consequence of their relatively shallow depth of ~1.8 μm. Fig. 4.23(a) was taken at the centre of a UV-exposed area, while Fig. 4.23(b) shows the edge of the exposed area; the features are only observed in the upper part of the image, where exposure had taken place.

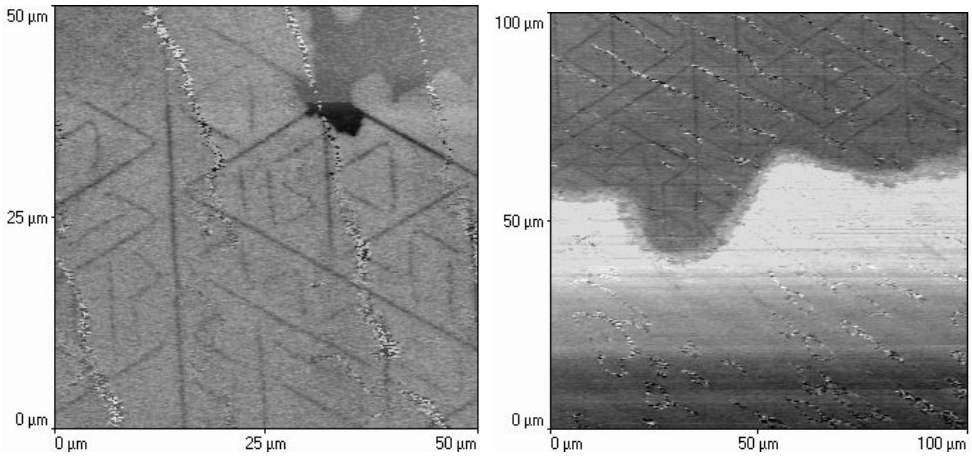

(a) Amplitude image of central region (b) Amplitude image of edge of site

Figure 4.23: SFM piezo-response of a $+z$ face exposed to 298 nm UV light (3 J cm^{-2}, 5 pulses).

Examination by SFM was also carried out on $-z$ face samples which had been prepared by exposure to pulsed UV light through a phase mask. The conditions were the same as for the samples shown in the SEM image in Fig. 4.17, which resulted in periodically arranged etch-resistant features. Figure 4.24 shows the SFM amplitude response to an *unetched* sample; again the resulting image is very similar to that obtained by etching and subsequent SEM imaging, and the periodicity of the dots is clear.

An interesting result was obtained when a voltage of approximately −100 V was applied through the SFM tip to a small 7×7 μm section of a UV-exposed area. The associated electric field caused domain-erasure, as confirmed by subsequent SFM imaging which showed an absence of dots in the central area. Figure 4.25(a) shows the SFM amplitude response to an area of the crystal surface with periodic domain inverted regions before domain erasure and Fig. 4.25(b) shows the same area, marked by a white box, after domain erasure. The relatively small voltage applied, much lower than the 11 kV required for traditional electric field poling of

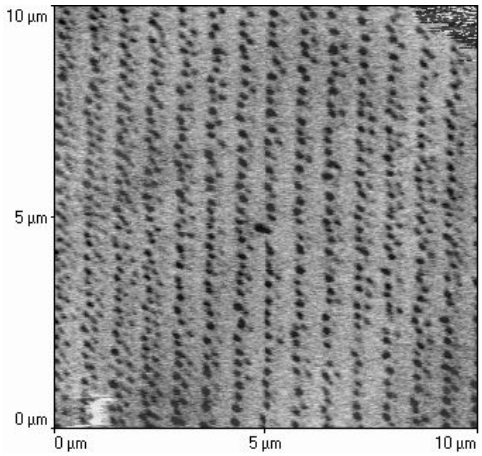

Figure 4.24: SFM piezo-response of an unetched $-z$ face exposed to pulsed UV light through a phase mask.

a bulk crystal, suggests that if the small features are domains, then they must be shallow, with depths of ~1 µm.

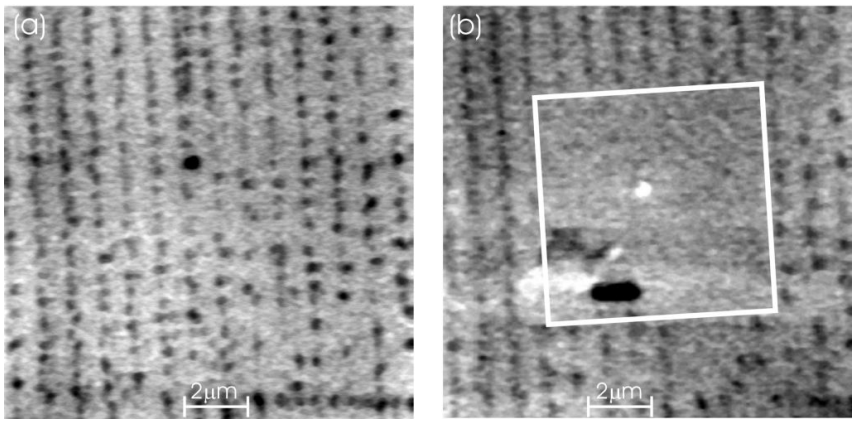

Figure 4.25: SFM images of the same area of a UV-exposed $-z$ face before (a) and after (b) domain erasure in the marked area by application of −100 V through the SFM tip.

SFM is a very useful technique for domain imaging, particularly for bulk domains. However some questions remain when it is applied to shallow surface domains, as might be the case for the UV-induced features discussed in this chapter. The problems are the lack of signal in the SFM phase response, which, in theory should be the definitive proof of the presence of domains. This could be a consequence of the shallow nature of the features being studied, resulting in the contribution from the bulk domain dominating the response from the surface domain, or could be an indication that the features are actually not domains. The amplitude response

images clearly show the UV-induced features, which in itself is a very useful capability as it does not require the destructive process of etching prior to imaging.

If the features are charge-related and not domains, then there is some uncertainty what their influence, if any, would be on the SFM. It is possible they would interfere with the piezoelectric response or the charged SFM tip sufficiently to also be detected in the amplitude image. Conversely, if the features were purely charge related, applying a charged SFM tip may simply remove the surface charges, but this does not appear to be the case.

It seems probable that the SFM results are genuinely showing micro-domains in both the $-z$ and $+z$ faces. In this case, light-induced charge generation is likely to be an important part of the mechanism which leads to domain formation. Morozovska et al. (2003) have produced a theory of micro-domain formation in ferroelectric photorefractive crystals, where photovoltaic currents lead to surface charge accumulation and subsequent microdomain formation.

4.5 Summary

Lithium niobate was exposed to pulsed UV radiation of wavelengths between 248 and 329 nm, on both the $+z$ and $-z$ faces. On the $+z$ face, acid etching of ablation areas revealed complicated patterns of trenches, which were 150 - 300 nm wide and approximately 1.8 μm deep. Scanning force microscopy was used to visualise these trenches without using an acid etch, thus showing they were created by the UV pulse.

Etch frustration was found to be possible following exposure of the $+z$ face, with a narrow range of fluences around 70 mJ cm^{-2}. Large areas of etch frustration could be achieved, consisting of micrometre-scale individual etch-resistant features. Phase and amplitude masks were used to pattern the light beam and hence control the etch frustration on the crystal surface.

4.6 References

Houe, M. and P. D. Townsend. "Thermal polarization reversal of lithium niobate." *Applied Physics Letters*, **66**(20), 2667 (1995).

Hu, G., T. Tang and J. Xu. "Tip effects of piezoelectric-mode atomic force microscope for local piezoelectric measurements of an $SrBi_2Ta_2O_9$ thin film." *Japanese Journal of Applied Physics*, **41**(11B), 6793 (2002).

Mailis, S., P. T. Brown, C. L. Sones, I. Zergioti and R. W. Eason. "Etch frustration in congruent lithium niobate single crystals induced by femtosecond ultraviolet laser irradiation." *Applied Physics A*, **74**, 135 (2001).

Mizuuchi, K., A. Morikawa, T. Sugita, K. Yamamoto, N. Pavel and T. Taira. "Continuous-wave ultraviolet generation at 354 nm in a periodically poled MgO : $LiNbO_3$ by frequency tripling of a diode end-pumped Nd : $GdVO_4$ microlaser." *Applied Physics Letters*, **85**(18), 3959 (2004).

Morozovska, A. N., E. A. Eliseev, V. V. Obukhovsky and V. V. Lemeshko. "Photo-microdomains in ferroelectrics: formation and light scattering caused by them." *Semiconductor Physics, Quantum Electronics and Optoelectronics*, **6**(3), 324 (2003).

Rosenman, G., R. Shur, Y. E. Krasik and A. Dunaevsky. "Electron emission from ferroelectrics." *Journal of Applied Physics*, **88**(11), 6109 (2000).

Rosenman, G., P. Urenski, A. Agronin, Y. Rosenwaks and M. Molotskii. "Submicron ferroelectric domain structures tailored by high-voltage scanning probe microscopy." *Applied Physics Letters*, **82**(1), 103 (2003).

Sones, C. L., S. Mailis, V. Apostolopoulos, I. E. Barry, C. Gawith, P. G. R. Smith and R. W. Eason. "Fabrication of piezoelectric micro-cantilevers in domain-engineered $LiNbO_3$ single crystals." *Journal of Micromechanics and Microengineering*, **12**(1), 53 (2002).

Sones, C. L., S. Mailis, W. S. Brocklesby, R. W. Eason and J. R. Owen. "Differential etch rates in z-cut $LiNbO_3$ for variable HF/HNO_3 concentrations." *Journal of Materials Chemistry*, **12**, 295 (2001).

Terabe, K., M. Nakamura, S. Takekawa, K. Kitamura, S. Higuchi, Y. Gotoh and Y. Cho. "Microscale to nanoscale ferroelectric domain and surface engineering of a near-stoichiometric $LiNbO_3$ crystal." *Applied Physics Letters*, **82**(3), 433 (2003).

CHAPTER

FIVE

Raman Spectroscopy of Recently Poled Lithium Niobate

Raman scattering was discovered by C.V. Raman in the early twentieth century, and since then has progressed to become a technique that is used in many areas of science and analysis of materials. It is an excellent way of studying lithium niobate, as it is fast, non-destructive and sensitive to small changes in the crystal structure that may occur, for instance, during the repoling process. When used with a microscope system it may also be used to examine micron-sized areas.

For these reasons micro-Raman spectroscopy was investigated as a potential method for studying domain structures produced by electric-field poling in lithium niobate. If it was found to be useful for these type of measurements, Raman spectroscopy could also be used to determine whether the structures formed during the LIFE experiments (Chapter 3) and UV exposures (Chapter 4) were in fact domain inverted regions.

5.1 Theory of Raman Scattering

In Raman spectroscopy, the quantised lattice vibration waves (phonons) of a crystal interact with photons from an incident laser beam. When an inelastic collision occurs, the photons are scattered after having either lost or gained energy from the

crystal. These two possible cases are named Stokes and anti-Stokes scattering, and are illustrated in Figure 5.1.

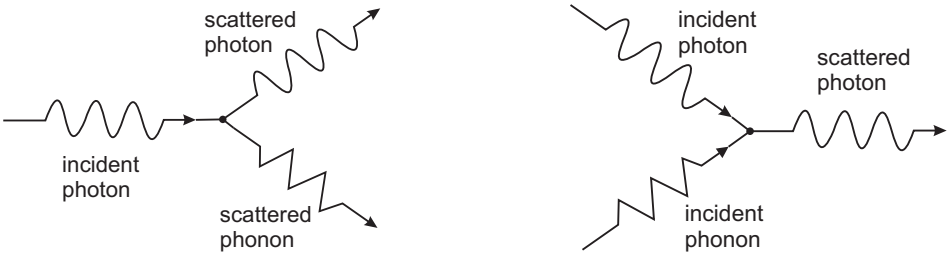

(a)Stokes:

- Phonon emitted
- Crystal gains energy
- Raman lines of lower frequency than incident light

(b)Anti-Stokes:

- Phonon absorbed
- Crystal loses energy
- Raman lines of higher frequency than incident light

Figure 5.1: Stokes and Anti-Stokes Raman Scattering

At room temperature, a crystal's ground state vibrational energy level will be more highly populated than those of the excited states, so the Stokes lines are usually of higher intensity than the anti-Stokes lines. This is evident in the Raman spectrum of CCl_4, shown in Figure 5.2. Therefore normally only the Stokes lines are recorded, so a typical Raman spectrum shows only frequencies lower than the frequency of the laser source. Each line in the spectrum represents a crystal phonon, which corresponds to a particular lattice vibration with a particular energy. This is given by the 'Raman shift' from the exciting wavelength, measured in wavenumbers (reciprocal centimetres). In the case of Stokes scattering, this is a negative number, but the minus sign is usually dropped.

A crystal consists of pN atoms, where p is the number of atoms in the crystal's primitive cell, and N is the total number of primitive cells. Each atom has three degrees of freedom (one for each direction along x, y, z), so the crystal will have $3pN$ degrees of freedom in total. As N is large, a crystal can have a very large number of different vibrations. However, a Raman spectrum will be relatively simple, as only the vibrations which occur in phase will be detected. Consequently, a crystal has only $3p$ branches to its dispersion relation (ω vs k). Of these branches, there will be $3p - 3$ optical phonon branches and 3 acoustic phonon branches (Kittel, 1996). Lithium niobate belongs to the C_{3v} point group, and the primitive cell contains two formula weights (10 atoms), which results in 3 acoustic branches and 27 optical branches of the dispersion relation.

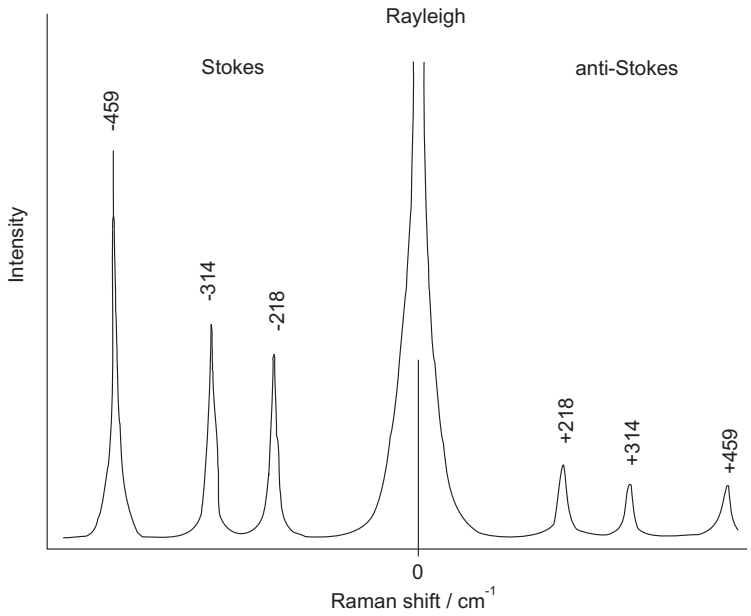

Figure 5.2: Raman spectrum of CCl_4, reproduced from Ferraro et al. (2003)

Acoustic phonons are of low frequency at small wavevectors, and the 3 modes comprise of one longitudinal acoustic (LA) mode and two transverse acoustic (TA) modes. When acoustic phonons are involved in Raman scattering this is termed 'Brillouin scattering'. The shifts that are observed in Brillouin scattering are approximately 1 cm^{-1}, small compared to the shifts of 10 cm^{-1} to 4000 cm^{-1} typically seen in Raman scattering (Hayes and Loudon, 1978).

Optical phonons are of higher frequency than acoustic phonons; because of this they were first detected by optical methods, which is why they are so-named. They can also be polarised as transverse optic (TO) and longitudinal optic (LO) modes (Kaganov, 1981). The correct term for optical phonon scattering is 'polariton scattering', although the generic term Raman scattering is more frequently used. A polariton is a quasi-particle consisting of a photon coupled to an exciton (which may be formed when an incident photon excites an electron in the crystal from the valence band to the conduction band, forming an electron-hole pair), plasmon or long-wavelength polar optical phonon (Claus et al., 1975). Consequently, a Raman effect can be caused by many types of excitation, but for the purposes of this document, it is Raman scattering from phonon-type polaritons that is of most importance. Bearing in mind the true nature of the scattering, we will consider the scattering as being from optical phonons.

Using group theory and the symmetry of the unit cell it is possible to calculate the symmetry of the phonons within a crystal, and hence which of these phonons will be Raman active. The irreducible representations of the vibrations with wavevector, **k**, near zero (close to the centre of the first Brillouin Zone where most Raman scattering occurs) are found to be (Repelin et al., 1999):

$$\Gamma_{optical} = 4A_1 + 5A_2 + 9E \tag{5.1}$$

$$\Gamma_{acoustic} = A_1 + E \tag{5.2}$$

The symbol A describes ionic motion along the polar axis and E represents modes which are doubly degenerate with motion perpendicular to the polar axis. Counting the doubly degenerate modes twice there are a total of 30 vibrations, as expected, with 3 acoustic and 27 optical modes. Not all of the phonons within a crystal will necessarily be Raman active, the classical theory of the Raman Effect explains why:

When a crystal experiences the electric field of electromagnetic radiation, the electrons are attracted to the positive pole of the field. This creates an induced dipole moment, and polarises the crystal. The size of the induced dipole, μ, will depend on the electric field, E, and the electronic polarisabilty, α, so:

$$\mu = \alpha E \tag{5.3}$$

The electric field oscillates as $$E = E_0 \cos(\omega t) \tag{5.4}$$

so the induced dipole will oscillate as $$\mu = \alpha E = \alpha E_0 cos(\omega t) \tag{5.5}$$

An oscillating dipole emits radiation of its own frequency, so the above formula gives the classical derivation of Rayleigh scattering, i.e. elastic scattering with no change in frequency.

However, if the polarisability associated with a phonon mode can be written as a power series of the phonon amplitude, u, then:

$$\alpha = \alpha_0 + \alpha_1 u + \alpha_2 u^2 + \ldots \tag{5.6}$$

where $u(t) = u_0 \cos(\Omega t)$, with Ω as the phonon frequency, then the induced dipole moment, μ, is (taking only α_0 and α_1 terms):

$$\begin{aligned}\mu &= \alpha E_0 \cos(\omega t) \\ \mu &\approx (\alpha_0 + a_1 u_0 \cos(\Omega t)) E_0 \cos(\omega t) \\ &\approx \alpha_0 E_0 \cos(\omega t) + \alpha_1 u_0 E_0 \cos(\Omega t) \cos(\omega t) \\ &\approx \alpha_0 E_0 \cos(\omega t) + \frac{1}{2}\alpha_1 u_0 E_0 \left(\cos\{(\omega + \Omega)t\} + \cos\{(\omega - \Omega)t\}\right)\end{aligned} \tag{5.7}$$

The oscillating dipole can then emit photons at frequencies ω, $(\omega + \Omega)$ and $(\omega - \Omega)$, corresponding to Rayleigh, anti-Stokes and Stokes scattering, respectively. However, for a phonon mode to be Raman active, it must cause a change in a component of the electronic polarisability; this is the Raman selection rule (Ferraro et al., 2003).

As Raman scattering is a quantum process, there are a few other conditions that also need to be satisfied. Because phonons are only 'quasi-particles', their propagation is not associated with mass transport, as they do not have real momentum. Instead the quantity $\hbar\mathbf{k}$ is known as 'quasi-momentum', and needs to be conserved like real momentum, as in an inelastic collision with a photon:

$$\hbar\mathbf{k_i} = \hbar\mathbf{k_s} \pm \hbar\mathbf{k_p} \tag{5.8}$$

hence

$$\mathbf{k_i} = \mathbf{k_s} \pm \mathbf{k_p} \tag{5.9}$$

where $\mathbf{k_i}$, $\mathbf{k_s}$ and $\mathbf{k_p}$ are the wave-vectors of the incident and scattered photons and the phonon, respectively. Energy conservation also requires that

$$\omega_i = \omega_s \pm \omega_p \tag{5.10}$$

where ω_i, ω_s and ω_p are the angular frequencies of the incident and scattered photons and the phonon, respectively.

Returning to the concept of the Raman selection rule, only the A_1 and E modes cause a change in a component of the electronic polarisability, as shown by the C_{3v} group character table in Table 5.1 (only A_1 and E have the Cartesian coordinates of

x, y or z). Consequently only these phonons are Raman (and also infrared) active. Lithium niobate therefore has a theoretical maximum of 13 Raman peaks, from the 4 A_1 and 9 E optical phonons.

Table 5.1: Character Table for the C_{3v} Group

C_{3v}	E	$2C_3$	$3\sigma_v$	linear functions	quadratic functions
A_1	1	1	1	z	$x^2 + y^2, z^2$
A_2	1	1	-1	R_z	
E	2	-1	0	$(x, y)(R_x, R_y)$	$(x^2 - y^2, xy)(xz, yz)$

However, for phonons in ionic crystals which are infrared (IR) active (as defined by the infrared selection rule; a mode will be IR active if the vibration produces a change in the electric dipole) the long range electric field lifts the degeneracy of longitudinal (LO) and transverse (TO) phonons (Parlinski and Li, 2000). In the case of $LiNbO_3$ all the Raman modes are also IR active, which results in a doubling of the number of phonons that may be observed, up to 26 peaks, as each Raman active phonon has (TO) and (LO) modes. In total there will be 9 E(TO), 9 E(LO), 4 A_1(TO) and 4 A_1(LO) phonons.

The number of Raman peaks which can be observed depends on the relative orientation of the crystal and the light detected by the Raman spectrometer, and the polarisation of the light. A notation of the type A(BC)D has been developed by Damen et al. (1966) to specify the orientation used, where:

A: Direction of **k**-vector of incident exciting light.

B: Polarisation of the incident light.

C: Polarisation of scattered light detected.

D: Direction of **k**-vector of detected scattered light.

A situation described as X(YZ)Y would correspond to light incident on the x face of a crystal, polarised along the y axis. The detected light has polarisation along the z direction, exiting from the y face of the crystal (i.e. at 90° to the incoming light, a common configuration used so the signal is not overwhelmed by the exciting laser light).

Group theory can also be used to predict which of the phonons may be detected with a particular experimental configuration. This subject has been reviewed by Loudon (1964). The principle used is that a phonon can only participate in a first order Raman transition if its irreducible representation (i.e. A_1, A_2 or E for

lithium niobate) matches one of the irreducible representations which occurs in the reduction of the representation of the polarisablilty tensor. For uniaxial crystals, such as lithium niobate, Loudon gives the Raman scattering efficiency as:

$$S = \left[\sum_{\rho,\sigma,\tau=x,y,z} e_i^{\sigma} R_{\sigma\rho}^{\tau} \left(\alpha\zeta^{\tau} + \beta k^{\tau} \right) e_s^{\rho} \right]^2 \tag{5.11}$$

where e_i and e_s are components of the polarisation unit vectors for the incident and scattered light, respectively, along the principal axes σ and ρ. ζ and k are unit vector components of the phonon polarization and propagation direction, while α is a constant, and β is proportional to the electric field strength. In uniaxial crystals β is always zero for transverse phonons. Finally, R^{τ} represents the components of the Raman tensor. For the C_{3v} point group, the matrices of the non-vanishing components of the Raman tensor, again from Loudon (1964), are :

$$\begin{aligned} R[E(-x)] &= \begin{pmatrix} 0 & -c & -d \\ -c & 0 & 0 \\ -d & 0 & 0 \end{pmatrix} \\ R[E(y)] &= \begin{pmatrix} c & 0 & 0 \\ 0 & -c & d \\ 0 & d & 0 \end{pmatrix} \\ R[A_1(z)] &= \begin{pmatrix} a & 0 & 0 \\ 0 & a & 0 \\ 0 & 0 & b \end{pmatrix} \end{aligned} \tag{5.12}$$

The $-x$, y and z in brackets, after the irreducible representation, indicate the polarisation direction of the phonon. The letters a, b, c, and d are related to the scattering intensities, and are dependent on the bond lengths within the crystal.

The Raman tensor matrices are used to deduce which phonons will be detected by a particular experimental configuration. If multiplication of the matrix by the light polarisation vectors gives a non-zero answer, then phonons of that symmetry may be detected. For instance, to see whether a X(ZZ)Y configuration may detect A_1

phonons, the scattering efficiency is determined:

$$S(z[A_1(z)]z) \propto \left[e_i^{\sigma} R_{\sigma\rho}^{\tau} e_s^{\rho}\right]^2 \tag{5.13}$$

$$\propto \left[\begin{pmatrix} 0 & 0 & 1 \end{pmatrix} \begin{pmatrix} a & 0 & 0 \\ 0 & a & 0 \\ 0 & 0 & b \end{pmatrix} \begin{pmatrix} 0 \\ 0 \\ 1 \end{pmatrix} \right] \propto b^2 \tag{5.14}$$

As the result is 'b^2', the A_1 phonons would be detected. Note that the direction of the incident and scattered light has not been considered yet. The same orientation cannot be used to detect E phonons of any polarisation, i.e.:

$$S(z[E(y)]z) \propto \left[\begin{pmatrix} 0 & 0 & 1 \end{pmatrix} \begin{pmatrix} c & 0 & 0 \\ 0 & -c & d \\ 0 & d & 0 \end{pmatrix} \begin{pmatrix} 0 \\ 0 \\ 1 \end{pmatrix} \right]^2 = 0 \tag{5.15}$$

$$S(z[E(-x)]z) \propto \left[\begin{pmatrix} 0 & 0 & 1 \end{pmatrix} \begin{pmatrix} 0 & -c & -d \\ -c & 0 & 0 \\ -d & 0 & 0 \end{pmatrix} \begin{pmatrix} 0 \\ 0 \\ 1 \end{pmatrix} \right]^2 = 0 \tag{5.16}$$

All of the possible combinations of the configuration and symmetry of phonons are listed in Table 5.2, with the non-zero results highlighted in bold-type.

Table 5.2: Summary of phonons which may be detected with a particular configuration of polarisation of light in a Raman experiment

Phonon Symmetry	Input Polarisation[Raman Tensor]Output Polarisation		
$A_1(z)$	**X [$A_1(z)$] X = a**	Y [$A_1(z)$] X = 0	Z [$A_1(z)$] X = 0
	X [$A_1(z)$] Y = 0	**Y [$A_1(z)$] Y = a**	Z [$A_1(z)$] Y = 0
	X [$A_1(z)$] Z = 0	Y [$A_1(z)$] Z = 0	**Z [$A_1(z)$] Z = b**
$E(y)$	**X [$E(y)$] X = c**	Y [$E(y)$] X = 0	Z [$E(y)$] X = 0
	X [$E(y)$] Y = 0	**Y [$E(y)$] Y = −c**	**Z [$E(y)$] Y = d**
	X [$E(y)$] Z = 0	**Y [$E(y)$] Z = −d**	Z [$E(y)$] Z = 0
$E(-x)$	X [$E(-x)$] X = 0	**Y [$E(-x)$] X = −c**	**Z [$E(-x)$] X = −d**
	X [$E(-x)$] Y = −c	Y [$E(-x)$] Y = 0	Z [$E(-x)$] Y = 0
	X [$E(-x)$] Z = −d	Y [$E(-x)$] Z = 0	Z [$E(-x)$] Z = 0

Thus it is possible to say, judging from the polarisation of the incident and scattered light whether a phonon of a particular symmetry may be detected. However, more information is required to determine whether these phonons are of transverse (TO) or longitudinal (LO) nature. To do this, we need to consider the principle of conservation of momentum, and consequently wave-vector, using equation (5.9).

Taking an example, Schaufele and Weber (1966) report that using a scattering configuration of Y(ZZ)X only transverse phonons with A_1 symmetry may be detected. Looking up 'ZZ' in Table 5.2, we see that indeed only A_1 phonons (polarised in the z direction) should be detected, but this gives no indication as to whether these phonons are longitudinal or transverse. Figure 5.3 shows the scattering diagram for this configuration.

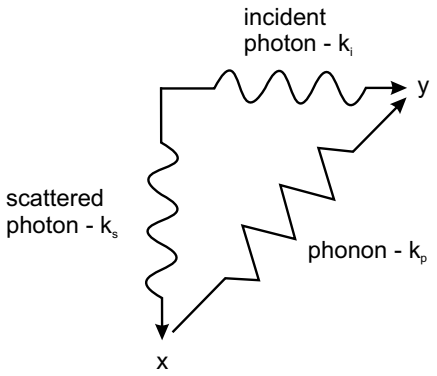

Figure 5.3: Scattering Diagram, showing conservation of momentum. Light is incident along the y axis, with detected light that is scattered along x.

This shows that the phonon wavevector is propagating in the xy plane. We then need to consider the polarisation of the photons and phonon, which are shown by small crosses in Figure 5.4, representing polarisation in the z plane. From the Raman tensor we know that the polarisation of the A_1 phonon is polarised along the z direction, so the only possible polarisation is that shown in Figure 5.4, which is perpendicular to the phonon propagation direction, hence the phonon mode is a transverse A_1(TO). Longitudinal modes cannot be detected with this geometry.

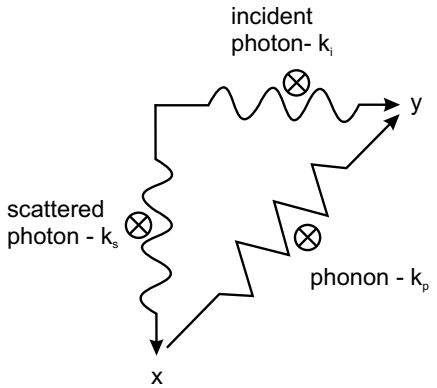

Figure 5.4: Scattering Diagram for the Y(ZZ)X configuration - A_1(TO) only detected

Another example, from Ridah et al. (1997) is that purely transverse E(TO) modes will be detected in the X(ZY)Z configuration, but using X(YZ)Y allows both transverse and longitudinal modes to be observed. These situations are illustrated in Figure 5.5.

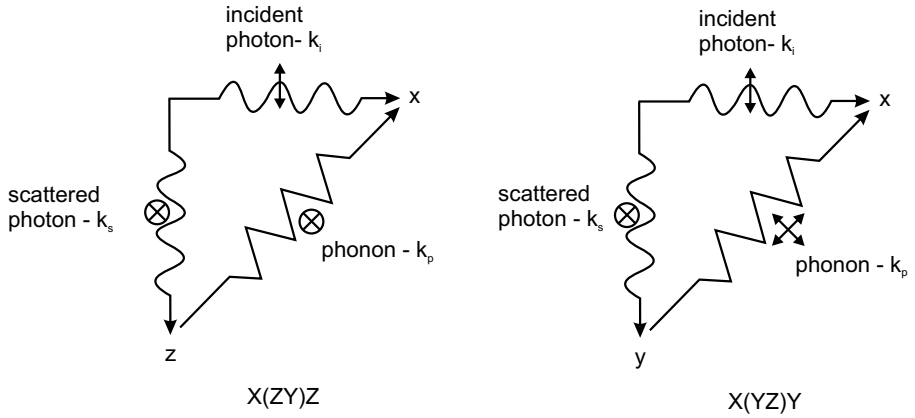

Figure 5.5: Scattering Diagram for the X(ZY)Z and X(YZ)Y configurations

After again referring to Table 5.2, only the E(y) phonons (polarised along the y axis) will be detected in both of the scattering configurations. In the case of X(ZY)Z, the phonon polarisation can only be along the y direction, perpendicular to the propagation direction, i.e. resulting in transverse phonons. It cannot be polarised any other way, as that would involve a component along the z axis, which is forbidden (no E vibrations can have polarisation in the z direction (Scott and Porto, 1967). For the X(YZ)Y geometry, this is not a problem and the phonon can be polarised in one of two directions, which are parallel and perpendicular to the direction of **k**. Thus, both transverse E(TO) and longitudinal E(LO) phonons may be detected.

In the next section, some new experimental Raman results are reported, taken on recently repoled lithium niobate. The experiments were carried out using a Raman microscope, which by its nature has a back-scattering geometry. The crystal was positioned so the incident light was polarised along the y axis, and a polariser was used to select the scattered light also polarised parallel to y axis. This results in a scattering configuration of Z(YY)Z. Using the group theoretical and momentum conserving methods mentioned, it is possible to determine which phonons may be observed.

The incident and scattered polarisations are (YY), which means the $A_1(z)$ and E(y) modes will be active. Figure 5.6 shows the scattering configuration. The E phonons can only be polarised along the y direction, making them transverse (TO) and the A_1 phonons are polarised along z, parallel to the direction of propagation, so are

longitudinal (LO). This proves that for the Z(YY)Z configuration in lithium niobate only the E(TO) and A_1(LO) phonon modes may be active. This is in agreement with advice I have received from Professor Marc Fontana of the University of Metz, France (private communication).

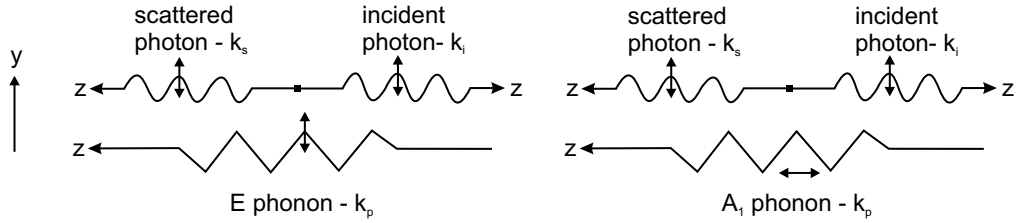

Figure 5.6: The Z(YY)Z scattering geometry for E and A_1 phonons

The frequencies of all the possible phonons that may be observed in lithium niobate by Raman spectroscopy still appear to be a source of controversy. Schaufele and Weber (1966) were the first authors to report the Raman spectrum of lithium niobate. However, they only reported the frequencies of 10 transverse modes. Further studies were soon carried out, by Barker and Loudon (1967), Kaminow and Johnston (1967) and others. However, none of these carry a definitive list of the phonon frequencies, and are often contradictory.

It is the E phonons that proved to be particularly hard to assign, however Ridah et al. (1997) have published a list of frequencies of the E(LO) and E(TO) phonons that appears to be widely accepted. The number of phonons also corresponds to that which is expected from the group theory arguments. Part of the problem in reaching this assignment was that some of the modes do not appear in the spectrum of congruent lithium niobate and are only apparent in the stoichiometric material, which has only become available relatively recently. Ridah used stoichiometric lithium niobate to help his assignments. Other phonon frequencies, of low intensity, had been previously reported, but Ridah did not include these in his results, on the basis that they were not true first-order Raman peaks and were either a result of intrinsic crystal defects or were due to two-phonon interactions.

However, even Ridah's version is incomplete, as no mention is made of longitudinal A_1(LO) phonons at all and only a brief reference is made to the transverse A_1(TO) modes. This seems to be a feature in common with many other papers in this field. By compiling results from two sources (Ridah et al., 1997; Kaminow and Johnston, 1967), which are mostly in agreement with each other, a definitive list of the phonons which may be detected by Raman spectroscopy of lithium niobate is shown in Table 5.3.

Table 5.3: All possible phonons which may be appear in the Raman spectrum of lithium niobate. * denotes phonons that only appear in stoichiometric crystals.

E(TO) / cm^{-1}	E(LO) / cm^{-1}	A_1(TO) / cm^{-1}	A_1(LO) / cm^{-1}
153	187	252	273
177*	195	276	331
238	240	333	428
264	299	633	874
322	345*		
370	424		
432	456		
580	625*		
610*	878		

An accurate list of phonon frequencies allows assignment of Raman peaks to particular phonons, and can then be used as a check when comparing results with what was expected from the basis of group theory. The width of particular peaks can also be used as a measure of the composition of the crystal (Ridah et al., 1997). Recently, authors such as Caciuc et al. (2000) have calculated the phonon frequencies from first principles, using the atomic displacements of each phonon mode. This means it is possible to visualise the movement of atoms within each lattice vibrational wave, and so perhaps to be able to understand the implication of a change in frequency of a particular phonon. For instance, the $A_1(TO_2)$ phonon was found to be "essentially the z-vibration of Li ions with respect to the (relatively rigid) rest of the crystal".

5.2 Experimental Details

All Raman spectra were taken using a Renishaw Raman microscope, model RM2000, equipped with a 1 mW He-Ne laser operating at 633 nm. The first stage of the experiment was to take four independent Raman spectra at four locations on a virgin *z*-cut congruent $LiNbO_3$ crystal. The crystal was then removed from the spectrometer and a small area was repoled, using a standard electric-field technique (see Section 2.4.1 for details). The sample was immediately returned to the Raman microscope for acquisition of repeated scans over periods of several hours.

The Raman spectrum was collected using a Z(YY)Z orientation (180° back scattering collection), determined by the configuration of the instrument used. The polarisation of the incident light was determined by the polarisation of the laser,

whilst the polarisation of the scattered light was selected using a combination of a polariser and a half-wave plate.

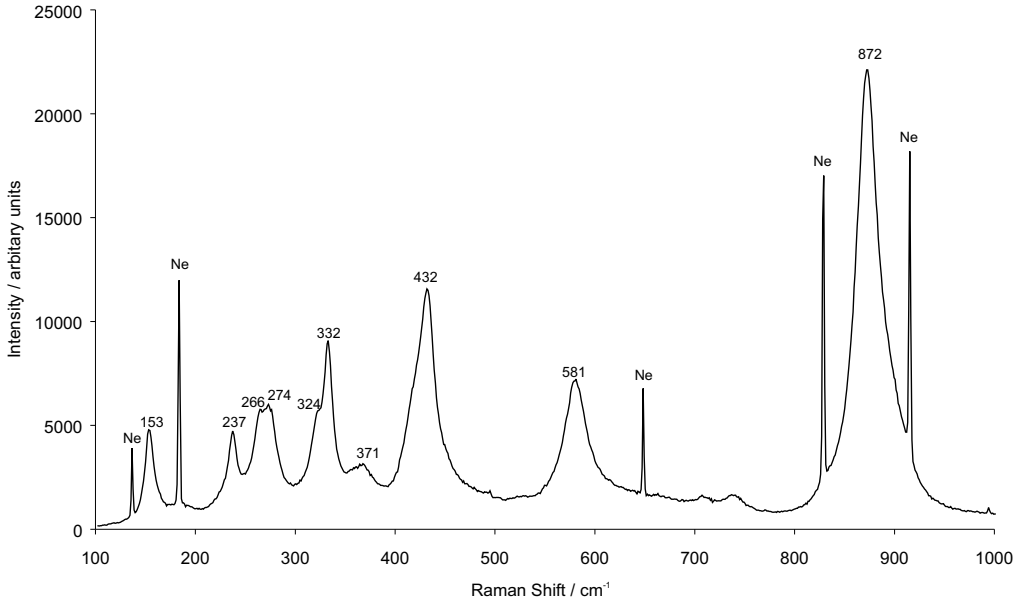

Figure 5.7: A typical $LiNbO_3$ Raman spectrum, collected using the Z(YY)Z geometry. The sharp peaks marked with 'Ne' are neon calibration lines.

A typical Raman spectrum of lithium niobate is shown in Figure 5.7. Ten Raman peaks can be distinguished using the Z(YY)Z orientation. With reference to the previous section, we would expect to see nine E(TO) and four A_1(LO) phonons, a total of thirteen peaks. The discrepancy is explained by discounting the two phonons which only appear in stoichiometric lithium niobate and noticing the 433 cm^{-1} peak is not symmetric, so the 424 cm^{-1} phonon is also contributing to that peak, although it can not be individually resolved. The Raman shift frequencies that are detected are summarised in Table 5.4 and compared to results from the literature (Ridah et al., 1997; Kaminow and Johnston, 1967). From this we can determine which phonon is responsible for a particular peak.

Small changes in the positions of several Raman peaks in the repoled sample were observed compared to the virgin material. To ensure the highest degree of accuracy and consistency possible, two methods of calibration were used. The first was the standard procedure of using a spectrum of a test sample (silicon) with a well known and defined peak at 520 cm^{-1}, which was used to calibrate the scale of the spectrometer at the start of the experiment.

However, as it was possible that some drift of the calibration of the Raman spectrometer could occur (due to temperature variations within the lab) over the

Table 5.4: Summary of Raman peaks from the Z(YY)Z configuration, and the corresponding phonons

Experimentally Detected Peak / cm^{-1}	Peaks reported in the literature / cm^{-1}	Phonon
154	153	$E(TO_1)$
-	177 (stoichiometric only)	$E(TO_2)$
237	238	$E(TO_3)$
266	264	$E(TO_4)$
324	322	$E(TO_5)$
371	370	$E(TO_6)$
432	432	$E(TO_7)$
582	580	$E(TO_8)$
-	610 (stoichiometric only)	$E(TO_9)$
274	273	$A_1(LO_1)$
333	331	$A_1(LO_2)$
(obscured)	428	$A_1(LO_3)$
873	874	$A_1(LO_4)$

several hours required to take the measurements, a second calibration was used, with light from a neon source guided into the spectrometer, to provide calibration marks recorded on to each spectrum. A fibre-optic launch was used to ensure reproducible and steady conditions for the neon light. Several atomic emission lines occur at a convenient frequency for this purpose. Six neon lines were used, with wavelengths as shown in Table 5.5, taken from Lide (1994). The wavelengths of the neon emission lines were converted to a wavenumber shift from the wavelength of the exciting helium-neon laser radiation at 632.8 nm. The neon lines are the sharp peaks that appear in the Raman spectrum shown in Figure 5.7, and are denoted with 'Ne'. The source was switched off whilst the central part of the spectrum was acquired, as the neon line at 650 nm coincides with the Raman peak at 433 cm^{-1}.

Table 5.5: Neon Emission Lines (* = relative to He-Ne laser wavelength, 632.817 nm)

Wavelength in air / nm	Absolute Frequency / cm^{-1}	Relative Frequency* / cm^{-1}
638.299	15666.63	135.73
640.225	15619.52	182.85
650.653	15369.18	433.19
659.895	15153.92	648.45
667.828	14973.92	828.44
671.704	14887.50	914.87

The Renishaw Raman spectrometer used in this work has a frequency resolution of ∼1 cm^{-1}. As some of the changes in peak positions after poling are relatively small (around 0.6 cm^{-1}), the data from the complete Raman spectrum is taken and separated into parts that correspond to the individual peaks. A Lorentzian curve is then fitted to the data, according to the equation

$$y = y_0 + \frac{a}{1 + \left(\frac{x - x_0}{b}\right)^2} \tag{5.17}$$

from which a more accurate peak centre, x_0, can be determined. The result of the curve fitting is shown in Figure 5.8. This procedure was applied to the neon peaks as well as the Raman peaks for lithium niobate, further increasing the precision of the calibration procedure. For each Ne peak 30 separate measurements and subsequent Lorentzian best fits were performed, yielding an average value of standard deviation of 0.027 cm^{-1}.

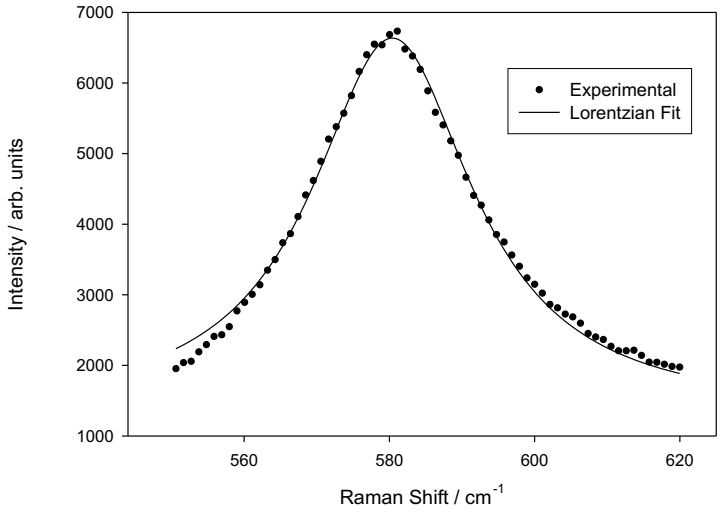

Figure 5.8: Lorentzian fit to a single Raman peak.

5.3 Results

A virgin crystal of z-cut congruent lithium niobate, with dimensions of 2 cm (x direction) by 3 cm (y direction) by 300 μm (z direction), was used as the test sample. Before poling, four independent Raman spectra were taken, in two different locations on the $-z$ face of the crystal, to establish the precise positions of the Raman

peaks of the virgin material. Domain inversion was then induced in a 7 mm by 3 mm area of the sample, using a voltage of 7.2 kV, a current of 500 μA and a charge of 39.3 μC. The sample was then returned to the Raman spectrometer, and spectra were acquired approximately every 8 min, for a period of 4 h.

Six representative Raman peaks, at 153, 237, 432, 581 cm^{-1} (E(TO)) and 332, 872 cm^{-1} (A_1(LO)) with uniform shapes most suitable for fitting to a Lorentzian profile were chosen for calibration and analysis following the experiments. The fitted Lorentzian curve gave an accurate value for the centre of the peak, as recorded by the spectrometer. This value was then corrected using the difference in the measured position from the reference value of the corresponding neon emission line.

Figure 5.9 shows the results for the calibrated peak positions for these six Raman bands, before and after poling. It is clear in all cases that there is a definite shift in peak position following repoling. Some of the bands (at 153, 237, 581 and 872 cm^{-1}, Fig. 5.9(a), (b), (e) and (f)) show a shift to a lower value of wavenumber, whereas the peaks at 332 and 432 cm^{-1} (Figs. 5.9(c) and (d)) show a shift in the opposite sense, to a higher wavenumber. The peaks at 153, 237 and 432 cm^{-1} experience a subsequent recovery towards their original position, while the 332 and 581 cm^{-1} peaks seem to recover, but not to their original value. Figure 5.9(e) representing the 872 cm^{-1} peak shows the largest shift of ~0.6 cm^{-1}, but no recovery process is apparent over the four hours of measurement. Included in each figure is a dashed line which is the average value of peak position for the four measurements on the virgin material before repoling.

The solid line in Figs. 5.9(a) and (d) represents a least squares regression performed to produce an exponential curve fit to the data. A standard exponential decay curve was fitted to the peak at 432 cm^{-1}, while all the 153 cm^{-1} peak was fitted to an exponential rise to maximum curve. The equations used were:

$$\text{Exponential decay:} \qquad y = y_0 + a\exp(-t/\tau) \tag{5.18}$$

$$\text{Exponential rise to maximum:} \qquad y = y_0 + a(1 - \exp(-t/\tau)) \tag{5.19}$$

For the exponential decay curve, y_0 is the average value of peak position before poling and τ is the time constant that corresponds to the time, t, when y (the peak centre) has returned to 1/e of its original value, y_0. The parameters a and τ are determined by the least-squares fitting process.

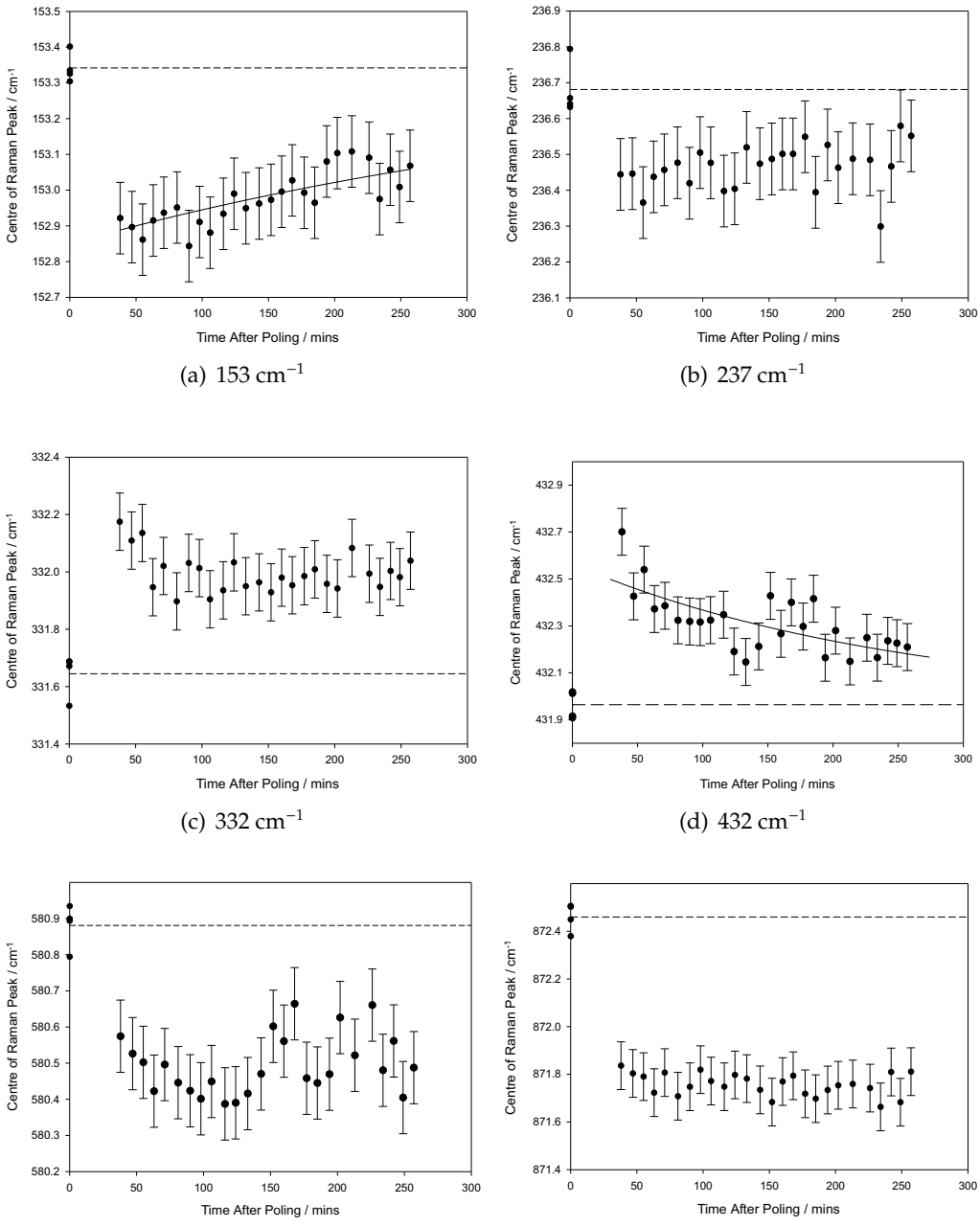

(a) 153 cm^{-1} (b) 237 cm^{-1}

(c) 332 cm^{-1} (d) 432 cm^{-1}

(e) 581 cm^{-1} (f) 872 cm^{-1}

Figure 5.9: Measured positions of the peaks for the six Raman lines of $LiNbO_3$, before and after repoling. Dashed lines represent the peak centre for the virgin material.

The exponential rise to maximum curve is similar, but inverted to allow the peak position to increase so that it recovers to the value taken before poling. The y-intercept, y_0, is estimated using a linear extrapolation and the a parameter was chosen so that $(y_0 + a)$, is equal to the mean peak centre value, the maximum in the curve. The least squares regression provides the time constant τ.

The data shown in Figure 5.9(a) and (d) is replotted in Figure 5.10(a) and (b), with the exponential curves extrapolated to longer times after poling, to show clearly the recovery process by which these two Raman bands return to their original position following repoling. The time constant for these curves (equivalent to the 1/e recovery time) is 476 minutes for the 153 cm^{-1} peak and 250 minutes for the 432 cm^{-1} peak. Each Raman peak appears to have its own recovery time, with the 432 cm^{-1} band being the fastest and the 872 cm^{-1} band the slowest, if indeed it does show any recovery process at all. The data from the curves shown in Figure 5.9(a)–(f) is summarised in Table 5.6.

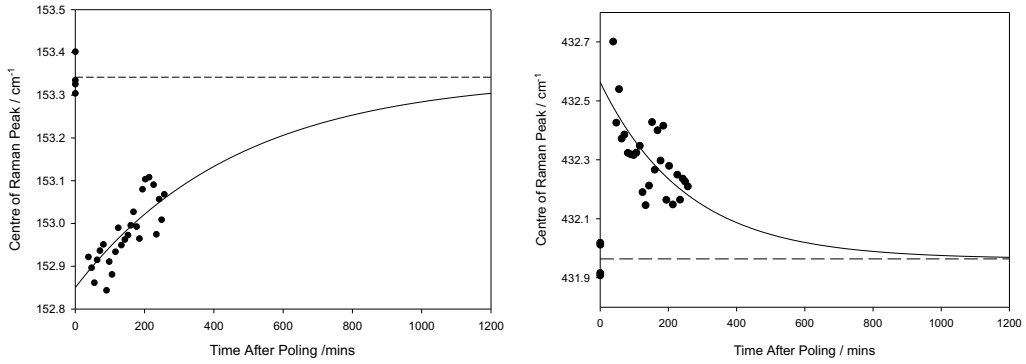

(a) 153 cm^{-1} (b) 432 cm^{-1}

Figure 5.10: Exponential fits to the Raman lines at 153 cm^{-1} and 432 cm^{-1} showing the time constant for recovery.

Table 5.6: Summary of results and parameters from fitting of exponential curves to the data

Raman peak (cm^{-1})	Peak centre before poling (cm^{-1})	Peak centre after poling (cm^{-1})	Difference (cm^{-1})	% change	y_0 (cm^{-1})	a (cm^{-1})	τ (min)
153	153.34	152.90	-0.44	-0.29	152.85	0.492	476
237	236.68	236.42	-0.26	-0.11	-	-	-
332	331.65	332.09	0.45	0.13	-	-	-
432	431.96	432.51	0.55	0.13	431.96	0.5994	250
581	580.88	580.51	-0.37	-0.06	-	-	-
872	872.46	871.79	-0.67	-0.08	-	-	-

5.4 Discussion

We believe this is the first report of evidence that there is a dynamic recovery process that occurs in recently repoled lithium niobate, which can be tracked and measured using Raman spectroscopy. We have seen a previous report of the use of micro-Raman for such a measurement (Laubacher et al., 2000), but this only discloses that there is a shift of several tenths of a wavenumber for a single (unspecified) line, and does not discuss details of any recovery processes for example. Laubacher et al. further suggest that the shift observed is likely to be due to either stress or inequivalence of electric-field poled domains compared to natural poling. No additional details were provided on the time delay between repoling and measuring the small Raman shifts observed.

Following publication of our results (Scott et al., 2004), another group published a paper describing the investigation of domain walls in periodically poled lithium niobate (PPLN) using Raman spectrum mapping (Kong et al., 2004). They scanned across several PPLN periods and reported that Raman lines at 152, 580 and 873 cm^{-1} showed a periodic *increase* of between 0.5 cm^{-1} and 1.5 cm^{-1} with the same period as the PPLN (no mention of any recovery was made). This change is of a similar magnitude as was observed in our experiments, except that we detected a *decrease* in the Raman shift. This difference occurs because we were studying a $-z$ face which had been repoled to become $+z$, whereas Kong et al. studied what had been a $+z$ face prior to electric field repoling. Hence a 'new' $+z$ face has a lower Raman shift , while a 'new' $-z$ face has a greater Raman shift for these three lines. This is not solely due to an inherent difference between $+z$ and $-z$ faces; Kong et al. reported that there was no change in Raman shift between the two z faces of a virgin crystal, which was in agreement with our experiments.

The question then remains of what causes the change in Raman shift. Kong et al. propose a mechanism based on the domain walls between neighbouring domains, and the associated electric fields and stresses which distort the crystal lattice. They suggest that on one side of a domain, Nb^{5+} ions will be closer to neighbouring Nb^{5+} ions, which are on the other side of the domain wall, than at the other side of the domain.

This explanation, while interesting, seems unlikely when applied to the results of our experiments. The period of the PPLN Kong et al. used was 22 μm, so each domain was relatively narrow, hence the influence of the domain wall may be sufficient to affect the Raman shift all the way across the domain. However, in

our experiments, the domain inverted area was about 7 mm by 3 mm, significantly larger than in Kong's work. Thus it seems unlikely that the domain wall would influence the Raman spectra taken in the centre of the domain, relatively far from the edge of the domain.

The internal field in lithium niobate is well known (Gopalan and Gupta, 1997; Ro et al., 1999), and is described in detail in Section 2.3.8. It is not thought to be a real, measurable electric field, but instead describes the difference in the coercive field required to pole a crystal in the forward direction compared to the reverse direction (back poling). The internal field is thought to be caused by a defect complex of an antisite niobium ion (a Nb ion occupying a Li site, $(Nb_{Li})^{4+}$) and four lithium vacancies $(v_{Li})^{-}$ (Yatsenko et al., 1997; Kim et al., 2001), see Section 2.3.8. After a sufficient period of time, the internal field recovers and realigns along the new direction of spontaneous polarisation. The presence of defects extends throughout congruent lithium niobate crystals, and antisite ions would certainly affect the phonons which are detected by Raman scattering and hence could be responsible for the shifts that we observe.

The six Raman peaks that were studied arise from both E(TO) and A_1(LO) phonon modes. Using the results from Caciuc et al. (2000), the ionic movement responsible for each mode can be deduced. In the E modes, the vibrations of the Nb and Li ions are restricted to the x and y planes, while in the A_1 modes the metal ions can only move along the z axis. A summary of each phonon mode is given in Table 5.7, below:

Table 5.7: Selected phonon modes in lithium niobate.

Frequency	Mode	Description
153 cm^{-1}	$E(TO)_1$	Movement of Nb and O ions only; deformation of Nb-O framework.
237 cm^{-1}	$E(TO)_3$	Movement of all ions
332 cm^{-1}	$A_1(LO)_2$	Vibration of Li ions in antiphase to Nb ions, no O ion movement.
432 cm^{-1}	$E(TO)_7$	Movement of all ions, with large Li displacement
581 cm^{-1}	$E(TO)_8$	Movement of all ions
872 cm^{-1}	$A_1(LO)_4$	O ion movement only; Torsion of individual octahedra

Perhaps the most interesting point arising from our own measurements concerns the differences in deduced recovery times for the five lines we have studied. It is clear for example that the line at 872 cm^{-1} has not recovered during the four hour period of our measurements, while the line at 432 cm^{-1} has made a substantial recovery

having a $1/e$ relaxation time of 250 minutes. This is consistent with previous papers that have examined the multistep electronic and ionic relaxation processes that can occur in both lithium niobate and lithium tantalate, following electric field repoling. Time constants have been observed for the recovery of the internal field for example that vary from 55 ms (Ro and Cha, 2000), following repoling in the forward direction, through several days (Gopalan and Gupta, 1997), to being incomplete even after a month (Gopalan and Mitchell, 1998). Previous authors have used multiple single exponential fits to these processes as well as stretched exponentials (Ro and Cha, 2000). It is clear that the recovery of the internal field is mediated by two, and possibly three, separate relaxation processes, which are of electronic and ionic origins respectively. The longer time constants observed here are consistent with the ionic recovery process as probed by Raman spectroscopy, and themselves show a variation of time constants in the range of several hours and above. Our data is not of sufficiently accuracy in the present study however to attempt anything other than the fitting of a simple single exponential fit.

It is possible that the Raman laser light could influence the results that were obtained, as a 1 mW beam focused to a spot size of 25 μm has a power density of 160 W cm^{-2}. Most of this is either transmitted through or reflected from the sample, but some may be absorbed leading to light induced heating or light generated charges. However, none of the Raman peaks measured before poling showed any change in their positions, despite exposure to light, so the laser light is unlikely to be the cause of the measured change in peak positions following poling. However, it could influence the rate of recovery of Raman peaks, this possibility could be examined as future work by varying the laser power and measuring the time constants.

5.5 Summary

Raman spectroscopy was used to study the positions of six representative Raman peaks of lithium niobate, before and for four hours after domain inverting a $-z$ area to become $+z$. Each Raman spectrum was calibrated using neon emission lines to eliminate calibration errors of the spectrometer. A Lorentzian curve was fitted to the experimental Raman intensities to find accurate positions of the peak centres.

Each Raman peak studied showed a small, but measurable, change in position following poling of less than 1 cm^{-1}. Four peaks decreased in wavenumber, while two increased. Additionally, two peaks were observed to show some recovery

toward their original positions over the course of the experiment, with time constants of several hours.

5.6 References

Barker, A. S. and R. Loudon. "Dielectric properties and optical phonons in $LiNbO_3$." *Physical Review*, **158**(2), 433 (1967).

Caciuc, V., A. V. Postnikov and G. Borstel. "Ab initio structure and zone-center phonons in $LiNbO_3$." *Physical Review B*, **61**(13), 8806 (2000).

Claus, R., L. Merten and J. Brandmuller. *Light Scattering by Phonon-Polaritons* (Springer-Verlag, Berlin, 1975).

Damen, T. C., S. P. S. Porto and B. Tell. "Raman effect in zinc oxide." *Physical Review*, **142**(2), 570 (1966).

Ferraro, J. R., K. Nakamoto and C. W. Brown. *Introductory Raman Spectroscopy* (Academic Press, New York, 2003), second edition.

Gopalan, V. and M. C. Gupta. "Origin and characteristics of internal fields in $LiNbO_3$ crystals." *Ferroelectrics*, **198**, 49 (1997).

Gopalan, V. and T. E. Mitchell. "Wall velocities, switching times, and the stabilization mechanism of 180 degree domains in congruent $LiTaO_3$ crystals." *Journal of Applied Physics*, **83**(2), 941 (1998).

Hayes, W. and R. Loudon. *Scattering of Light by Crystals* (John Wiley and Sons, New York, 1978).

Kaganov, M. I. *Electrons, Phonons, Magnons* (Mir Publishers, Moscow, 1981).

Kaminow, I. P. and W. D. Johnston. "Quantitative determination of sources of the electro-optic effect in $LiNbO_3$ and $LiTaO_3$." *Physical Review*, **160**(3), 519 (1967).

Kim, S., V. Gopalan, K. Kitamura and Y. Furukawa. "Domain reversal and nostoichiometry in lithium tantalate." *Journal of Applied Physics*, **90**(6), 2949 (2001).

Kittel, C. *Introduction to Solid State Physics* (John Wiley and Sons Inc., New York, 1996), 7th edition.

Kong, Y. F., J. J. Xu, B. Li, S. L. Chen, Z. H. Huang, L. Zhang, S. G. Liu, W. B. Yan, H. D. Liu, X. Xie, L. H. Shi, X. C. Li and G. Y. Zhang. "The asymmetry between the

domain walls of periodically poled lithium niobate crystals." *Optical Materials*, **27**(3), 471 (2004).

Laubacher, E., Y. Guan and P. Yaney. "Study of periodically poled lithium niobate using scanning Raman microprobe spectroscopy." In "Meeting of the American Physical Society, Ohio Section Spring Meeting," (University of Cincinnati, Cincinnati, 2000).

Lide, D. R. *CRC Handbook of Chemistry and Physics* (CRC Press, Boca Raton, 1994).

Loudon, R. "The Raman effect in crystals." *Advances in Physics*, **13**, 423 (1964).

Parlinski, K. and Z. Q. Li. "Ab initio calculations of phonons in $LiNbO_3$." *Physical Review B*, **61**(1), 272 (2000).

Repelin, Y., E. Husson, F. Bennani and C. Proust. "Raman spectroscopy of lithium niobate and lithium tantalate: Force field calculations." *Journal of Physics and Chemistry of Solids*, **60**, 819 (1999).

Ridah, A., P. Bourson, M. D. Fontana and G. Malovichko. "The composition dependence of the Raman spectrum and new assignment of the phonons in $LiNbO_3$." *Journal of Physics: Condensed Matter*, **9**, 9687 (1997).

Ro, J. H. and M. Cha. "Subsecond relaxation of internal fields after polarization reversal in congruent $LiNbO_3$ and $LiTaO_3$ crystals." *Applied Physics Letters*, **77**(15), 2391 (2000).

Ro, J. H., S.-K. Kang, S.-W. Shin, N.-E. Yu, H.-K. Kim and M. Cha. "Room temperature ferroelectric hysteresis loops of bulk lithium niobate crystals." *Journal of the Korean Physical Society*, **35**, s1496 (1999).

Schaufele, R. F. and M. J. Weber. "Raman scattering by lithium niobate." *Physical Review*, **152**(2), 705 (1966).

Scott, J. F. and S. P. S. Porto. "Longitudinal and transverse optical lattice vibrations in quartz." *Physical Review*, **161**(3), 903 (1967).

Scott, J. G., S. Mailis, C. L. Sones and R. W. Eason. "A Raman study of single-crystal congruent lithium niobate following electric-field repoling." *Applied Physics A*, **79**(3), 691 (2004).

Yatsenko, A. V., E. N. Ivanova and N. A. Sergeev. "NMR study of intrinsic defects in congruent $LiNbO_3$. 1. "Unoverlapping" defects." *Physica B: Condensed Matter*, **240**(3), 254 (1997).

CHAPTER

SIX

Surface Second Harmonic Generation

Second harmonic generation (SHG) is an application of lithium niobate in its own right. However, this chapter details the use of SHG from a lithium niobate surface as a technique for studying ferroelectric domains, in a similar way as described in Chapter 5, but without the need for a Raman microscope. Surface SHG can be used to discriminate between $+z$ and $-z$ faces, provide information on crystal orientation and study the crystal following electric field poling.

The experiments in this chapter were carried out in collaboration with Tleyane Sono and his supervisor, Dr. Jeremy Frey, from the School of Chemistry.

6.1 Introduction

Second harmonic generation is a nonlinear optical effect, and is an extremely useful technique for changing the wavelength of light in a nonlinear material. However it can also be used as a powerful diagnostic tool for material analysis. Surface second harmonic generation is a special case of SHG, where the second harmonic signal is generated at the surface of a medium, rather than in the bulk. It is used in surface science as a useful probe of the structure and dynamics of surfaces, see for instance Fordyce et al. (2004).

The technique has also been applied to studying ferroelectric crystals, through the visualisation of ferroelectric domains (Kurimura and Uesu, 1997) and domain walls (Bozhevolnyi et al., 1998). Additionally, Jung et al. (2000) have proposed a method for determining the direction of the crystal axes using SHG. A major advantage of using surface SHG is that it is non-destructive. Traditionally, ferroelectric domains in lithium niobate have been revealed by using differential etching, whereby a $-z$ face will etch in a suitable acid, but a $+z$ face will not. While this does allow the domains to be visualised, it also severely damages the surface of the sample. Clearly, a technique that does not have this disadvantage would be extremely useful, for instance in quality control applications during the production of periodically poled lithium niobate (PPLN) for quasi-phase matched devices.

In the experiments described in this chapter, we have studied the second harmonic generation from lithium niobate surfaces. It should be noted that although lithium niobate is often used for frequency-conversion applications, such as the doubling crystal in Optical Parametric Oscillators (OPOs), we can be confident that we are using a surface-only effect in the present experiments. This is because the pump wavelength is 532 nm, resulting in the generation of the second harmonic at 266 nm. This wavelength is strongly absorbed in lithium niobate, so any signal observed must be generated in the first few atomic layers of the crystal.

6.2 Theory of Second Harmonic Generation

After the development of the laser in the 1960s, and the corresponding increase in availability of high optical powers, it was found that linear optics was only part of of the range of optical phenomenon, occurring at low powers. At high powers, new, nonlinear processes could take place, including harmonic generation. The basis for this is that the oscillations of dipoles in an optical material can not respond to an incoming light beam in a totally linear way. As the amplitude of these oscillations increases, due to a large E-field from the incident light, the response becomes less linear.

A material's linear polarisation, $\mathbf{P}$, is defined by:

$$\mathbf{P} = \epsilon_0 \boldsymbol{\chi} \mathbf{E} \tag{6.1}$$

where ϵ_0 is the vacuum permittivity and $\mathbf{E}$ is the applied optical electric field. As the polarisation response is generally not exactly parallel to the driving field, due to the

electrons in a crystal experiencing different restoring forces in different directions, a susceptibility tensor, χ, is introduced.

If the nonlinear components of the susceptibility are small, χ can be represented by a power series:

$$\chi = \chi^{(1)} + \chi^{(2)}\mathbf{E} + \chi^{(3)}\mathbf{E}^2 + \ldots \tag{6.2}$$

which can then be substituted into equation (6.1), giving

$$\mathbf{P} = \epsilon_0(\chi^{(1)}\mathbf{E} + \chi^{(2)}\mathbf{E}^2 + \chi^{(3)}\mathbf{E}^3 + \ldots) \tag{6.3}$$

$\chi^{(1)}$ is the linear susceptibility, and $\chi^{(n)}$ is the coefficient for the n-th order nonlinear process. Higher-order terms have a smaller magnitude than lower-order components. Figure 6.1 shows a typical variation of polarisation with electric field for the linear and nonlinear cases.

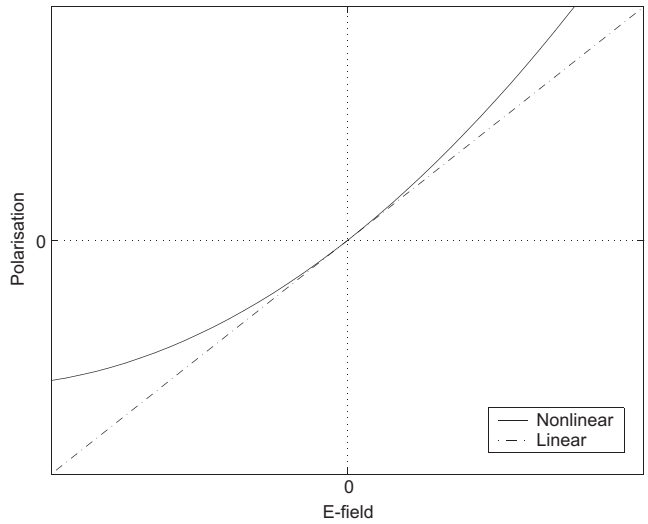

Figure 6.1: Linear and nonlinear response of polarisation, P, to an applied field, *E*.

A consequence of this expansion is that for materials with inversion symmetry (i.e. which are centrosymmetric) all even-order coefficients must be zero. The reason for this is that if the polarisation is inverted (using the inversion symmetry operator, I_{op}) it becomes;

$$I_{op}\mathbf{P} = \epsilon_0(-\chi^{(1)}\mathbf{E} - \chi^{(2)}\mathbf{E}^2 - \chi^{(3)}\mathbf{E}^3 + \ldots) \tag{6.4}$$

However, as the electric field vector is also inverted,

$$I_{op}\mathbf{E} = -\mathbf{E} \tag{6.5}$$

substituting this back into equation (6.4) gives

$$I_{op}\mathbf{P} = \epsilon_0(-\boldsymbol{\chi}^{(1)}\mathbf{E} + \boldsymbol{\chi}^{(2)}\mathbf{E}^2 - \boldsymbol{\chi}^{(3)}\mathbf{E}^3 + \ldots) \tag{6.6}$$

Comparing equations (6.4) and (6.6), it is clear that $\boldsymbol{\chi}^{(2n)} = 0$, so there can be no second-order effects for a centrosymmetric material. As second harmonic generation is a second order effect, it can therefore only occur in a material without a centre of inversion.

It can be shown that second harmonic generation arises from a nonlinear polarisation response, by assuming the electric field $E = \cos(\omega t)$ and substituting into an approximation for the polarisation;

$$\begin{aligned}\mathbf{P} &\approx \epsilon_0\boldsymbol{\chi}^{(1)}\mathbf{E} + \epsilon_0\boldsymbol{\chi}^{(2)}\mathbf{E}^2 \\ &\approx \epsilon_0\boldsymbol{\chi}^{(1)}\cos(\omega t) + \epsilon_0\boldsymbol{\chi}^{(2)}\cos^2(\omega t)\end{aligned} \tag{6.7}$$

then using the trigonometric identity $\cos^2\theta = \frac{1}{2}(1 + \cos 2\theta)$

$$\begin{aligned}&\approx \epsilon_0\boldsymbol{\chi}^{(1)}\cos(\omega t) + \frac{1}{2}\epsilon_0\boldsymbol{\chi}^{(2)}[1 + \cos(2\omega t)] \\ &\approx \frac{1}{2}\epsilon_0\boldsymbol{\chi}^{(2)} + \epsilon_0\boldsymbol{\chi}^{(1)}\cos(\omega t) + \frac{1}{2}\epsilon_0\boldsymbol{\chi}^{(2)}\cos(2\omega t)\end{aligned} \tag{6.8}$$

The first term in equation (6.8) is the DC field, the second is the response at the fundamental drive frequency, and the third term is the response at the second harmonic frequency, 2ω. The first order effects are much stronger than the second order ones.

6.2.1 The nonlinear coefficient

The susceptibility tensor, $\boldsymbol{\chi}^{(2)}$, is termed a third rank tensor, as it is the product of three vectors relating to the polarisation and two light fields, of frequency ω_1 and ω_2. In second harmonic generation these two beams are of the same frequency. It is common for the susceptibility tensor to be replaced by the nonlinear tensor $\boldsymbol{d}$, which can be measured experimentally. The two are related by:

$$d_{ijk} = \frac{1}{2}\chi^{(2)}_{ijk} \tag{6.9}$$

$\boldsymbol{d}$ is also a $3 \times 3 \times 3$ tensor, with 27 elements, which relates the components of $\mathbf{E}$ to the components of $\mathbf{P}$. An individual element d_ijk describes the nonlinear coupling

which generates a polarisation along the i-axis, by the interaction of fields along the j and k axes. d_{ijk} can be contracted into 2D notation, using the inherent symmetry that is found in the expression for nonlinear susceptibility, called intrinsic permutation (Shen, 1984). This is possible as the order of the two electric field intensities is not significant. This reduces the 27 elements of d_{ijk} to an 18 element 3×6 matrix.

$$d_{ijk} = \begin{pmatrix} d_{xxx} & d_{xyy} & d_{xzz} & d_{xyz} & d_{xxz} & d_{xxy} \\ d_{yxx} & d_{yyy} & d_{yzz} & d_{yyz} & d_{yxz} & d_{yxy} \\ d_{zxx} & d_{zyy} & d_{zzz} & d_{zyz} & d_{zxz} & d_{zxy} \end{pmatrix} \tag{6.10}$$

To simplify the tensor, the two indicies j and k can be replaced with a single index, l, which uses the contracted Voigt notation (Lines and Glass, 2001), where x is replaced by 1 , y by 2 and z by 3. The notation is summarised below:

jk	11	22	33	23, 32	13, 31	12, 21
l	1	2	3	4	5	6

This results in a nonlinear tensor d_{il}:

$$d_{il} = \begin{pmatrix} d_{11} & d_{12} & d_{13} & d_{14} & d_{15} & d_{16} \\ d_{21} & d_{22} & d_{23} & d_{24} & d_{25} & d_{26} \\ d_{31} & d_{32} & d_{33} & d_{34} & d_{35} & d_{36} \end{pmatrix} \tag{6.11}$$

The number of elements in the nonlinear tensor can be further reduced by considering the structural symmetry of the material. This is known as Neumann's principle, which states that "the symmetry elements of any physical property of a crystal must include all the symmetry elements of the point group of the crystal". This results in some elements being equal to zero, while others become related to each other. Lithium niobate belongs to the 3m point group, which has 5 independent non-vanishing elements. These are reproduced below, from Shen (1984), with additional notation and values of certain coefficients in lithium niobate added:

Table 6.1: Independent Non-Vanishing Elements of $\chi^{(2)}$ for the 3m group

ijk notation		Voigt Notation	Value (pm V^{-1})
$xzx = yzy$	131 = 232	15 = 24	
$xxz = yyz$	113 = 223	15 = 24	
$zxx = zyy$	311 = 322	31 = 32	$d_{31} = -5$
zzz	333	33	$d_{33} = 33$
$yyy = -yxx =$ $-xxy = -xyx$	222 = −211 = −112 = −121	22 = −21 = −16	$d_{22} = 3$

The nonlinear tensor in materials with 3m symmetry then becomes:

$$\boldsymbol{d}_{il} = \begin{pmatrix} 0 & 0 & 0 & 0 & d_{15} & -d_{22} \\ -d_{22} & d_{22} & 0 & d_{15} & 0 & 0 \\ d_{31} & d_{31} & d_{33} & 0 & 0 & 0 \end{pmatrix} \tag{6.12}$$

A further simplification can be made using the Kleinman (1962) conjecture, which reduces the number of elements to only 3. The approximation is that the nonlinear tensor remains unchanged when the Cartesian indices are rearranged (i.e. $d_{ijk} = d_{kij} = d_{jki}$ etc). Under this approximation $d_{15} = d_{31}$. However this assumption is only valid if the dispersion of d can be neglected, so it can only be used in a lossless medium, or when the frequencies in the medium are far from any band-edge. In the surface second harmonic generation experiments with lithium niobate, the incident light had a wavelength of 532 nm, with a second harmonic at 266 nm. As the second harmonic wavelength is well into the absorption band of lithium niobate, Kleinman symmetry will *not* be assumed.

6.2.2 Surface SHG

Surface SHG has traditionally been applied to study aspects of surface chemistry, including molecular adsorption, orientation and coverage (Corn and Higgins, 1994). The advantage of surface SHG is that it can be applied to any medium, including those which possess a centre of symmetry. This initially appears to be in contradiction with the rule that only non-centrosymmetric materials can take part in SHG. However, Brown et al. (1965) first demonstrated SHG by reflection from a (centrosymmetric) metal boundary and later Rudnick and Stern (1971) presented a theory which attributed this SHG to the fact that the surface itself breaks the centrosymmetric symmetry of the bulk.

Zhang et al. (1990) used second harmonic generation to study molecular orientation at a surface and developed a model based on the theoretical framework of Bloembergen and Pershan (1962). The model used two layers of linear media bounding a thin nonlinear middle layer. In this section we apply this model, with modifications, to the case of surface SHG from lithium niobate, assuming that the surface of lithium niobate may be treated as a thin layer separate from the bulk, with

air forming the top layer. The second order nonlinear polarisation can be written:

$$\begin{pmatrix} P_x \\ P_y \\ P_z \end{pmatrix} = \epsilon_0 \begin{pmatrix} 0 & 0 & 0 & 0 & d_{15} & -d_{22} \\ -d_{22} & d_{22} & 0 & d_{15} & 0 & 0 \\ d_{31} & d_{31} & d_{33} & 0 & 0 & 0 \end{pmatrix} \begin{pmatrix} E_x^2 \\ E_y^2 \\ E_z^2 \\ 2E_yE_z \\ 2E_xE_z \\ 2E_xE_y \end{pmatrix} \tag{6.13}$$

The field components E_x, E_y and E_z inside the surface layer are related to the linearly polarised fundamental wave with field vector **E** at an angle γ to the plane of incidence by

$$\begin{pmatrix} E_x \\ E_y \\ E_z \end{pmatrix} = \begin{pmatrix} a\cos\gamma \\ c\sin\gamma \\ b\cos\gamma \end{pmatrix} \mathbf{E} \tag{6.14}$$

where a, b and c are Fresnel coefficients, given by:

$$\begin{aligned} a &= \frac{2\sqrt{\epsilon_{r1}}\cos\theta_{r1}\cos\theta_{t1}}{(\sqrt{\epsilon_{t1}}\cos\theta_{r1} + \sqrt{\epsilon_{r1}}\cos\theta_{t1})} \\ b &= \frac{2\sqrt{\epsilon_{r1}}\cos\theta_{r1}\sqrt{\epsilon_{t1}}\sin\theta_{m1}}{\sqrt{\epsilon_{m1}}(\sqrt{\epsilon_{t1}}\cos\theta_{r1} + \sqrt{\epsilon_{r1}}\cos\theta_{t1})} \\ c &= \frac{2\sqrt{\epsilon_{r1}}\cos\theta_{r1}}{(\sqrt{\epsilon_{t1}}\cos\theta_{t1} + \sqrt{\epsilon_{r1}}\cos\theta_{r1})} \end{aligned} \tag{6.15}$$

The dielectric constants of each layer, (r, m and t) have corresponding subscripts, while the subscript number refers to the fundamental or harmonic frequency. The layers and various angles in these coefficients are as specified by the schematic diagram in Figure 6.2.

The angles of the fundamental wave are related to the incident angle, θ_i by the boundary conditions given below.

$$\sqrt{\epsilon_{r1}}\sin\theta_i = \sqrt{\epsilon_{r1}}\sin\theta_{r1} = \sqrt{\epsilon_{m1}}\sin\theta_{m1} = \sqrt{\epsilon_{t1}}\sin\theta_{t1} \tag{6.16}$$

An addition needs to be made to the theory of Zhang et al. to allow for rotation of the lithium niobate crystal around the z axis (a variation of the azimuthal angle, ϕ), which was not included before as the system they were modelling was rotationally isotropic. This is achieved by considering the transformation law for $\boldsymbol{\chi}^{(2)}$ which

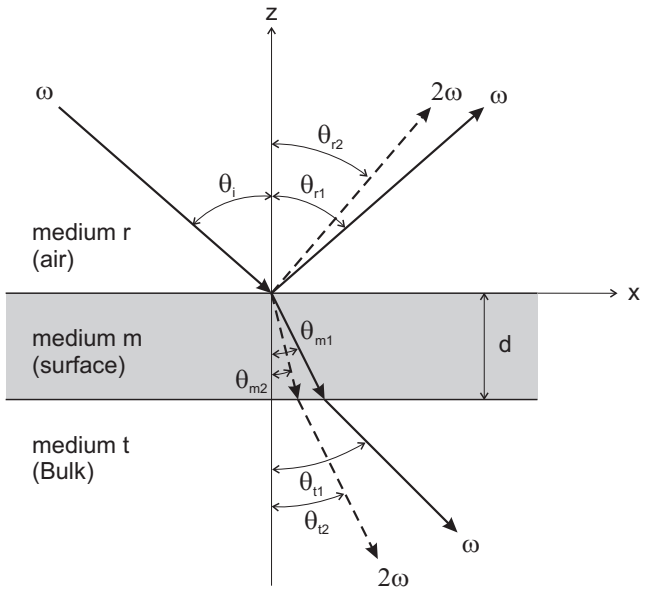

Figure 6.2: SHG from a three layer structure. In this case the surface (of thickness d) and bulk both consist of $LiNbO_3$, while the top layer is air.

corresponds to the rotation of the coordinate system, which is

$$\chi'^{(2)}_{pqr} = \boldsymbol{R}_{pi}\boldsymbol{R}_{qj}\boldsymbol{R}_{rk}\chi^{(2)}_{ijk} \tag{6.17}$$

where $\boldsymbol{R}$ is a rotation matrix, shown below, which defines a clockwise rotation about the z axis.

$$\boldsymbol{R} = \begin{pmatrix} \cos\phi & \sin\phi & 0 \\ -\sin\phi & \cos\phi & 0 \\ 0 & 0 & 1 \end{pmatrix} \tag{6.18}$$

Applying this to equation (6.12) results in a modified second order nonlinear tensor, which is dependent on the azimuthal angle:

$$\boldsymbol{d}(\phi) = \begin{pmatrix} -\sin(3\phi)d_{22} & \sin(3\phi)d_{22} & 0 & 0 & d_{15} & \cos(3\phi)d_{22} \\ -\cos(3\phi)d_{22} & \cos(3\phi)d_{22} & 0 & d_{15} & 0 & \sin(3\phi)d_{22} \\ d_{31} & d_{31} & d_{33} & 0 & 0 & 0 \end{pmatrix} \tag{6.19}$$

and the resulting 3ϕ dependence of the d_{22} coefficient on the azimuthal angle clearly reveals the crystal symmetry.

Zhang et al. used the results of Bloembergen and Pershan and assumed that $d \ll \lambda$, to find the p and s components of the electric field (input polarisation, $\gamma = 0°$ and

90° respectively) of the reflected second harmonic wave as:

$$E_p^{(2\omega)} = -4\pi i \frac{\omega d}{c} \frac{(-1)(\sqrt{\epsilon_{t2}/\epsilon_{m2}})\sin\theta_{m2} P_z^{nl} + \cos\theta_{t2} P_x^{nl}}{(\sqrt{\epsilon_{t2}}\cos\theta_{r2} + \sqrt{\epsilon_{r2}}\cos\theta_{t2})}$$
$$E_s^{(2\omega)} = -4\pi i \frac{\omega d}{c} \frac{P_y^{nl}}{(\sqrt{\epsilon_{t2}}\cos\theta_{t2} + \sqrt{\epsilon_{r2}}\cos\theta_{r2})} \tag{6.20}$$

We can assume that the dielectric constants in air are equal to unity (i.e. $\epsilon_{r1} = \epsilon_{r2} = 1$) and then by substituting equations (6.13) (6.14) and (6.19) into (6.20) the p and s components of the electric field of the reflected second harmonic can be simply written as a function of γ:

$$E_p^{(2\omega)} = X(A\cos^2\gamma + B\sin^2\gamma + C\sin 2\gamma)E^2$$
$$E_s^{(2\omega)} = Y(F\cos^2\gamma + G\sin^2\gamma + H\sin 2\gamma)E^2 \tag{6.21}$$

where A, B, C, F, G, H, X and Y are functions of the nonlinear coefficients, reflection and refraction angles and the Fresnel coefficients defined earlier:

$$A = \left[\sqrt{\frac{\epsilon_{t2}}{\epsilon_{m2}}}\sin\theta_{m2}(a^2 d_{31} + b^2 d_{33}) + (\cos\theta_{t2})(2abd_{15} - \sin(3\phi)a^2 d_{22})\right]$$
$$B = \left[\sqrt{\frac{\epsilon_{t2}}{\epsilon_{m2}}}\sin\theta_{m2} c^2 d_{31} + (\cos\theta_{t2})(\sin(3\phi)c^2 d_{22}\right]$$
$$C = \left[(\cos\theta_{t2})(\cos(3\phi)acd_{22})\right]$$
$$F = \left[-\cos(3\phi)a^2 d_{22}\right] \tag{6.22}$$
$$G = \left[\cos(3\phi)c^2 d_{22}\right]$$
$$H = \left[(bcd_{15} + \cos(3\phi)acd_{22})\right]$$
$$X = \frac{4\pi i\omega d(-1)}{c(\sqrt{\epsilon_{t2}}\cos\theta_{r2} + \sqrt{\epsilon_{r2}}\cos\theta_{t2})}$$
$$Y = \frac{4\pi i\omega d(-1)}{c(\sqrt{\epsilon_{t2}}\cos\theta_{t2} + \sqrt{\epsilon_{r2}}\cos\theta_{r2})}$$

Using equation (6.21) the measured intensity of the SHG signal can be fitted to γ, the angle the E-field vector makes with the plane of incidence, and hence the coefficients in equation (6.22) can be determined.

Experiments can also be carried out by varying the sample's azimuthal angle, with the fundamental beam polarisation fixed. The equations for s and p polarised SH fields from s and p polarised fundamental beams are shown in Table 6.2.

Table 6.2: Second Harmonic fields as a function of sample azimuthal angle.

	$\gamma = 0°= p$	$\gamma = 90°= s$
$E_p^{(2\omega)} =$	XAE^2	XBE^2
$E_s^{(2\omega)} =$	$-Y\cos(3\phi)a^2d_{22}E^2$	$Y\cos(3\phi)c^2d_{22}E^2$

Further experiments by Tom et al. (1983) showed that the SHG reflection from crystalline silicon was also dependent on the cut and orientation of the face, which was unexpected based on the theory of Bloembergen and Pershan. The authors used a theory incorporating the surface and also the bulk responses to explain their results. As silicon is centrosymmetric, no SHG is expected from the bulk, but they claim magnetic-dipole and electric-quadrupole terms are responsible for the observed bulk response.

For a (111) silicon surface with C_{3v} symmetry (the same as lithium niobate) Tom et al. expect the nonlinear susceptibility tensor to have three isotropic and one anisotropic terms, and that only the anisotropic term is responsible for *s*-polarised SH radiation from a pure *s* or *p* polarised fundamental. Under these conditions, when a sample is rotated around 360° the second harmonic electric field has the form $E \propto \cos 3\phi$, which represents the trigonal symmetry of the material, and hence the second harmonic intensity $I \propto E^2 \propto \cos^2 3\phi$. This results in a recorded SH signal with a pattern of six identical peaks. However, when the analyser was rotated away from the *s* polarisation, Tom et al. found that isotropic terms are introduced, and that interference between the isotropic and anisotropic terms affects the amplitudes of alternate peaks, resulting in the almost complete disappearance of three of the peaks when the SHG signal was recorded as a function of rotation angle with *p* polarised SH reflection and *p* polarised excitation.

As lithium niobate shares the same symmetry as a (111) silicon surface, it is expected that it will also show the same trends during SHG as the sample is rotated. This is evident from the A and B terms defined in equation (6.22) which have isotropic and anisotropic parts. However, these terms are only used with a *p* polarised SH, so as with silicon, *s* polarised SH from a pure *p* or *s* fundamental will only be anisotropic, and hence six peaks are expected as the sample is rotated through 360°.

Sipe et al. (1987) produced a general phenomenological theory on second harmonic generation from surfaces of centrosymmetric cubic crystals, based on electric dipole, electric quadrupole and magnetic dipole sources, to explain the results that Tom et al. and others had reported in a range of crystals.

Andersson et al. (1999) later studied second harmonic reflection from calcite, which also has C_{3v} symmetry and is centrosymmetric but is not a cubic crystal. They also succeeded in measuring the relative phases of the susceptibility tensor components by varying the polarisation of the fundamental beam. They reported that this measurement was very sensitive to the phase of the different susceptibility tensor components, and not just the modulus as was the case for azimuthal rotation.

Based on the work of these earlier authors, Kurimura and Uesu (1997) constructed a second harmonic generation microscope to visualise periodically poled ferroelectric domains. This operated using the difference in sign of the nonlinear coefficients from neighbouring oppositely orientated domains, and the resulting π phase difference. Contrast between domains was achieved by interference of the second harmonic from lithium niobate with a second SH wave from a uniform plate.

Recently Jung et al. (2000) described a method to determine the x and y crystal axes of nonlinear uniaxial materials, including lithium niobate, using anisotropic surface SHG, instead of the more common technique of X-ray diffraction.

6.3 Experimental Details

The aim of the experiments described here was to use surface SHG on lithium niobate, to identify domains and hence $-z$ and $+z$ faces of lithium niobate. We also wished to investigate whether the SHG from a surface was affected by domain inversion.

A frequency doubled pulsed Nd:YAG laser (Spectron SL400) was used to provide the fundamental beam at a wavelength of 532 nm, with a repetition rate of 20 Hz and energy of 0.2 mJ/pulse. The set-up of the SHG apparatus is shown in Figure 6.3. The beam was delivered to the sample via an adjustable arm, which determined the angle of incidence of the beam. The arm also contained two half-wave plates with a polariser between the two, to allow the power of the fundamental beam (first half-waveplate) and the angle of polarisation (second half-waveplate) to be varied. The arm also contained a 20 cm focussing lens followed by a UV filter to remove any SHG that had been generated from the preceding optics.

The beam was then directed on to a lithium niobate sample, which was mounted on a rotation stage. After the sample, a second adjustable arm contained the optics and detectors to analyse the SHG signal from the sample surface. A visible filter was used to remove any reflected green fundamental light and an analyser

controlled the polarisation of the second harmonic signal, which was detected by a monochromator and photomultiplier tube. The signal was then passed to an amplifier and computer. The SHG signal was normalised to a reference signal from the laser, to allow for any fluctuations in laser power. To reduce error, each SHG measurement (for a particular angle) was an average of the SHG from 1000 laser pulses.

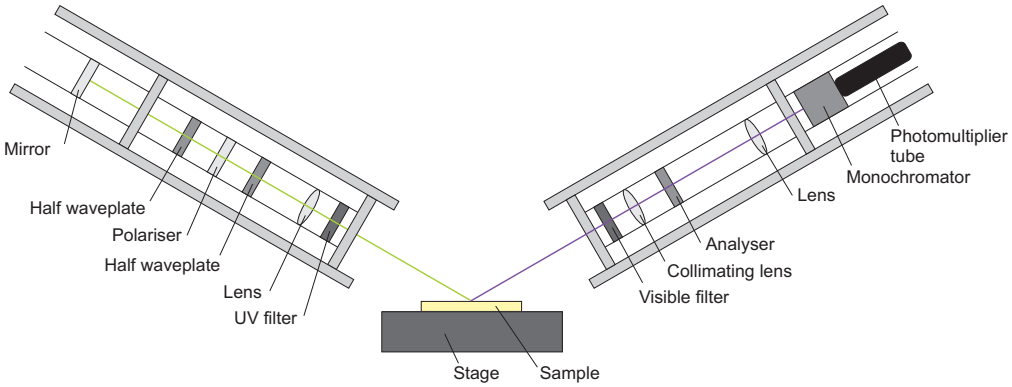

Figure 6.3: Schematic diagram of the SHG apparatus.

The various SHG parameters are summarised in Table 6.3. The two main variables were the sample azimuthal angle ϕ and the fundamental light polarisation angle, γ, thus two types of experiment were possible, based on sample rotation or fundamental beam polarisation rotation. The SHG polarisation Γ was fixed at the start of each experiment. Polarisation angles of 90° corresponded to *s*-polarised light, while 0° corresponded to *p*-polarised light. The two 'arms' of the apparatus delivering the incident beam and collecting the SH beam, were fixed at 60° to the sample.

Table 6.3: SHG experimental parameters.

Angle	Label	
Angle of incidence of fundamental beam	θ_i	fixed at 60°
Angle of detection of SHG	θ_{r1}	fixed at 60°
Output (SHG) light polarisation angle	Γ	fixed for single experiment
Incident light polarisation angle	γ	
Sample azimuthal angle	ϕ	

The first stage in each experiment was poling a region of the lithium niobate sample, by the usual electric-field method as described in Section 2.4.1. The sample was then taken to the SHG lab and the second harmonic reflection was measured as a function of azimuthal angle. Following this, the sample was rotated to the angle that corresponded to the maximum of the smaller of the two peaks, as this appeared to

give a larger difference in SHG between the various faces. The azimuthal angle was then fixed at this position. With the sample correctly orientated, the SH intensity was recorded as a function of the fundamental polarisation angle, for virgin $+z$ and domain inverted $-z$ faces. The sample was then turned over, and a rotation experiment conducted again to reorientate the crystal. Finally the SHG from virgin $-z$ and domain inverted $+z$ faces as a function of fundamental polarisation was recorded.

6.4 Results

A typical SH signal recorded as a function of the azimuthal angle, over 120° has two peaks, as shown in Figure 6.4. A complete 360° rotation would show six peaks, representing the crystal symmetry as expected from the theory. This experiment was used to orientate the sample before measuring the SHG as a function of the fundamental beam polarisation. The sample was rotated to the maximum of the smaller peak, which in this example corresponds to ~28°.

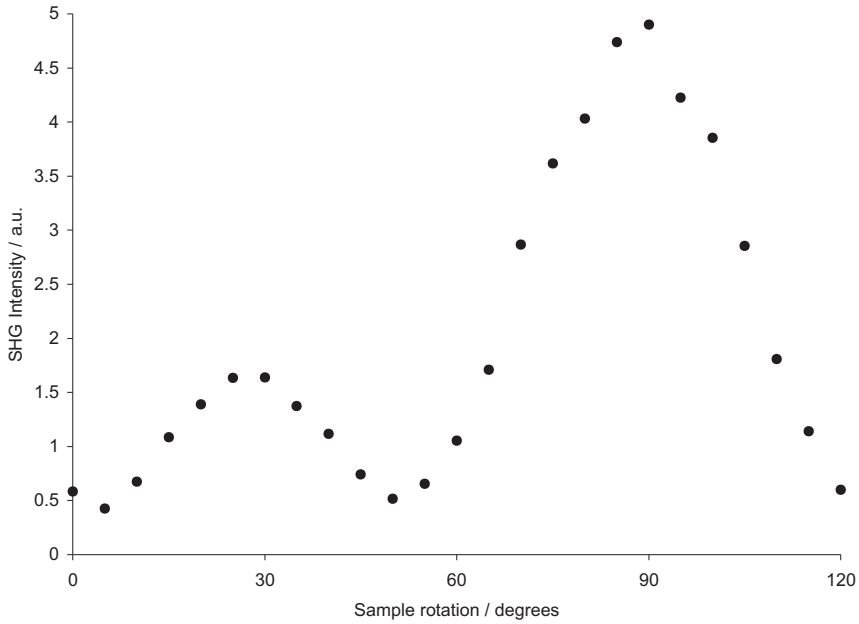

Figure 6.4: SHG from lithium niobate as a function of the azimuthal rotation of the sample. Taken with fundamental polarisation $\gamma = 90°$ and SH polarisation $\Gamma = 0°$.

Figure 6.5 shows the SHG versus the rotation angle of the half-waveplate and hence the polarisation of the fundamental beam. It was recorded with the SH polarisation fixed by the analyser to be *p*-polarised. The sample had been poled approximately

one hour before the SHG experiments were conducted. Measurements were made on the original virgin faces and also the domain inverted areas. The results show that several differences in SHG occur between the various faces:

- The SH signal from the virgin $-z$ face is greater than from the virgin $+z$ face.
- The SH signal from the repoled $-z$ face is much greater than from the repoled $+z$ face.
- The SH signal from the repoled $-z$ face is slightly greater than from the virgin $+z$ face.

The largest change appears for the repoled $+z$ face, which has a SHG intensity of only 60 % of that from a virgin $-z$ face, i.e. domain inversion reduces the SHG from a $-z$ face by 40 %. The intensity from the virgin $+z$ face was 88 % of that from the virgin $-z$ face.

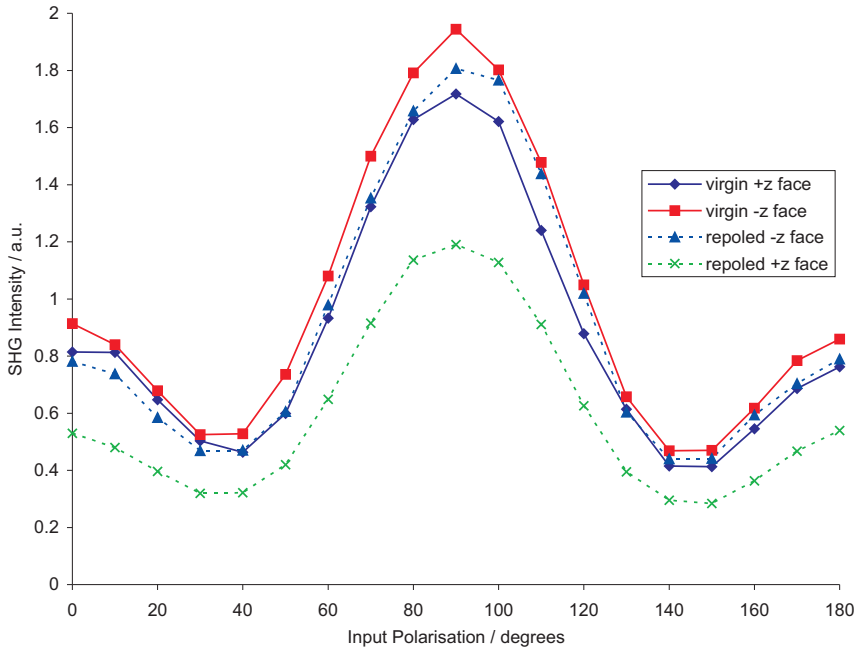

Figure 6.5: SHG from recently-poled lithium niobate, with SHG polarisation $\Gamma = 0° = p$.

Figures 6.6 and 6.7 show results taken on the same recently-poled sample, but with the polarisation of the detected SH at 45° and 90°. Fig. 6.6 looks similar to that taken with $\Gamma = 0°$, but the SH intensity is lower overall and there is little difference in intensity from the virgin and repoled $-z$ faces.

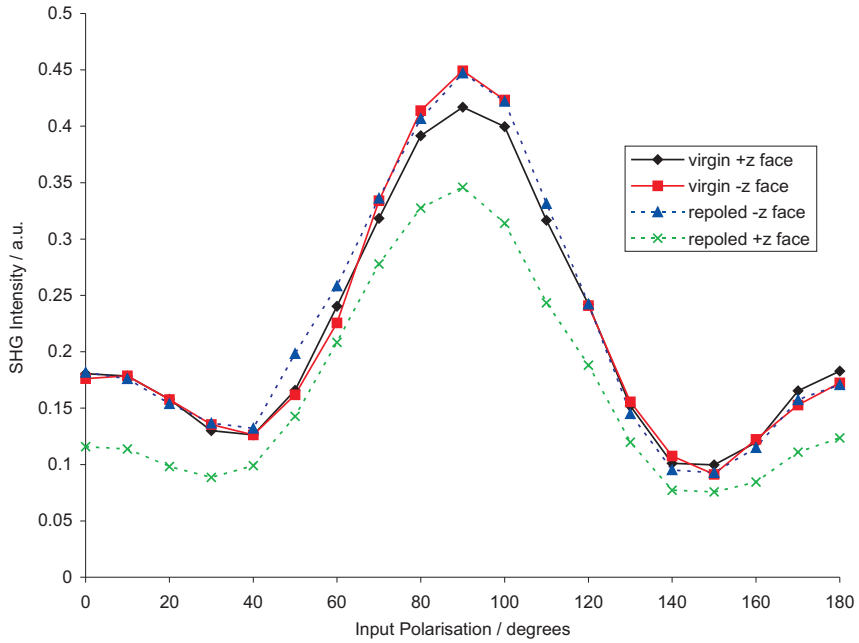

Figure 6.6: SHG from recently-poled lithium niobate, measured with output polarisation $\Gamma = 45°$.

Figure 6.7 shows that the intensity of the SHG with $\Gamma = 90°$ was over an order of magnitude less than obtain for $\Gamma = 0°$. The positioning of the peaks is also different, with two peaks of approximately the same intensity centred at 45° and 135°. Additionally, there is very little difference in SHG signal between all four faces in the first peak, but the intensities of the repoled $+z$ and $-z$ faces are lower for the second peak (with fundamental polarisation greater than 90°). The reasons for this behaviour are unclear.

As the SH intensity from repoled lithium niobate faces was found to be less than from virgin faces, an experiment was conducted where the peak SH intensity was measured from a new sample (Sample 2) over four hours, to see if any recovery in intensity occurred over that time. The results of this are shown in Figure 6.8. The experiment started approximately two hours after the sample had been poled. As the results show, the changes in SH intensity with time are small. The middle (blue) trace represents the raw SH data, before any normalisation to the laser power had been carried out. The top (black) trace shows the laser reference signal, which was slightly increased over the first 60 minutes. When this is taken into consideration, the lower, corrected SHG trace (red) does show a slight increase or recovery, over the duration of the experiment. However, the change is very small, so this result is inconclusive, but does suggest any recovery would take place over a long period of time, on the scale of days or weeks.

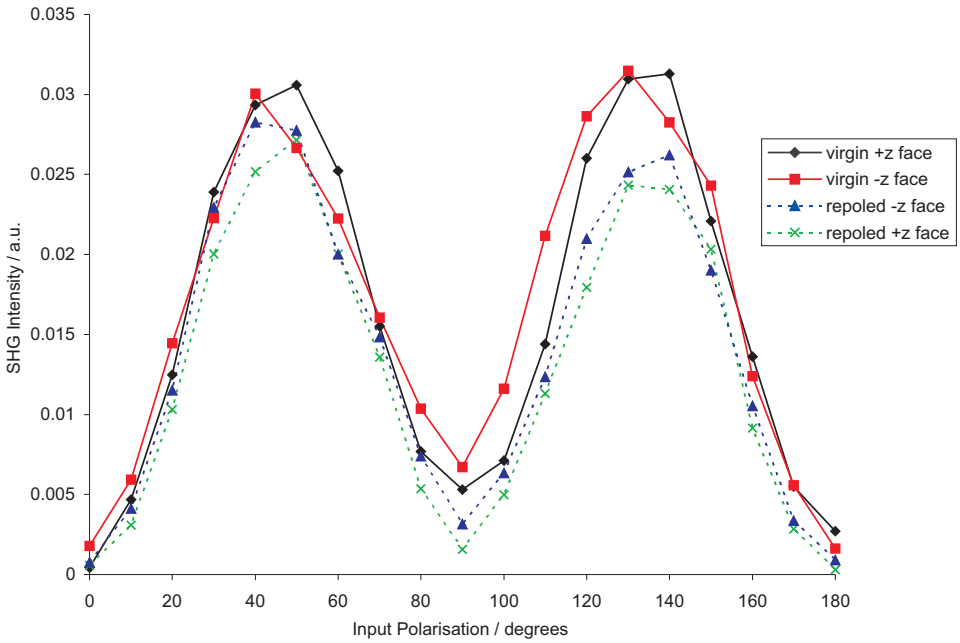

Figure 6.7: SHG from recently-poled lithium niobate, measured with output polarisation $\Gamma = 90° = s$.

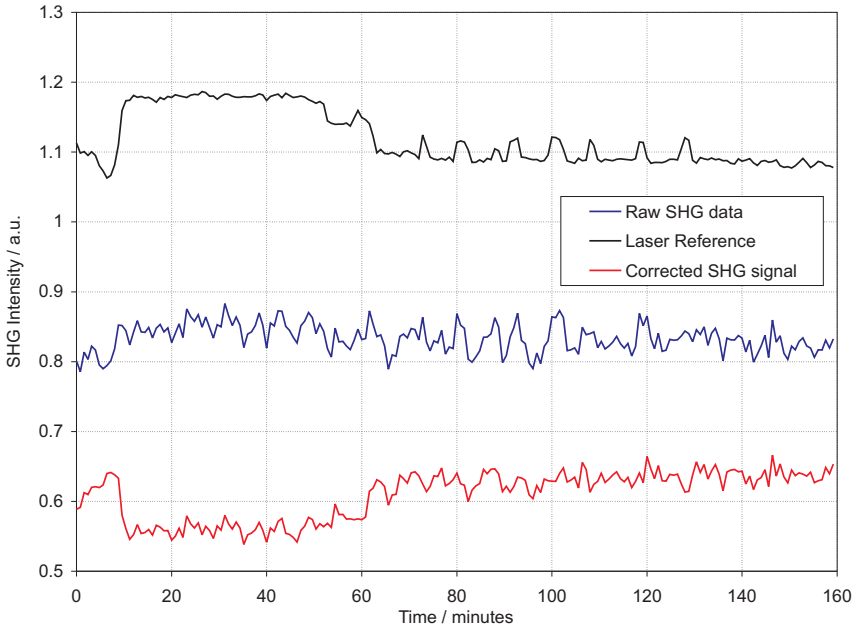

Figure 6.8: Time dependent SHG from $+z$ lithium niobate face.

To confirm that any recovery in intensity occurred over a long period of time, SHG from the original sample was examined again, four months after the initial experiments. The results are shown in Figure 6.9 and reveal that the SH intensity from the repoled $+z$ face four months after poling was ~80 % that of the virgin

$-z$ face, indicating that some recovery had taken place. However, the SHG was approximately the same from each of the other three faces, including the two virgin faces, which were expected not to have changed, and still be distinguishable.

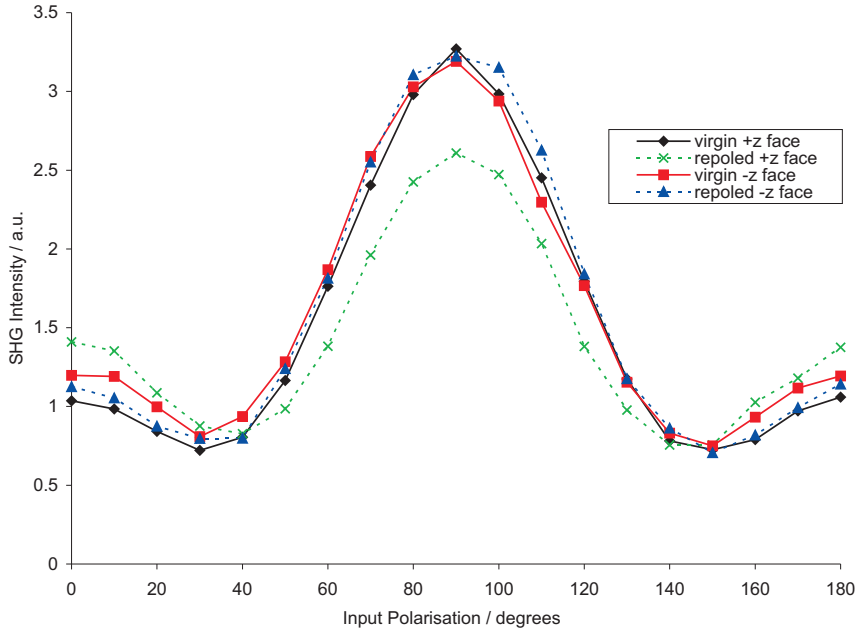

Figure 6.9: SHG from a lithium niobate sample, taken 4 months after poling, measured with output polarisation $\Gamma = 0°$.

Further experiments were then conducted on the sample that been used in the time-dependent experiment (Sample 2). The SHG was measured again, three months after the sample had been poled and the results are shown in Figure 6.10. These results show that the SH intensity from the repoled $+z$ face was approximately the same as that from the repoled $-z$ face and the virgin $+z$ face, with the intensity from the virgin $-z$ face being slightly greater. These relative intensities are rather different than those obtain from the four month old sample. In this sample the SH from the repoled $+z$ face seems to have completely recovered to be essentially the same as from virgin $+z$ face. However, it is not known why in this case the SH from the repoled $-z$ face is significantly lower than from the virgin $-z$ face, and why there is almost no difference in SH intensity between the repoled $-z$ and $+z$ faces.

6.5 Summary

Surface second harmonic generation was used to identify domains in lithium niobate, by the variation of intensity of the SH signal from z faces. Surface SHG can also be used to orientate an unknown lithium niobate sample.

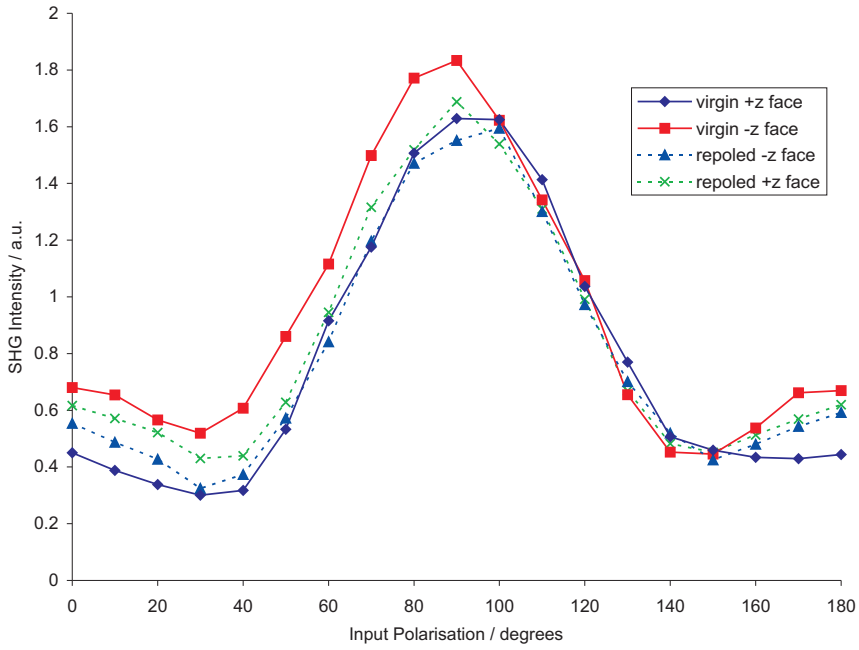

Figure 6.10: SHG from lithium niobate sample 2, taken 3 months after poling, measured with output polarisation $\Gamma = 0°$.

A pulsed Nd:YAG laser operating at 532 nm was used, hence the SH wavelength was 266 nm, which is below the UV absorption edge, thus ensuring the surface-selectivity. The intensity of the SH from repoled domains was also observed to vary depending on which face was being examined. For a recently poled sample, the most intense SH signal was obtained for a virgin $-z$ face, followed by repoled $-z$, virgin $+z$ and then repoled $+z$ faces.

It is thought that the SH intensity from repoled samples will recover towards that from virgin samples over time, and experiments on a four month old sample found that intensity from virgin and repoled $-z$ faces was essentially identical. However, there was still a large difference between virgin and repoled $+z$ faces and the intensity from the two virgin faces was also identical. Results of experiments on a three month old sample were also inconclusive, so this area would benefit from further study.

6.6 References

Andersson, S. K., M. C. Schanne-Klein and F. Hache. "Symmetry and phase detection of second harmonic reflection from calcite surfaces." *Physical Review B*, **59**(4), 3210 (1999).

Bloembergen, N. and P. S. Pershan. "Light waves at the boundary of nonlinear media." *Physical Review*, **128**(2), 606 (1962).

Bozhevolnyi, S. I., K. Pedersen, T. Skettrup, X. Zhang and M. Belmonte. "Far and near-field second-harmonic imaging of ferroelectric domain walls." *Optics Communications*, **152**(4-6), 221 (1998).

Brown, F., R. E. Parks and A. M. Sleeper. "Nonlinear optical reflection from a metallic boundary." *Physical Review Letters*, **14**(25), 1029 (1965).

Corn, R. M. and D. A. Higgins. "Optical second harmonic generation as a probe of surface chemistry." *Chemical Reviews*, **94**, 107 (1994).

Fordyce, A. J., W. J. Bullock, R. D. Spencer-Smith and J. G. Frey. "Probing possible structural models at the air / H_2SO_4(aq) interface: A second harmonic generation study." *Physical Chemistry Chemical Physics*, **6**(9), 2415 (2004).

Jung, C., B. K. Rhee and D. Kim. "Simple methods for determining the crystalline axes of nonlinear uniaxial crystal with second-harmonic generation." *Applied Optics*, **39**(28), 5142 (2000).

Kleinman, D. A. "Theory of second harmonic generation of light." *Physical Review*, **128**(4), 1761 (1962).

Kurimura, S. and Y. Uesu. "Application of the second harmonic generation microscope to nondestructive observation of periodically poled ferroelectric domains in quasi-phase-matched wavelength converters." *Journal of Applied Physics*, **81**(1), 369 (1997).

Lines, M. E. and A. M. Glass. *Principles and Applications of Ferroelectrics and Related Materials* (Oxford, 2001).

Rudnick, J. and E. A. Stern. "Second-harmonic radiation from metal surfaces." *Physical Review B*, **4**(12), 4274 (1971).

Shen, Y. R. *The Principles of Nonlinear Optics* (Wiley-Interscience, New York, 1984).

Sipe, J. E., D. J. Moss and H. M. Driel. "Phenomenological theory of optical second- and third-harmonic generation from cubic centrosymmetric materials." *Physical Review B*, **35**(3), 1129 (1987).

Tom, H. W. K., T. F. Heinz and Y. R. Shen. "Second-harmonic reflection from silicon surfaces and it relation to structural symmetry." *Physical Review Letters*, **51**(21), 1983 (1983).

Zhang, T., C. Zhang and G. Wong. "Determination of molecular orientation in molecular monolayers by second-harmonic generation." *Journal of the Optical Society of America B*, **7**(6), 902 (1990).

CHAPTER

SEVEN

Conclusions

7.1 Light Induced Frustrated Etching

The light induced frustration of etching is a technique for surface structuring lithium niobate. It allows complete frustration of etching to be achieved on the $-z$ face at high laser intensities, and at lower intensities a partial frustration occurs, which is characterised by the formation of distinctive self-organised intricate patterns consisting of unetched material surrounded by etched areas. It operates by the combined action of visible wavelength laser light with an etchant, usually a mixture of hydrofluoric and nitric acid.

Chapter 3 showed that large areas of sub-micron structures were produced on the $-z$ face of iron doped lithium niobate. The size of sites was observed to vary between 250 μm to 2.3 mm, with larger sites occurring for larger spot size of the laser beam and longer duration of exposure. Sites form after only five seconds of exposure to acid and light.

Within each site a variety of structures can be produced. With sufficient laser intensity, total frustration of etching may be induced, forming a smooth area at the centre of the site. If the intensity is not great enough, then densely-packed dots are observed. Away from the centre of the site, lines are formed, preferentially along one of three directions separated by 120° ; this behaviour is related to the underlying trigonal symmetry of the crystal. These lines may be densely packed, and change

directions to fill in all the available space, or at the edges of the site they become less densely packed, tend to be straight with less changes of direction and are narrower the further from the centre of the site they extend. Towards the edges of the site lines form that can extend for distances of over hundreds of microns.

Analysis of the structures formed was carried out by electric-field atomic force microscopy (E-AFM), which determined that they carry a positive charge compared the surrounding $-z$ areas, which was likely to have been present during their formation and hence was probably responsible for their formation.

Two-dimensional Fourier transform analysis has also been conducted to find the spatial frequencies present in the SEM images. The resulting star-shaped patterns of images taken at the edges of the sites confirm that the LIFE features preferentially form at 60° and 120° to each other, while transforms of images taken at the centre of the site usually do not have any directionality, but show a characteristic scale length.

The exact mechanism behind the observed frustration of etching is still open to discussion, but either the formation of ferroelectric microdomains or optically generated charge generation followed by migration (photovoltaic current) are the two main possibilities. Of these two, the photovoltaic effect provides a better fit to the experimental results and gives a possible explanation of the symmetry of the patterns that are formed.

The LIFE technique has the potential to create structures that could be used as rib-waveguides, surface relief gratings and even moving parts for MEMS applications. LIFE structures could also be used as a mask to define areas for electric-field domain inversion through the crystal, for use in frequency conversion devices and as interdigital electrodes for surface acoustic wave devices. The length scales achieved with LIFE, of micrometre and sub-micrometre dimensions, are compatible with these sorts of applications, and the etch depth can be varied to achieve the size structures that are required. For instance, the LIFE sites that have been demonstrated in this thesis vary in size from $\sim$ 100 μm to 2.2 mm, depending on the beam spot size and etch times. However, within these large macro structures, small etch frustrated features with widths of between 0.6 μm to 0.2 μm have been observed.

Comparing the dimensions of structures achievable using LIFE with those required for current applications of surface structures on lithium niobate, as given in Table 1.1, shows that LIFE is potentially very useful for producing rib waveguides, surface relief gratings, photonic band gap materials and even surface acoustic wave devices.

For instance, rib waveguides require features of approximately 2 μm dimensions, which could be achieved by LIFE, and also by other techniques including reactive ion etching. However, as discussed in Section 2.4.3 structures formed by RIE require a mask to define their shape and often suffer from limited side-wall fidelity and formation of a surface film which reduces the quality. Consequently, at this length scale conventional etching is likely to be the best option at present. However, for finer scale structures with widths of around 350 nm and depths of ~ 1 μm, as required for photonic bandgap devices and surface relief gratings, conventional techniques may not be appropriate, particularly due to the difficulty of lithography at submicron scales and limited side-wall verticality. For these sorts of applications the LIFE technique holds much promise, although further work is required to establish the available spatial resolution and gain more control of the patterns of structures which are formed.

It is instructive to consider the power and utility of the LIFE technique, especially compared to other methods of etching and surface structuring lithium niobate. There are numerous ways of etching lithium niobate, with the most common being wet etching, but dry etching with ion beams is also important, (see Sections 2.4.2 and 2.4.3 for further details on etching techniques). However as a method of surface structuring, LIFE has advantages over each of these other techniques.

Wet etching, as with conventional HF acid etching, is relatively inexpensive as it does not require sophisticated equipment and produces a uniform etch over the exposed areas. However, to produce surface structures a mask must be defined on the crystal surface using photolithography, which is either resistant to the acid, or used to produce domains of the opposite orientation which do not etch. Currently in industry photolithography is cheap, but it is an additional stage that is not necessary with LIFE, and each extra processing stage costs time and money. Using a mask with photolithography is also a less flexible approach for producing a variety of patterns than using a laser beam to define the unetched area, as for the total frustration of etching with LIFE technique. Ion beam techniques are much more selective than wet etching, so are more suited to producing surface structures, but the equipment is expensive to own and operate. Additionally, no other etching technique, to the best of our knowledge, produces the sort of self-organised structures that have been observed in the partially frustrated etching experiments.

Currently the results of LIFE apply only to a physical demonstration of potential and not yet to devices. So at present LIFE is probably of more interest to research groups within universities for instance, than as a commercial method for the production of devices. Such groups may not have access to cleanroom facilities and mask aligners,

so a method of producing structures without the need for photolithography may be of interest. Additionally some devices are based on structures produced using the differential etching between domains, which requires the additional step of electric field poling and so again complicates the process and increases cost. Groups without a high voltage equipment and a poling rig could therefore also be interested in LIFE.

As discussed in Chapter 1 surface structures are useful and an area of commercial interest. Also self-organised, submicron structures are also of academic interest. If it was possible to exert more influence over the precise patterns they form (to create periodic gratings etc) as suggested in Further Work, then certainly LIFE would be a technique for making real devices. However, we have not produced devices using this technique at present, and the current limitations of the technique limit its usefulness for device production. This conclusion is why future students in our group are increasingly using UV exposure to produce surface structures and micro-domains instead. However, it is the belief of the author that LIFE is at the very least interesting and in future may become both powerful and useful.

7.1.1 Future Work

One of the most interesting features of the LIFE technique, the self-organisation of features, may also be considered a weakness as it limits the control that can be exercised over their formation. However, large areas of parallel lines have been observed, so it may be possible to develop the technique to grow gratings with user-defined spacing, by using different illumination conditions. The use of an alternative ferroelectric with a different crystal symmetry, such as C_{2v}, may make grating formation easier.

Future experiments could also be undertaken using a purpose-made phase mask (i.e. not a simple photoresist mask on the reverse of the lithium niobate sample) with an optimal longer period, which would result in lower angles of diffraction, greater overlap and more interference between the orders. This may give a better result than that obtained in Chapter 3, where the use of a phase mask with a relatively short period only changed the shape of the site and not the patterns formed.

Fourier transform analysis was carried out on some of the SEM images obtained of the LIFE surface structures, which showed the preferred directionality and typical length scales of the structures formed. However, it is possible that more detailed information could be obtained through further mathematical analysis of the images and discussions with Dr D'Alessandro and Dr Dennis from the School

of Mathematics are in progress. They suggest that wavelet analysis or Minkowski functionals of the integral geometry could be calculated which would aid further study of the variation of the patterns produced with the incident light intensity. These functionals could include the area (fraction of black and white image that is white), the perimeter (the total length of the line between black and white areas) and the Euler characteristic (a measure of how 'holey' the image is).

Work is currently being undertaken within the group using green laser light to reduce the coercive field of undoped lithium niobate, and so allow light-controlled poling. The light has been shown to reduce the coercive field by a factor of 89 % (Sones et al., 2005b). When combined simultaneously with an electric field of lower magnitude than the normal coercive field, poling will occur in the exposed areas only, thus allowing the light-defined pattern to be transfered to the ferroelectric domain structure. It is likely that this phenomenon is a result of optically-generated charges via the bulk photovoltaic effect, and so is related to the light-induced frustration of etching.

Recently Crouch et al. (2004) have reported the production of 'black silicon'; laser structured silicon with interesting optical properties that occur as a consequence of the micrometre-scale structures formed on the crystal surface. The sharp, conical microstructures are formed by either femtosecond or nanosecond laser irradiation of a silicon wafer in a chamber filled with SF_6. Exposed areas are called black silicon due to the below-band gap light absorption that occurs due to these structures. Photocurrent generation has also been observed. Future work could be to apply these or other techniques to LIFE experiments to attempt to produce 'dark lithium niobate' with unusual optical properties.

7.2 Ultraviolet Exposure of Lithium Niobate

Lithium niobate crystals were exposed to pulsed ultraviolet radiation, at various wavelengths and fluences, with the aim of investigating the possibility of all-optical poling. The effect of this illumination depends on whether it has been applied to a $-z$ or $+z$ surface. Etching a $+z$ surface that had been exposed to UV light of sufficient intensity to cause ablation reveals narrow features (150 - 300 nm wide) that are at a lower topographical level than the surrounding areas of crystal. The features, or 'trenches', are mostly continuous lines which can extend for hundreds of microns, but may also change direction so form distinctive patterns with three-fold symmetry. The features are only created within areas that have been ablated

by the laser pulse, which requires a fluence of ~0.5 J cm^{-2}. Above this minimum limit, the formation of trenches appears to be insensitive to the fluence used, with similar patterns being created with a range of fluences up to ~10 J cm^{-2}. Using focussed ion beam milling, the trenches were found to have a maximum depth of ~1.8 μm. Scanning force microscopy was used to reveal the presence of these features without the need for etching.

UV exposure of $-z$ faces creates etch-resistant features; large areas may be formed, which consist of many small individual features. Patterning has been achieved using both amplitude and phase masks, which results in self-ordering of the small features. The fluences used were below the ablation limit, so were lower than for $+z$ faces, and no surface damage was visible following exposure. However the formation of features was strongly dependent on the fluence, with etch resistance only being observed for a relatively narrow range of fluences. Scanning force microscopy could again resolve the presence of these features even before they were etched, additionally the spots could be 'erased' by application of 100 V to the SFM tip.

The origin of the UV-induced features on the $+z$ and $-z$ faces is still a matter of debate. However, the formation of micro-domains fits the available evidence, such as the etch-frustrated features on the $-z$ face and etched trenches on the $+z$ face. Micro-domain erasure by application of 100 V on the $-z$ face is also consistent with the voltages required to pole bulk areas of crystals, and the growth of trenches originating in pre-existing micro-domains on the $+z$ also supports the idea that these are optically-induced domains. The 1.8 μm depth of the trenches as measured on the $+z$ face also suggests that the origin of the features is more likely to be ferroelectric domains than surface charges. The UV light is of a wavelength that is strongly absorbed by lithium niobate, so the laser pulses result in rapid heating to ~1100 °C, which is close to the Curie temperature and could thus allow domain inversion. However, light-induced charge generation is likely to be an important part of the mechanism related to the formation of these domains, and may explain why only small trenches are formed rather than larger scale domains.

The results of the experiments described in this paper have been published; Valdivia et al. (2005) describes the results of $+z$ face exposure, while the $-z$ face results are presented in Sones et al. (2005a) and Mailis et al. (2005).

7.2.1 Future Work

There is scope for further refinement and development of the techniques described in this chapter to allow closer control over the structures which are formed. In particular, the ability to use spatially defined light patterns in $+z$ face exposure could allow the optical production of sub-micrometre periodic domain gratings. If required, subsequent electric field poling could be used to drive the domains all the way through the crystal. Submicron periodic domains would be extremely useful for UV quasi-phase-matching, electro-optic Bragg gratings and photonic crystal structures.

Recent work by Iain Wellington, Chris Valdivia and Collin Sones on UV exposure through a phase mask has been addressing the problem of controlling the patterns that are produced. An example of their results is shown in Figure 7.1 which shows an exposed and ablated area that has large regions of parallel trenches which are again believed to be domains. These would clearly be much more suitable for use as gratings.

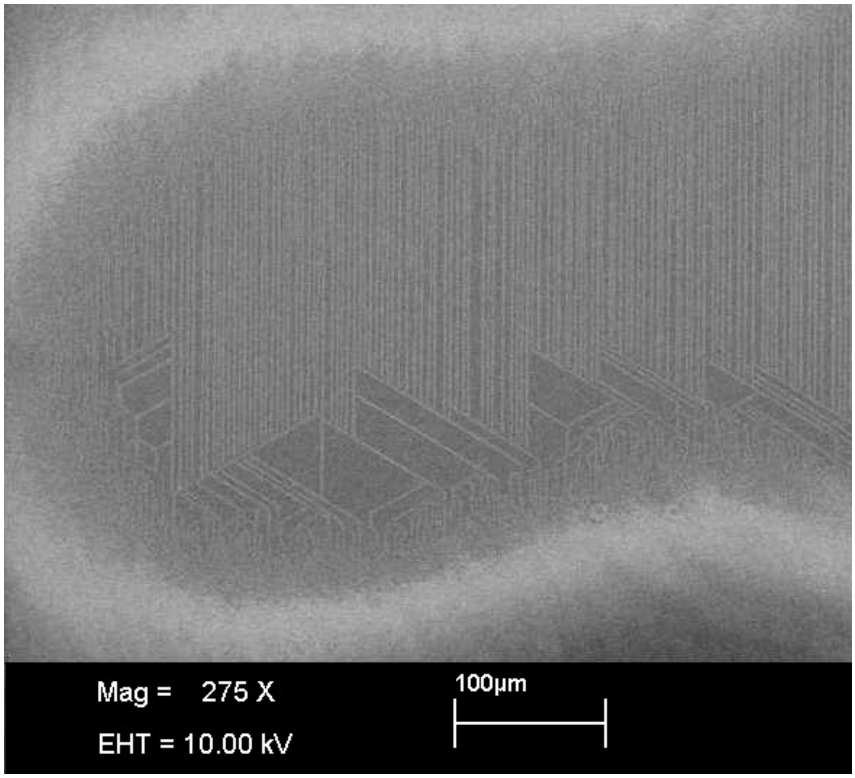

Figure 7.1: UV exposure through a phase mask of $+z$ face of lithium niobate.

Exposure of the $-z$ face also has great potential for producing controlled structures, especially if a laser with a more uniform beam was used, which would allow more precise control of the fluence applied and hence the features which are formed.

7.3 Raman Spectroscopy of Recently Poled Lithium Niobate

Raman spectroscopy was used to study the effect of the repoling process on lithium niobate. Using the Z(YY)Z back scattering configuration Raman spectra of lithium niobate were recorded before and after electric-field repoling.

Four spectra were taken at different locations on the $-z$ face before poling, then after poling the sample was returned to the spectrometer and spectra taken at regular intervals for four hours. Ten Raman peaks from each spectrum of lithium niobate were observed, which was as expected from group theory. Six of these were chosen for peak fitting to a Lorentzian curve to find their precise centres and each peak was also calibrated using a neon emission line that was recorded simultaneously with each Raman spectrum.

This analysis revealed that following poling, all six peaks showed a shift in position of $\sim$1 cm^{-1}, with some increasing in wavenumber, while others showed a decrease. Additionally, four of the peaks showed some evidence of recovery toward their original positions with time. Time constants for two the recovery of two peaks were deduced that fall in the range of several hours and above, and which is consistent with those previously published for ionic recovery processes whose time constants are in the hours to days region (and above). The time constant is 476 min for the 153 cm^{-1} peak and 250 min for the peak at 432 cm^{-1}.

The cause of this change and subsequent recovery following repoling is not known for certain at present, but is likely to be related to the internal field which has been measured to show recovery with similar time scales.

Raman spectroscopy was not used for analysis of LIFE and UV-induced structures, mainly due to the difficulty of positioning the sample accurately enough to be sure only the chosen structures were contributing to the Raman spectrum. Instead, surface SHG was examined for possible application to this area.

7.3.1 Future Work

Future experiments on the Raman spectroscopy of lithium niobate could include studying annealed samples to see if the annealing process allows the Raman peaks to return to their original (pre-poling) locations. The experiments described in Chapter 5 studied the change in position of the Raman peaks of a $-z$ face when it was poled to become $+z$, so the converse experiments, studying the $+z$ face being domain inverted to become $-z$ could also provide interesting results. A sample that had been forwards poled then backwards repoled could also be examined to see what effect, if any, this process would have.

As mentioned in the Discussion section of Chapter 5, the probe laser beam could influence the rate of recovery of the Raman peaks to their original positions. The influence of this could be studied by changing the beam power and checking for any corresponding change in the recovery time constants.

7.4 Surface Second Harmonic Generation

Surface SHG from lithium niobate has been shown to be a potentially very useful technique for non-destructively studying poled lithium niobate. It can be used to locate the x and y axes of the crystal, and distinguish between $+z$ and $-z$ faces of virgin crystals.

Experiments were conducted on poled lithium niobate samples. A fundamental pulsed laser beam of wavelength 532 nm was directed on to a lithium niobate surface and the reflected second harmonic signal at 266 nm was recorded as either a function of sample rotation angle, ϕ, or the angle of polarisation of the incident beam, γ.

The variation of SH signal with sample rotation was used to orientate the sample before further experiments were conducted. For a rotation of 120°two peaks were observed, as expected from theory. Measurements of the SH signal with input polarisation were compared for virgin and repoled $+z$ and $-z$ faces.

No significant difference was recorded in the SH signal from the +z and -z faces when the SH polarisation $\Gamma = s$, hence most results were recorded using $\Gamma = p$. The reason for this difference is clear when the equations for s and p polarised SHG, (using a p-polarised fundamental) are compared, as shown below.

$$E_p^{(2\omega)} = X\left[\sqrt{\frac{\epsilon_{t2}}{\epsilon_{m2}}}\sin\theta_{m2}c^2d_{31} + (\cos\theta_{t2})(\sin(3\phi)c^2d_{22}\right]E^2 \tag{7.1}$$

$$E_s^{(2\omega)} = Y\cos(3\phi)c^2d_{22}E^2 \tag{7.2}$$

$E_s^{(2\omega)}$ is dependent only on d_{22}, while $E_p^{(2\omega)}$ is dependent on d_{22} and d_{31}. As d_{31} has a component along the z axis, whereas d_{22} does not, it is likely that the measurement of d_{31} is sensitive to changes in the orientation of the crystal, and that the changes in SHG from a poled area also arise due to a change in d_{31}.

Surface SHG was shown to be able to distinguish between repoled and virgin areas, as a difference in SH intensity of 40 % occurred between a virgin $-z$ face and a recently repoled $+z$ face. It seems likely that this difference will recover over time, in a similar way to the shifted Raman peaks returned to their original wavenumber positions, as was discussed in Chapter 5. However, the recovery of SHG intensity appears to be slower than that of the Raman peaks, with only small increases in intensity occurring over six hours after poling. Measurements made after longer periods of time are inconclusive, as a three month-old sample shows complete recovery, while a four month-old sample has not fully recovered. The time dynamics of this process are thus suitable for further study, but due to time limitations could not be fully investigated as part of this PhD thesis.

7.4.1 Future Work

Further work could also be conducted to use surface SHG to measure the nonlinear coefficients, which would be of interest when using doped or modified lithium niobate, in waveguide applications for instance. The surface SHG technique could also be used to provide useful information on the period length in periodically poled lithium niobate, which is difficult to measure non-destructively with current techniques (for instance selective etching is routinely used to visualise PPLN, but this necessarily damages the crystal surface). This would work by selecting a suitable sample orientation and fundamental beam polarisation, and then scanning the beam across the PPLN (or moving the sample relative to the beam) and measuring the SH intensity. The alternating domains would affect the intensity and hence a plot of intensity versus position would reveal the period of the PPLN.

7.5 References

Crouch, C. H., J. E. Carey, J. M. Warrender, M. J. Aziz, E. Mazur and F. Y. Genin. "Comparison of structure and properties of femtosecond and nanosecond laser-structured silicon." *Applied Physics Letters*, **84**(11), 1850 (2004).

Mailis, S., C. L. Sones, J. G. Scott and R. W. Eason. "UV laser-induced ordered surface nanostructures in congruent lithium niobate single crystals." *Applied Surface Science*, **247**(1-4), 497 (2005).

Sones, C. L., C. E. Valdivia, J. G. Scott, S. Mailis, R. W. Eason, D. A. Scrymgeour, V. Gopalan, T. Jungk and E. Soergel. "Ultraviolet laser-induced sub-micron periodic domain formation in congruent undoped lithium niobate crystals." *Applied Physics B*, **80**, 341 (2005a).

Sones, C. L., M. C. Wengler, C. E. Valdivia, S. Mailis, R. W. Eason and K. Buse. "Light-induced order-of-magnitude decrease in the electric field for domain nucleation in MgO-doped lithium niobate crystals." *Applied Physics Letters*, **Accepted** (2005b).

Valdivia, C. E., C. L. Sones, J. G. Scott, S. Mailis, R. W. Eason, D. A. Scrymgeour, V. Gopalan, T. Jungk, E. Soergel and I. Clark. "Nanoscale surface domain formation on the +z face of lithium niobate by pulsed ultraviolet laser illumination." *Applied Physics Letters*, **86**(2), 022906 (2005).

APPENDIX

A

Diagnostic Equipment

A.1 Scanning Electron Microscope (SEM)

Scanning Electron Microscope (SEM) images have been used extensively throughout this work, to visualise the surface structures that have been created on lithium niobate. An SEM was chosen over an optical microscope due to the much higher resolution images that an SEM can achieve. As its name implies, an SEM uses a beam of electrons to create the image. The electrons are controlled using magnetic fields, which focus and scan the electron beams. Figure A.1 shows a schematic illustration of an SEM.

A beam of electrons are emitted from a tungsten filament in the electron gun and are then accelerated along the SEM tube by the anode. The electron beam is then collimated by condensing coils. Scanning coils are used to deflect the beam, typically to raster-scan over an area of the sample surface. A final magnetic objective then focusses the beam on to the sample surface. The SEM beam path and sample chamber requires a vacuum to operate, as otherwise gas molecules would hinder the electron beam and cause the filament to rapidly burn out.

When the primary electrons strike the surface of the sample, a number of interactions take place leading to the production of:

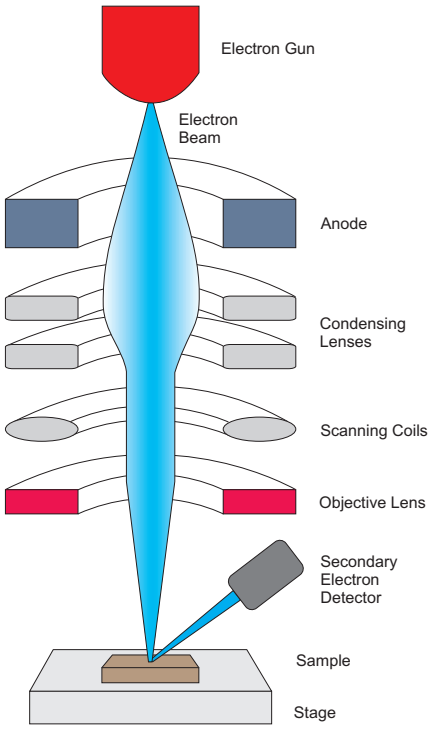

Figure A.1: Schematic diagram showing the components of a typical scanning electron microscope.

- **Backscattered electrons**: Elastically scattered primary electrons, of high energy.
- **Secondary electrons**: Lower energy electrons ejected from the valence-band of the material by the primary electrons.
- **Auger electrons**: The primary electrons may cause an electron to be ejected from inner shell orbitals, leaving a vacancy which is then filled by an electron from an outer shell. This can cause an Auger electron to be emitted to conserve energy.
- **X-rays**: The interaction of the primary electrons with the atoms of the sample can also result in X-ray emission.

The backscattered and secondary electrons are most commonly used in SEMs. Backscattered electrons can give topographic and compositional information about the material being examined, but because they can be scattered from within a relatively deep area, the topographic contrast is not as good as that obtained from secondary electrons, which originate from within a few Angstroms of the surface. For this reason, the secondary electrons are normally used to produce topographic

images. The electrons are detected by a scintillator-photomultiplier which passes the data to a computer for processing.

Sample preparation is relatively simple for use in an SEM, with the two requirements being that the sample must be able to resist the vacuum inside the sample chamber (which is usually only an issue for biological samples) and that the sample must be electrically conductive. When imaging non-conductive samples, a thin coating ~10 nm of gold can be applied using a sputter coater, to prevent charge build-up.

A.2 Focussed Ion Beam (FIB)

A focussed ion beam system operates in a very similar way to a scanning electron microscope, except that a beam of gallium ions are used instead of electrons. The gallium ions are emitted from a liquid-metal ion source.

FIBs can be used for imaging, but as their beam is positively charged the emission and detection of secondary electrons is reduced for insulators. However, the major advantage of FIBs is that they can be used for ion beam milling, where material can be removed from the surface of the sample being examined due to the momentum of the gallium ions. This is particularly useful for obtaining cross-sectional images and of course micro-machining and photolithographic mask repairs. FIB systems can also be used to selectively deposit metals such as platinum and tungsten.

A.3 Photospectrometer

A photospectrometer (also known as a UV/Vis spectrometer) is used to measure the absorption (or transmission) of light through a material over a range of wavelengths around the visible, including the near-UV and near-IR. The spectrometer used to obtain the results presented in this thesis was a Varian Cary 500 with a range of 175 - 3000 nm. The spectrometer consists of two light sources (one for visible/IR and one for UV), a chopper, a monochromator, a sample compartment and finally two detectors (a photomultiplier for UV/Visible light and a PbS detector for IR). A computer is then used for data collection. A simplified schematic diagram of a photospectrometer is shown in Figure A.2.

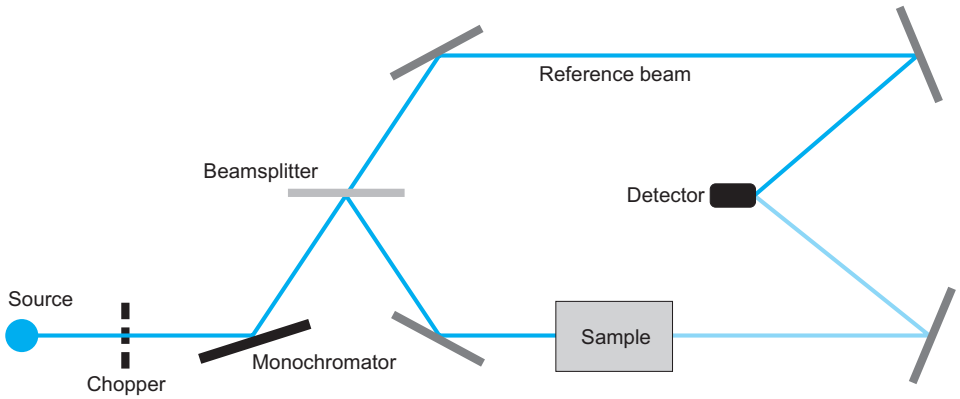

Figure A.2: Schematic diagram illustrating the operation of a photospectrometer.

A.4 Atomic Force Microscope (AFM)

Atomic force microscopy measures the forces between the atoms of a surface and those of a fine tip brought very close to the surface. These measurements, when combined with a scanning action of the tip allows the topography of a surface to be measured. The AFM tip is attached to a cantilever, which is deflected as the tip moves over the surface. This deflection is measured by a laser beam which is reflected from the top of the cantilever on to a quadrant photodiode detector. The signals from the detector are passed to lock-in amplifiers and on to a computer from processing. A piezoelectric tube is used to provide very precise positioning and scanning of the sample. The operation of an AFM is illustrated in Figure A.3.

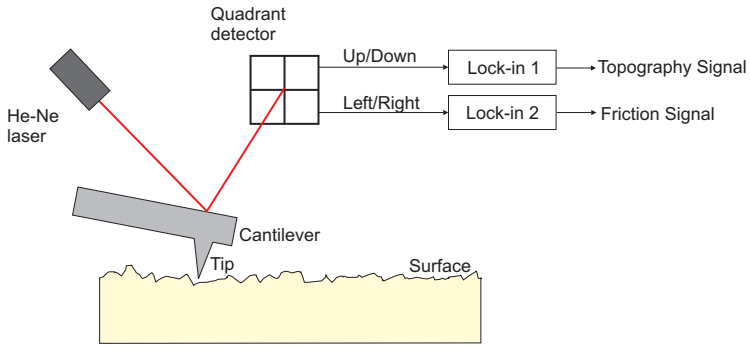

Figure A.3: Schematic diagram illustrating the operation of an atomic force microscope.

An AFM usually uses a feedback loop, where the height of the tip as adjusted as it moves over the surface to maintain a constant force, and prevent the tip from crashing into the surface. However, the feedback system can be bypassed, in which

case the tip is positioned at a constant height and the force measured. This is generally only used for very flat samples.

The interaction between the tip and surface can be described by the Lennard-Jones potential, which has the form:

$$V_{LJ} = 4\epsilon\left[\left(\frac{\sigma}{r}\right)^{12} - \left(\frac{\sigma}{r}\right)^{6}\right] \tag{A.1}$$

where ϵ and σ are parameters that depend on the interacting atoms and r is the separation between them. This relationship is plotted in Figure A.4. At fairly large separations the force is attractive and becomes greater as r decreases. But once the minimum in V_{LJ} is reached, any further decrease in r causes the potential to rapidly increase and become repulsive (as is normally experienced when two objects are pushed together).

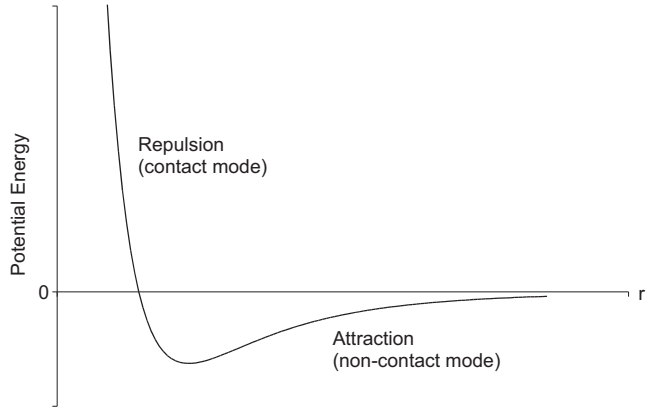

Figure A.4: The Lennard-Jones potential.

The contrast in AFM images can be obtained from either the attractive or repulsive regime, using the attractive force is known as *non-contact mode*, while *contact mode* uses the repulsion between atoms. Contact mode is the most commonly used in AFM, as the magnitude of the force is larger, and so easier to detect. There is also a large lateral force exerted on the tip in contact mode, caused by friction, which may also be measured. However, this can be a problem as it may cause damage to the tip, which reduces the resolution of the AFM. This can be avoided by using non-contact mode, but the smaller forces experienced by the tip make measurement difficult.

An alternative to is to use a compromise called *tapping mode*, where the cantilever is placed above the surface, and then oscillated at its resonant frequency. In this way,

the tip still makes contact with the surface, but only for a short time during each oscillation. The interaction between the tip and the surface affects the oscillation, so a topographic image can be formed by measurements of the amplitude of the oscillations. The phase difference between the piezo driving oscillations and the detected oscillations can also be used to form an image which reveals other properties such as elasticity and adhesion of the sample.

The main advantage of AFMs over SEMs is that quantitative measurements on feature height, surface roughness and friction can be made. Additionally, little sample preparation is necessary to image any surface (both conductors and insulators) and no coatings are required. It is also suitable for non-destructive imaging of biological samples as an AFM does not need to be operated in a vacuum.

However, AFMs can only image relatively small areas, with maximum sizes of around 80 by 80 μm, which compares poorly with the millimeter by millimeter areas possible with SEM. The time taken to obtain large, high-resolution images by AFM can also be considerably longer than the equivalent required for SEM, as the tip has to physically scan a single line at a time, and slower scanning speeds give better results.

APPENDIX

B

Matlab Scripts

Appendix B contains the source code of the programs that were used to produce the Fourier transform images and LIFE model referred to in the main script. They were written in Matlab Version 6, Release 12.

B.1 Fourier Transforms

B.1.1 Simple Fourier transform routine

```
im=imread('filename.tif'); % filename must start with a letter
crop=im(200:350, 200:350);
ftrans=fft2(crop,1024,1024);
shift=fftshift(ftrans);
logabshift=log(abs(shift));

subplot(1,2,1); imshow(crop,[]), title('Original Image')
subplot(1,2,2); imshow(logabshift,[]), title('Log of Abs of Fourier
    Trasform of Image'), %colormap(bone)

aa=max(logabshift(:));
bb=255/aa;
scalab=logabshift*bb;
ulas=uint8(scalab);
imwrite(ulas, ['outputfilename.tif'])
```

B.1.2 Advanced Fourier transform routine

```
% SEM Fourier Transform Routine - for ORC SEM - also produces a circular
    average line

clear

name='h80-q-02' % enter name of file - must start with a letter
mag=2000 % enter the magnification of the image here

tif='.tif';
jpg='.jpg';

sem=imread([name,tif]);
crop=imcrop(sem,[0,0,729,729]); %Reduces SEM image to a square
ftrans=fft2(crop); % performs fourier transform, NB no padding the
    original image
shift=fftshift(ftrans); % shifts the ft so that the zero frequency
    component is in the centre
logabshift=log(abs(shift)); % takes log and abs of ft, to improve
    contrast.

if mag == 500
    lengthofscalebar=14; %in pixels
    valueofscalebar=10; % in microns
    axlab=[ -0.6 -0.4 -0.2 0 0.2 0.4 0.6];
end

if mag == 1000
    lengthofscalebar=30;
    valueofscalebar=10;
    axlab=[-2.5 -2 -1.5 -1 -0.5 0 0.5 1 1.5 2 2.5];
end

if mag == 2000
    lengthofscalebar=63; %in pixels
    valueofscalebar=10; % in microns
    axlab=[-3 -2 -1 0 1 2 3];
end

if mag == 4000
    lengthofscalebar=264;
    valueofscalebar=20;
    axlab=[-6 -4 -2 0 2 4 6];
end

if mag == 5000
    lengthofscalebar=14;
    valueofscalebar=1;
    axlab=[-6 -4 -2 0 2 4 6];
end

if mag == 10000
    lengthofscalebar=662;
    valueofscalebar=20;
    axlab=[-16 -12 -8 -4 0 4 8 12 16];
```

```
end

[semheight,semwidth]=size(sem);
[cropheight,cropwidth]=size(crop);
[ftheight,ftwidth]=size(logabshift);
a=(semwidth/lengthofscalebar)*valueofscalebar;
b=(semheight/lengthofscalebar)*valueofscalebar;
c=(cropheight/lengthofscalebar)*valueofscalebar;
sempixel=valueofscalebar/lengthofscalebar; % a pixel in the original SEM
    image represents this many microns in real life.
ftpixel=(1/(ftwidth*sempixel));
ftscale=ftpixel*ftwidth*0.5;

iptsetpref('ImShowAxesVisible','on')
j=figure(1);
set(j,'papertype','a4')
set(j,'paperpositionmode','auto')

subplot(2,1,1), imshow([0,a], [0,b],sem), title(['Original Image - ',name
    ]), xlabel('microns'),ylabel('microns')
subplot(2,2,3), imshow([0,c],[c,0],crop,[]), title('Cropped Area of Image
    for FT'),xlabel('microns'),ylabel('microns'),set(gca,'YDir','normal')
    ,set(gca,'xDir','normal')
subplot(2,2,4), imshow([-ftscale,ftscale],[ftscale,-ftscale],logabshift
    ,[]), title('Fourier Transform of Image'), set(gca,'YDir','normal'),
    set(gca,'xDir','normal'), xlabel('microns^-^1'),ylabel('microns^-^1'),
    set(gca,'ytick',axlab),set(gca,'xtick',axlab)

ft='ft';
fti='fti';

saveas(j, [ft,name,jpg])

scalab=uint8(logabshift*255/(max(logabshift(:)))); %rescales logabshift
    and converts to uint8 for saving
imwrite(scalab, [fti,name,jpg])

% This section produces a 1D plot, by summing multiple points on a line
    from the centre of the FT

line=zeros(2,351);
line(1,:)=(0:350)*ftpixel;
line=line';
count=0;
for n=0:350
    count=count+1;
for theta=0:359
    i=fix(365+n*sin(theta*pi/180)); %rounds to zero
    j=fix(365+n*cos(theta*pi/180));
    line(count,2)=line(count,2)+logabshift(i,j);
end
end

li='li';
fig2=figure(2);
%plot(line(:,1),line(:,2))
```

```
xdata=line(50:175,1); %choose the range of the gaussian fit here
ydata=line(50:175,2); % and here.
xdata=xdata';
ydata=ydata';

x0=[0.5,3000,1000,1];
options=optimset('lsqcurvefit');
options=optimset('MaxIter',800,'MaxFunEvals',4000);
lb=[];
ub=[];
[x,resnorm,residual,exitflag,output]=lsqcurvefit(@gauss,x0,xdata,ydata,lb
    ,ub,options)
y=gauss(x,xdata);

result=mat2str(x(1),4) % Displays the value for x0
plot(line(:,1),line(:,2),xdata,y), xlabel('Spatial␣Frequency␣/␣microns
    ^-^1'), ylabel('Intensity␣of␣Fourier␣Transform␣/␣arb.␣units'), title([
    '1D␣Sum␣of␣2D␣Fourier␣Transform␣from␣image␣',name,'␣with␣x0␣=␣',result
    ,'␣microns^-^1']);
saveas(fig2,[li,name,jpg])
```

B.2 Life Model

```
% Life Model v5

% Takes FT
% Leaves a 5 pixel border
% program stops if no spots are growing
% Easily adjustable canvas size
% Gaussian Distribution of dots

clear
n=10000 % number of spots
canvas=550 % pixels wide by pixels high (square)

% ---- Creates empty matrices and defines things

area=uint8(zeros((canvas))); % allows 'area' to have values 255 to 0,
startspots=zeros(n,2);
spots=zeros(n,2);
spotdir=zeros(n,1);
spotstop=zeros(n,1);
changedirtime=zeros(n,1);
t=0;
centre=canvas/2;

% ---- Random Number Bit for Gaussian spot location and direction

gausswidth=canvas/6;

for i=1:n
for j=1:2
while startspots(i,j)==0
    x2=(rand*(canvas-20)+10); % choose a random number, within canvas
        limits
```

```
    prob=(exp(-0.5*(((x2-centre)/gausswidth)^2))); % calculate
        probability, giving guassian shape
if prob > rand
    startspots(i,j)=round(x2);
end
end
end
end

spotdir=round((rand(n,1).*2))*120; % choose 1 of 3 directions for spots
spots=startspots;

for i=1:n
area(startspots(i,2),startspots(i,1))=255;
end

% ---- main loop repeats until all spots are stopped
while ~all(spotstop)
    t=t+1;
changedir=zeros(n,1);

for i=1:n

% ---- checks for screen edges
if (spots(i,1) == 6) | (spots(i,2) == 6) |( spots(i,1) == (canvas-6)) | (
    spots(i,2) == (canvas-6))
    spotstop(i,1)=1;
end

% ---- collision detection - no line 5 pixels from new spot

if (spotdir(i,1) == 0) & (spotstop(i,1) ==0)
for x=-3:3, for y=-4:-1
if (area((spots(i,2)+y),(spots(i,1)+x))==255)
    spotdir(i,1)=round((rand+1))*120; % changes spot direction if blocked
        to 120 or 240 degrees
    startspots(i,2)=spots(i,2);
    startspots(i,1)=spots(i,1);
    changedirtime(i,1)=t-1;
    changedir(i,1)=changedir(i,1)+1;
end, end, end, end

if changedir(i,1)>2;
    spotstop(i,1)=1;
end

if (spotdir(i,1) == 120) & (spotstop(i,1) ==0)
for x=1:5, for y=-2:3
if (spotdir(i,1) == 120) & (area((spots(i,2)+y),(spots(i,1)+x))==255) & (
    spotstop(i,1) ==0)
    spotdir(i,1)=240*(round(rand)); % changes spot direction if blocked
        to 0 or 240 degrees
    startspots(i,2)=spots(i,2);
    startspots(i,1)=spots(i,1);
    changedirtime(i,1)=t-1;
    changedir(i,1)=changedir(i,1)+1;
end, end, end,end
```

```
if changedir(i,1)>2;
    spotstop(i,1)=1;
end

if (spotdir(i,1) == 240) & (spotstop(i,1) ==0)
for x=-5:-1, for y=-2:3
if (spotdir(i,1) == 240) & (area((spots(i,2)+y),(spots(i,1)+x))==255) & (
    spotstop(i,1) ==0)
    spotdir(i,1)=120*round(rand); % changes spot direction if blocked to
        0 or 120 degrees
    startspots(i,2)=spots(i,2);
    startspots(i,1)=spots(i,1);
    changedirtime(i,1)=t-1;
    changedir(i,1)=changedir(i,1)+1;
end, end, end, end

if changedir(i,1)>2;
    spotstop(i,1)=1;
end

% ----  grows the lines

r=t-changedirtime(i,1);

if (spotdir(i,1) == 0) & (spotstop(i,1) ==0)
    spots(i,2)=startspots(i,2)-r;
    area(spots(i,2),spots(i,1))=255;
if  area((spots(i,2)),(spots(i,1))-1)~=255;
    area((spots(i,2)),(spots(i,1))-1)=175;
end
if area((spots(i,2)),(spots(i,1))+1)~=255;
   area((spots(i,2)),(spots(i,1))+1)=175;
end
end

if (spotdir(i,1) == 120) & (spotstop(i,1) == 0)
    dy=sin(pi*30/180)*r;
    dx=cos(pi*30/180)*r;
    spots(i,2)=fix(startspots(i,2)+dy);
    spots(i,1)=fix(startspots(i,1)+dx);
    area(spots(i,2),spots(i,1))=255;
if  area((spots(i,2)-1),(spots(i,1)))~=255;
    area((spots(i,2)-1),(spots(i,1)))=175;
end
if area((spots(i,2)+1),(spots(i,1)))~=255;
   area((spots(i,2)+1),(spots(i,1)))=175;
end
end


if (spotdir(i,1) == 240) & (spotstop(i,1) == 0)
    dy=sin(pi*30/180)*r;
    dx=cos(pi*30/180)*r;
    spots(i,2)=fix(startspots(i,2)+dy);
    spots(i,1)=fix(startspots(i,1)-dx);
    area(spots(i,2),spots(i,1))=255;
```

```
    if area((spots(i,2)-1),(spots(i,1)))~=255;
    area((spots(i,2)-1),(spots(i,1)))=175;
    end
    if area((spots(i,2)+1),(spots(i,1)))~=255;
    area((spots(i,2)+1),(spots(i,1)))=175;
    end
end
end
imshow(area),axis on
%f=getframe;
end

%movie(f,1,30)
lifemodel='Gaussian Life model - ';
jpg='.jpg';
spots=' spots - ';
can=' canvas';
fou='g FT - ';
num=int2str(n);
canvassize=int2str(canvas);
imwrite(area,[lifemodel,num,spots,canvassize,can,jpg]);

ft=fft2(area);
shift=fftshift(ft);
logabshift=log(abs(shift));
aa=max(logabshift(:));
bb=255/aa;
scalab=logabshift*bb;
ulas=uint8(scalab);
imwrite(ulas, [fou,num,spots,canvassize,can,jpg])
```

APPENDIX

C

Publications

The publications that have arisen from work presented in this thesis are listed below.

C.1 Journal Publications

J. G. Scott, S. Mailis, C. L. Sones and R. W. Eason. "A Raman study of single-crystal congruent lithium niobate following electric-field repoling." *Applied Physics A*, **79**, 691, (2004).

J. G. Scott, A. J. Boyland, S. Mailis, C. Grivas, O. Wagner, S. Lagoutte and R. W. Eason. "Self-ordered sub-micron structures in Fe-doped $LiNbO_3$ formed by light-induced frustration of etching." *Applied Surface Science*, **230**, 138, (2004).

C. E. Valdivia, C. L. Sones, J. G. Scott, S. Mailis, R.W Eason, D. A. Scrymgeour, V. Gopalan, T. Jungk, E. Soergel, I. Clark. "Nanoscale surface domain formation on the +z face of lithium niobate by pulsed UV laser illumination." *Applied Physics Letters*, (2005).

C.2 Conference Publications

J. G. Scott, A. J. Boyland and R. W. Eason. "Sub-micron filamentary structures formed during light induced frustrated etching of Fe-doped lithium niobate: Results and modelling." *CLEO Europe/EQEC*, Munich, 22-27 June 2003.

C. L. Sones, J. G. Scott, R. W. Eason, S. Mailis. "Laser induced organisation and size control of nano-scale etch-resistant features in lithium niobate single crystals." *CLEO/IQEC 2004*, San Francisco, 16-21 May 2004.

T. Sono, L. Danos, J. G. Frey, J. G. Scott, S. Mailis and R. W. Eason. "Second harmonic generation (SHG) via reflection from +z and −z faces of a z-cut $LiNbO_3$ crystal." *Chemical Physics Conference: Perspective and Prospects*, Orsay, France, 5-8 July 2004.

C. E. Valdivia, C. L. Sones, J. G. Scott, S. Mailis, R. W. Eason, D. A. Scrymgeour, V. Gopalan and I. Clark. "Nano-scale ultraviolet laser-induced ferroelectric surface domains in lithium niobate." *CLEO Europe*, Munich, 12-17 June 2005, (Invited).

S. Mailis, C. L. Sones, C. E. Valdivia, I. T. Wellington, A. C. Muir, J. G. Scott and R. W. Eason. "UV radiation-induced surface wetting changes in lithium niobate single crystals." *CLEO Europe*, Munich, 12-17 June 2005.

C.3 Related Publications

S. Mailis, C. Riziotis, P. G. R. Smith, J. G. Scott, and R. W. Eason. "Continuous wave ultraviolet radiation induced frustration of etching in lithium niobate single crystals." *Applied Surface Science*, **206**, 46, (2003).

S. Mailis, C. L. Sones, J. G. Scott, I. E. Barry, P. G. R. Smith and R. W. Eason. "Microstructuring lithium niobate: A multi-directional approach." *Recent Research Developments In Applied Physics*, **7**, 333, (2004).

C. L. Sones, C. E. Valdivia, J. G. Scott, S. Mailis, R. W. Eason, D. A. Scrymgeour, V. Gopalan, T. Jungk and E. Soergel. "Ultraviolet laser induced sub-micron periodic domain formation in congruent undoped lithium niobate crystals." *Applied Physics B*, **80**, 341, (2004).

S. Mailis, C. L. Sones, J. G. Scott and R. W. Eason. "UV laser-induced ordered surface nanostructures in congruent lithium niobate single crystals." *Applied Surface Science*, **247**, 497, (2005).